The origin and basin-wide distribution of clay-coated grains in siliciclastic reservoirs: Insights from modern analogues, ancient analogues and clay coat synthesis and transformation experiments

Volume 1

Alison Hendry



This thesis is submitted in partial fulfilment for the degree of Doctor of Philosophy from the School of Natural and Environmental Sciences at Newcastle University

November 2024

Abstract

This thesis used an experimental approach to study the formation and diagenetic transformation of precursor clay coats. In biotic microcosms, clay-coat coverage increased with *chlorophyll-a* and total carbohydrate concentration (proxies for biofilm abundance). This confirms that biofilms promote the formation of clay-coated grains. In abiotic microcosms, clay-coat coverage increased with increasing salinity. This indicates that clay coats can also form in the absence of biofilms.

Hydrothermal pressure chamber experiments were conducted using sediment from Ravenglass Estuary at a pressure of 10MPa and varying temperature (60, 90, 150 and 250°C). Clay mineral coatings, with a composition like authigenic chlorite, formed during the experiments carried out at 150 and 250°C. This indicates that authigenic chlorite can form from clay coats taken from modern day analogues via pressure chamber experiments.

Clay-coated grains in a modern deep marine (Bute Inlet) and a shallow marine (Ravenglass Estuary) setting were studied. Clay coats in Ravenglass Estuary showed a positive correlation with total carbohydrate and *chlorophyll-a* content, confirming a biofilm origin for clay-coated grains. Clay-coat coverage was low in Bute Inlet. Clay coats in Bute Inlet showed no relationship with total carbohydrate or *chlorophyll-a*. Analysis of mineralogical and textural data suggest detrital mineralogy and sediment maturity exhibits a significant control on the formation of clay-coated grains.

The results from the experimental and modern analogue studies were used to study chlorite-coated grains in the Mid Jurassic Brent Group, North Sea. Chlorite coats were present in low amounts and had a minor effect on reservoir quality. Reservoir quality was controlled by grain size and facies. Chlorite coat coverage and abundance was variable within facies and showed no relationship with texture.

The results and conclusion from this thesis can be utilized in future academic and industry research aiming to predict the distribution of clay-coated grains in subsurface reservoirs.

Acknowledgements

Firstly, I would like to thank my parents Judith and Charles for their ongoing support throughout my studies, I would not have been able to complete my PhD if it were not for their financial and emotional support over the past three years.

A huge thank you to my sister Lauren for being an amazing listener, flat mate, best friend, confidant, comedian, questionable chef, even more questionable dish washer and all-round cheerleader during my PhD. My PhD would not have been as enjoyable without her sunny demeanour and 6.30am wake up calls, every day.

I would also like to thank my partner Stephen for being my ‘favourite rock of all” and for being a 6ft6 shoulder to cry on during challenging aspects of my PhD.

Special thanks to my supervisors Sanem Acikalin, Sven Lahme, Cees van der Land and Shannon Flynn for all their support and guidance through-out my three years at Newcastle University.

Thank you to the Engineering and Physical Science Research Council (EPSRC) for funding my PhD. I hope that this project meets their expectations and can help drive and develop future projects. I would also like to thank the International Association of Sedimentologists (IAS) for providing me with a research grant to help fund my trip to British Columbia, Canada.

Many thanks to the research staff and crew of John Strickland and CCGS Vector for their help with fieldwork planning, execution, and sample collection during the 2018 cruise of Bute Inlet, British Columbia, Canada.

I would also like to thank Dimitrios Charlaftis and Stuart Jones from Durham University for collaborating during pressure chamber experiments and for providing in depth discussions on the transformation of clay minerals during burial and diagenesis.

Lastly, I would like to thank Gareth Rogers at CGG Robertson for his support running QEMSCAN analysis and Dorothy Pane from Badley Ashton for her support conducting SEM analysis on samples from Bute Inlet, Ravenglass Estuary, and pressure chamber experiments.

Table of contents **Page**

Chapter 1. Introduction 1
1.1 Background 1
1.1.1 Reservoir quality 2
1.1.2 Quartz overgrowths 2
1.1.3 Allogenic vs authigenic clay coated grains 3
1.2 Current knowledge on clay-coated grains in siliciclastic reservoirs 5
1.2.1 Inhibition of quartz cement by clay-coated grains 5
1.2.2 Chlorite coated grains 6
1.2.3 Clay coating via bioturbation 7
1.2.4 Large scale controls on the formation of clay-coated grains 7
1.3 Major challenges associated with predicting the distribution of chlorite coats 9
1.4 The role of biofilms in the formation of clay-coated grains 9
1.4.1 Sedimentation of diatoms 11
1.4.2 Quantitative analysis of EPS and biofilms 12
1.5 Current approaches to predicting the distribution of chlorite-coated grains 14
1.6 Study approach 14
1.7 Research themes and questions 16
1.7.1 The origin and distribution of precursor clay-coated grains in shallow marine and deep-water turbidite systems 18
1.7.2 The transformation of precursor clay-coated grains during burial and diagenesis 20
1.7.3 The origin and distribution of clay-coated grains in ancient sandstone reservoirs 21
1.8 Organisation of thesis 21

Chapter 2. Materials and Methods 26
2.1 Modern analogue study sites 26
2.1.1 Bute Inlet 26
2.1.2 Ravenglass Estuary 30
2.2 Sampling of modern sediment 33
2.3 Grain size analysis 36

2.4 Chlorophyll-a analysis 36
2.5 Extracellular polymeric substance (EPS) analysis 37
2.5.1 Colloidal and bound EPS extraction 37
2.5.2 Colloidal and bound EPS quantification 38
2.6 Petrography 40
2.6.1 Clay-coat grain coverage and abundance quantification 40
2.6.2 QEMSCAN mineralogy analysis 42
2.7 Scanning electron microscopy (SEM) and energy dispersive spectroscopy (EDS) analysis 42
2.8 Ancient study site 43
2.8.1 Don field and Don Southwest field, block 211/18, northern North Sea 43
2.8.2 Sedimentary logging of ancient cores 45
2.8.3 Analysis of thin sections from ancient cores 46
2.9 Statistical analysis 46
2.10 Biofilm and saline clay coat synthesis experiments 47
2.10.1 Cultivation of diatoms 47
2.10.2 Biofilm clay coat synthesis experiments 49
2.10.3 Salinity clay coat synthesis experiments 50
2.11 Clay coat transformation pressure chamber experiments 51
2.11.1 Geochemical modelling of the precipitation of minerals during pressure chamber experiments 53

Chapter 3. Biofilm and salinity controls on the formation of clay-coated grains 54
ABSTRACT 54
3.1 Introduction 55
3.1.1 Biofilm-sediment interactions 56
3.1.2 Clay flocculation due to high salinity 57
3.1.3 Research theme and questions 57
3.2 Materials and methods 58
3.2.1 EPS clay coat synthesis experiments 58
3.2.2 Salinity clay coat synthesis experiments 59

3.2.3 Clay coat synthesis experiment sampling 60
3.2.4 Sediment analysis 60
3.3 Results 62
3.3.1 EPS concentration 62
3.3.2 Relationship between EPS and clay coat grain coverage 64
3.3.4 Relationship between salinity and clay coat grain coverage 68
3.4 Discussion 71
3.4.1 The impact of biofilms on the formation of clay-coated grains 71
3.4.2 The impact of salinity on the formation of clay-coated grains 71
3.4.3 Chlorophyll-a as a proxy for EPS concentration 72
3.5 Conclusion and recommendations 72

Chapter 4. The origin and distribution of clay-coated grains in shallow and deep marine sedimentary systems 74
ABSTRACT 74
4.1 Introduction 75
4.1.1 Research theme and questions 78
4.1.2 Geological setting 78
4.2 Materials and methods 83
4.2.1 Sediment sampling 83
4.2.2 Sediment analysis 85
4.2.3 Mapping 86
4.2.4 Pearson correlation coefficient analysis 86
4.3 Results 86
4.3.1 Textural analysis 86
4.3.2 Mineralogy 94
4.3.3 EPS analysis 96
4.3.4 Clay-coat coverage 101
4.3.5 SEM analysis 105
4.4.1 Bute Inlet statistical analysis 109
4.4.2 Ravenglass Estuary statistical analysis 119
4.5 Discussion 130

4.5.1 Distribution of EPS across shallow marine and deep-water turbidite systems 130
4.5.2 Relationship between clay coat coverage and EPS across shallow marine and deep-water turbidite systems 131
4.5.3 Textural controls and depositional controls on clay coat formation in modern shallow marine and deep-water turbidite system analogues 132
4.5.4 The formation of precursor clay-coated grains in modern shallow marine and deep-water turbidite system analogues 133
4.6 Conclusion 134

Chapter 5. The transformation of precursor clay coats during diagenesis 135
ABSTRACT 135
5.1 Introduction 136
5.1.1 Research theme and questions 137
5.2 Materials and methods 138
5.2.1 Sediment sampling 139
5.2.2 Experiment set up 139
5.2.3 Thin section analysis 140
5.2.4 Automated mineralogy 142
5.2.5 SEM and EDS analysis 142
5.2.5 Geochemical modelling 142
5.3 Results 143
5.3.1 Surface sediment 143
5.3.2 60°C, 10MPa Experiment 147
5.3.3 90°C, 10MPa experiment 149
5.3.4 150°C, 10MPa experiment 151
5.3.5 250°C, 10MPa experiment 153
5.3.6 Geochemical modelling 156
5.4 Discussion 162
5.4.1 The transformation of precursor clay-coats 162
5.4.2 Comparison of clay coats formed in pressure chamber experiments and natural chlorite-coated sandstone reservoirs. 163
5.5 Conclusion 163

Chapter 6. Chlorite clay-coated grains and their effect on reservoir quality in Mid Jurassic Brent Group reservoirs, northern North Sea 165
ABSTRACT 165
6.1 Introduction 166
6.1.1 Regional geology 168
6.1.2 Research theme and questions 171
6.2 Materials and methods 172
6.2.1 Wells and data sets 172
6.2.2 Pearson's correlation coefficient analysis 173
6.3 Results 173
6.3.1 Facies and interpretations 173
6.3.2 Texture and mineralogy 184
6.3.3 Authigenic chlorite clay-coated grains 187
6.3.4 Paragenesis of authigenic phases 188
6.3.5 Reservoir quality 189
6.3.6 Statistical analysis 191
6.4 Discussion 193
6.4.1 Textural and depositional controls on the formation of clay-coated grains 193
6.4.2 The origin of clay-coated grains 194
6.4.3 Comparison of clay coated grains in the ancient case study and the shallow marine modern analogue system 197
6.5 Conclusion 197

Chapter 7. Summary and further work 199
7.1 Overview 199
7.2 The origin and distribution of precursor clay-coated grains in shallow marine and deep-water turbidite systems 199
7.2.1 How does EPS content and salinity impact the formation of clay-coated grains in the clay coat synthesis experiments? 199
7.2.2 How is EPS distributed across modern shallow marine and deep-water turbidite system analogues? 200

7.2.3 Is there a relationship between EPS content and clay coat coverage in modern shallow marine and deep-water turbidite system analogues? 201
7.2.4 What are the textural and depositional controls on clay coat formation in modern shallow marine and deep-water turbidite system analogues? 202
7.2.5 How are precursor clay-coated grains formed in modern shallow marine and deep-water turbidite system analogues? 203
7.3 The transformation of precursor clay coats during burial and diagenesis 203
7.3.1 How do precursor clay mineral coats transform during diagenesis to form authigenic clay mineral coats? 203
7.3.2 Are authigenic clay coats formed during pressure chamber experiments comparable to authigenic clay coats present in natural settings? 204
7.4 The origin and distribution of clay-coated grains in ancient sandstone reservoirs 205
7.4.1 What are the textural and depositional controls on the formation of clay-coated grains in the ancient reservoir case study? 205
7.4.2 What is the origin of clay-coated grains present in the ancient sandstone reservoir case study? 206
7.4.3 How does the distribution of chlorite coats in the ancient case study compare to the distribution of precursor clay coats in the shallow marine modern analogue system? 207
7.5 The wider importance of EPS 207
7.6 Application of machine learning to clay coat analysis 208
7.7 Analysis of clay coated grains for carbon capture and storage projects 209

References 211

List of figures **Page**

Figure 1.1. Reservoir units of the Halten Terrace, offshore mid-Norway. A) Chlorite-coated reservoir unit from Tilje Formation, Smørbukk Field, chlorite coats (chl) are well developed around detrital quartz (qtz) grains. B) Quartz-cemented reservoir unit from Garn Formation, Kristin Field (modified from Martinius et al., 2005). 2

Figure 1.2. A) Allogenic and B) authigenic clay-coated grains (modified from Wilson, 1992). 4

Figure 1.3. Likely and unlikely scenarios for the development of chlorite-coated grains in sandstone reservoirs (Dowey et al., 2012). 9

Figure 1.4. SEM image of clay-coated sand grain (Wooldridge et al., 2017a). 10

Figure 1.5. Conceptual diagram of microbial biofilm developed at the sediment-water interface (modified from Decho, 2000). 11

Figure 1.6. Summary of the main research themes and research questions addressed in this study. 17

Figure 2.1. A) Bathymetric map of Bute Inlet (modified from Pope et al., 2022). B) – G) East-West channel cross section at the mooring points M1, M2, M3, M4, M5 and M6. H) Number of density flows observed at each mooring point between March and November 2018. 28

Figure 2.2. Simplified map of gross depositional environments across Bute Inlet (modified from Hage et al., 2022). 29

Figure 2.3. Bathymetric map of Ravenglass Estuary (modified from Griffiths et al., 2018). 31

Figure 2.4. Depositional sub-environments across Ravenglass Estuary (Griffith et al., 2018). 32

Figure 2.5. Map of sample locations across Bute Inlet. Black dots = sample locations (n=71). Produced using ArcGIS Pro Version 3.2 34

Figure 2.6. Map of sample locations across Ravenglass Estuary. Black dots = sample locations (n = 76). Produced using ArcGIS Pro Version 3.2. 35

Figure 2.7. Plate containing completed phenol sulphuric acid assay reaction. 39

Figure 2.8. Standard curve constructed to quantify the carbohydrate content of samples. 39

Figure 2.9. Method used to quantify grain clay-coat coverage in petrographic thin sections. 40
Figure 2.10. Examples of different clay coat morphologies from Wooldridge at al., 2017b a) and b) are a ridged clay coat, c) and d) are a bridged clay coat and e) and f) are a clumped clay coat. 41
Figure 2.11. Map showing location of study wells and the Don field and Don Southwest field (map obtained from Oil and Gas Authority. 2015). 44
Figure 2.12. Gross depositional environment for the Dons area of the Brent Delta (Went et al., 2013). A) Sea level lowstand emphasizing the lowstand fluvio-estuarine channels. B) Sea-level highstand emphasizing the progradational shoreface and back barrier facies. 45
Figure 2.13. Growth curve for Chaetoceros sp. Black dots = average of three replicates. Error bar = Standard deviation 48
Figure 2.14. EPS clay coat synthesis experimental set up 50
Figure 2.15. Salinity clay coat synthesis experimental set up 51
Figure 2.16. Hydrothermal pressure chamber experimental set up 52
Figure 3.1. Chlorophyll-a content for the 15-day EPS experiment. Error bars represent the standard deviation across three replicates 63
Figure 3.2. Total carbohydrate content for the 15-day EPS experiment. 63
Figure 3.3. Average clay-coat grain coverage vs total carbohydrate concentration. 65
Figure 3.4. Thin section images of clay coat synthesis EPS experiments. 66
Figure 3.5. SEM images of clay coat synthesis EPS experiments. 67
Figure 3.6. Average clay-coat grain coverage vs salinity 68
Figure 3.7. Thin section images of clay coat synthesis salinity experiments. 69
Figure 3.8. SEM images of clay coat synthesis salinity experiments. 70
Figure 4.1. Map of Bute Inlet (Hage at al., 2022). A) Location of Bute Inlet within British Columbia, Canada. B) Map showing watershed of the Homathko and Southgate rivers which feed Bute Inlet. 80
Figure 4.2. Generalized geology map of western British Columbia (Cecil et al., 2018). 81

Figure 4.3. Geological setting of the Ravenglass Estuary, United Kingdom (Griffiths et al., 2019). A) Bedrock geology with estuarine zones lower Irt. B) Quaternary drift deposits. 82
Figure 4.4. Mean grain size across Bute Inlet, B.C, Canada. 90
Figure 4.5. Grain sorting across Bute Inlet, B.C, Canada. 91
Figure 4.6. Grain size across Ravenglass Estuary. 92
Figure 4.7. Grain sorting across Ravenglass Estuary. 93
Figure 4.8. The concentration of EPS present in surface sediment across Bute Inlet, B.C, Canada. 97
Figure 4.9. The concentration of chlorophyll-a present in surface sediment across Bute Inlet, B.C, Canada. 98
Figure 4.10. The concentration of EPS present in surface sediment across Ravenglass Estuary, UK. 99
Figure 4.11. The concentration of chlorophyll-a present in surface sediment across Ravenglass Estuary, UK. 100
Figure 4.12. Average clay coat coverage of samples from Bute Inlet coloured by depositional facies. 102
Figure 4.13. Average clay coat coverage of samples from Ravenglass Estuary coloured by depositional facies. 102
Figure 4.14. Clay coat morphologies across Bute Inlet. A) Clean texturally immature sediment from Homathko sand flat, sample 13. B) Continuous and discontinuous clay coats in sediment from Southgate mixed flat, sample 41. C) Clay lamina partially coating quartz in sediment from channel thalweg, sample 22. D) Discontinuous clay coats in sediment from distal lobe, sample 36. 103
Figure 4.15. Clay coat morphologies across Ravenglass Estuary. A) discontinuous coats in sample 25 (mud flat). B) Clay bridging (red triangle) quartz grains (Q) in sample 8 (mixed flat). C) Clay floc (yellow triangle) in sample 41 (sand flat). D) Discontinuous clay coats (purple triangle) and clay bridge (red triangle) in sample 18 (tidal bar). E) Aggregate of fine-grained quartz within clay bridging network (red dashed line) in sample 66 (tidal inlet). F) Diatom (black triangle) encased by clay bridge in sample 29 (mud flat). 104

Figure 4.16. SEM images of sediment from Homathko sand flat, Bute Inlet. A) Clay-coated sediment with EPS strands bridging quartz grains. B) Clay-coated diatom attached to quartz grain. 105
Figure 4.17. SEM image of sediment from distal lobe, Bute Inlet. 106
Figure 4.18. SEM image of sediment from mixed flat, Ravenglass Estuary. A) Clay-coated sediment with EPS bridges. B) Clay and EPS-coated quartz grain. C) Clay-coated diatom. 107
Figure 4.19. SEM image of diatom attached to sediment from tidal bar, Ravenglass Estuary. 108
Figure 4.20. Total Carbohydrate content vs average clay-coat coverage in Bute Inlet. 110
Figure 4.21. Chlorophyll-a content vs average clay-coat coverage in Bute Inlet. 111
Figure 4.22. Mean grain size vs average clay-coat coverage in Bute Inlet. 111
Figure 4.23. Sorting vs average clay-coat coverage in Bute Inlet. 112
Figure 4.24. Clay fraction vs average clay-coat coverage in Bute Inlet. 112
Figure 4.25. Chlorophyll-a content vs total carbohydrate content in Bute Inlet. 113
Figure 4.26. Mean grain size vs total carbohydrate content in Bute Inlet 113
Figure 4.27. Sorting vs total carbohydrate content in Bute Inlet. 114
Figure 4.28. Clay fraction vs total carbohydrate content in Bute Inlet. 114
Figure 4.29. Chlorophyll-a vs mean grain size in content in Bute Inlet. 115
Figure 4.30. Chlorophyll-a vs sorting in content in Bute Inlet. 115
Figure 4.31. Chlorophyll-a vs clay fraction in content in Bute Inlet 116
Figure 4.32. Mean grain size vs sorting in content in Bute Inlet. 116
Figure 4.33. Mean grain size vs clay fraction in content in Bute Inlet. 117
Figure 4.34. Sorting vs clay fraction in content in Bute Inlet. 117
Figure 4.35. Total Carbohydrate content vs average clay-coat coverage in Ravenglass Estuary. 121
Figure 4.36. Chlorophyll-a content vs average clay-coat coverage in Ravenglass Estuary. 121
Figure 4.37. Mean grain size vs average clay-coat coverage in Ravenglass Estuary. 122
Figure 4.38. Sorting vs average clay-coat coverage in Ravenglass Estuary. 122

Figure 4.39. Clay fraction vs average clay-coat coverage in Ravenglass Estuary. 123
Figure 4.40. Chlorophyll-a content vs total carbohydrate content in Ravenglass Estuary. 123
Figure 4.41. Mean grain size vs total carbohydrate content in Ravenglass Estuary. 124
Figure 4.42. Sorting vs total carbohydrate content in Ravenglass Estuary. 124
Figure 4.43. Clay fraction vs total carbohydrate content in Ravenglass Estuary. 125
Figure 4.44. Chlorophyll-a vs mean grain size in content in Ravenglass Estuary. 125
Figure 4.45. Chlorophyll-a vs sorting in content in Ravenglass Estuary. 126
Figure 4.46. Chlorophyll-a vs clay fraction in content in Ravenglass Estuary. 126
Figure 4.47. Mean grain size vs sorting in content in Ravenglass Estuary. 127
Figure 4.48. Mean grain size vs clay fraction in content in Ravenglass Estuary. 127
Figure 4.49. Sorting vs clay fraction in content in Ravenglass Estuary. 127
Figure 5.1. Map showing location of sampling site, Ravenglass Estuary, UK (map generated in ArcGIS Pro version 3.1) 141
Figure 5.2. Thin section of starting material used in the pressure chamber experiments. 144
Figure 5.3. A) SEM and B) EDS signature of clay-coated material used in the pressure chamber experiments. 145
Figure 5.4. QEMSCAN image of the starting material used in pressure chamber experiments. 147
Figure 5.5. A) SEM and B) EDS signature of the 60°C pressure chamber experiment sample. 148
Figure 5.6. QEMSCAN image of the 60°C pressure chamber experiment sample. 149
Figure 5.7. A) SEM and B) EDS signature of the 90°C pressure chamber experiment sample. 150
Figure 5.8. QEMSCAN image of the 90°C pressure chamber experiment sample. 151
Figure 5.9. A) SEM and B) EDS signature of the 150°C pressure chamber experiment sample. 152
Figure 5.10. QEMSCAN image of 150°C pressure chamber experiment sample. 153
Figure 5.11. A) SEM and B) EDS signatures of rosette mineral formed in 250°C pressure chamber experiment. 155
Figure 5.12. QEMSCAN image of 250°C pressure chamber experiment sample. 156

Figure 5.13. Saturation indices of A) pure silica silicates and B) silicates that could have formed during the experiments 159
Figure 5.14. Saturation indices of A) carbonates, B) clays, and C) zeolites that could have formed during the experiments 160
Figure 5.15. A) Magadiite present in Lake Chad sediment (Sebag et al., 2001) B) Sodium silicate formed during 250°C pressure chamber experiment. 161
Figure 6.1. Synthetic stratigraphy for the North Sea Basin (Patruno et al., 2021). 169
Figure 6.2. Map of regional structural elements across the Northern North Sea (EnQuest, 2021). 170
Figure 6.3. Example of estuarine channel deposits between 3453.99m and 3455.82m, well 221/18a-22. 174
Figure 6.4. Example of upper shoreface deposits between 3433.27m and 3435.10m, well 221/18a-22. 176
Figure 6.5. Example of lower shoreface deposits between 3539.95m and 3541.78m, well 221/18a-22. 177
Figure 6.6. Example of lagoonal deposits between 3427.78m and 3429.61m, well 221/18a-22. 178
Figure 6.7. Example of barrier deposits between 3422.29m and 3424.12m, well 221/18a-22. 180
Figure 6.8. Example of swamp deposits between 3470.45m and 3472.28m, well 221/18a-22. 181
Figure 6.9. Example of distal shoreface deposits between 3699.05m and 3700.88m, well 221/18-N4. 182
Figure 6.10. Core log for wells in Block 211/18. 1:200 scale. See appendices C,D and E for full logs. 183
Figure 6.11. Thin section of sample from estuarine channel deposit. 185
Figure 6.12. QFL plot of samples from northern North Sea block 211/18. 187
Figure 6.13. Paragenetic sequence based on thin section observations. 189
Figure 6.14. Porosity vs permeability of study samples by facies. 190
Figure 6.15. SEM image of well-developed chlorite coats in estuarine channel sample in well 211/18a-N7 at 15463ft. (Natural Environment Research Council, item ID: 123897). 195

Figure 6.16. Schematic diagram of authigenic clay coat formation and impact on reservoir quality. 196

List of tables **Page**

Table 2.1. Clay coat morphology definitions. 42
Table 2.2. Pearson correlation coefficient analysis statistical cut offs. 47
Table 4.1. Criteria used to assign depositional facies for samples collected in the field. 84
Table 4.2. Sediment textural properties by depositional facies across Bute Inlet. 88
Table 4.3. Sediment textural properties by depositional facies across Ravenglass Estuary. 89
Table 4.4. Bulk mineralogy measured by QEMSCAN in Bute Inlet and Ravenglass Estuary. 95
Table 4.5. Correlation matrix for Bute Inlet. 118
Table 4.6. Correlation matrix for Ravenglass Estuary. 129
Table 5.1. Summary of bulk mineralogy and average clay coat coverage. 146
Table 6.1. Texture and mineralogy by sample (Data supplied by Natural Environment Research Council, item ID: 123897). Tr = trace. Average clay coat coverage and clay coat abundance, obtained during this study is also shown. 186
Table 6.2. Clay coat coverage and clay coat abundance statistics by facies. 188
Table 6.3. Porosity and permeability statistics by facies. 190
Table 6.4. Correlation matrix for North Sea petrography data. 192

Appendices

Appendix A. Ravenglass Estuary Data

Appendix B. Bute Inlet Data

Appendix C. 221/18a-22 core description

Appendix D. 221/18a-N7 core description

Appendix E. 221/18-N4 core description

Chapter 1. Introduction

1.1 Background

In deeply buried sandstone reservoirs (>3km), quartz overgrowths are the main diagenetic phase responsible for the reduction of porosity and permeability, which drastically reduces the volume of recoverable hydrocarbons (Bloch et al., 2002; Lander et al., 2008).

Clay-coats (especially chlorite coats) developed around detrital quartz grains often prevent the precipitation of porosity-occluding quartz cement during progressive burial and diagenesis (Bloch et al., 2002; Anjos et al., 2003; Dowey et al., 2012; Cao et al., 2018). Therefore, sandstones containing clay-coated grains (Figure 1.1A) may retain a higher level of primary porosity during deep burial, compared to more quartz rich sandstones with a lower clay content (Figure 1.1B). Previous studies indicate that the presence of clay-coated grains can result in porosities which are 10% higher than expected for a given burial depth (Ehrenberg, 1993).

This thesis focuses on the results from experimental and modern analogue studies related to understanding the formation, distribution and thermal transformation of clay coated grains in clastic sedimentary systems.

Chlorite is the most widely reported clay mineral which forms clay coats and inhibits quartz overgrowths (Ehrenberg, 1993; Bloch et al., 2002: Ehrenberg, Ajdukiewicz and Larese, 2012).

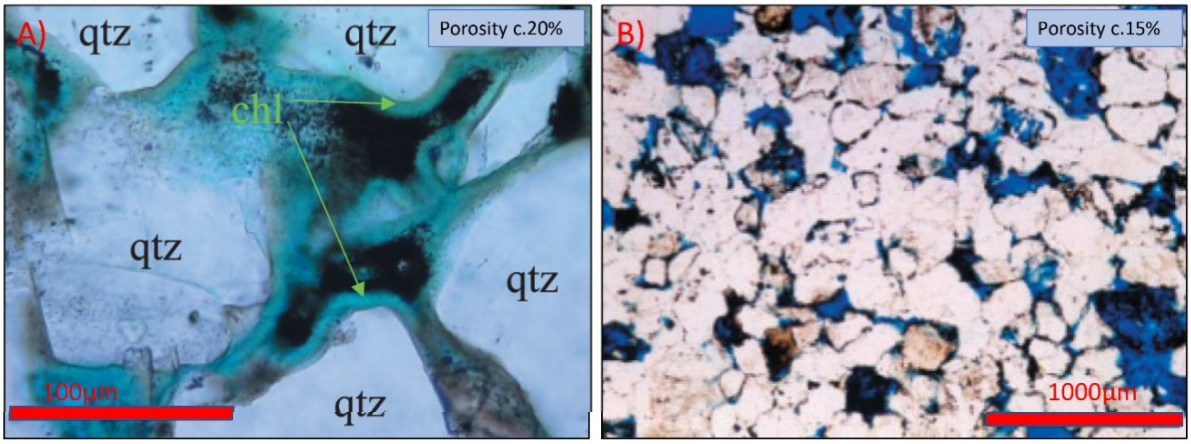


Figure 1.1. Reservoir units of the Halten Terrace, offshore mid-Norway. A) Chlorite-coated reservoir unit from Tilje Formation, Smørbukk Field, chlorite coats (chl) are well developed around detrital quartz (qtz) grains. B) Quartz-cemented reservoir unit from Garn Formation, Kristin Field (modified from Martinius et al., 2005).

1.1.1 Reservoir quality

Porosity and permeability are the two main parameters which determine reservoir quality. Porosity determines the storage capacity of a reservoir and permeability determines how effectively hydrocarbons can flow to a producing well. Reservoir quality is mainly controlled by a combination of depositional character (grainsize, sorting, detrital clay content and mineralogy), the volume and morphology of authigenic cement and the level of mechanical and chemical compaction (Worden and Morad, 2000).

The initial porosity and permeability of sediment is controlled by textural factors such as grainsize, sorting and detrital clay content, which relate to provenance and depositional environment (Worden and Morad, 2000). The primary depositional character of sediment influences diagenesis and the resulting authigenic mineralogy and reservoir quality of a sandstone (Worden and Morad, 2000).

1.1.2 Quartz overgrowths

Quartz overgrowths are recognised as the main authigenic phase responsible for the loss of porosity and permeability in deeply buried sandstone reservoirs (Bloch et al., 2002; Lander et al., 2008).

Several studies have modelled quartz cementation and other diagenetic processes using an experimental and mathematical approach (Berner, 1980; Canal et al., 1995; Walderhaug et al., 2009). For example, Walderhaug et al. (2009) used mathematical modelling to accurately predict the porosity and volume of quartz cement present in Brent Group samples from the northern North Sea. The volume of quartz cement present in samples at any given depth was highly variable (Walderhaug et al., 2009). They concluded that the volume of quartz cement present in a reservoir is a function of grain size, quartz clast content and the extent of grain coatings, which collectively cause large differences in the amount of quartz surface area available for the development of quartz overgrowths (Walderhaug et al., 2009).

Grain coatings such as microquartz and clay mineral coats preserve primary porosity by limiting the formation of quartz overgrowths during diagenesis (Worden and Morad, 2000; Bloch et al., 2002; Dutton et al., 2012; Stricker and Jones 2016). Therefore, predicting the distribution of grain coats in the subsurface is vital for modelling the volume of quartz cement and identifying sandstone reservoirs where a high level of primary porosity has been preserved. This thesis focuses exclusively on clay mineral grain coats. A detailed description of how micro quartz grain coatings influence quartz overgrowths and reservoir quality can be found in (Bloch et al., 2002).

It is worth nothing that clay coats do not inhibit the precipitation of other authigenic pore-filling cements such as carbonates or zeolites which are also commonly present in sandstone reservoirs (Bloch et al., 2002).

1.1.3 Allogenic vs authigenic clay coated grains

Clay coats, which are also known as clay coatings, pore-lining clays or clay rims can be allogenic or authigenic in origin. Allogenic clay coats (Figure 1.2A) often form by clay infiltration and usually have laminar morphology (Pitman et al., 1992). Clay coats form via infiltration when a clay-rich fluid percolates through sand-sized sediment (Dowey et al 2013).

Authigenic clay coats (Figure 1.2B) form as new or regenerated minerals and often have radial morphologies (Pitman et al., 1992). Authigenic clay coats may form via the

diagenetic transformation of detrital precursor clay coats or via the in-situ dissolution and recrystallization of dissolved material (Worden and Morad, 2000). Authigenic clay coats are consistently thicker in depressions on grain surfaces (Figure 1.2). As a result, authigenic clay coats tend to be more extensively developed in fine grained sediment compared to coarser grained sediment, due to coarser grains being more rounded and therefore less likely to have embayments on their surface (Wilson, 1992). Detrital clay coats are thought to be rare in fluvial and near shore marine environments due to clay-coats being rapidly removed in high energy aquatic environments where grain collision is common (Wilson, 1992).

This thesis focuses exclusively on authigenic clay coats, specifically chlorite clay coats formed via the transformation of detrital precursor clay coats. A detailed discussion of clay coats formed via infiltration and their implications on reservoir quality can be found in Molenaar (1986) and Moraes and De Ros (1990).

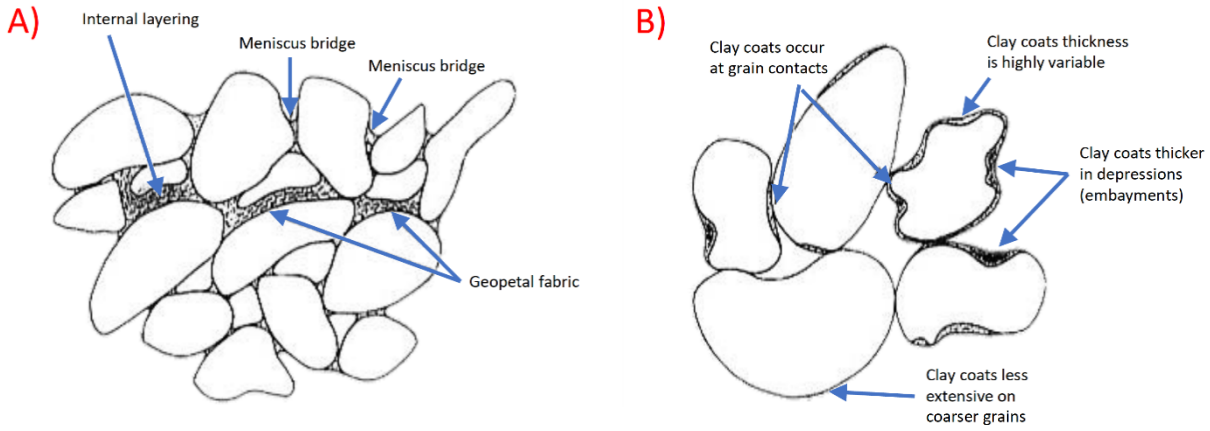


Figure 1.2. A) Allogenic and B) authigenic clay-coated grains (modified from Wilson, 1992).

1.2 Current knowledge on clay-coated grains in siliciclastic reservoirs

1.2.1 Inhibition of quartz cement by clay-coated grains

Models of quartz cementation indicate clay coats prevent the growth of quartz cement by blocking nucleation sites on the surface of host detrital-quartz grains, where the key factor controlling the inhibition of quartz cementation is the completeness of coats (Billault et al., 2003; Lander et al., 2008). Therefore, extensive, continuous clay coats can be effective in inhibiting quartz cement formation in sandstone reservoirs, regardless of their origin, mineralogy or morphology (Pittman et al., 1992).

Clay coat mineralogy is an important secondary control on the ability of clay coats to inhibit quartz cementation (Ajdukiewicz and Larese, 2012). Different clay minerals have a range of morphologies and will behave differently during burial and diagenesis resulting in varying effects on the porosity and permeability of a sandstone reservoir.

Clay coat mineral assemblages commonly consist of smectite, illite, mixed-layer illite/smectite, chlorite or mixed-layer chlorite/smectite. Chlorite is acknowledged as being the most efficient clay mineral for retarding quart cementation (Heald and Larese, 1974; Bloch et al., 2002; Anjos et al., 2003; Dowey et al., 2012; Cao et al., 2018).

Illite coats may also reduce porosity and permeability by promoting quartz pressure solution and subsequent localized quartz cement. This occurs where pore-bridging illite coats located at quartz-grain contacts are subject to pressure, which causes quartz to undergo pressure solution and form localised quartz cement (Thomson and Stancliffe, 1990; Wilson, 1992; Heald and Baker, 1997). Clay coats are not currently acknowledged as effecting the precipitation of epitaxial cements such as carbonate and sulphate cements (Pittman et al., 1992).

The thickness of clay coats is usually in the range of a few nanometres, however coat thickness can reach 10–15μm in depressions on host detrital grains (Wilson, 1992; Worden et al., 2020). If clay coat thickness exceeds a certain level, clay minerals may start to infill pores and reduce porosity and permeability, resulting in a negative impact on reservoir quality. The volume of clay required to significantly coat detrital sand grains and preserve porosity ranges from around 3-13% (total rock volume) and is subject to much debate (Dowey et al., 2012; Pittman et al., 1992).

1.2.2 Chlorite coated grains

Chlorite is a 2:1:1 clay mineral which is usually iron or magnesium rich (Worden et al., 2020). Chlorite clay-coated reservoirs are associated with a wide range of ages and depositional environments, typically but not exclusively associated with shallow marine environments (Dowey et al., 2012).

Previous studies of chlorite-coated reservoirs have identified a precursor clay mineral such as berthierine or smectite as essential for chlorite coat formation, where chlorite forms through the thermal alteration of a precursor clay mineral with increasing temperature and pressure (Ehrenberg, 1993; Ryan and Reynolds, 1996; Anjos et al., 2003).

Berthierine precursor clay coats are usually associated with deposition in a marine environment, whereas smectite precursor coats are usually associated with a continental setting (Worden et al., 2020). The alteration of precursor clay minerals to form chlorite usually occurs during diagenesis at temperatures greater than 60-70°C (Worden and Morad, 2003).

Berthierine was identified as the likely precursor to iron rich- chlorite-coated grains present in Lower Jurassic sandstone reservoirs on the Norwegian Continental Shelf (Ehrenberg, 1993). This was based on the progressive increase in chlorite with depth, where the shallowest samples consist of a mixed layer chlorite-serpentine clay (thought to be berthierine) which becomes less abundant with increasing burial. Berthierine clay coats are reported to have transformed into radially orientated chlorite coatings prior to quartz cementation (Ehrenberg, 1993).

In the Central Graben, UK North Sea, smectite has been proposed as a precursor for grain-coating chlorite, due to authigenic chlorite having a similar chemical and morphological characteristics to smectite (Humphreys et al., 1989). For chlorite formation from a smectite precursor, either a source of aluminium or loss of silica is required (Chang et al., 1986).

Chlorite may also form via the dissolution and recrystallization of volcanic rock fragments and iron and magnesium-rich detrital grains (Pay et al., 2000; Anjos et al., 2003; Dowey et al., 2012). For example, chlorite present in Lower Cretaceous reservoir units of the

Britannia Field, North Sea, UK is reported as being sourced from the underlying Jurassic Forties Igneous Province (Blackbourn and Thompson, 2000).

Artificial chlorite-coated grains, similar to naturally occurring chlorite-coated grains have been successfully synthesised by placing berthierine-coated sandstones from the Norwegian Continental Shelf in a hydrothermal bomb, during an experimental study carried out by Aagaard et al. (2000).

1.2.3 Clay coating via bioturbation

Clay coats may be generated by the passing of sand through the gut of a range of marine sediment-feeding organisms such as polychaete worms, limpets and gastropods (Wilson, 1992). Experimental studies which introduced *Arenicola marina* worms to interbedded sand and crushed slate, conclude that the ingestion and digestion of sediment by worms can produce grain-coats similar to those present in natural settings (Needham et al., 2004; Worden et al., 2006; Needham et al., 2006). When sediment was ingested, a biofilm was formed on sand grains which promoted clay mineral attachment (Needham et al., 2004; Worden et al., 2006; Needham et al., 2006). The consumption and digestion of sediment by worms also causes chemical alternations of clay minerals (Needham et al., 2004).

Wooldridge (2017a) tested the relationship between lugworm abundance and clay coat coverage across Ravenglass Estuary to determine if a similar clay coat formation mechanism could be responsible for the formation of clay-coated grains in modern shallow marine environments. They conclude that no signification relationship exists between clay coat coverage and the abundance of lug worms (Wooldridge, 2017a).

1.2.4 Large scale controls on the formation of clay-coated grains

A comprehensive review of published literature on ancient siliciclastic reservoirs containing chlorite-coated grains can be found in Dowey et al. (2012). Figure 1.3 provides a summary of the main factors controlling the formation of chlorite-coated grains (modified from Dowey et al., 2012).

Depositional Environment: Based on data gathered from 54 published examples, Dowey et al. (2012) concluded chlorite-coated grains are largely found in sandstones originally deposited in coastal zones, especially delta-related depositional environments. This relationship is in agreement with observations made in earlier studies (Bloch et al., 2002; Ehrenberg, 1993). However, porosity-preserving inherited clay rims are also common in a large number of aeolian reservoirs in North America and in aeolian units of the Rotliegendes sandstones in the North Sea (Wilson, 1992). Multiple river systems and overall proximity to active river systems is also essential for the formation of clay minerals and clay-coated grains (Dowey et al., 2012).

Age: The abundance of siliciclastic reservoirs containing chlorite-coated grains increases over geological time from the Devonian to the Cretaceous period, with no examples existing prior to the Devonian period (Dowey et al., 2012). This trend is likely the result of a drilling bias, with few hydrocarbon wells drilled to depths greater or equivalent to the Devonian period.

Depositional latitude: The review of 54 published examples of reservoirs containing chlorite-coated grains suggests chlorite-coated reservoirs are deposited in paleolatitudes between 60°N to 60°S (Dowey et al., 2012). Tropical and temperate climates are important for the generation of clay minerals (via geochemical weathering) and therefore the production of clay-coated grains. Paleolatitude controls the climate of a region which determines the level of rainfall a region receives and thus the extent of weathering of the hinterland to produce soil and abundant clay-minerals.

Provenance: Hinterland geology is also an important parameter for the formation of clay minerals and clay-coated grains. Clay minerals are aluminium phyllosilicates with variable amounts of iron and magnesium. Therefore, a mixed hinterland consisting of both felsic and mafic mineral-rich lithologies is essential for the subsequent weathering and formation of clay minerals.

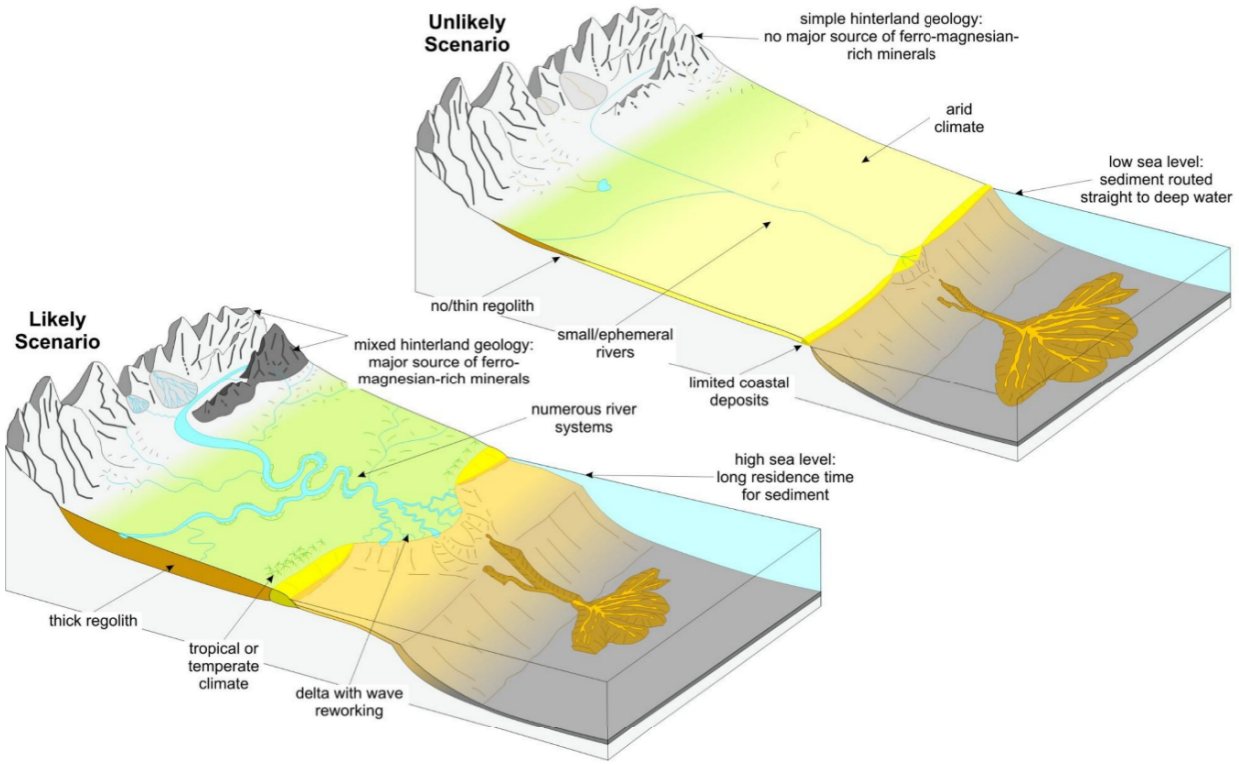


Figure 1.3. Likely and unlikely scenarios for the development of chlorite-coated grains in sandstone reservoirs (Dowey et al., 2012).

1.3 Major challenges associated with predicting the distribution of chlorite coats

Although the relationship between chlorite coated-grains and quartz cement inhibition is well known, the factors controlling whether clays are pore-lining or pore-filling, remains poorly constrained, along with the processes responsible for the formation of precursor clay coats (Dowey et al., 2012; Wooldridge et al., 2017a; Virolle et al., 2018). This makes predicting the spatial distribution of clay-coated grains in subsurface siliciclastic reservoirs extremely difficult.

1.4 The role of biofilms in the formation of clay-coated grains

Recent studies have identified biofilms as potentially playing a pivotal role in the formation of clay-coated grains, by forming an adhesive coat on the surface of sand grains (Figure 1.4) which acts as a binding site for clay particles (Wooldridge et al., 2017a; Virolle et al., 2018; Duteil et al., 2020).

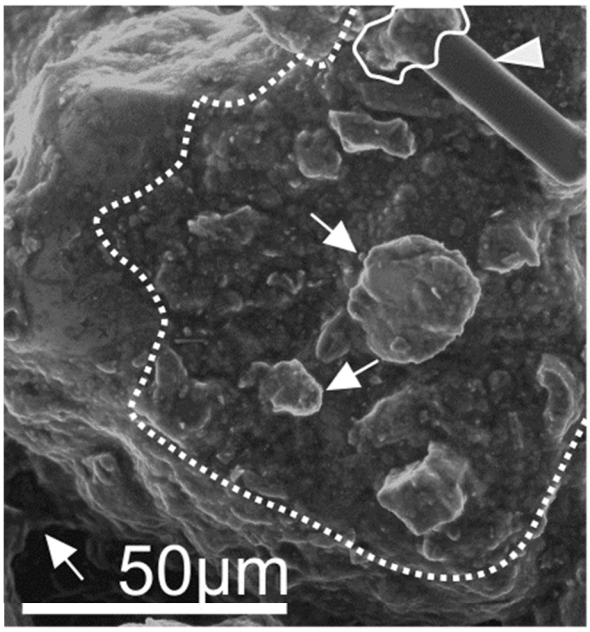


Figure 1.4. SEM image of clay-coated sand grain (Wooldridge et al., 2017a). Clay mineral attachment (white arrows) associated with areas of quartz grain covered by biofilm (outline of biofilm = white dotted line).

Biofilms are common to almost all aquatic environments and consist of an assortment of microbial cells embedded in a network of sticky extracellular polymeric substances (Figure 1.5), secreted by microorganisms such as cyanobacteria and diatoms (Underwood et al., 1995; Jesus et al., 2009). Within intertidal environments, extracellular polymeric substances (EPS) are often secreted by motile diatoms living in the top few cm of sediment, in order to facilitate vertical movement in response to daily sunlight and tidal cycles (Edgar and Pickett-Heaps, 1982; Decho, 1990; Stal, 2003; Garwood et al., 2015). EPS produced by diatoms consist of around 40-90% polysaccharides, with minor amounts of proteins, nucleic acids and lipids (Flemming and Wingender, 2010).

The adhesive nature of EPS is due to the presence of charged functional groups and neutral oxygen groups, which allows EPS to bind organic and non-organic compounds and minerals (Decho, 1990). In the presence of divalent cations (such as calcium), negatively charged carboxyl groups present in EPS can form bridges with clay minerals (De Winder et al., 1999). As a result, the presence of EPS increases the cohesiveness

and aggregation of clay-sized material (<63μm) in sedimentary systems (Stal, 2003; Chen et al., 2017).

Furthermore, a series of flume tank experiments conducted using xanthan gum as a proxy for EPS, indicate small quantities of EPS (0.1-1%) have a significant effect on the morphology of bed forms (dunes and ripples) and sediment transportation (Parsons et al., 2016).

Current studies on biofilm-sediment interactions are dominated by research conducted in intertidal and shallow marine environments (Stal, 2003; Wooldridge et al., 2017a; Duteil et al., 2020). Jones (2017) recognised the need for more research on the influence of biofilms on sediment dynamics in other sedimentary environments.

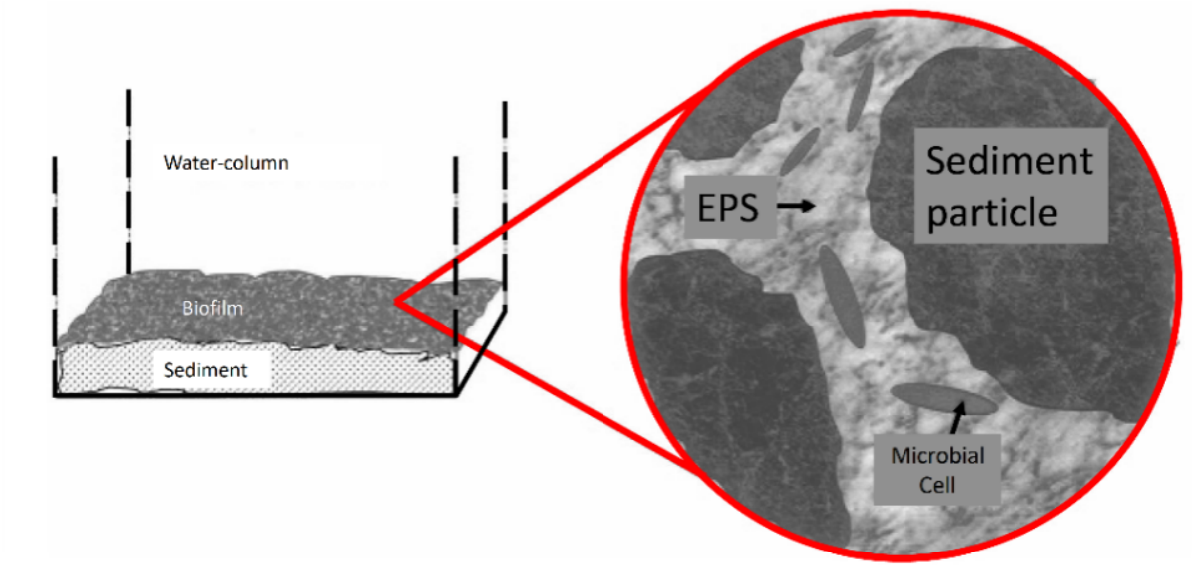


Figure 1.5. Conceptual diagram of microbial biofilm developed at the sediment-water interface (modified from Decho, 2000).

1.4.1 Sedimentation of diatoms

Benthic diatoms attach to sediment at the sediment water interface via forming biofilms. Planktonic diatoms adhere to sediment particles whilst descending in the water column and are then incorporated into sediment via co-deposition with sediment particles. Diatoms can attach to sediment via two mechanisms: the adhesion of diatoms to sediment

particles larger than themselves such as sand grains, and the electrostatic attraction of finer clay particles to the surface of diatom cells. The rate by which diatoms are co-deposited with sediment is a function of the settling velocity. The settling velocity of sediment is governed by particle size where particles greater than 15μm, such as sand, take approximately one tidal cycle or less to settle, whereas clay particles which are less than 15μm will take longer to settle (Lintern, 2003). All clay particles are also affected by electrostatic forces such as van der Waals forces (Lintern, 2003). Salinity can increase the settling velocity of smaller particles such as clays by causing clays to flocculate (Lintern, 2003).

1.4.2 Quantitative analysis of EPS and biofilms

Unfortunately, there is no single established method for extracting and quantifying the volume of extracellular polymeric substances present in a sediment sample (Underwood et al., 1995; Stal, 2003). This makes defining the relationship between biofilms and clay-coated grains complex.

Chlorophyll-a is an established biomarker proxy that is often used to analyse sediment samples for biofilm abundance (Underwood et al., 1995; Stal, 2003; Wooldridge et al., 2017a). *Chlorophyll-a* is the main photosynthetic pigment used by diatoms and many other microphytobenthic organisms, where a high concentration of *chlorophyll-a* is associated with high bio-productivity and a high abundance of biofilms (Underwood and Smith, 1998; Stal, 2003).

Chlorophyll-a can be easily and cheaply extracted from sediment samples using a high purity solvent (usually methanol or acetone). The concentration of *chlorophyll-a* present in the sample extract can then be determined using either traditional spectroscopic methods or through High-performance liquid chromatography (HPLC).

Wooldridge et al. (2017a) discovered a significant positive correlation (Pearson's coefficient of 0.745 with a P value of <0.001) exists between the concentration of *chlorophyll-a* and the extent of clay-coat grain coverage in sediment samples taken from Ravenglass Estuary, Cumbria, UK. As a result, they concluded that the origin and

distribution of clay-coated sand grains in marginal marine environments is primarily controlled by biofilms (Wooldridge et al., 2017a).

This is the first study to directly research the relationship between biofilms and the formation of clay-coated grains and is credited as having the potential to “revolutionize” the understanding of clay-coated grains in relation to predicting the reservoir quality of ancient, deeply buried sandstone reservoirs (Jones, 2017).

However, the use of *chlorophyll-a* as a proxy for biofilm abundance is subject to much debate (Grant et al., 1986; Stal, 2003). For example, an extensive study conducted by Blanchard et al. (2000) indicated the significance of the relationship between *chlorophyll-a* and EPS is largely a function of sediment type and depth, with no significant relationship existing for sand dominated samples or samples collected 5-10mm from the sediment surface. This suggests *chlorophyll-a* may not serve as a reliable proxy for biofilm abundance.

An alternative and far more direct approach to measuring biofilm abundance is the quantification of the total carbohydrate content of EPS fractions extracted from sediment samples, through the use of colorimetric assays (Dubois et al., 1956; Underwood et al., 1995).

The phenol-sulphuric assay can be used to show relative content of carbohydrate present in a sample, expressed in relative terms to a single carbohydrate (usually glucose). This assay is sensitive to a range of carbohydrates, including sugars and polysaccharides, which are the main components of microbial EPS, making it a useful measure to quantify the volume of EPS present in a sediment sample (Underwood et al., 1995).

However, early studies showed the total carbohydrate concentration of a sediment sample, measured using the phenol-sulphuric assay, varies depending on sample storage conditions and the protocol used for EPS extraction (Underwood et al., 1995). For example, sediment samples from the Severn Estuary, UK, stored at -70°C contained significantly higher (Tukey’s test, $P < 0.001$) total carbohydrate concentrations, compared to identical fresh, freeze dried and oven dried sediment samples (Underwood et al., 1995).

1.5 Current approaches to predicting the distribution of chlorite-coated grains

Current approaches to understanding and predicting the distribution of chlorite-coated grains in the subsurface rely on data from well bores, which are then used to predict sedimentary facies that are likely and unlikely to contain chlorite-coated grains (Hillier 1994; Berger et al., 2009). Predictions made using this approach are limited by low spatial resolution, as data are often only available for the cored interval from one or two wells. This can result in clustered or small datasets which can make linking sedimentary facies to the absence or presence of chlorite-coated grains extremely difficult. Furthermore, the factors controlling the occurrence of clays- whether they are pore-lining or pore-filling remains poorly constrained, along with the processes responsible for the formation of precursor clay coats (Dowey et al., 2012; Wooldridge et al., 2017a; Virolle et al., 2018). This makes predicting the spatial distribution of clay-coated grains in subsurface siliciclastic reservoirs extremely difficult.

Another approach to predicting the distribution of clay-coated grains in ancient deeply buried reservoirs is the use of outcrop data. This involves identifying surface outcrops that are representative of deeply buried reservoirs and using outcrop clay mineral coat data to predict the distribution of clay-coated grains in the subsurface. Unfortunately, clay minerals at outcrop are prone to excessive alteration and chemical weathering, due to their interaction with water at the surface of the earth (Retallack and Dilcher, 2012). This makes outcrop studies largely unsuitable for predicting the distribution of clay-coated grains in the subsurface.

1.6 Study approach

This study attempted to improve the understanding of the origin and distribution of clay-coated grains using the following approaches:

1) The design and execution of clay coat synthesis experiments. This involves forming clay-coated grains in variable experimental conditions in a controlled laboratory environment. This allows the link between clay coat formation and variables such as biofilm abundance to be directly studied without any interference from external variables, which are often present in natural systems. In order for the results from

lab experiments to be useful, care must be taken to ensure that lab experiments are representative of the conditions found in natural settings.

2) The design and execution of hydrothermal pressure chamber clay coat transformation experiments. This involves placing clay-coated sediment from an active modern analogue into a hydrothermal pressure chamber, at a range of temperatures to simulate shallow burial and diagenesis. This will allow the transformation of precursor clay-coats during burial and diagenesis to be studied. By doing so, this may help answer key questions related to how clay-coated grains observed in modern analogues relate and transform to continuous chlorite coats observed in ancient analogues. The transformation of precursor clay-coats to chlorite clay coats usually occurs over millions of years, therefore hydrothermal pressure chamber experiments, which typically last several days may provide a slightly unrealistic representation of the processes occurring naturally throughout geological time.

3) The use of two different modern analogues to ancient deeply buried sandstone reservoirs. Modern analogues provide the unique opportunity to directly study the processes responsible for the formation of clay-coated grains from known depositional environments. This is often not possible in consolidated ancient sediments, where process and depositional signatures may be overprinted by diagenesis. Modern analogues also allow a high-resolution study of clay coat formation and distribution across an entire sedimentary system which is not possible in ancient wellbore studies. This allows a large dataset to be collected, increasing the reliability of predictions and trends identified using this approach. However, it may be difficult to translate surface observation made in modern analogues to sedimentary packages in subsurface ancient reservoirs.

4) The results from the experimental and modern analogue studies were used to assess chlorite coated grains in ancient sandstone reservoir in a well-studied hydrocarbon basin. Clay coats present in modern day systems are thought to serve as analogues to precursor coats for chlorite coats present in ancient sandstone

reservoirs. Therefore, the distribution of clay coats identified in the modern shallow marine analogue in (3) should help predict the distribution of chlorite coats in an ancient shallow marine system. By studying clay-coat distribution in a well-studied, producing hydrocarbon basin may provide vital information which can help determine the origin of clay-coated grains in underdeveloped and underexplored hydrocarbon basins.

1.7 Research themes and questions

This study uses an experimental approach to study the formation and diagenetic transformation of precursor clay coats. A modern analogue approach is used to study the distribution of clay coated grains in deep marine (Bute Inlet) and shallow marine (Ravenglass Estuary) settings. The results from the experimental and modern analogue studies are then used to assess the distribution of chlorite-coated grains in the Mid Jurassic Brent Group, North Sea.

A total of ten main research questions have been identified and investigated in this thesis (Figure 1.6). These research questions can be grouped into three main overarching themes 1) The origin and distribution of precursor clay-coated grains in shallow marine and deep-water turbidite systems 2) The transformation of precursor clay-coated grains during burial and diagenesis 3) The origin and distribution of clay-coated grains in ancient sandstone reservoirs.

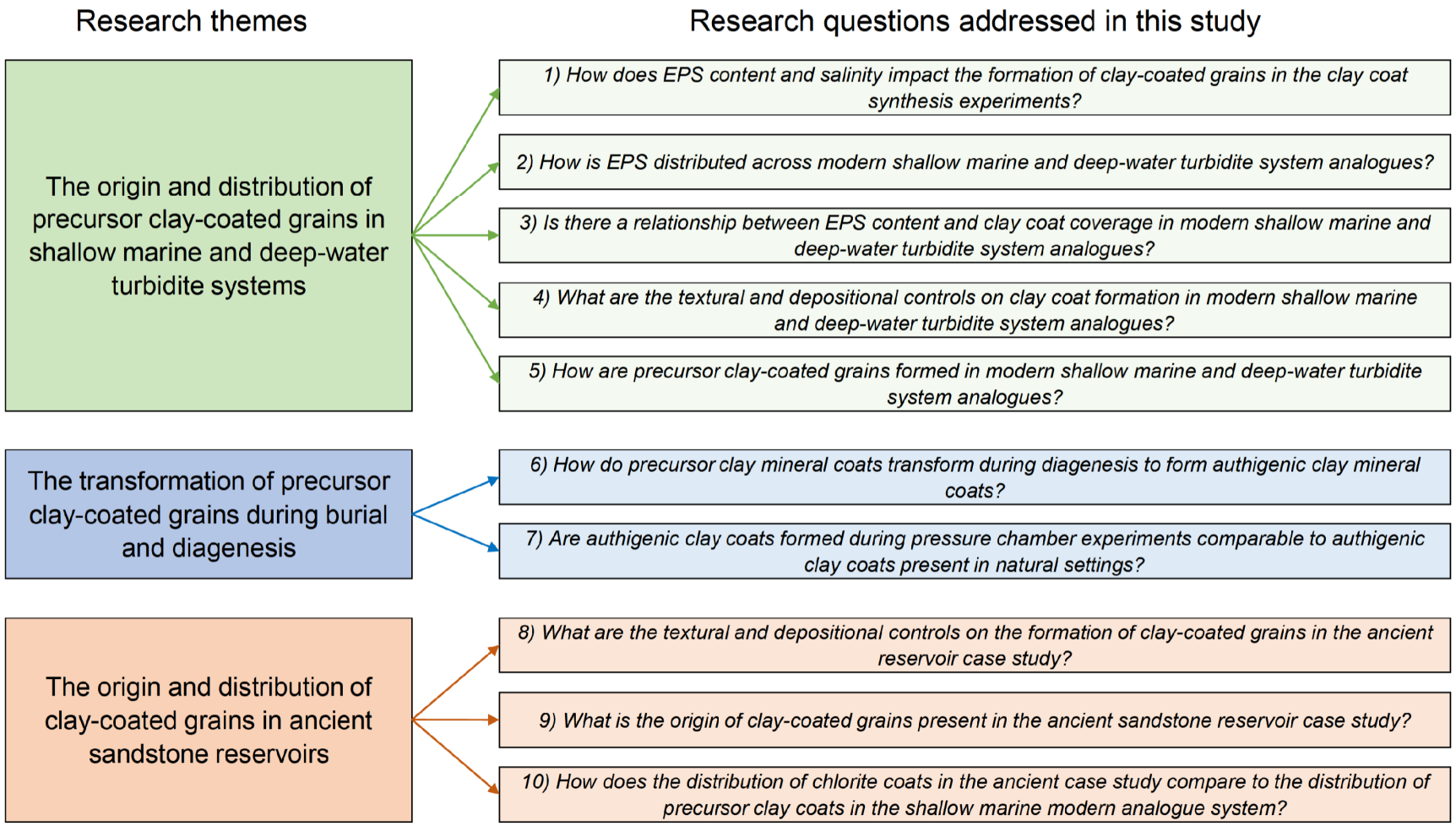


Figure 1.6. Summary of the main research themes and research questions addressed in this study.

1.7.1 The origin and distribution of precursor clay-coated grains in shallow marine and deep-water turbidite systems

Rational: Understanding how precursor clay coated-grains form is key to being able to predict the distribution of chlorite coated grains in subsurface sandstone reservoirs. Recent modern analogue studies have hypothesized biofilms play a pivotal role in the formation of precursor clay coats, by forming an adhesive layer on the surface of sand grains which acts as a binding site for clay particles (Jones, 2017; Wooldridge et al., 2017a).

In this study, a series of experiments modelled on natural systems were carried out to form clay-coated grains in a controlled laboratory environment in the presence and absence of biofilms. This allowed the link between biofilms and the formation of clay-coated grains to be studied directly without any interference from external variables. This is the first study to utilize an experimental approach to investigate the effect of EPS on the formation of clay-coated grains. A set of abiotic clay coat synthesis experiments was also carried out using a range of salinities to investigate the effect of increasing salinity on clay flocculation and the formation of clay-coated grains. The results from these experiments may help define the factors promoting the formation of clay-coated grains in natural systems.

The link between EPS and clay coat formation was also investigated via a modern analogue approach. Sediment from two modern analogues (Ravenglass Estuary and Bute Inlet) was analyzed for clay coat coverage alongside total carbohydrate and *chlorophyll-a* content (proxies for EPS). This allowed any correlation between clay-coat formation and EPS to be identified.

Ravenglass Estuary is a shallow, well mixed, macro-tidal estuary fed by three main rivers, the Esk, the Irt and the Mite. Ravenglass Estuary was selected as a study site as previous studies have identified a link between biofilms and the formation of clay-coated grains (Wooldridge et al., 2017a).

Bute Inlet is a north-south trending, 70km-long and 4km-wide fjord fed by seasonal melt water from up-dip glaciers and permanent ice sheets. Sediment enters the fjord via two main rivers (Homathko and Southgate) which form deltas at the head of the fjord. Sediment is transported from the two deltas to the fjord floor by quasi monthly turbidity currents. Bute Inlet was selected as a study site because it is one of a small number of

active deep-water turbidite systems in the world. This makes Bute Inlet one of the best places to study the formation of clay-coated grains in deep-water turbidite sedimentary systems. No prior work has been conducted on EPS or clay-coat coverage in Bute Inlet.

The main purpose of re-studying clay-coat distribution and biofilm abundance in Ravenglass Estuary is to compare clay-coat distribution and formation in shallow marine (Ravenglass Estuary) with deep-marine systems (Bute Inlet). All previous studies linking EPS to clay-coat coverage have been limited to shallow marine depositional systems (Jones, 2017). Studying EPS distribution and clay-coat coverage in Bute Inlet provided the opportunity to test whether clay-coat coverage can be linked to biofilm abundance in deep-water turbidite systems.

Modern analogues provide the unique opportunity to study the active formation of clay-coated grains in a range of depositional environments. Furthermore, modern analogues allow the textural and depositional controls on the formation of clay-coated grains to be studied in high resolution for an entire system. The controls on the formation of clay-coated grains in modern analogues can then be used to predict facies in subsurface reservoirs that are likely/unlikely to contain clay-coated grains. This may allow reservoirs with unusually high porosities (related to the presence of clay-coated grains) to be identified and exploited.

For each modern analogue, the link between depositional environment, sediment texture (grain size, sorting and clay size fraction) and clay-coat coverage was studied to identify the dominate controls on clay-coat coverage.

Research questions:

1) *How does EPS content and salinity impact the formation of clay-coated grains in the clay coat synthesis experiments? (concluded in 7.2.1)*

2) *How is EPS distributed across modern shallow marine and deep-water turbidite system analogues? (concluded in 7.2.2)*

3) *Is there a relationship between EPS content and clay coat coverage in modern shallow marine and deep-water turbidite system analogues? (concluded in 7.2.3)*

4) *What are the textural and depositional controls on clay coat formation in modern shallow marine and deep-water turbidite system analogues? (concluded in 7.2.4)*

5) *How are precursor clay-coated grains formed in modern shallow marine and deep-water turbidite system analogues? (concluded in 7.2.5)*

1.7.2 The transformation of precursor clay-coated grains during burial and diagenesis

Rational: Clay-coated grains present in modern analogues often have a range of morphologies such as clay floccules, discontinuous clay coats and clay bridges (Dowey et al., 2012; Wooldridge et al., 2017a; Virolle et al., 2018), whereas chlorite coats in ancient subsurface sandstone reservoirs usually display a continuous morphology (Ehrenberg, 1993; Salem et al., 2005; Cao et al., 2018). To date, very little research has been conducted on the transformation of precursor clay-coats to form authigenic chlorite coats. Conducting a series of hydrothermal pressure chamber experiments at a range of temperatures, allows the different stages of precursor clay coat mineral transformation to be studied for the first time.

Research questions:

6) How do precursor clay mineral coats transform during diagenesis to form authigenic clay mineral coats? (concluded in 7.3.1)

7) Are authigenic clay coats formed during pressure chamber experiments comparable to authigenic clay coats present in natural settings? (concluded in 7.3.2)

1.7.3 The origin and distribution of clay-coated grains in ancient sandstone reservoirs

Rational: Using the insights from experimental and modern analogue studies to assess the distribution of chlorite coats in an ancient reservoir case study can help work towards building a model which predicts the distribution of chlorite coats in the subsurface. This determined the relationship between clay-coat formation and facies, grain texture (grain size and sorting) and reservoir quality (porosity and permeability). Studying the controls on the formation of clay-coated grains in a well-studied hydrocarbon basin may help enhance the prediction of the distribution of clay-coated grains in poorly studied and underdeveloped hydrocarbon basins.

Research questions:

8) What are the textural and depositional controls on the formation of clay-coated grains in the ancient reservoir case study? (concluded in 7.4.1)

9) What is the origin of clay-coated grains present in the ancient sandstone reservoir case study? (concluded in 7.4.2)

10) How does the distribution of chlorite coats in the ancient case study compare to the distribution of precursor clay coats in the shallow marine modern analogue system? (concluded in 7.4.3)

1.8 Organisation of thesis

This thesis has been written in the style of papers. As a result, some ideas and concepts may be repeated throughout the thesis. Each chapter is intended to be modified for publication in a suitable journal at a later date. Chapter 2 provides a detailed account of the material and methods used throughout this project. An overview of each technical chapter (Chapter 3 to 6) can be found below. Chapter 7 discusses the key results of this project and recommends areas for future academic research.

Chapter 3: The formation of precursor clay-coated grains: Insights from clay coat synthesis experiments

Overview:

This chapter provides an overview of a series of clay coat synthesis experiments carried out in the absence and presence of EPS, secreted by diatoms, under controlled laboratory conditions. This study is the first to use an experiment approach to directly tests the effect of EPS on the formation of clay-coated grains. This chapter also gives the results from a series of abiotic clay coat synthesis experiments, conducted using a range of salinities, which test the effect of increasing salinity on the formation of clay-coated grains. Understanding how precursor clay-coated grains form is vital to predicting their distribution.

Work contributed:

Alison Hendry: Responsible for designing and running experiments, sample collection, all sample analysis and the production of all text and figures.

Sanem Acikalin: Responsible for providing project supervision, in depth research discussions and detailed manuscript review.

Sven Lahme: Responsible for providing project supervision and in-depth research discussions.

Cees van der Land: Responsible for providing project supervision, in depth research discussions and detailed manuscript review.

Shannon Flynn: Responsible for providing project supervision, in depth research discussions and detailed manuscript review.

Chapter 4: The origin and distribution of clay-coated grains in shallow marine and deep-water turbidite sedimentary systems

Overview:

This chapter details the study of surface sediment in Ravenglass Estuary, Cumbria, UK and Bute Inlet, a deep-water turbidite system in British Columbia, Canada. The study determines the mineralogy and distribution of clay-coated grains across Ravenglass Estuary and Bute Inlet. This study also investigates the biological and non-biological controls on the formation of clay-coated grains in modern shallow marine and deep-water turbidite sedimentary systems. By doing so, this chapter aims to improve the understanding of the origin and distribution of clay-coated grains in modern analogues which may help improve the understanding and prediction of clay-coated grains present in ancient subsurface reservoirs.

Work contributed:

Alison Hendry: Responsible for field work planning and execution, sample collection, all sample analysis and the production of all text and figures.

Sanem Acikalin: Responsible for providing project supervision, field work assistance, in depth research discussions and detailed manuscript review.

Cees van der Land: Responsible for providing project supervision, in depth research discussions and detailed manuscript review.

Shannon Flynn: Responsible for providing project supervision, in depth research discussions and detailed manuscript review.

John Strickland and CCGS Vector research staff and crew members: Bute Inlet fieldwork planning, execution and sample collection.

Chapter 5: The transformation of precursor clay-coated grains during diagenesis

Overview:

This chapter provides a summary of the results from a series of pressure chamber experiments conducted at Durham University. The experiments involved placing surface sediment, collected from a tidal bar in Ravenglass Estuary, in a pressure chamber at temperatures ranging from 60-250°C. The samples where then analysed using classic petrography, SEM and QEMSCAN (Quantitative Evaluation of Materials by Scanning Electron Microscopy) for changes in clay-coat morphology and mineralogy with increasing temperature.

Work contributed:

Alison Hendry: Responsible for designing and running experiments, sample collection, all sample analysis and the production of all text and figures.

Dimitrios Charlaftis: Responsible for helping to design and run experiments.

Sanem Acikalin: Responsible for providing project supervision, in depth research discussions and detailed manuscript review.

Stuart Jones: Responsible for providing in depth research discussions.

Cees van der Land: Responsible for providing project supervision, in depth research discussions and detailed manuscript review.

Shannon Flynn: Responsible for providing project supervision, in depth research discussions and detailed manuscript review. Also caried out the basic geochemical modelling.

Chapter 6: Chlorite coated grains in Mid Jurassic Brent Group reservoirs, northern North Sea

Overview:

This chapter uses the findings from the experimental and modern analogue studies to assess chlorite clay-coated grains present in Middle Jurassic Brent Group (Rannoch, Etive and Ness Formations) in the Northern North Sea, Quad 211, Block 18. A total of 240m of core, from three wells was logged and split into facies at the British Geological Survey, Keyworth. A total of 33 thin section, covering the three cores were analysed for detrital and diagenetic mineralogy, clay-coat coverage and reservoir quality. Additional textural (grain size and sorting) and conventional core analysis (Helium porosity and Horizontal permeability) data and a sub-set of SEM images were sourced from the National Geoscience Data Centre (Natural Environment Research Council item ID: 123897). All data were compiled and analysed to investigate textural and facies controls on clay-coat coverage and the effect of chlorite-coated grains on reservoir quality.

Work contributed:

Alison Hendry: Responsible for logging core, thin section analysis, data gathering, processing data and the production of all text and figures.

Sanem Acikalin: Responsible for providing project supervision, in depth research discussions and detailed manuscript review.

Cees van der Land: Responsible for providing project supervision, in depth research discussions and detailed manuscript review.

Shannon Flynn: Responsible for providing project supervision, in depth research discussions and detailed manuscript review.

Chapter 2. Materials and Methods

2.1 Modern analogue study sites

Two modern analogues were selected for the study of the formation and surface distribution of clay-coated grains: Ravenglass Estuary, Cumbria, UK and Bute Inlet, a deep-water turbidite system in British Columbia, Canada. The main aim of the study was to determine the mineralogy and distribution of clay-coated grains across the two different modern analogue systems. The biological and non-biological controls on the formation of clay-coated grains in both systems were assessed via gathering a large volume of textural, biological and environmental data from both locations. By doing so, this study identified links between depositional environment, grain size and sorting, EPS concentration and clay-coat coverage across marginal marine (Ravenglass Estuary) and deep-water turbidite systems (Bute Inlet). During this study, a new method for EPS extraction and quantification for modern sediments was also developed and compared to the traditional use of *chlorophyll-a* as a proxy for EPS.

2.1.1 Bute Inlet

Bute Inlet (Figure 2.1) is a north-south trending, 70km-long and 4km-wide fjord which ranges from around 200 to 655m in depth (Zeng et al., 1991). The fjord is fed by seasonal melt water from up-dip glaciers and permanent ice sheets. Sediment enters the fjord via two main rivers (Homathko and Southgate) which form deltas at the head of the fjord. Homathko River is thought to contribute more than 75% of the total annual water inflow to the fjord, with a discharge that can reach up to 1600m^3 per second in summer (Zeng et al., 1991). Sediment is transported from the head of the two deltas to the fjord floor by quasi monthly turbidity currents, via a single submarine channel. Sediment is sourced from the cordilleran hinterland which is dominated by a mixture of granodiorite and quartz diorite (Roddick and Woodsworth, 2006). A simplified map of gross depositional environments across Bute Inlet (modified from Hague et al., In press) is shown in Figure 2.2. Bute Inlet was selected as a study site as it is one of a small number of active submarine deep-water turbidite systems in the world. This makes Bute Inlet one of the

best places to study the distribution of clay minerals and the formation of clay-coated grains in deep-water turbidite sedimentary systems. Furthermore, Bute Inlet provides the unique opportunity to study clay-coated grains across a range of aquatic depositional environments (fluvial, deltaic, submarine and fjord floor) within a single, relatively closed sedimentary system with a simple hinterland geology. This may allow the distribution and formation of clay-coated grains in deep-water system to be better understood, compared to a more complex region.

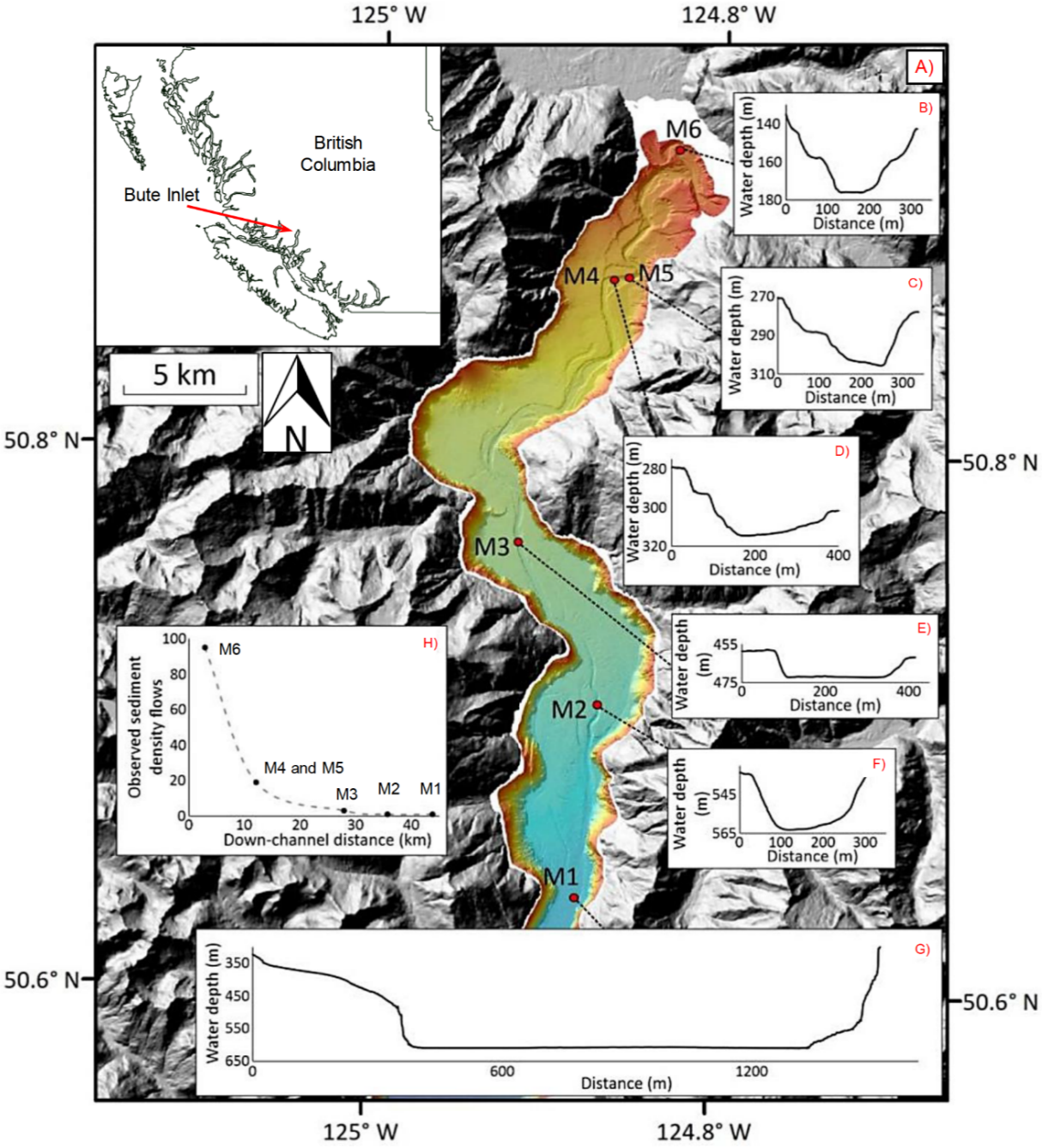


Figure 2.1. A) Bathymetric map of Bute Inlet (modified from Pope et al., 2022). B) – G) East-West channel cross section at the mooring points M1, M2, M3, M4, M5 and M6. H) Number of density flows observed at each mooring point between March and November 2018.

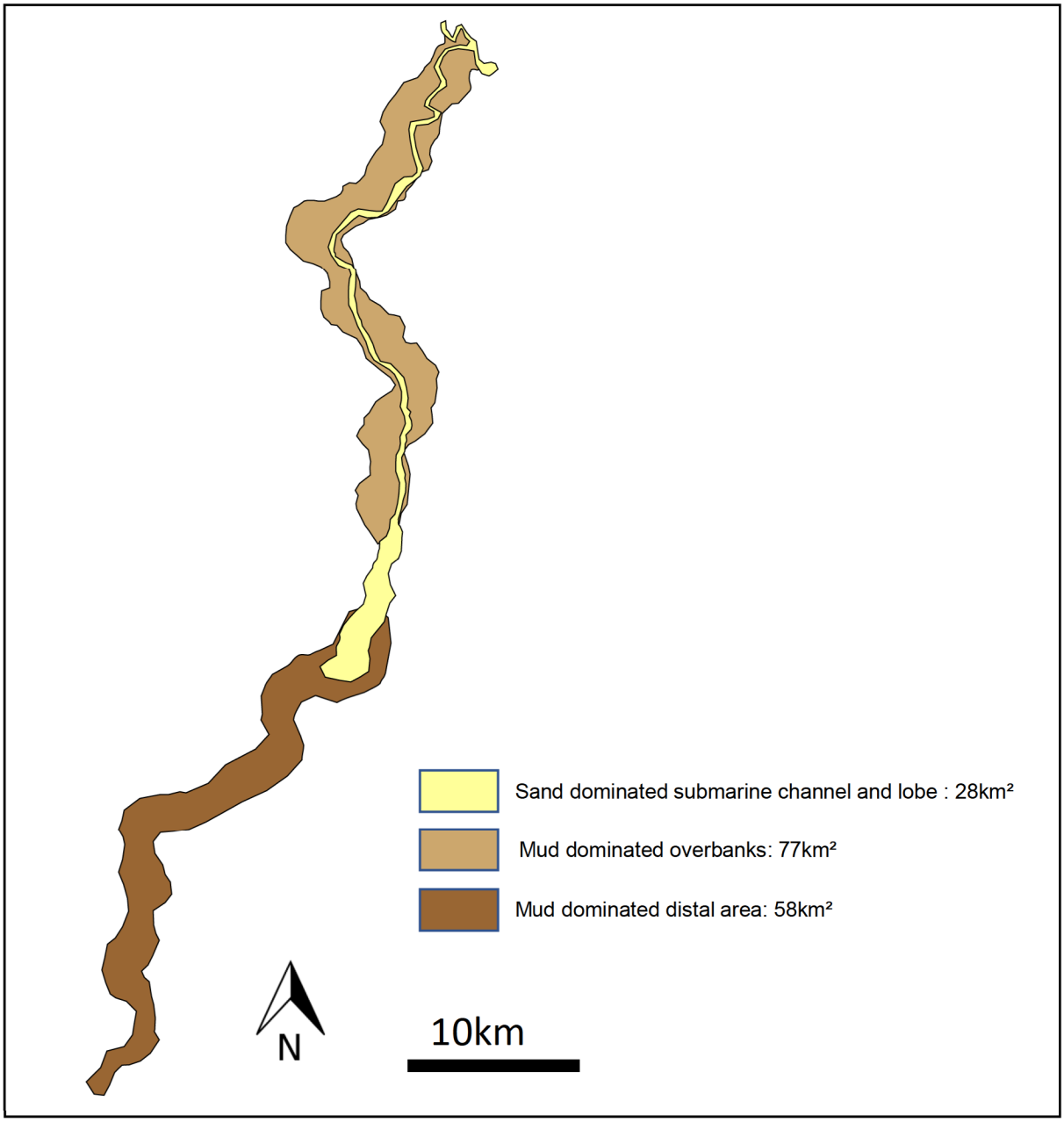


Figure 2.2. Simplified map of gross depositional environments across Bute Inlet (modified from Hage et al., 2022). Note onshore depositional environments associated with an intertidal setting are not shown.

2.1.2 *Ravenglass Estuary*

Ravenglass Estuary is a shallow, well mixed, macro-tidal estuary located in northwest England, UK (Figure 2.3). The estuary is fed by three main rivers, the Esk, the Irt and the Mite. Sediment is sourced from the surrounding upland geology which includes the Sellafield Member sandstones, Wilmslow Sandstone Formation, Skiddaw Group siltstone and sandstones, Eskdale Granite and Birker Fell Andesite Formation. Depositional sub-environments across Ravenglass Estuary (Griffith et al., 2018) are shown in Figure 2.4. Ravenglass Estuary was selected as a field site as previous studies have identified the presence of clay-coated sand grains across the estuary and suggested a link between clay-coat grain coverage and biofilm abundance, where biofilm abundance was measured using *chlorophyll-a* as a proxy for EPS (Wooldridge et al., 2017a; Wooldridge et al., 2018). This allowed a new proxy for EPS (total carbohydrate) to be tested in this study site and compared to the previously used proxy *chlorophyll-a*. Lastly, Ravenglass Estuary has a mixed hinterland, which provides a quartzo-feldspathic rich sediment source, similar to the sediment source expected for many ancient sandstone reservoirs.

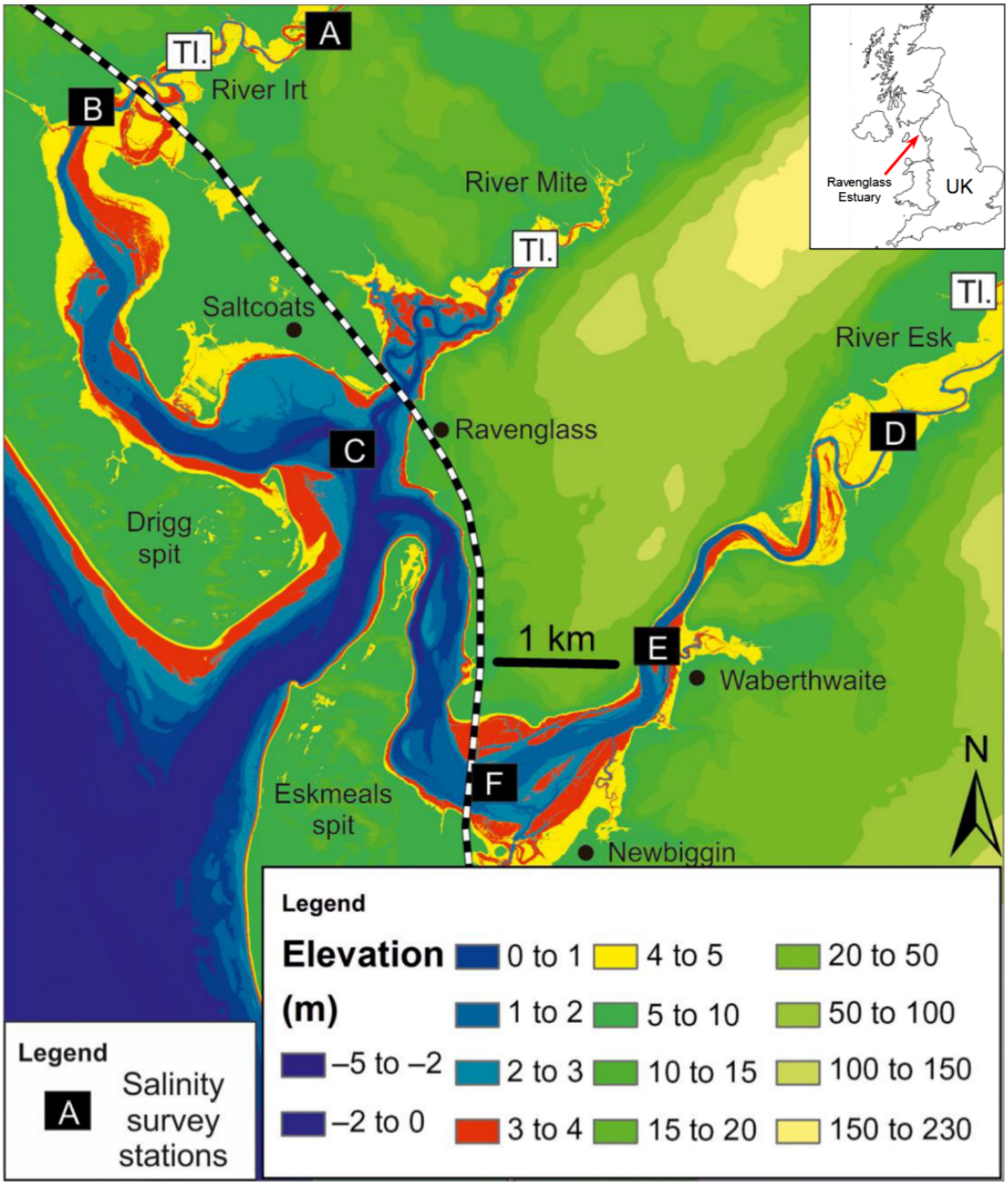


Figure 2.3. Bathymetric map of Ravenglass Estuary (modified from Griffiths et al., 2018). TI = tidal limits. Labels A-F shows the location from which salinity data has previously been measured.

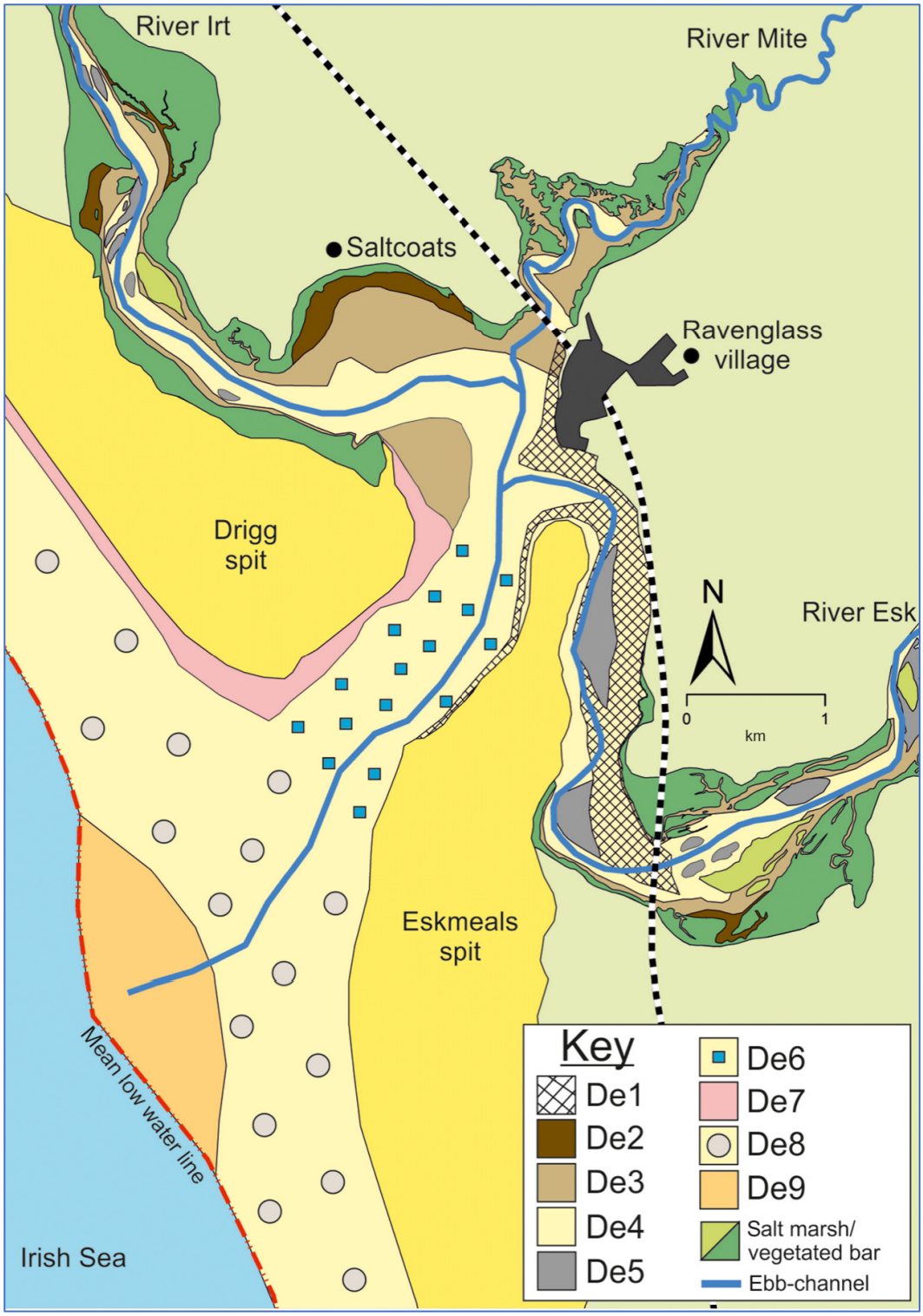


Figure 2.4. Depositional sub-environments across Ravenglass Estuary (Griffith et al., 2018). De1 = gravel bed, De2 = mud-flat, De3 = mixed-flat, De4 = sand-flat; De5 = tidal bars and dunes, De6 = tidal-inlet, De7 = backshore, De8 = foreshore and De9 = pro-ebb delta.

2.2 Sampling of modern sediment

Surface sediment was collected from a total of 76 locations across Ravenglass Estuary (Figure 2.5) during a two-week sampling campaign in March 2018. Samples were taken from across the entire estuary, covering mud flat, mixed flat, sand flat, tidal bar and tidal inlet depositional sub-environments.

Sediment samples from a total of 71 locations across Bute Inlet (Figure 2.6) were collected during a month-long sampling campaign in May 2018. Samples were collected from proximal to distal parts of the system covering mixed flat, sand flat, tidal bar, submarine channel thalweg, submarine channel terraces and distal lobe depositional sub-environments.

A Garmin eTrek handheld GPS (UTM WGS84) with an accuracy of 1m was used to mark sample locations across Ravenglass Estuary. Onshore sample locations across Bute Inlet were marked using the same handheld GPS device. Samples collected from deep water locations across Bute Inlet were marked using a high-resolution satellite navigation system built into the research vessel. The latitude and longitude coordinate of each sample location can be found in Appendix A (Ravenglass Estuary) and Appendix B (Bute Inlet), along with information on the depositional sub-environment.

Sediment samples were collected using a method proposed by Wyness (2017) from exposed land during low tide and from box cores and grab samples for deep marine sediment. Three mini-cores (1.5 cm diameter) were collected from each location, to provide enough material for laboratory analysis. This technique allowed the top 5cm of sediment to be collected, without any major disturbance. All samples were stored in a freezer (-20°C) until subsequent processing and analysis.

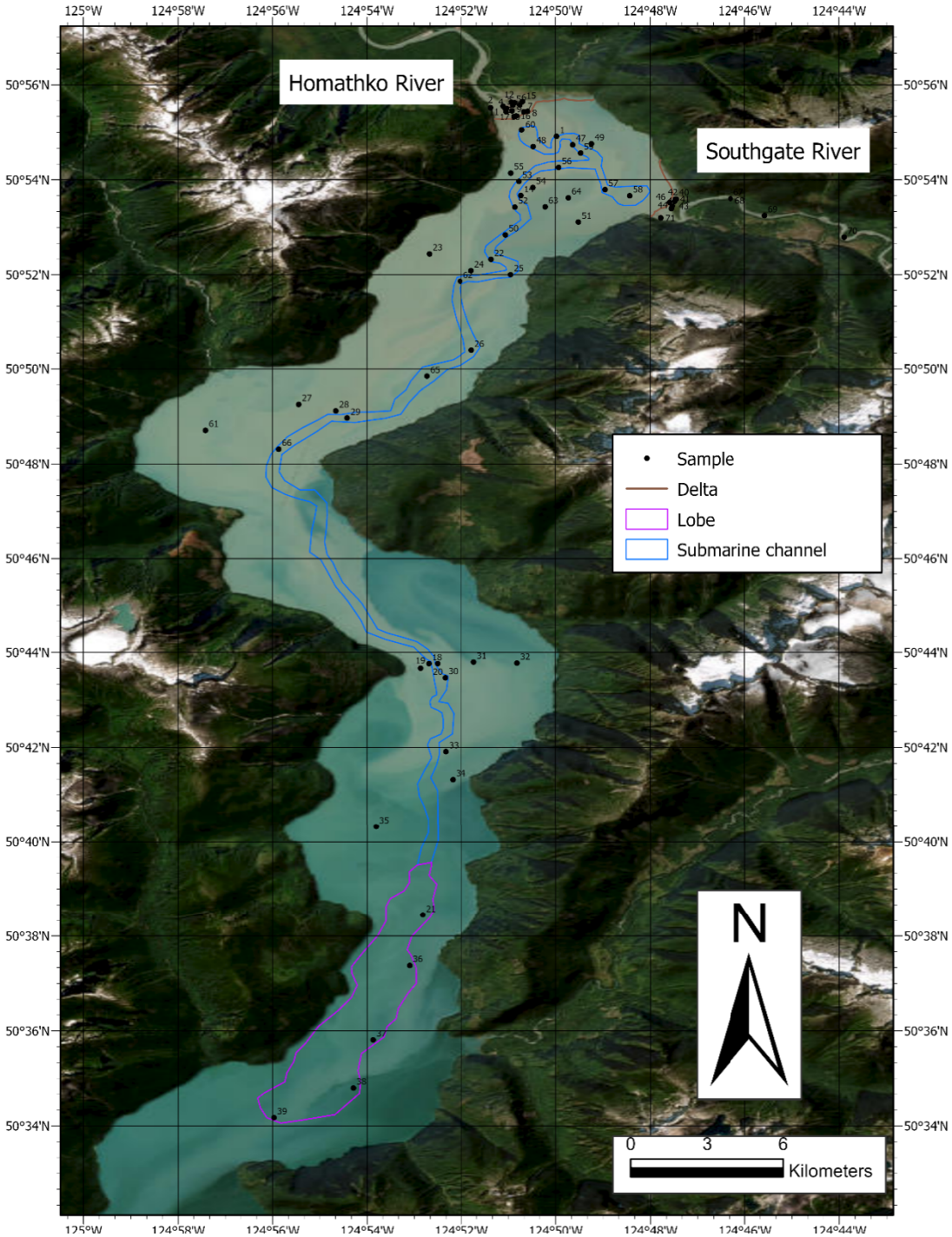


Figure 2.5. Map of sample locations across Bute Inlet. Black dots = sample locations (n=71). Produced using ArcGIS Pro Version 3.2.



Figure 2.6. Map of sample locations across Ravenglass Estuary. Black dots = sample locations (n = 76). Produced using ArcGIS Pro Version 3.2.

2.3 Grain size analysis

Grain size analysis was performed using a Beckmann Coulter LS230 particle analyser (Beckman Coulter Inc., Brea, California, USA) in order to determine if there was any relationship between clay-coat coverage or biofilm abundance and grain size and sorting. Approximately 1 gram of freeze-dried sediment was dispersed in sodium hexametaphosphate suspension fluid with the aid of an ultra-sonic bath. The sample and suspension fluid were then placed in a sample vessel, where particles are suspended by a stirring bar, driven by a magnetic stirring motor. A laser beam was then passed through the sampling vessel and scattered by the particles held in suspension. The scattered light detected by a built-in photo-detector array was then used alongside a mathematic algorithm to produce a particle size distribution plot for each sample. The resulting grain size distribution data was then inputted to Gradistat (version 6) software (Blott and Pye, 2001) to determine mean grain size, clay size fraction content (wt. % < 2µm) and grain sorting (as defined by Folk and Ward, 1957).

2.4 *Chlorophyll-a* analysis

Chlorophyll-a was extracted from sediment samples using methanol as an extraction solvent. Approximately 250mg of freeze-dried sediment was added to a 1.5 Eppendorf tube along with 1 mL of pure methanol. Samples were wrapped in aluminium foil and placed in a freezer (-20°C) for 16 hours. The extracts were then transferred and filtered through a 0.45µm filter membrane into a clean Eppendorf tube.

Standard solutions, with a *chlorophyll-a* concentration ranging from 0 to 40µg per ml were prepared in pure methanol using *chlorophyll-a* extracted from the algae *Anacystis nidulans* (Sigma-Aldrich). Standard solutions were subject to the same extraction and analytical procedure as samples.

A multi-channel pipette was used to add 300µl of each standard solution and sample extract into triplicate wells. The absorbance of the sample extract or standard solution contained in each was read at 652, 665 and 750 nm using a SpectraMax M3 Multi-Mode Microplate Reader (Molecular Devices, LLC, San Jose, California, USA).

The *chlorophyll-a* content of the standard solutions and sample extracts was quantified using an equation provided in Porra et al. (1989), where *chlorophyll-a* (µg/mL) = 16.29 $A^{665.2}$ - 8.54 $A^{652.0}$, where $A^{665.2}$ is the optical density at 665.2nm minus the optical density at 750nm and $A^{652.0}$ is the optical density at 652nm minus the optical density at 750nm. The *chlorophyll-a* values obtained for standard solutions using this equation indicate an average error of +/- 1.5 µg/ml.

2.5 Extracellular polymeric substance (EPS) analysis

Total carbohydrate content is an established proxy used to infer the EPS content of sediment (DuBois et al., 1956; Underwood et al., 1995; Chen et al., 2017). This assay is sensitive to a range of carbohydrates, including sugars and polysaccharides (the main components of microbial EPS) making it a suitable proxy for the EPS content of a sediment sample (Underwood et al., 1995).

Colloidal EPS (loosely bound) and bound EPS fractions were extracted from roughly 350µg of freeze-dried sediment by modifying the extraction method used in Chen et al. (2017). The total carbohydrate content of colloidal and bound sediment extracts was quantified using the phenol-sulphuric acid colorimetric assay, with glucose used as the standard solution (DuBois et al., 1956).

2.5.1 *Colloidal and bound EPS extraction*

Colloidal (loosely bound) and bound EPS fractions were extracted from sediment samples by modifying the extraction method outlined in Chen et al., (2017). Approximately 350mg of freeze-dried sediment was weighed into a clean 1.5 ml Eppendorf tube along with 600µl of sterile deionised water. The sample was incubated at room temperature for 30 minutes, vortexing thoroughly every 10 minutes. After incubation, samples were centrifuged at 4000g at 4°C for 10 minutes and the resultant supernatant (containing the colloidal EPS fraction) was transferred into a clean 1.5 ml Eppendorf tube. The colloidal EPS fraction was then centrifuged at 13,200g for 20 minutes to ensure the complete removal of suspended solids.

In order to extract the bound EPS fraction, 50mg of cation exchange resin (Dowex Marathon C, Na+, Sigma-Aldrich) was added to the sediment pellet retained in the original Eppendorf tube along with 600µl of sterile deionized water. The sediment pellet was re-suspended and incubated at 4°C for 60 minutes, vortexting every 10 minutes. Following incubation, sediment samples were centrifuged at 10,000g at 4°C for 15 minutes and the resulting supernatant was filtered through a 0.45µm filter membrane into a clean Eppendorf tube.

2.5.2 *Colloidal and bound EPS quantification*

The carbohydrate content of extracted colloidal and bound EPS fractions was quantified by modifying the phenol-sulphuric assay method used in Wyness (2017), with D(+)-Glucose (Fisher Scientific) as the analytical standard. Standard solutions, with glucose concentrations of 0, 50, 100, 200, 300 and 500µg per ml were prepared from a stock solution consisting of 1mg of glucose dissolved in sterile deionized water. All standard solutions were subject to the same extraction and analytical procedure as sediment samples.

A multi-channel pipette was used to add 40µl of each glucose standard solution and extracted EPS fraction to triplicate wells in a clear sterile 96-well plate. The multi-channel pipette was then used to add 40µl of 5% w/v phenol solution, immediately followed by 190µl of concentrated sulphuric acid to each well with rapid mixing, achieved via pipetting.

The well plate (Figure 2.7) was then incubated for 40 minutes at 30°C and the absorbance of each well at 486nm was measured using a SpectraMax M3 Multi-Mode Microplate Reader (Molecular Devices, LLC, San Jose, California, USA).

The absorbance of standard solutions at 486nm was used to construct a standard curve (Figure 2.8), which allowed the carbohydrate content (µg per gram of sediment, dry weight) of each sediment sample to be quantified. Colloidal and bound carbohydrate values were added together for each sample to give the total carbohydrate content.

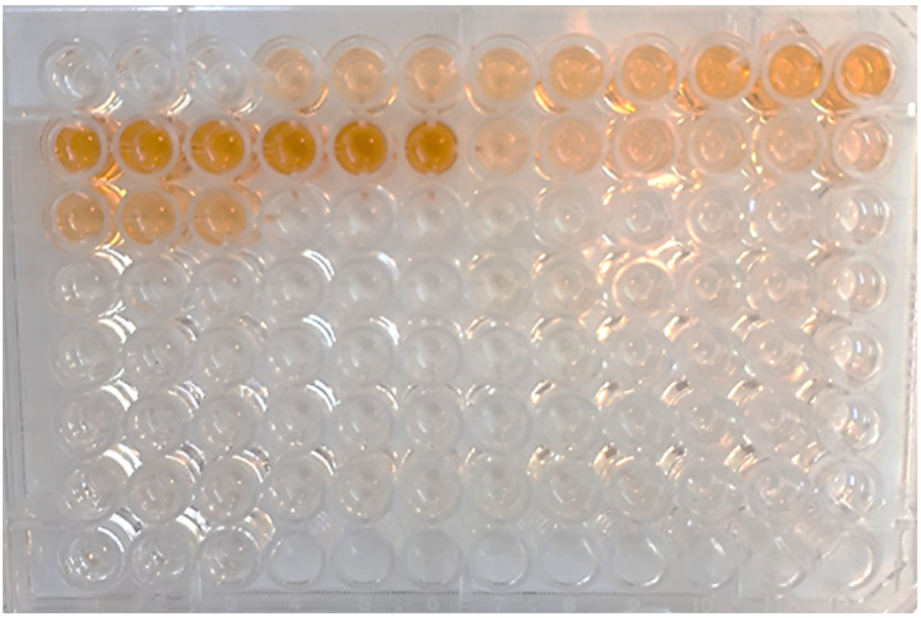


Figure 2.7. Plate containing completed phenol sulphuric acid assay reaction. The more yellow the colour of the reaction product the more total carbohydrate the sample contains.

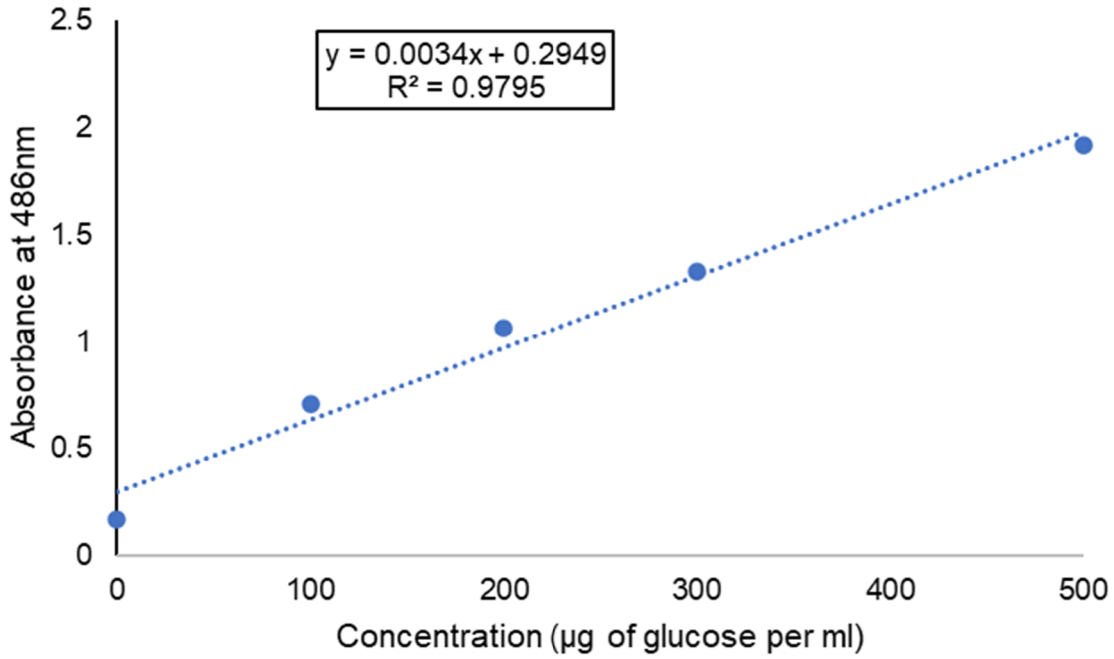


Figure 2.8. Standard curve constructed to quantify the carbohydrate content of samples.

2.6 Petrography

Thin sections of undisturbed sediment (contained in frozen mini sediment cores) from the two modern analogues were produced by Independent Petrographic Services Ltd, Aberdeen, UK. Thin sections were analysed at Newcastle University, using a DM2700 P Leica microscope (Leica Microsystems, Wetzlar, Germany) equipped with a PetrogLite stepping stage (Conwy Valley Systems Limited, Conwy, UK) to record mineral composition and clay-coat coverage.

2.6.1 *Clay-coat grain coverage and abundance quantification*

Grain clay-coat coverage (%) was quantified using the method adopted by Wooldridge et al. (2017a). For an individual sand grain, the grain clay-coat coverage (%) was quantified by measuring the length of the outer perimeter of the grain that is coated, relative to the total perimeter of the grain (Figure 2.9). This process was repeated 50 times for each thin section to give an average grain clay-coat coverage. Clay-coat abundance (%) was quantified via point counting (50 counts per sample. Repeat analysis of samples indicated an average analytical error of ±2.1%.

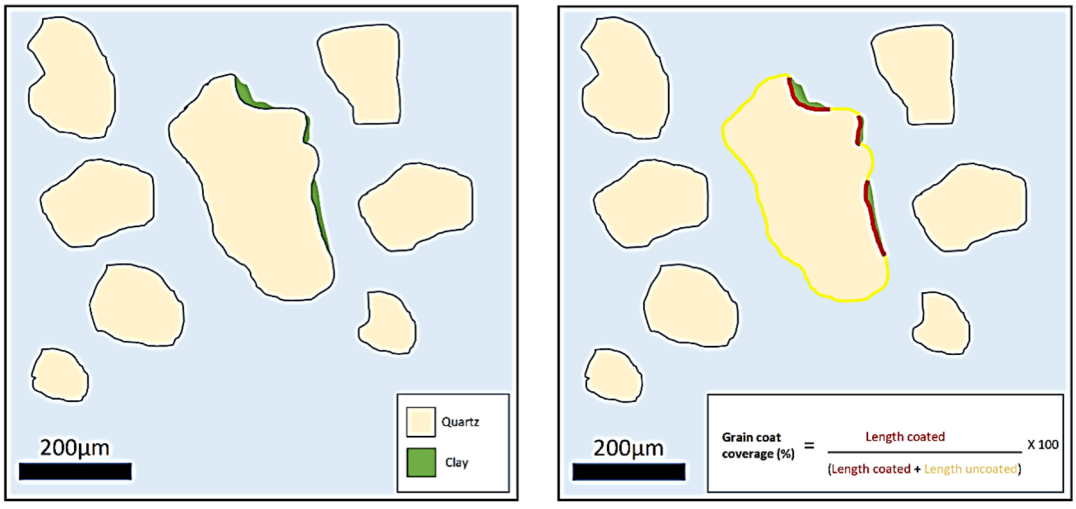


Figure 2.9. Method used to quantify grain clay-coat coverage in petrographic thin sections.

Figure 2.10 shows typical clay coat morphologies identified by Wooldridge et al., 2017b. Table 2.1 summarises the morphologies used to describe clay coats throughout this thesis.

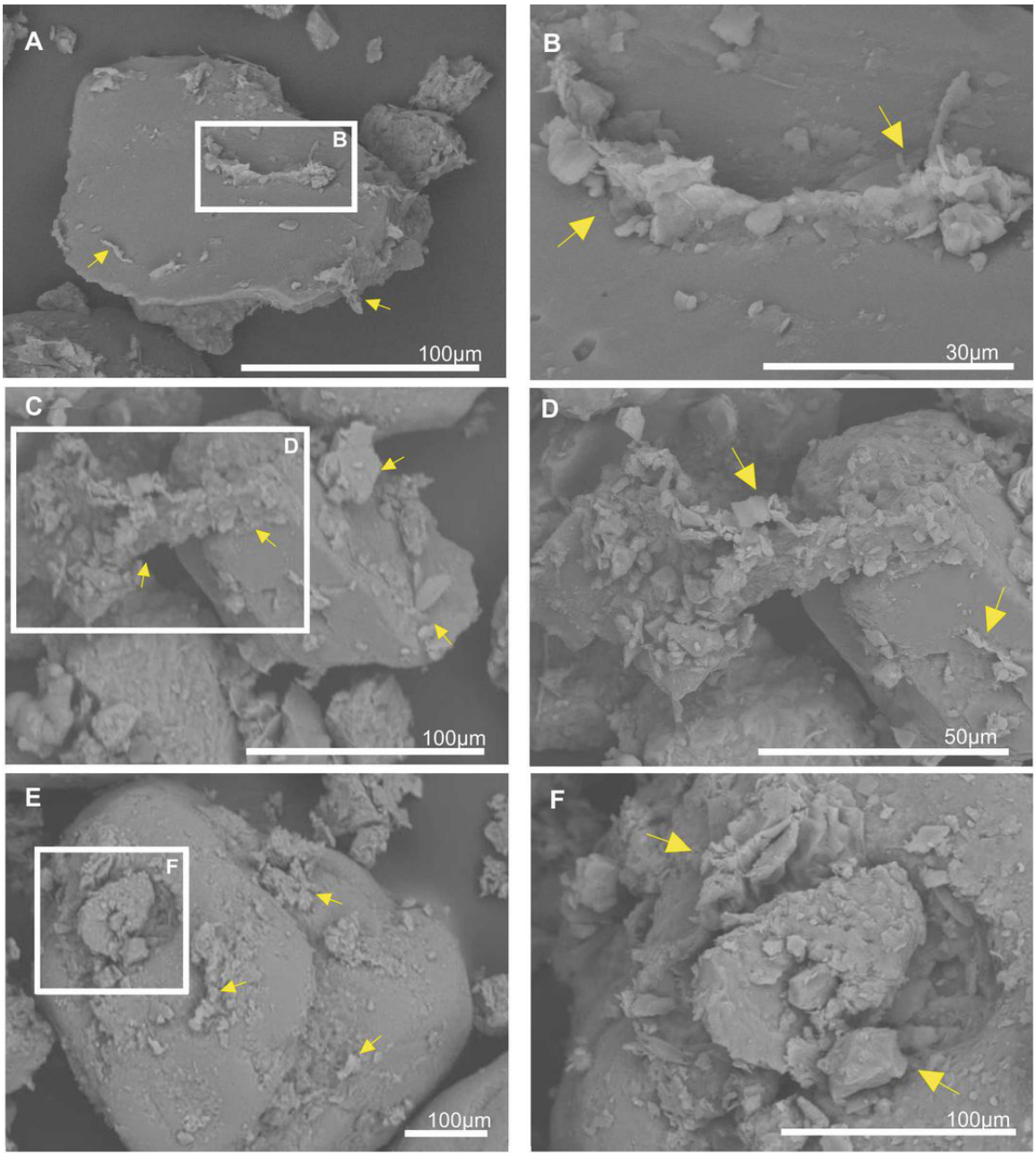


Figure 2.10. Examples of different clay coat morphologies from Wooldridge at al., 2017b a) and b) are a ridged clay coat, c) and d) are a bridged clay coat and e) and f) are a clumped clay coat.

Clay coat morphology	Definition
Floc	Cluster of clay particles attached to the surface of a single quartz grain.
Clay bridge	Clay particles which form a bridge between two separate quartz grains.
Discontinuous clay coating	Clay particles which extend and partially coat the surface of an individual quartz grain.
Clay laminae style coating	Where a quartz grain is partially coated by clay as a result of clay laminations within a sediment sample.

Table 2.1. Clay coat morphology definitions.

2.6.2 *QEMSCAN mineralogy analysis*

Automated mineralogy (QEMSCAN) was performed on a subset of polished, carbon-coated thin sections to determine the mineralogical composition of sediment samples collected from different depositional sub-environments across Ravenglass Estuary and Bute Inlet. QEMCAN analysis was performed using a FEI QEMSCAN 650F Scanning Magnetic Microscope (Thermo Fisher Scientific, Waltham, Massachusetts, USA) at CGG Robertson, Llandudno.

2.7 Scanning electron microscopy (SEM) and energy dispersive spectroscopy (EDS) analysis

Sediment samples were critically point dried, mounted on aluminium stubs and coated with a thin layer of gold. Samples were analysed under low vacuum conditions using a TESCAN Vega 3LMU Scanning Electron Microscope (TESCAN, Brno, Czech Republic) equipped with a Bruker XFlash 6-30 EDS detector (Bruker, Billerica, Massachusetts) at Newcastle University Medical School. Samples were analysed at both low (x250) and high (x1000) magnification to analyse the overall texture of sediment and micron-scale bio-

sediment interactions. Energy dispersive spectroscopy (EDS) is an element analysis technique that measures the energy and intensity distribution of X-ray signals produced by exposing a sample to an electron beam (Gibson, 2005). EDS analysis can be performed on a single point, a line or a targeted area at a high level of precision. Each element has a unique X-ray spectrum which can be used to measure the elemental composition of a sample. The elemental composition of a sample can then be used to infer the mineralogy of a sample due to the known elemental composition of common minerals, for example quartz is rich in Silicon (Si).

2.8 Ancient study site

2.8.1 Don field and Don Southwest field, block 211/18, northern North Sea

Don field and Don Southwest field are located in block 211/18, in the northern North Sea, roughly 275 miles (442km) north-east of Aberdeen (Figure 2.11). Oil is present in Mid-Jurassic Brent Group reservoirs, which are split into 5 regionally correlatable formations: The Broom, Rannoch, Etive, Ness and Tarbert Formations. This study focused on the Rannoch and Etive Formations. This study focuses exclusively on the Rannoch Formation and the Etive Formation.

This area was selected as a study site because the Brent Group represents one of the most established and productive hydrocarbon plays present on the UK Continental Shelf (Deegan and Scull., 1977; Went et al., 2003). Furthermore, many of the reservoir units of the Brent Group were originally deposited in shallow marine delta and estuarine environments (Figure 2.12), and have a quartzo-feldspathic rich sediment source, similar to the modern sediment present in Ravenglass Estuary. This allows the clay-coat grain coverage, morphology and mineralogy present in the ancient reservoir units of block 211/18 to be compared to clay-coated grains present in modern sediment found across Ravenglass Estuary. By doing so, this study aims to identify if the controls on clay-coat coverage in subsurface ancient reservoirs can be related to the controls on clay-coat coverage in modern settings.

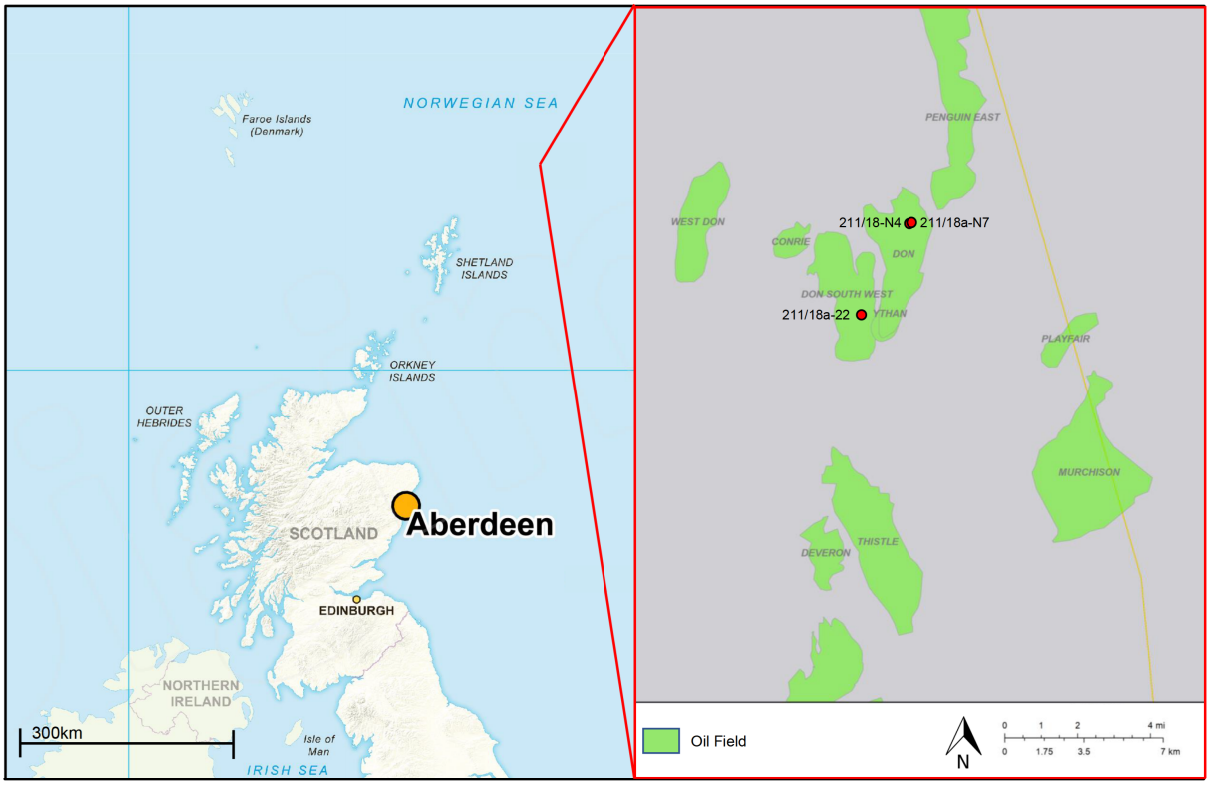


Figure 2.11. Map showing location of study wells and the Don field and Don Southwest field (map obtained from Oil and Gas Authority. 2015).

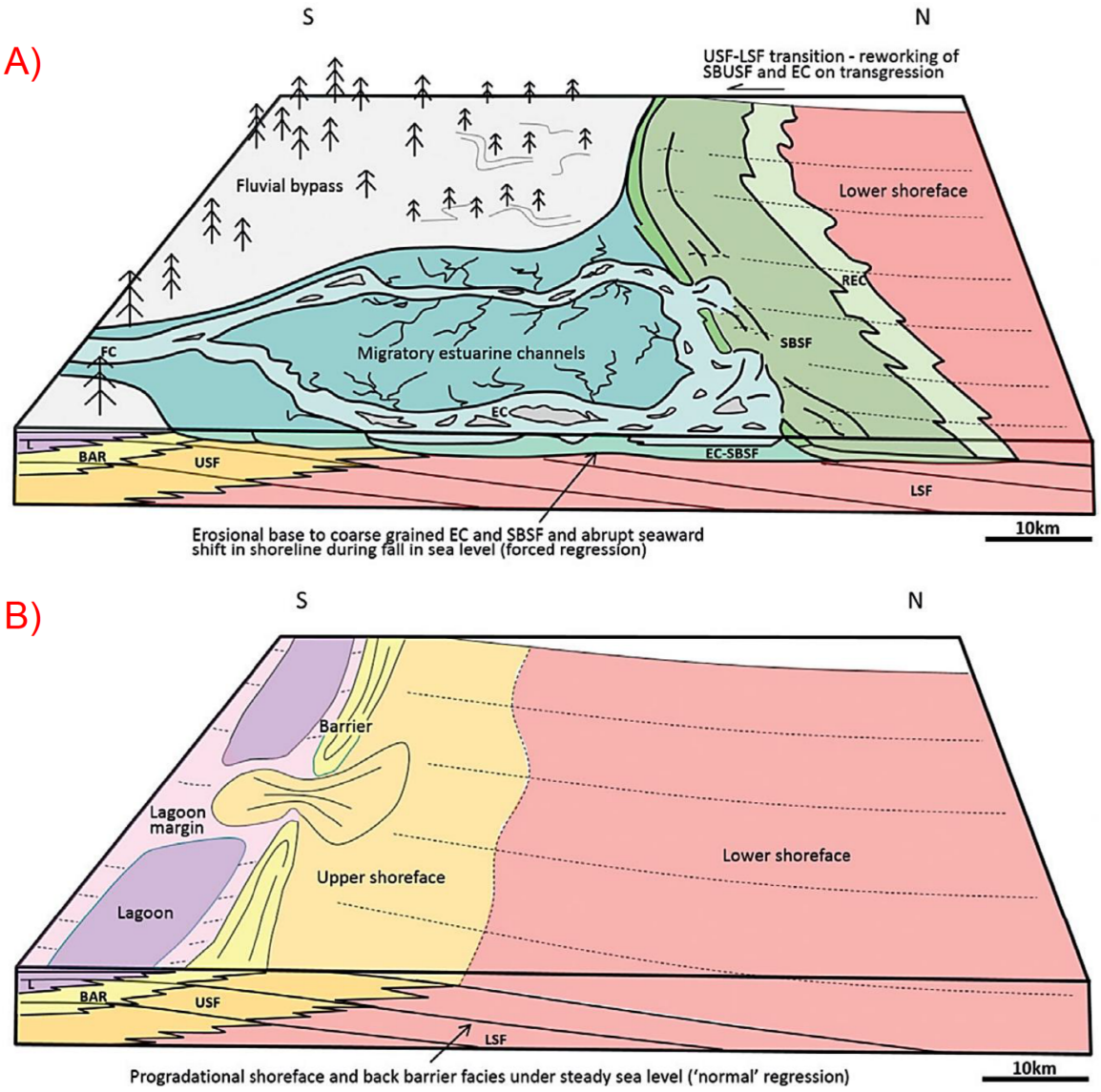


Figure 2.12. Gross depositional environment for the Dons area of the Brent Delta (Went et al., 2013). A) Sea level lowstand emphasizing the lowstand fluvio-estuarine channels. B) Sea-level highstand emphasizing the progradational shoreface and back barrier facies. BA = Barrier, EC = Estuarine channel, L = Lagoon, LSF = Lower shoreface, SB= Storm base, USF = upper shoreface.

2.8.2 Sedimentary logging of ancient cores

A total of approximately 240m of core from three wells (211/18-N4, 211/18a-N7 and 211/18a-22) was logged in detail at the British Geological Survey in Keyworth, UK in March 2020. For each well, changes in colour, lithology, grain size, sedimentary structures

and bioturbation was recorded and logged at a scale of 1:100. Facies were then assigned based on grain size, sedimentary structures and bioturbation.

2.8.3 Analysis of thin sections from ancient cores

From the three wells, a total of 33 thin sections where photographed and analysed using a petrographic microscope equipped with a camera. Notes were made on detrital and authigenic mineralogy, reservoir quality, grain size, sorting and clay-coat coverage. A paragenetic sequence of diagenetic events was also constructed using thin section observations.

Additional conventional core analysis (CCA) data (Helium porosity and Horizontal Permeability) from core plugs, Scanning Electron Microscopy (SEM) images and a subset of XRD results were obtained from the National Geoscience Data Centre (NGDC) for horizons corresponding to the 33 thin sections (Natural Environment Research Council, item ID: 123897).

2.9 Statistical analysis

Data from the ancient case study and the two modern analogues was subject to statistical analysis. A Pearson's correlation coefficient statistical test was used to determine if a significant relationship exists between two variables. Table 2.2 displays the numerical cut offs used in this study. If two variables have a positive relationship, one variable increase as the other variable increases.

Coefficient values (R-values) range from +1 to -1, where +1 indicates a perfect positive correlation, -1 indicates a perfect negative correlation and 0 indicates no relationship exists. A coefficient value between ± 0.50 and ± 1 indicates a strong correlation between two variables, whereas a coefficient value between ± 0.30 and ± 0.49 indicates a moderate correlation exists between two variables. A coefficient value between 0 and ±0.29 indicates a weak correlation exists between two variables. P-values were calculated from R-values at a significance level of 0.05.A P-values describes how likely it is that an observed data trend has occurred by random chance (i.e. that a null hypothesis is true).

In this study, P-values less than 0.05 suggest that the relationship is significant and that there is a less than 5% chance that the data trend has been produced by random chance.

Pearson correlation coefficient (R) value	Strength	Relationship
>0.5	Strong	Positive
Between 0.3 and 0.5	Moderate	Positive
Between 0.1 and 0.3	Weak	Positive
0	None	No relationship
Between 0.1 and -0.3	Weak	Negative
Between -0.3 and -0.5	Moderate	Negative
<-0.5	Strong	Negative

Table 2.2. Pearson correlation coefficient analysis statistical cut offs.

2.10 Biofilm and saline clay coat synthesis experiments

2.10.1 Cultivation of diatoms

Growth media were prepared by mixing 1L of Artificial Sea Water with 20mL of Guillard's (F/2) Marine Water Enrichment Solution (Sigma-Aldrich) to produce a bulk sea water growth media with a salinity of 25ppt. The growth media was stored at -5°C prior to the cultivation of diatoms.

A stock solution of the marine diatom *Chaetoceros sp.* (strain number: CCAP 1010/38) was obtained from the Scottish Association for Marine Science (SAMS) Culture Collection of Algae and Protozoa (CCAP). This genus was selected because *Chaetoceros sp.* is one of the most common marine planktonic diatoms in the world and has been observed in the coastal area surrounding Ravenglass Estuary (Kennington et al., 1999).

The stock solution of *Chaetoceros sp.* was gently homogenised and a 6mL aliquot was extracted and added to a bell-shaped glass culture flask, filled with 60mL of autoclaved

bulk sea water growth media. The culture flask was sealed with a cotton bung to prevent contamination, whilst maintaining aerobic growth conditions. This process was done in triplicate. The flasks were maintained at 20°C +/- 1°C and placed below aquarium light (2000 lux), equipped with a timer programmed to simulate 12 hours of darkness and 12 hours of light over a 24-hour period. CCAP recommend a temperature of 20°C to encourage the growth of *Chaetoceros sp.* in a laboratory setting. The surface water temperature in natural settings such as Ravenglass Estuary is likely to be lower.

The cell concentration was measured each day over the 10-day growth period, using a Neubauer improved cell counting chamber and a DM2700 P Leica polarising microscope (Leica Microsystems, Wetzlar, Germany).

Once growth rate (Figure 2.13) had reached the exponential phase on day 4 (cell concentration of ~1.25x 10^6 cells per mL), cell solutions from all three flasks were pooled and homogenized to produce a bulk concentrated cell solution.

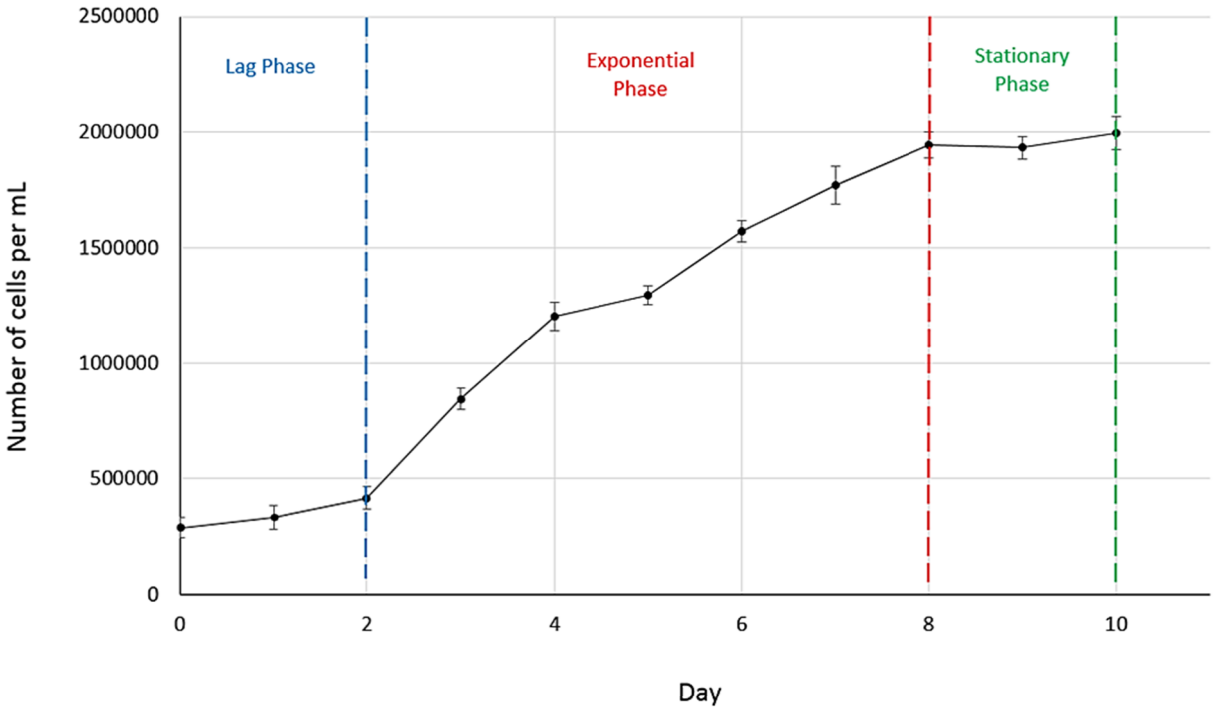


Figure 2.13. Growth curve for *Chaetoceros sp.* Black dots = average of three replicates. Error bar = Standard deviation

2.10.2 Biofilm clay coat synthesis experiments

The relationship between biofilms and the formation of clay-coated grains in shallow marine environments was investigated using an array of microcosms under controlled laboratory conditions (Figure 2.14). Artificial Sea Water (13L) was mixed with 260mL of Guillard's (F/2) Marine Water Enrichment Solution (Sigma-Aldrich) to produce a bulk sea water growth media with a salinity of 25ppt.

Individual sediment mixtures were prepared for each microcosm by mixing 300g of pure quartz sand (average grain size of 170µm) with 9.3g of calcium bentonite clay. This produced a sediment mixture with a clay content of 3%, which is the minimum content required to enable clay-coated grains to form (Dowey et al., 2012).

Calcium bentonite belongs to the smectite clay mineral group and forms via the alteration of glassy volcanic tuff or silica bearing rocks such as granite and basalt in the presence of water (Inglethorpe et al., 1993). Calcium bentonite is widely commercially available in the form of a dark grey to brown powder which is easily identified using a petrographic microscope. By selecting calcium bentonite as the clay mineral in this study ensured the easy identification and quantification of clay-coated quartz grains.

Each sediment mixture was added to a 1L borosilicate beaker containing 600 mL of autoclaved bulk sea water growth media. Beakers were covered with a transparent film and sediment was left to settle naturally for 3 days. A total of fifteen microcosm experiments were set up (3 sacrificial replicates for each of the sampling days and control experiment).

A 4mL aliquot of the bulk cell solution prepared in Chapter 2.10 was added to twelve of the fifteen microcosms and the remaining three microcosms were inoculated with 4ml of sterile sea water growth media as abiotic controls. Microcosms were maintained at 20°C +/- 1°C and placed under an artificial aquarium light (2000 lux), equipped with a timer programmed to simulate 12 hours of darkness and 12 hours of light over a 24-hour period. Each microcosm was stirred gently every second day using a spatula to simulate sediment resuspension whilst limiting the disruption of biofilms. The microcosms experiments ran for, 0, 5, 10 and 15 days, with three sacrificial replicate experiments for each day and control experiment. Sediment from the abiotic control experiments was sampled at the end of the 15-day period.

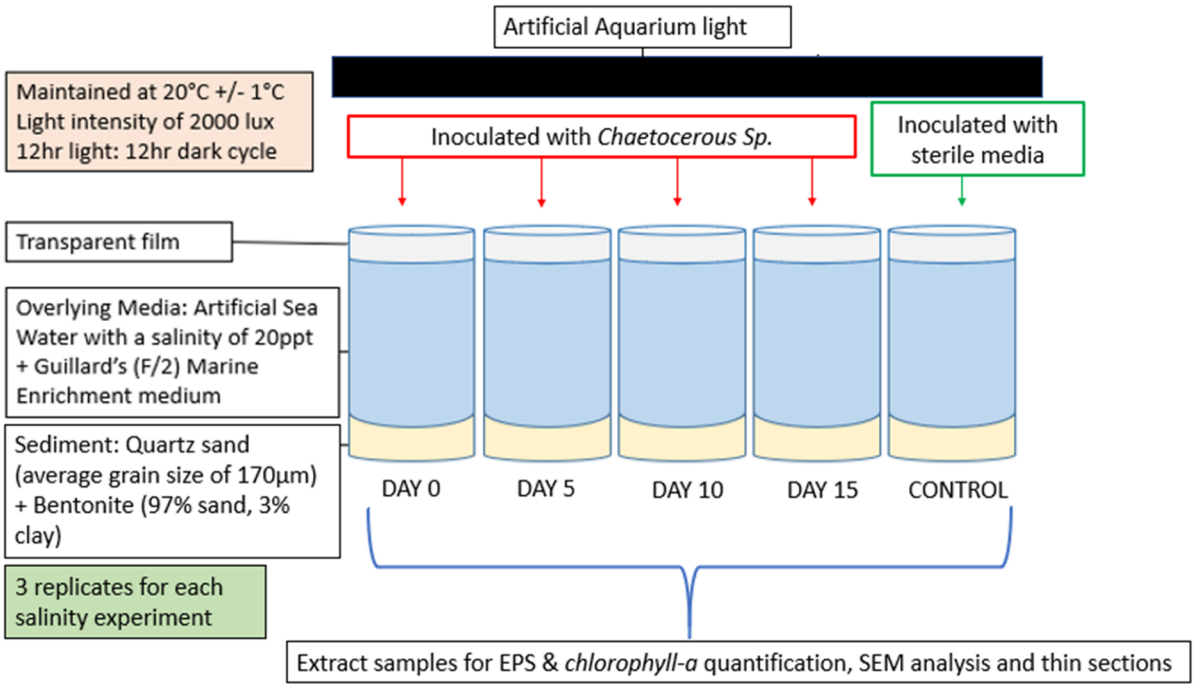


Figure 2.14. EPS clay coat synthesis experimental set up

2.10.3 Salinity clay coat synthesis experiments

To investigate the effect salinity has on the formation of clay-coated grains, an array of microcosms (Figure 2.15) was set up under controlled laboratory conditions.

Individual sediment mixtures, identical to the mixture prepared for the EPS clay coat synthesis experiments, were prepared for each microcosm by mixing 300g of quartz sand (average grain size of 170µm) with 9.3g of bentonite clay.

Solutions with a salinity ranging from 0 (deionised water), 15ppt, 30ppt and 45ppt were prepared by mixing Artificial Sea Salt with deionised water. The average salinity of sea water is 35ppt, however an extreme of 45ppt was used in this study to clearly define the relationship between salinity and the formation of clay-coated grains.

Each sediment mixture was added to a 1L beaker containing 600 mL of autoclaved saline solution. The sediment was then suspended in the overlying water column for 5 minutes at a speed of 200rpm using a VELP JLT 6 Flocculator (VELP Scientifica Srl, Province of

Monza and Brianza, Italy) to simulate sediment resuspension and allow sufficient time for the interaction of clay particles in the water column with the various electrostatic concentrations. After 5 minutes of resuspension, sediment was left to settle naturally for 3 days prior to sediment sampling. Three experimental replicates were set up for each of the saline conditions.

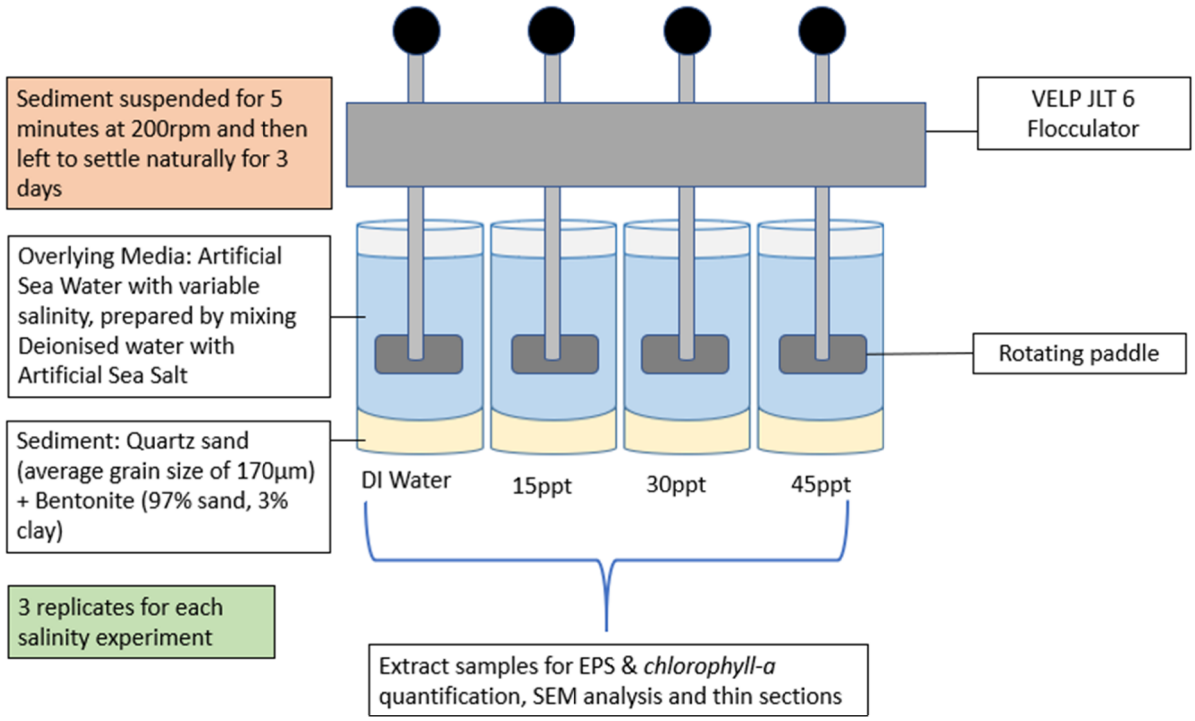


Figure 2.15. Salinity clay coat synthesis experimental set up

2.11 Clay coat transformation pressure chamber experiments

Bulk surface sediment (top 2 cm) was collected from a tidal bar located on the arm of the River Esk (SD 08568 94589) in Ravenglass Estuary.

Experiments were set up as depicted in Figure 2.16. Experiments were run under closed conditions, where samples were subjected to cooling and subsampling after each experimental run. Each experiment was run for 3 days. The experiments were limited to a maximum of 10MPa (equivalent to roughly 500m of burial). Therefore, this study

focused on the effect that increasing temperature has on the transformation of precursor clay-coated grains.

The starting sediment samples (5 grams) were placed into a steel mesh bag and added to the pressure chamber vessel, along with 5 grams of silica beads. Synthetic formation water was prepared for each experiment by mixing 10ml of Na_2CO_3 with 90ml of deionised water to form a 0.1M solution. The formation water composition used in the pressure chamber experiments was selected based on the composition of formation waters for Jurassic sandstone reservoirs in the North Sea and Haltenback Terrace (Egeberg and Aagaard, 1989; Aagaard et al., 1992).

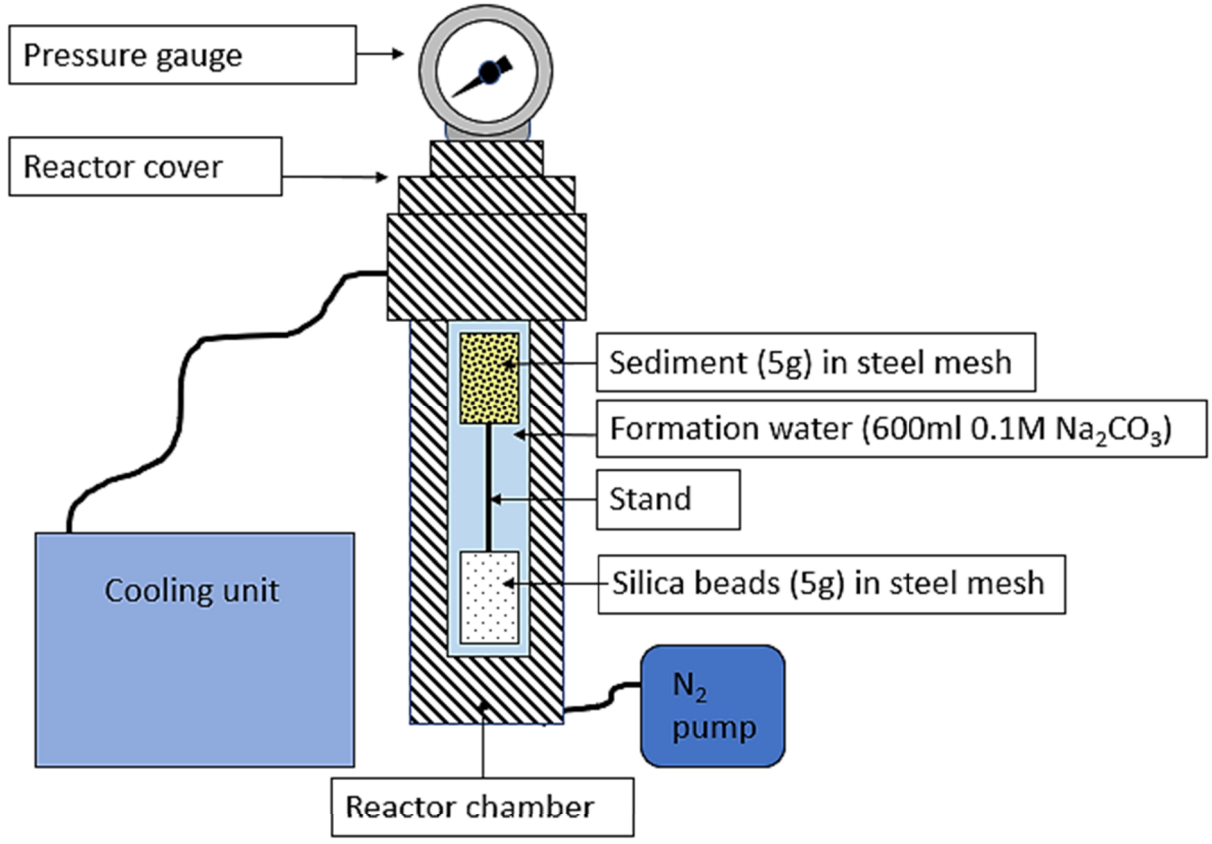


Figure 2.16. Hydrothermal pressure chamber experimental set up

2.11.1 Geochemical modelling of the precipitation of minerals during pressure chamber experiments

The saturation indices (SI) were modelled to identify the potential for the formation of new phases using the experimental conditions and temperatures the sediment could reach during diageneses using PREEQC and the WATEQ4F database (Parkhurst & Appelo 2013). For each model run, the solution was set as 100 mM/L carbonate and 200 mM/L sodium with the solution in equilibrium with anorthite, adularia, chlorite 7A, illite, and amorphous silica. The solution pH was calculated from the solution chemistry in each model run. Anorthite and adularia were chosen as the closest representative minerals for the feldspar present in the experiments, being primarily potassium and calcium-rich. Each model was run independently at each temperature, 60, 90, 150, and 250º C, to best approximate the diagenic endpoint of the sediment following burial. As the models use thermodynamics to predict the formation of phases based on geochemical gradients based on equilibrium, they do not account for reaction kinetics or activation energy. Therefore, the model can predict which mineral phases the conditions are thermodynamically favorable for, but the model can not tell with certainty if a phase will form.

Chapter 3. Biofilm and salinity controls on the formation of clay-coated grains

ABSTRACT: Chlorite-coated sand grains restrict the growth of quartz overgrowths during diagenesis by preventing contact between detrital quartz and diagenetic fluids. This preserves primary porosity and increases the storage capacity of a reservoir. Chlorite coats typically form via the thermal transformation of precursor clay coats such as berthierine. The processes responsible for the formation of precursor clay coats are poorly constrained. This makes predicting the distribution of chlorite-coated grains in the subsurface extremely difficult. Biofilms have been suggested to play a vital role in the formation of precursor clay coats by forming an adhesive layer on the surface of quartz grains which acts as a binding site for clay particles. Biofilms are common to almost all aquatic environments and consist of a mixture of microbial cells and extracellular polymeric substances (EPS). In intertidal environments the main microorganisms responsible for the formation of biofilms are diatoms.

This was the first study to adopt an experimental approach to directly test the link between clay-coat formation and biofilms. This study also investigated whether clay-coats can form abiotically due to high salinity conditions. High salinity conditions cause clay particles to flocculate and potentially attach to quartz grains.

Sediment mixtures of quartz sand (97%) and bentonite clay (3%) were added to both abiotic (salinity) and biotic (EPS) microcosms. Each biotic microcosms had a different concentration of EPS, secreted by the marine diatom *Chaetoceros sp*. Biotic microcosms were stirred gently to simulate sediment resuspension. Sediment in the abiotic microcosms was suspended in artificial sea water with variable salinities to investigate the effect of salinity on the formation of clay-coated grains.

Sediment from the experiments was subsampled to produce thin sections to quantify average clay-coat grain coverage. Scanning electron microscopy (SEM) was used to analyse clay-coat morphology and coverage at the grain scale. Total carbohydrate and *chlorophyll-a* content were used as geochemical proxies to measure EPS concentration.

In the biotic microcosms, clay-coat coverage increased from 4 to 22% with increasing EPS concentration. This confirms that biofilms enhance the formation of clay coated grains by causing clay particles to stick to quartz grains. Chlorite precursor clay coats are therefore more likely to form in depositional environments with high biofilm abundance such as tidal sand flats.

In the abiotic microcosms, clay-coat coverage increased from 2 to 25% with increasing salinity (deionised water to 45ppt). This indicates high salinity can promote the formation of clay coated grains by causing clay particles to flocculate and attach to quartz grains. The abiotic experiments also indicate that biofilms are not essential for clay coat formation.

In modern day estuarine systems, clay-coat coverage typically decreases from intertidal to open marine depositional settings (increasing salinity). This contradicts the results from the abiotic experiments in this study where there was an increase in clay coat coverage with increasing salinity. The abiotic experiments in this study did not consider external environmental variables. The lack of clay-coated grains present in high salinity natural environments is likely a result of high energy conditions, where clay-coats are rapidly removed due to extensive grain collision. This highlights that to fully understand the formation of precursor clay coats, an integrated approach is required which combines experimental observations with the processes operating in natural systems.

3.1 Introduction

Authigenic clay coats (commonly Fe-rich chlorite coats) can inhibit the formation of quartz overgrowths during diagenesis (Bloch et al., 2002; Anjos et al., 2003; Dowey et al., 2012; Cao et al., 2018). Chlorite clay-coats prevent the precipitation of quartz overgrowths by limiting the contact of detrital quartz grains with diagenetic fluids (Bloch et al., 2002; Billault et al., 2003; Lander et al., 2008). This process results in chlorite clay-coated reservoirs retaining a higher proportion of primary porosity during deep burial compared to cleaner, non-chlorite clay-coated reservoirs.

Chlorite is commonly formed via the progressive burial and thermal transformation of precursor clay mineral coats such as berthierine (Ehrenberg, 1993) or smectite (Humphreys et al., 1989). The processes responsible for the formation of precursors clay

coats remain unknown. Understanding how precursor clay coats form is essential to predict the distribution of chlorite clay-coated grains in the subsurface.

A recent study in Ravenglass Estuary, UKR suggests that biofilms are the main mechanism for the formation of clay-coated grains in modern shallow marine settings (Jones, 2017; Wooldridge et al., 2017a). Biofilms form an adhesive layer on the surface of sand grains which promotes the binding and entrapment of clay particles (Jones, 2017; Wooldridge et al., 2017a). These biogenic clay-coats are thought to represent precursors of the chlorite clay-coats observed in ancient reservoirs (Jones, 2017; Wooldridge et al. 2017a).

3.1.1 Biofilm-sediment interactions

Biofilms consist of a mixture of microbial cells and adhesive extracellular polymeric substances, secreted by microorganisms such as cyanobacteria and diatoms (Underwood et al., 1995; Jesus et al., 2009). Biofilms are common to almost all marine and non-marine environments (Jesus et al., 2009) and often agglomerate with sediment particles which can be incorporated into the biofilm through bio-stabilization (Jones, 2017). In intertidal environments, the main marine organisms responsible for the formation of biofilms are benthic and planktonic diatoms (Underwood et al, 1995; Stal, 2003).

Benthic diatoms form biofilms at the sediment-water interface. Planktonic diatoms adhere to sediment particles whilst descending in the water column and are then incorporated into sediment via co-deposition with sediment particles.

Diatoms can attach to sediment via two mechanisms: the adhesion of diatoms to sediment particles larger than themselves such as sand grains, and the electrostatic attraction of finer clay particles to the surface of diatom cells. The rate at which diatoms are co-deposited with sediment is a function of the settling velocity.

Previous studies of diatom-sediment interaction found that diatoms formed EPS “trails” to help facilitate their movement from one sediment particle to another (Stal, 2003; Garwood et al., 2015; Wooldridge et al 2017a). Diatoms detach from the EPS fibers during movement, leaving a network of adhesive EPS strands on the surface of sediment grains (Garwood et al., 2015; Wooldridge et al 2017a).

3.1.2 Clay flocculation due to high salinity

Alongside biofilms, high salinity environmental conditions also cause clay particles to flocculate (Zita and Hermansson, 1994). This process can be explained through Derjaugin, Landau, Verwey, and Overbeek (DLVO) theory (Derjaugin, and Landau, 1993). DLVO theory considers the balance between attractive van der Waals forces and repulsive electrostatic forces, existing between two surfaces, such as two clay particles. Clay particles have a net negative charge, with overlapping electrical double layers associated with a strong repulsive force via Van der Waals forces (Zita and Hermansson, 1994). As a result, clay particles in a media with a low electrolyte concentration are repelled by each other, which lowers the chances of collision and flocculation.

In fresh water (low electrolyte concentration) there is a lack of positively charged ions, which causes the negative repulsive forces existing between clay particles to dominate (Krahl et al., 2022). This causes clay particles to repel each other and limits the formation of clay floccules.

In saline water (high electrolyte concentration), there is an abundance of sodium ions which form a positively charged cloud around negatively charged clay particles. This causes a decrease in the repulsive forces existing between clay particles and increase the chances of particle collision and the formation of clay floccules (Zita and Hermansson, 1994; Krahl et al., 2022). Previous studies have concluded that salinities of 5-10ppt was sufficient to cause clay particles to reach flocculation equilibrium (Krahl et al., 2022).

As clay particles flocculate, they form aggregates which have a higher settling velocity than individual clay particles, allowing them to be co-deposited with larger quartz grains. To date, there have been no studies which aimed to investigate the effect of salinity on the formation of clay-coated grains.

3.1.3 Research theme and questions

This chapter aims to form precursor clay-coated grains in a controlled laboratory environment at a range of salinities and at different EPS concentrations. This is the first study to use an experiment approach to directly test the link between clay-coat formation and biofilms by forming precursor clay-coated grains in a controlled laboratory

environment. This study also investigated whether clay-coats can form abiotically due to high salinity conditions (45pt).

Forming clay-coated grains in a controlled laboratory environment allowed the link between biofilms and the environmental conditions that lead to the formation of precursor clay-coats to be directly investigated without interference by external variables, which are often present in natural systems.

This Chapter relates to the research theme “The origin and distribution of precursor clay-coated grains in shallow marine and deep-water turbidite systems” which is outlined in chapter 1.7.1. The key research question to be addressed in this chapter is:

- How does EPS content and salinity impact the formation of clay-coated grains in the clay coat synthesis experiments?

Understanding how environmental parameters such as biofilm abundance and salinity effect the formation of precursor clay-coats is an essential prerequisite to predicting the distribution of chlorite clay-coated grains in the subsurface.

3.2 Materials and methods

This section provides a summary of the methods used in this chapter. A more detailed description of methodology can be found in Chapter 2.

3.2.1 EPS clay coat synthesis experiments

The relationship between biofilms and the formation of clay-coated grains in shallow marine environments was investigated using an array of microcosms under controlled laboratory conditions (see Figure 2.14 in chapter 2 for set up).

Individual sediment mixtures were prepared for each microcosm by mixing 300g pure quartz sand (average grain size of 170µm) with 9.3g of calcium bentonite clay.

In natural marine systems chlorite is typically formed from a precursor clay mineral such as berthierine (Ehrenberg, 1993) or smectite (Humphreys et al., 1989). Smectite and berthierine are not commercially available therefore calcium bentonite was used instead.

Each sediment mixture was added to a 1L borosilicate beaker containing 600 mL of autoclaved bulk sea water growth media. Beakers were covered with a transparent film and sediment was left to settle naturally for 3 days. A total of fifteen microcosm experiments were set up (3 sacrificial replicates for each of the sampling days and control experiment).

A stock solution of *Chaetoceros sp.* (strain number: CCAP 1010/38) was obtained from the Scottish Association for Marine Science (SAMS) Culture Collection of Algae and Protozoa (CCAP). Diatoms were cultivated in growth media and harvested during the exponential growth phase (see Figure 2.13 in Chapter 2). Diatom cell cultures were added to the biotic microcosms. An abiotic control experiment was set up which consisted of sterilized sea water growth media being added to the microcosms instead of the diatom stock solution.

Microcosms were maintained at 20°C +/- 1°C and placed under an artificial aquarium light (2000 lux), equipped with a timer programmed to simulate 12 hours of darkness and 12 hours of light over a 24-hour period. The microcosms were left for 0, 5, 10 and 15 days to achieve different EPS concentrations, where 0 days represents the lowest EPS concentration and 15 days represents the highest EPS concentration.

After the designated number of days, each microcosm was stirred gently to simulate sediment resuspension and then left for three days to allow the sediment to settle, prior to sediment sampling. Three sacrificial replicate experiments were conducted for each of the experiments and the control experiment. Sediment from the abiotic control experiments was sampled at the end of the 15-day period.

3.2.2 Salinity clay coat synthesis experiments

To investigate the effect salinity has on the formation of clay-coated grains, an array of abiotic microcosms (see Figure 2.15 in chapter 2) were set up under controlled laboratory conditions.

Individual sediment mixtures, identical to the mixture prepared for the EPS clay coat synthesis experiments, were prepared for each microcosm.

Solutions with a salinity ranging from 0 (deionised water), 15ppt, 30ppt and 45ppt were prepared by mixing Artificial Sea Salt with deionised water. The average salinity of sea water is 35ppt, however an extreme of 45ppt was used in this study to test if clay coat coverage would reach an equilibrium at 35ppt or increase further in water with a salinity of 45ppt

Each sediment mixture was added to a beaker containing 600 mL of autoclaved saline solution. The sediment present in each beaker was then suspended in the overlying water column for 5 minutes at a speed of 200rpm using a VELP JLT 6 Flocculator (VELP Scientifica Srl, Province of Monza and Brianza, Italy) to simulate sediment resuspension and allow sufficient time for the interaction of clay particles in the water column with the various electrostatic concentrations. After 5 minutes of resuspension, sediment was left to settle for 3 days prior to sediment sampling. Three experimental replicates were set up for each of the saline conditions.

3.2.3 Clay coat synthesis experiment sampling

Sediment samples for SEM analysis, thin sectioning and quantifying the content of total carbohydrate and *chlorophyll-a* were extracted from the EPS experiments and salinity experiments. The water was carefully removed from each microcosm using a plastic syringe and sediment was sampled using modified plastic syringes, where the needle end of the syringe was removed to form a mini corer. All samples were stored at -20°C until further analysis

3.2.4 Sediment analysis

Total carbohydrate content was quantified from freeze-dried sediment samples as a proxy for EPS concentration. Colloidal (loosely bound) and bound EPS fractions were extracted from sediment samples using the method outlined in Chapter 2.5.1.

The total carbohydrate content of colloidal and bound sediment extracts was quantified using the phenol-sulphuric acid colorimetric assay (DuBois et al., 1956). Total carbohydrate content was also measured for sediment samples from the EPS control experiments and the salinity experiments to ensure no biological input was present in the abiotic experiments.

Chlorophyll-a content was quantified using the method outlined in Chapter 2.4. *Chlorophyll-a* content was quantified for samples from the clay coat synthesis experiments in order to compare the use of *chlorophyll-a* and total carbohydrate content as proxies for EPS abundance. *Chlorophyll-a* was also measured for sediment samples from the EPS control experiments and the salinity experiments to ensure no biological input was present in the abiotic experiments.

A thin section, of in-situ sediment, contained within a modified syringe was produced for the top 2cm of sediment taken from the microcosms after 0, 5, 10 and 15 days along with a sample from the control microcosm. Clay-coat coverage was quantified using the method put forward by Wooldridge et al., (2017a), which is outlined in Chapter 2.6.1. It was not possible to distinguish between EPS and clay via petrography. Grain coats produced in this study likely contain a mixture of EPS and clay particles. Clay coat morphology was described using terminology outlined in Table 2.1 in Chapter 2.

Wet sediment samples were collected from the EPS and salinity experiments using a sterilized scalpel and stored in aluminium foil at -20 degree °C. Sediment samples were mounted onto aluminium stubs, dried and gold coated prior to SEM analysis to image bio-sediment interactions and clay-coated grains. SEM analysis was performed using a TESCAN Vega 3LMU Scanning Electron Microscope (TESCAN, Brno, Czech Republic) at Newcastle University Medical School.

3.3 Results

3.3.1 EPS concentration

In the biotic microcosms, *chlorophyll-a* concentration was similar between day 0 to day 10 (Figure 3.1). *Chlorophyll-a* concentration on day 5 was lower than the *chlorophyll-a* concentration on day 0. EPS concentration increased with time as biofilms became more stabilized. The decrease in *chlorophyll-a* content from day 0 to day 5 and the similarity in *chlorophyll-a* values on day 0 to day 10 indicates that *chlorophyll-a* is not a reliable proxy for EPS concentration in this study. Therefore, the relationship between *chlorophyll-a* and clay coat coverage in this study is not discussed further.

The total carbohydrate content increased from 10μg per gram of sediment on day 0 to 505μg per gram of sediment on day 15 (Figure 3.2). This increase in total carbohydrate content with time reflects an increase in EPS concentration as a biofilm develops. The ratio of bound to colloidal carbohydrate also increased from day 0 to day 15. This is likely associated with biofilms becoming more established and more tightly bound to sediment with time (Yang et al., 2018). Biofilm growth occurred within the first 10 days with no statistically significant growth in EPS concentrations between days 10 and 15 (Figure 3.2).

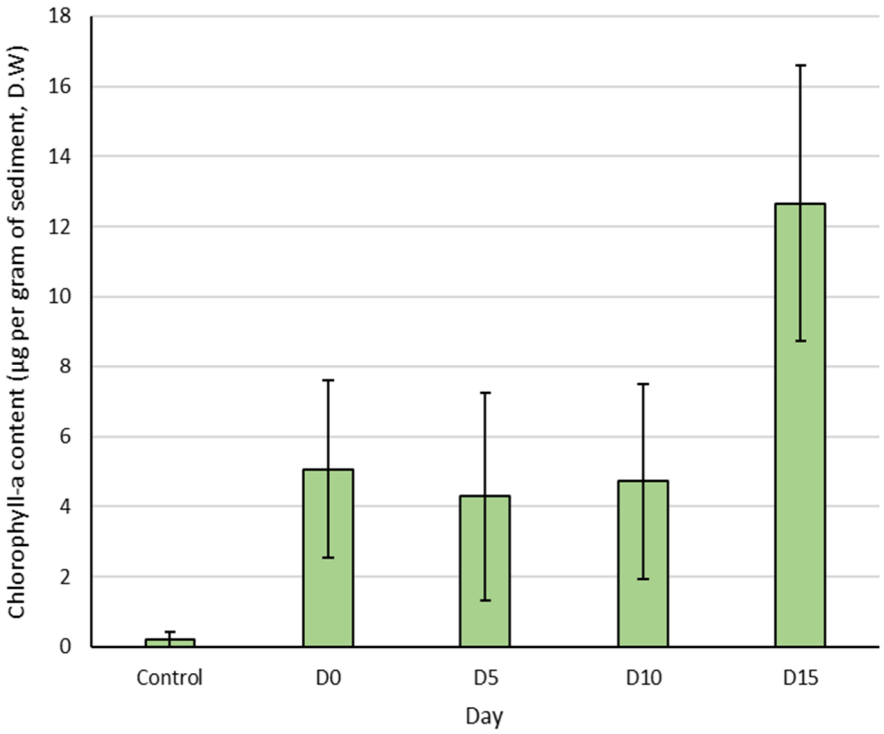


Figure 3.1. *Chlorophyll-a* content for the 15-day EPS experiment. Error bars represent the standard deviation across three replicates

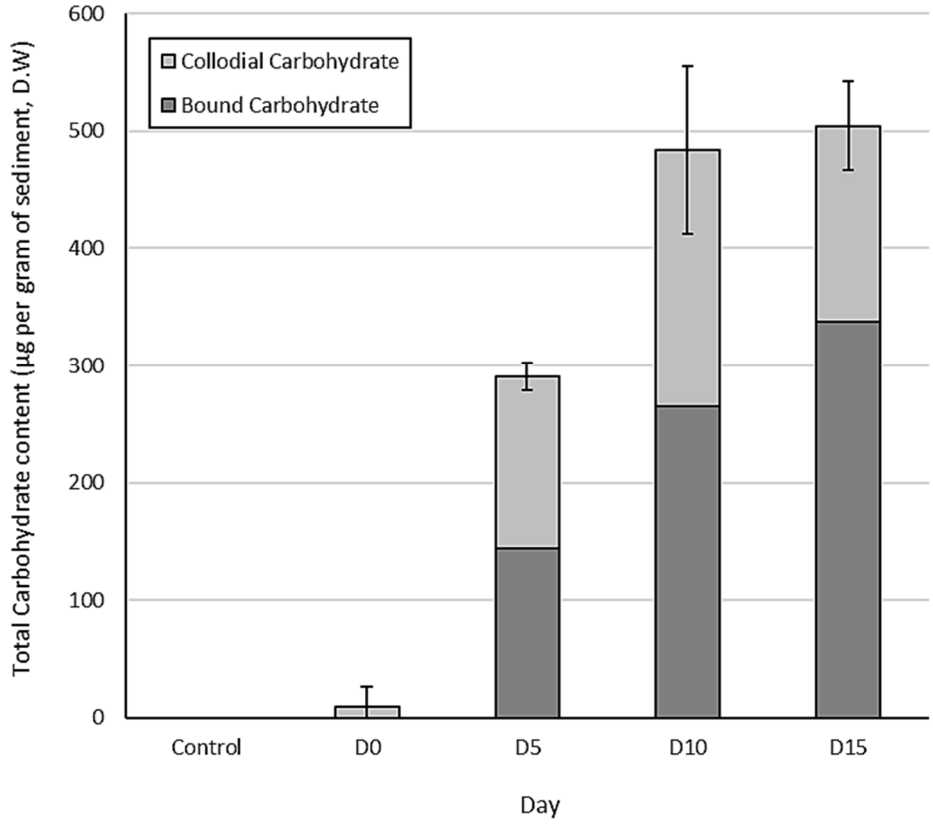


Figure 3.2. Total carbohydrate content for the 15-day EPS experiment. Error bars represent the standard deviation of total carbohydrate across three replicates

3.3.2 Relationship between EPS and clay coat grain coverage

In the biotic microcosms, average clay-coat grain coverage increased gradually from 4% to 22% from day 0 to day 15, with increasing total carbohydrate concentration (Figure 3.3).

Clay coat coverage was 3% in the control experiment (no EPS), which ran for the full 15 days (Figure 3.3). Several different clay coat morphologies were formed during the experiments (Figure 3.4).

The SEM images showed an increase in clay-coat coverage from day 0 to day 15, with clay-coated sand grains absent in the control experiment (Figure 3.5). Clay coated grains were less visible via SEM compared to petrography. The sediment samples from the laboratory experiments did not display EPS stalk or diatom trails, which are commonly observed in sediments covered by natural biofilms. Small clay floccules attached to the surface of quartz grains were observed after day 0 (Figure 3.5B), day 5 (Figure 3.5C), day 10 (Figure 3.5D) and day 15 (Figure 3.5F). Clay bridges connecting quartz grains were present in day 5 (Figure 3.5C), day 10 (Figure 3.5D) and day 15 (Figure 3.5F) sediment samples. Discontinuous clay coats partially covering quartz grains were identified in sediment from day 5 (Figure 3.5C) and day 15 (Figure 3.5E)

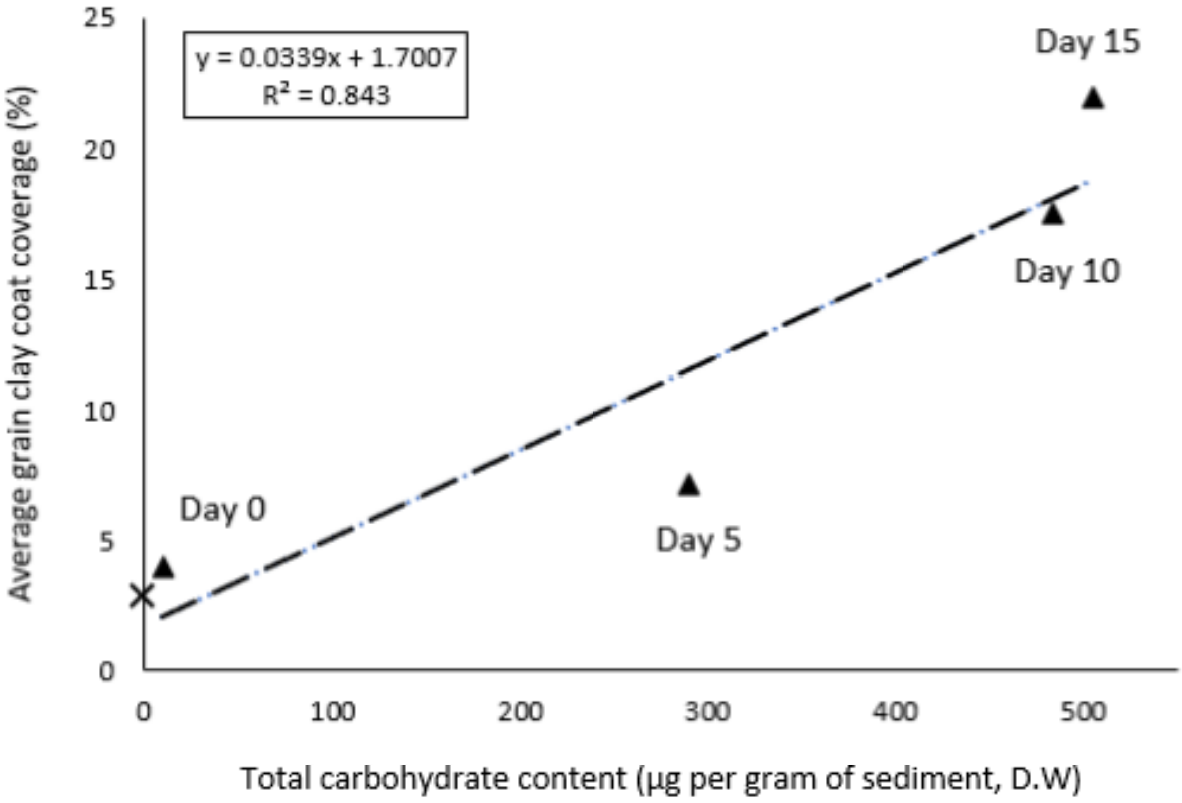


Figure 3.3. Average clay-coat grain coverage vs total carbohydrate concentration. X = control experiment. D.W = dry weight

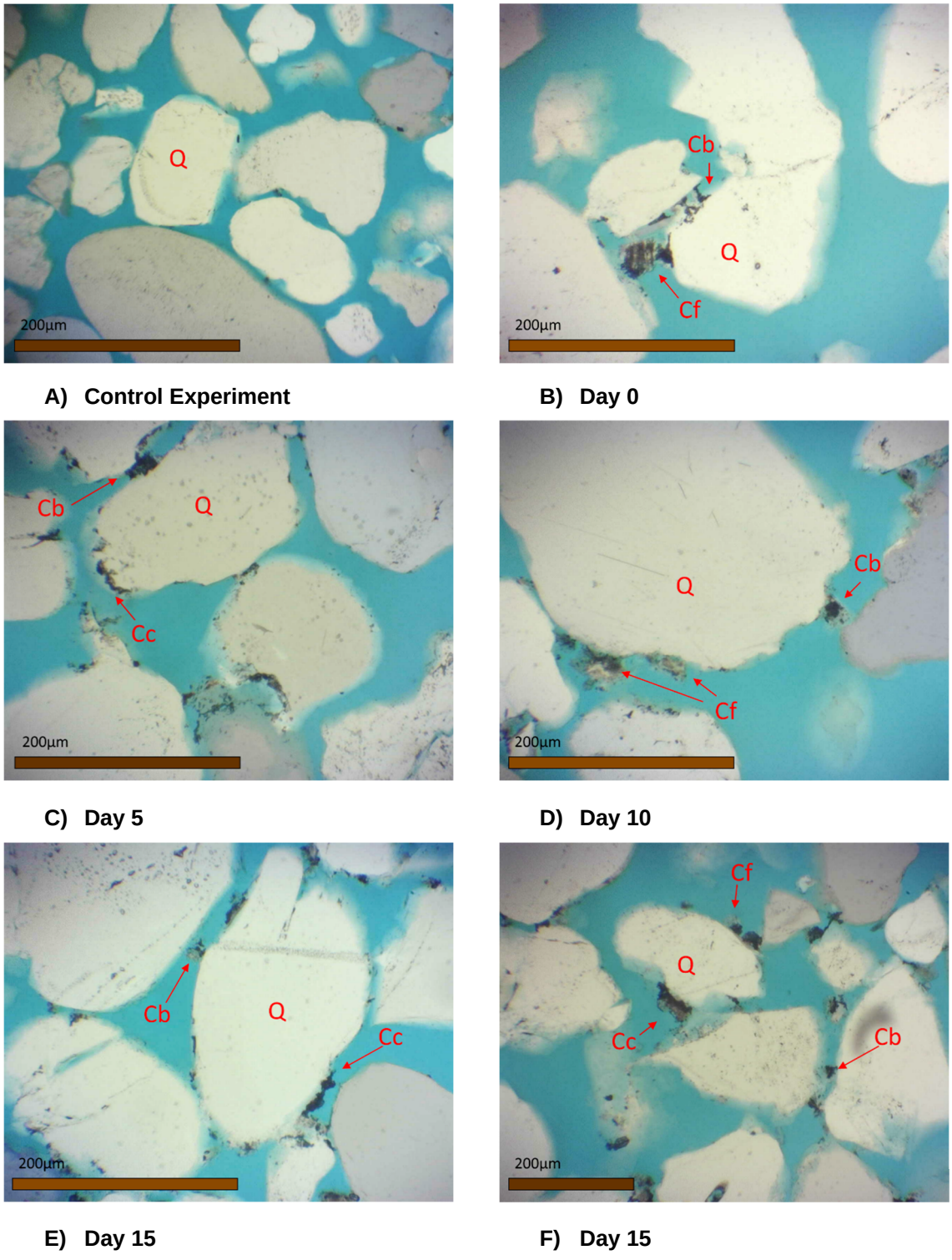
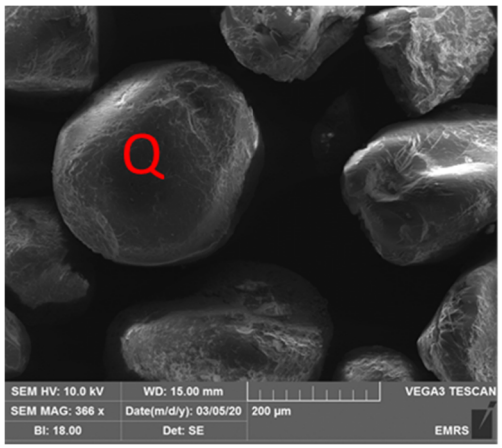
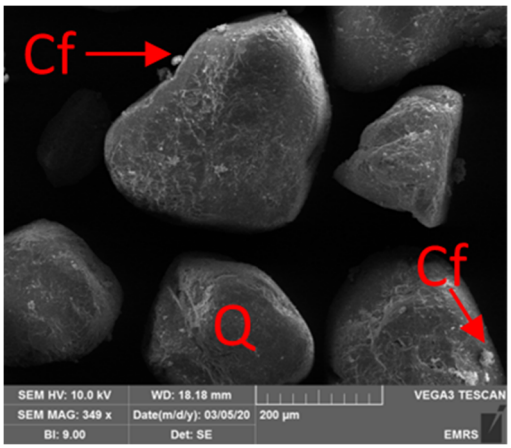


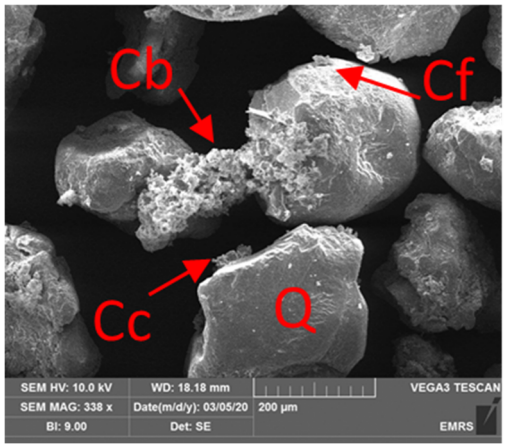
Figure 3.4. Thin section images of clay coat synthesis EPS experiments. Cb = clay bridge, Cf = clay floc, Cc = partial clay coating and Q = quartz



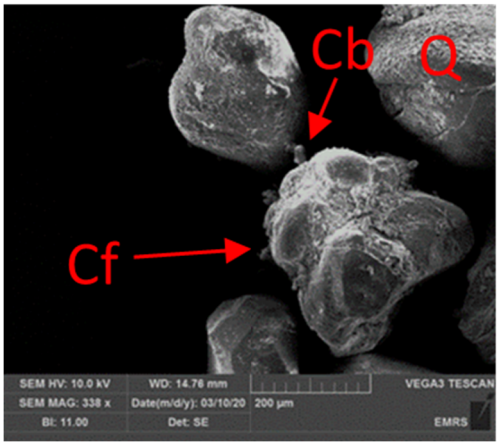
A) Control Experiment



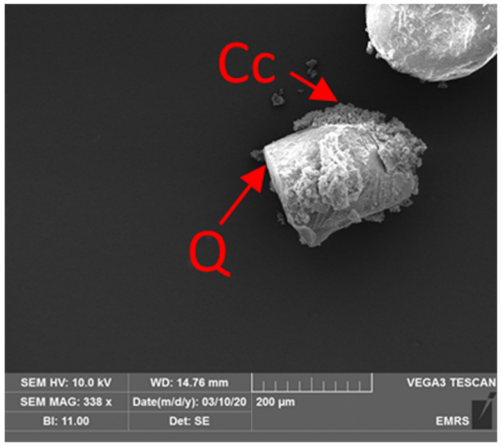
B) Day 0



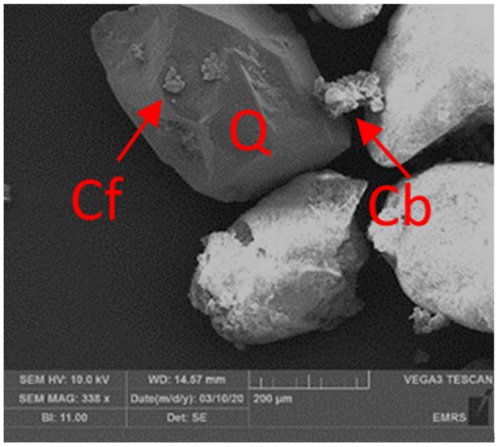
C) Day 5



D) Day 10



E) Day 15



F) Day 15

Figure 3.5. SEM images of clay coat synthesis EPS experiments. Cb = clay bridge, Cf = clay floc, Cc = partial clay coating and Q = quartz

3.3.4 Relationship between salinity and clay coat grain coverage

In the abiotic microcosms, average clay-coat grain coverage increased gradually from 2 to 25% with increasing salinity from deionised water to 45ppt (Figure 3.6). There was a low number of clay-coated sand grains in the freshwater experiment (Figure 3.7A). Clay-coat morphologies formed during the series of salinity experiments include flocs (Figure 3.7B,C), partial coatings (Figure 3.7B,D) and clay bridges (Figure 3.7B,C,D). Clay coated grains were less visible via SEM compared to petrography. The formation of clay-coated grains in the salinity experiments indicate that there are abiotic pathways for clay coat formation and that biofilms are not essential for the formation of clay coated grains.

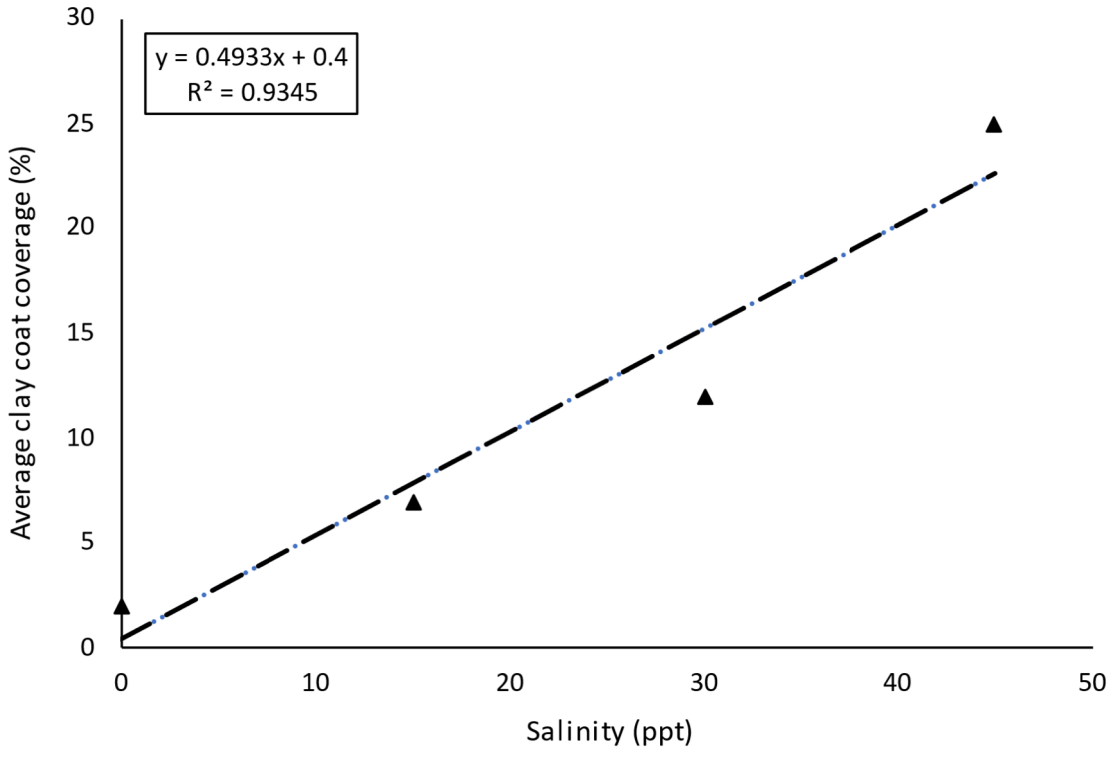
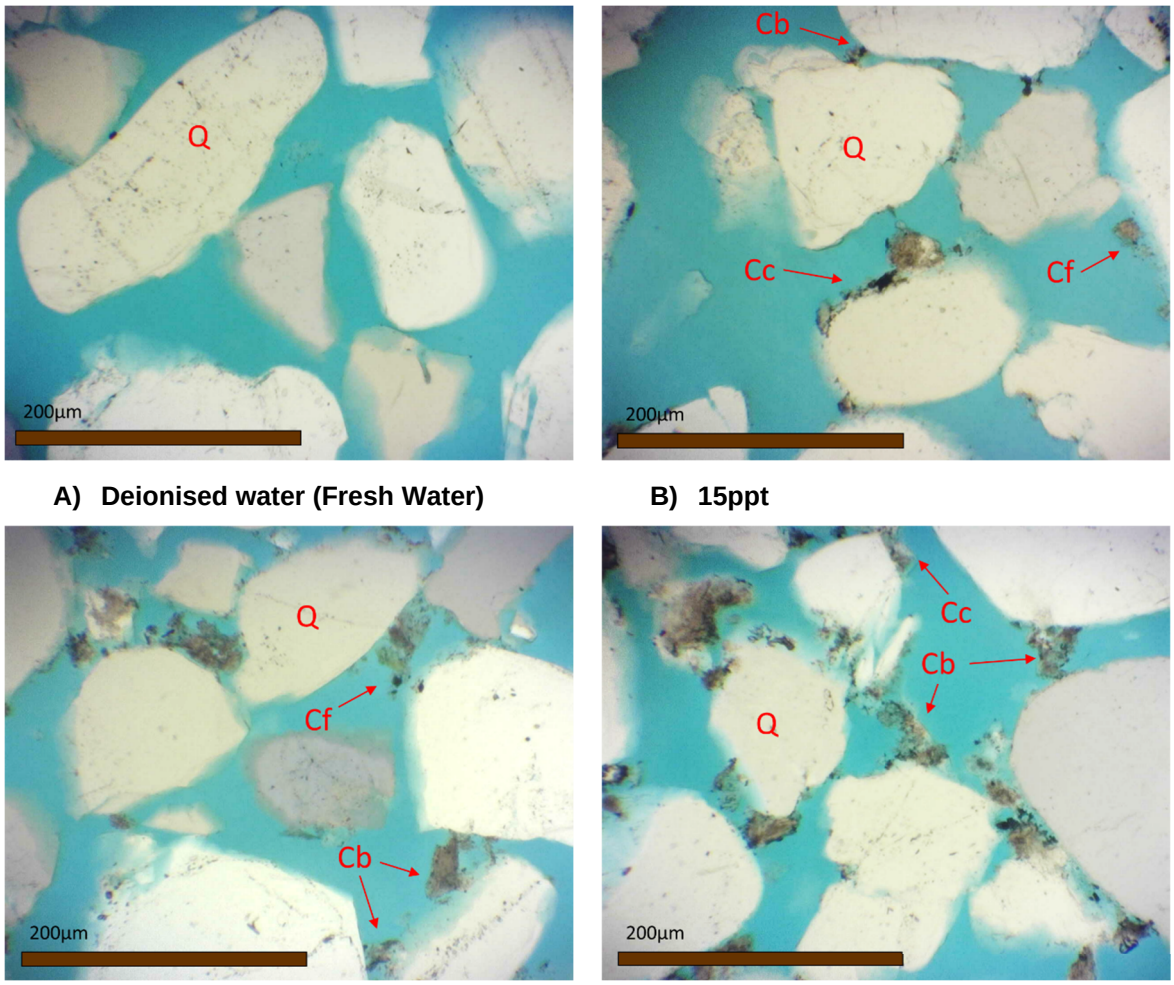


Figure 3.6. Average clay-coat grain coverage vs salinity

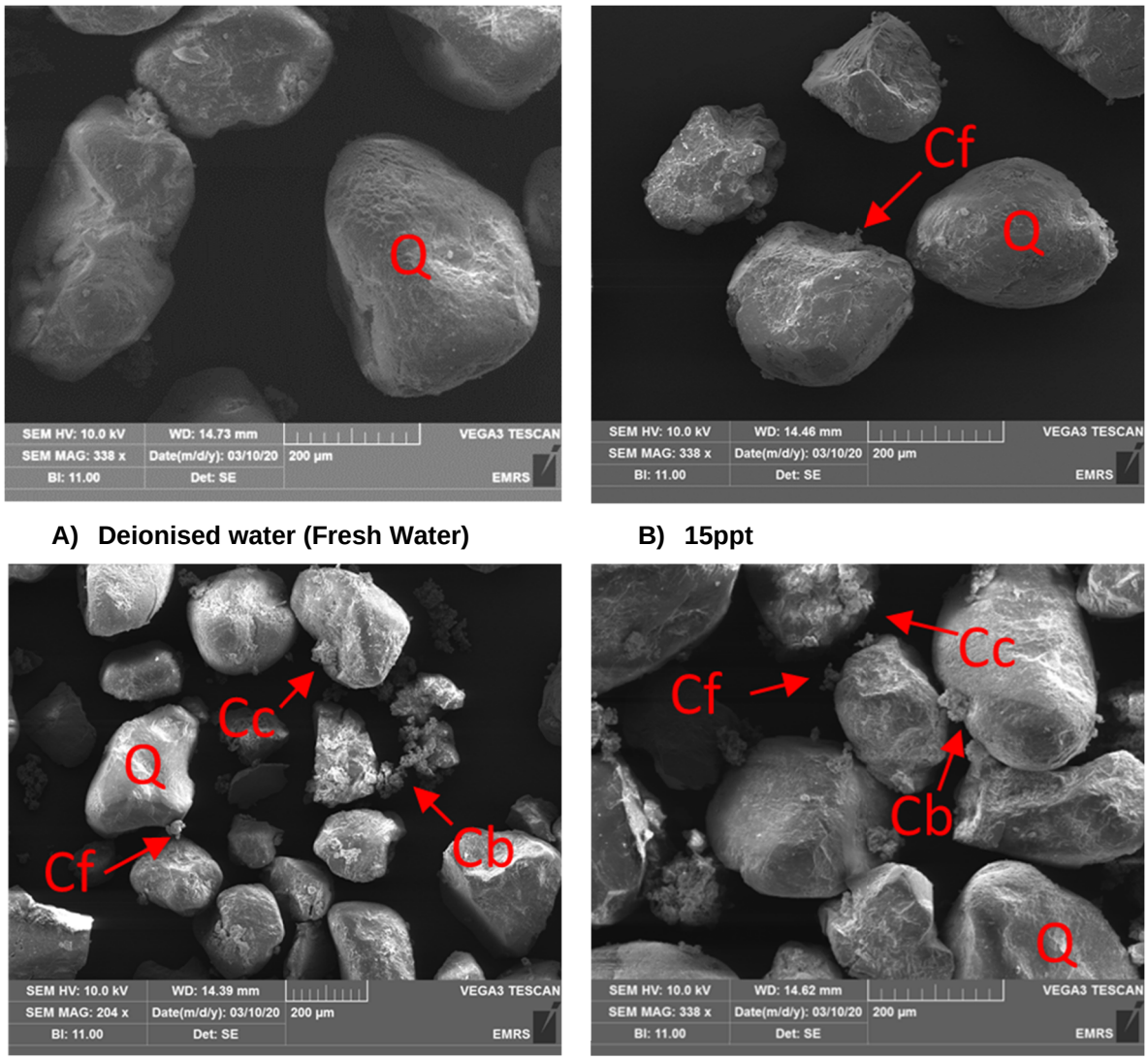


A) Deionised water (Fresh Water) **B) 15ppt**

C) 30ppt **D) 45ppt**

Figure 3.7. Thin section images of clay coat synthesis salinity experiments. Cb = clay bridge, Cf = clay floc, Cc = clay coating and Q = quartz

The SEM images show a significant increase in clay-coat coverage with increasing salinity from DI water to 45ppt, with clay-coated sand grains largely absent in the experiments conducted using deionised (fresh) water (Figure 3.8A). Small clay floccules attached to the surface of quartz grains were observed in the 15ppt (Figure 3.8B), 30ppt (Figure 3.8C) and 45ppt (Figure 3.8D) salinity microcosms. Clay bridges connecting quartz grains were identified in the 30ppt (Figure 3.8C) and 45ppt (Figure 3.8D) salinity microcosms. Discontinuous clay coats partially covering quartz grains were observed in 30ppt (Figure 3.8C) and 45ppt (Figure 3.8D) salinity microcosms.



A) Deionised water (Fresh Water) **B) 15ppt**

C) 30ppt **D) 45ppt**

Figure 3.8. SEM images of clay coat synthesis salinity experiments. Cb = clay bridge, Cf = clay floc, Cc = partial clay coating and Q = quartz

3.4 Discussion

This Chapter focused on the research theme “The origin and distribution of precursor clay-coated grains in shallow marine and deep-water turbidite systems” which is outlined in chapter 1.7.1. The key research question addressed in this chapter was “How does EPS content and salinity impact the formation of clay-coated grains in the clay coat synthesis experiments?”

3.4.1 The impact of biofilms on the formation of clay-coated grains

In this study clay-coat coverage increased from 4 to 22% with increasing EPS concentration (indicated by total carbohydrate concentration). This indicates the formation of clay coated grains is enhanced by the presence of biofilms and supports the biofilm origin of clay-coated grains observed in Ravenglass Estuary theorized by Wooldridge et al. (2017a).

The clay-coat morphologies formed during the EPS experiment include flocs, partial coatings and clay bridges (Figure 3.4), which were similar to the clay-coat morphologies formed during the salinity clay coat synthesis experiments (Figure 3.7) and clay-coated grains found in modern estuarine systems such as Ravenglass Estuary in the UK (Wooldridge et al., 2017a) and the Gironde Estuary in France (Virolle et al., 2018). This may indicate that clay-coated grains present in natural modern systems form via a similar mechanism to clay coated grains formed in this study.

3.4.2 The impact of salinity on the formation of clay-coated grains

The formation of clay-coated grains in the abiotic salinity experiments confirms biofilms are not essential for the formation of clay-coated grains.

In the salinity clay coat synthesis experiments, average grain clay-coat coverage increased from 2 to 25% with increasing salinity (deionised water to 45ppt). This increase is likely a result of the high concentration of electrolytes decreasing the size of the repulsive field surrounding clay particles, which increases the chances of clay particles colliding and interacting with quartz grains.

This study found an increase in clay-coat coverage with increasing salinity, which disagrees with clay-coat coverage distribution trends observed in natural estuarine systems such as Ravenglass Estuary (Wooldridge et al., 2017a) and the Gironde Estuary (Virolle et al., 2018). In these two modern estuarine systems there is a decrease in clay-coat coverage seaward as salinity increases. The seaward reduction in clay-coated grains observed in modern estuarine settings, is likely related to the removal of clay coats during sediment transportation, where clay-coats are rapidly removed due to extensive grain collision (Wilson 1992). This highlights the importance of an integrated approach when studying the formation of clay-coated grains, that considers experimental data and also the processes operating in natural systems.

3.4.3 Chlorophyll-a as a proxy for EPS concentration

In the biotic microcosms, total carbohydrate content increased from day 0 to day 15 (Figure 3.2). This is due to an increase in EPS concentration as biofilms become more established, with increasing bio productivity. *Chlorophyll-a* did not significant increase with increasing time and biofilm development. The measured *chlorophyll-a* content of sample replicates varied by as much as 50% (highlighted by overlap of error bars in Figure 3.1), especially at lower concentrations of *chlorophyll-a* (from day 0 to day 10). Therefore, in this study *chlorophyll-a* was deemed as an unreliable proxy for EPS concentration.

This supports the findings of an extensive study conducted by Blanchard et al. (2000), who concluded the relationship between *chlorophyll-a* and EPS is a function of sediment type and depth, and that there was no correlation for sand-dominated samples and samples collected from depths greater than 5-10mm from the sediment-water interface. We recommended that all studies which involve measuring biofilm abundance use total carbohydrate as a proxy for EPS and avoid the use of *chlorophyll-a*.

3.5 Conclusion and recommendations

Clay-coated sand grains formed during this study were similar to clay-coated grains found in modern analogues, which are thought to represent precursors to chlorite coats found in

deeply buried sandstone reservoirs (Dowey et al., 2012; Jones, 2017; Wooldridge et al., 2017a).

The main aim of this study was to use an experimental approach to investigate how EPS content and salinity impact the formation of clay-coated grains. An experimental approach allowed the relationship between EPS content and clay coat coverage to be studied in the absence of external variables. This study proved that an increase in EPS content directly resulted in an increase in clay coat coverage. This study confirms that biofilms act as an important adhesive material to facilitate the formation of clay-coated grains in shallow marine settings.

Clay-coated grains are also present in fluvial (Salem et al., 2005) and continental slope deposits (Bloch et al., 2002). Clay-coated grains in continental slope deposits (Atoka Formation, Arkoma basin, central USA) have been interpreted as forming in a marginal marine setting, prior to being transported to the continental slope (Bloch et al., 2002; Wooldridge et al., 2017a). This indicates that clay-coated grains, possibly with a biofilm origin, may be durable enough to withstand long -distance sediment transportation. Biofilms have also been recorded as facilitating the attachment of dust particles to sand-grain surfaces in desert environments (Belnap and Weber, 2013).

This study focused on defining the link between clay-coat formation as a function of biofilms and salinity. The link between clay-coat formation and sedimentary parameters such as grain size and mineralogy were not considered and may represent an important focus for future studies.

Chapter 4. The origin and distribution of clay-coated grains in shallow and deep marine sedimentary systems

ABSTRACT: Porosity and permeability are the two parameters which control reservoir quality. Quartz cement is the main diagenetic phase responsible for the loss of porosity and permeability of sandstone reservoirs during diagenesis.

Clay coats, especially chlorite clay coats, preserve primary porosity by inhibiting the precipitation of diagenetic quartz overgrowths. Chlorite clay coats are likely formed via the progressive burial and transformation of precursor clay mineral coats, such as berthierine or smectite. The formation process of precursor clay coats and the controls on the spatial distribution of precursor clay coats in sedimentary systems remains poorly understood. This makes predicting the distribution of chlorite-coated grains in the subsurface complex.

This study investigates the formation and distribution of clay-coated grains in Bute Inlet, which is a modern deep-water turbidite system in British Columbia, Canada. Surface sediment samples were analysed to establish grain size and sorting, detrital mineralogy and clay-coat coverage. *Chlorophyll-a* and total carbohydrate content, both proxies for extra cellular polymeric substances (EPS), were also measured to assess a potential biofilm-origin for clay-coated grains present in Bute Inlet. Clay-coated grains from Bute Inlet were compared to clay-coated grains present in the well-studied Ravenglass Estuary to consider different mechanisms of clay-coat formation and to identify the large-sale controls (depositional environment and provenance) of the formation of clay-coated grains.

Overall, clay-coat coverage (average % of the total perimeter of a sand grain which is coated) is significantly lower in Bute Inlet compared to Ravenglass Estuary. The highest clay-coat coverage was observed in sediment from distal lobe settings in Bute Inlet. Clay-coated grains form by a non-biofilm associated process in Bute Inlet, whereas at Ravenglass they form due to clay mineral attachment, facilitated by biofilms.

Analysis of mineralogical data from Bute Inlet and Ravenglass Estuary suggest detrital mineralogy plays a significant role in the formation of clay-coated grains, with arkosic

sands in Bute Inlet having lower levels of clay-coat coverage compared to more quartz-rich sediment in the Ravenglass Estuary.

Analysis of grain-size and sorting suggests that sediment maturity also exhibits a significant control on the formation of clay-coated grains. A high abundance of clay-coated grains is associated with sediment with a high textural maturity, which has a long residence time in shallow intertidal conditions (Ravenglass Estuary). A low abundance of clay-coated grains is typically associated with low textural maturity and sediment which has a short residence time in intertidal shallow marine conditions (Bute Inlet).

4.1 Introduction

Clay-coated sand grains have been observed in ancient (Ehrenberg, 1993; Anjos et al., 2003; Cao et al., 2018) and modern deposits (Dowey et al., 2012; Wooldridge et al., 2017a; Virolle et al., 2018). Clay-coated grains present an interesting sedimentary feature, where the factors responsible for the formation of clay-coated grains remains poorly understood (Dowey et al., 2012; Wooldridge et al., 2017a).

The presence of clay minerals in a siliciclastic reservoir has complex implications on porosity and permeability, the two parameters which govern reservoir quality. For example, the presence of clay mineral cements such as illite and kaolinite is often associated with reduced reservoir quality, due to clay mineral cements reducing porosity and permeability, by decreasing the diameter of pore throats (Pay et al., 2000; Ziegler et al., 2006; Islam, 2009; Waldmann and Gaupp, 2016).

In subsurface sandstone reservoirs, quartz overgrowths are the main diagenetic phase responsible for the reduction of porosity and permeability, which drastically reduces the volume of recoverable hydrocarbons (Bloch et al., 2002; Lander et al., 2008).

Clay-coats (especially chlorite coats) surrounding detrital quartz grains inhibit the precipitation of diagenetic quartz cement during progressive burial (Bloch et al., 2002; Anjos et al., 2003; Dowey et al., 2012; Cao et al., 2018). Consequently, sandstones containing clay-coated grains may retain a higher level of primary porosity during deep burial, compared to conventionally targeted cleaner sandstones.

Diagenetic models of quartz cementation indicate clay coats prevent the growth of quartz cement by blocking nucleation sites on the surface of detrital grains, where the key factor controlling the inhibition of quartz cementation is the completeness of coats (Billault et al., 2003; Lander et al., 2008). Clay coat mineral assemblages may consist of smectite, illite, mixed-layer illite/smectite, chlorite or mixed-layer chlorite/smectite. Chlorite is acknowledged as being the most efficient clay mineral for retarding quartz cementation (Heald and Larese, 1974; Dowey et al., 2012; Cao et al., 2018).

Previous studies of chlorite-coated reservoirs have identified a precursor clay mineral such as berthierine or smectite as essential for chlorite coat formation, where chlorite forms through the thermal alteration of a precursor clay mineral with increasing temperature and pressure (Ehrenberg, 1993; Ryan and Reynolds, 1996; Anjos et al., 2003). Artificial chlorite-coated grains, similar to naturally occurring chlorite-coated grains have been successfully synthesised by placing berthierine-coated sandstones from the Norwegian Continental Shelf in a hydrothermal pressure chamber, during an experimental study carried out by Aagaard et al. (2000). Authigenic chlorite can also form through the direct dissolution and recrystallization of volcanic rock fragments and iron and magnesium rich detrital grains (Anjos et al., 2000; Worden and Morad, 2003).

It is difficult to predict the subsurface distribution of chlorite coats because the exact process by which precursor clay coated grains form is unknown (Dowey et al., 2012; Wooldridge et al., 2017a: Jones, 2017).

Recent studies of shallow marine modern analogues suggest biofilms may play a pivotal role in the formation of precursor clay-coated grains, by forming an adhesive coat on the surface of sand grains which acts as a binding site for clay particles (Wooldridge et al., 2017a; Virolle et al., 2018; Duteil et al., 2020). Biofilms are common to almost all aquatic environments and consist of an assortment of microbial cells embedded in a network of adhesive extracellular polymeric substances (EPS), consisting of a mixture of carbohydrates, proteins, and DNA, which are secreted by microorganisms such as cyanobacteria and diatoms (Underwood et al., 1995; Jesus et al., 2009). Within intertidal environments, EPS is often secreted by diatoms living in the top few cm of the sediment, in order to facilitate vertical movement in response to daily sunlight and tidal cycles (Edgar and Pickett-Heaps, 1982; Decho, 1990; Stal, 2003; Garwood et al., 2015). Wooldridge et al. (2017a) provided the first evidence of a link between biofilms and clay-coat formation

by acknowledging a positive statistical correlation exists between clay-coat grain coverage and sediment *chlorophyll-a* content, a biomarker proxy used for biofilm abundance (Stal, 2003) across Ravenglass Estuary, UK.

Previous clay-coat modern analogue studies were dominated by shallow marine environments, with a lack of studies conducted in deep-marine and aeolian systems (Jones, 2017). This study assesses the origin and distribution of clay-coated grains across an active turbidite system.

Bute Inlet, a fjord associated deep-water turbidite system was selected as a study area due to its restricted catchment area and relatively easy access to the entire deep-marine system. The findings from Bute Inlet were compared to Ravenglass Estuary, which is an extensively studied shallow marine system to discuss the different mechanisms responsible for clay-coat formation in deep and shallow marine systems.

Studying the distribution of precursor clay-coated grains in modern analogues provides the unique opportunity to directly study the formation of clay-coated grains in an active depositional system. Clay-coated grains observed in Ravenglass Estuary (Woolridge et al., 2017) and other modern analogues, such as the Gironde Estuary, south-west France (Virolle et al., 2018) are thought to represent precursors to chlorite-coated grains observed in ancient deeply buried sandstone reservoirs. Therefore, understanding the formation of clay-coated grains in modern shallow and deep marine systems is key to understanding and predicting the spatial distribution of clay-coated grains in ancient subsurface sandstone reservoirs.

4.1.1 Research theme and questions

Chapter 3 focused on testing the relationship between grain clay coat formation and biofilms using a series of abiotic and biotic laboratory experiments. Clay coat grain coverage was found to increase as the concentration of EPS increased. This indicates that biofilms enhanced the formation of clay coated grains in the laboratory experiments by forming an adhesive surface on quartz grains.

This chapter aims to test if the laboratory observations made in the previous chapter can be applied to natural systems.

This Chapter focuses on the research theme “The origin and distribution of precursor clay-coated grains in shallow marine and deep-water turbidite systems” which is fully outlined in chapter 1.7.1. The key research questions to be addressed in this chapter are:

- How is EPS distributed across modern shallow marine and deep-water turbidite system analogues?
- Is there a relationship between EPS content and clay coat coverage in modern shallow marine and deep-water turbidite system analogues?
- What are the textural and depositional controls on clay coat formation in modern shallow marine and deep-water turbidite system analogues?
- How are precursor clay-coated grains formed in modern shallow marine and deep-water turbidite system analogues?

4.1.2 Geological setting

Bute Inlet (Figure 4.1) is a north-south trending, 70km-long and 4km-wide fjord which ranges from around 200 to 655m in depth (Zeng et al., 1991). The fjord is fed by seasonal melt water from up-dip glaciers and permanent ice sheets. Sediment enters the fjord via two main rivers, the Homathko and Southgate (Figure 4.1) which form deltas at the head of the fjord. The Homathko River is thought to contribute more than 75% of the total annual water inflow to the fjord, with a discharge that can reach up to 1600m^3 s-1 in summer (Zeng et al., 1991). Sediment is transported from the head of the two deltas to the fjord floor by quasi weekly turbidity currents in the freshet period, via a single submarine channel (Prior et al., 1994). Sediment is sourced from the cordilleran hinterland (Figure

4.2) which is dominated by the Coast Mountains batholith and metamorphic rocks (Cecil et al., 2018). The Coast Mountains batholith surrounding Bute Inlet is mainly composed of a mixture of granodiorite and quartz diorite (Roddick and Woodsworth, 2006).

Ravenglass Estuary is a shallow, well mixed, macro-tidal estuary in northwest England, UK (Figure 4.3A). The estuary is fed by three main rivers, the Esk, the Irt and the Mite and has a quartzo-feldspathic rich sediment source, including the Sherwood Sandstone Group, Eskdale Granite, Borrowdale Volcanic Group and Skiddaw Group siltstone and sandstones (Figure 4.3A). Ravenglass Estuary covers an area of roughly 5.6km², where 86% of the estuary is intertidal (Wooldridge et al., 2017b; Griffiths et al., 2019).

During the Quaternary period, drift deposits were deposited across the area in association with glacio-isostatic rebound and glacio-eustatic sea level change (McDougall, 2001; Griffiths et al., 2019). Ravenglass Estuary is primarily underlain by glacial till (Figure 4.3B. Glaciofluvial- deltaic and glaciolacustrine drift deposits are mainly restricted to the area surrounding the River Irt (Figure 4.3B). Barrier spits and raised marine deposits make up the most seaward area of the Estuary.

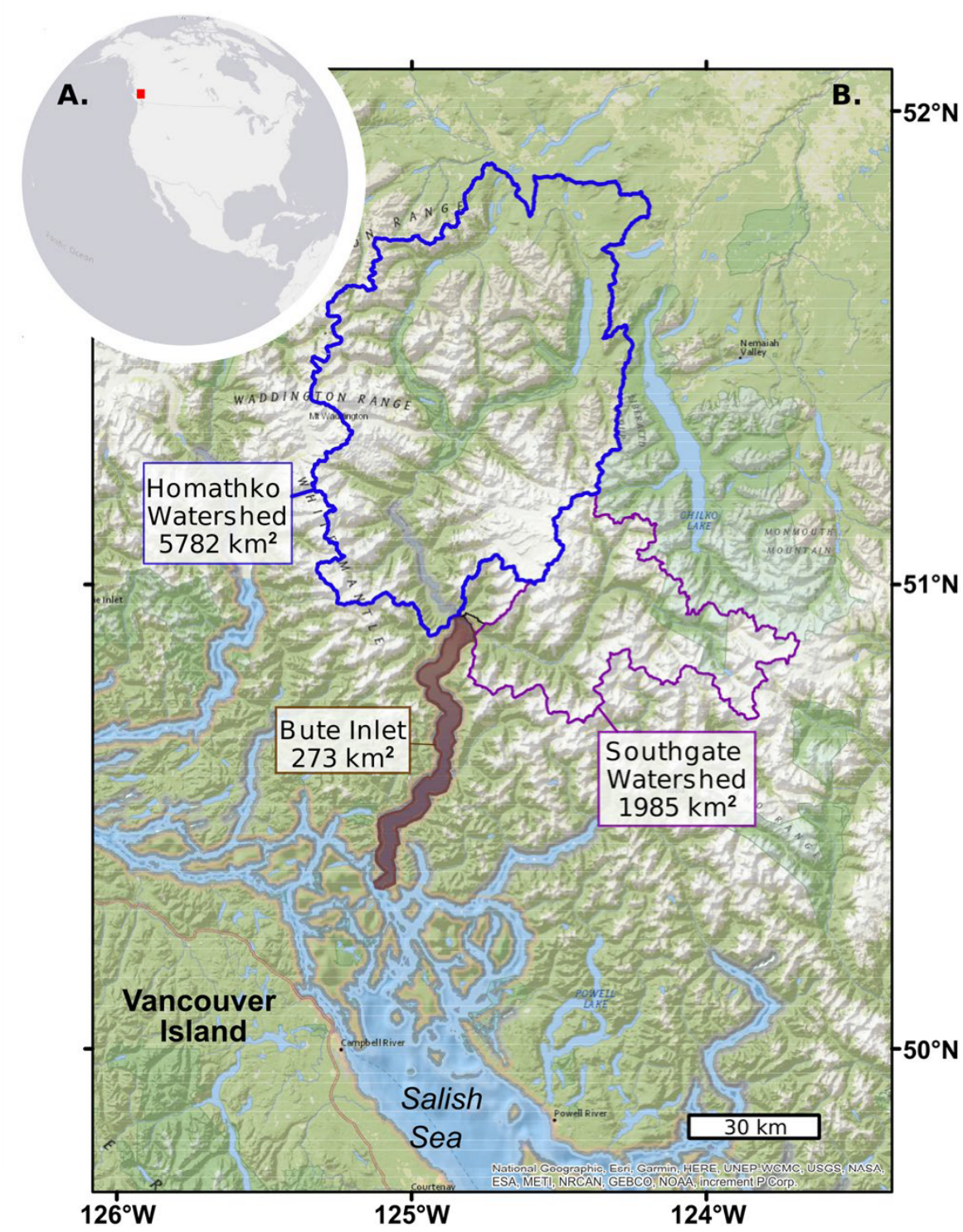


Figure 4.1. Map of Bute Inlet (Hage at al., 2022). A) Location of Bute Inlet within British Columbia, Canada. B) Map showing watershed of the Homathko and Southgate rivers which feed Bute Inlet.

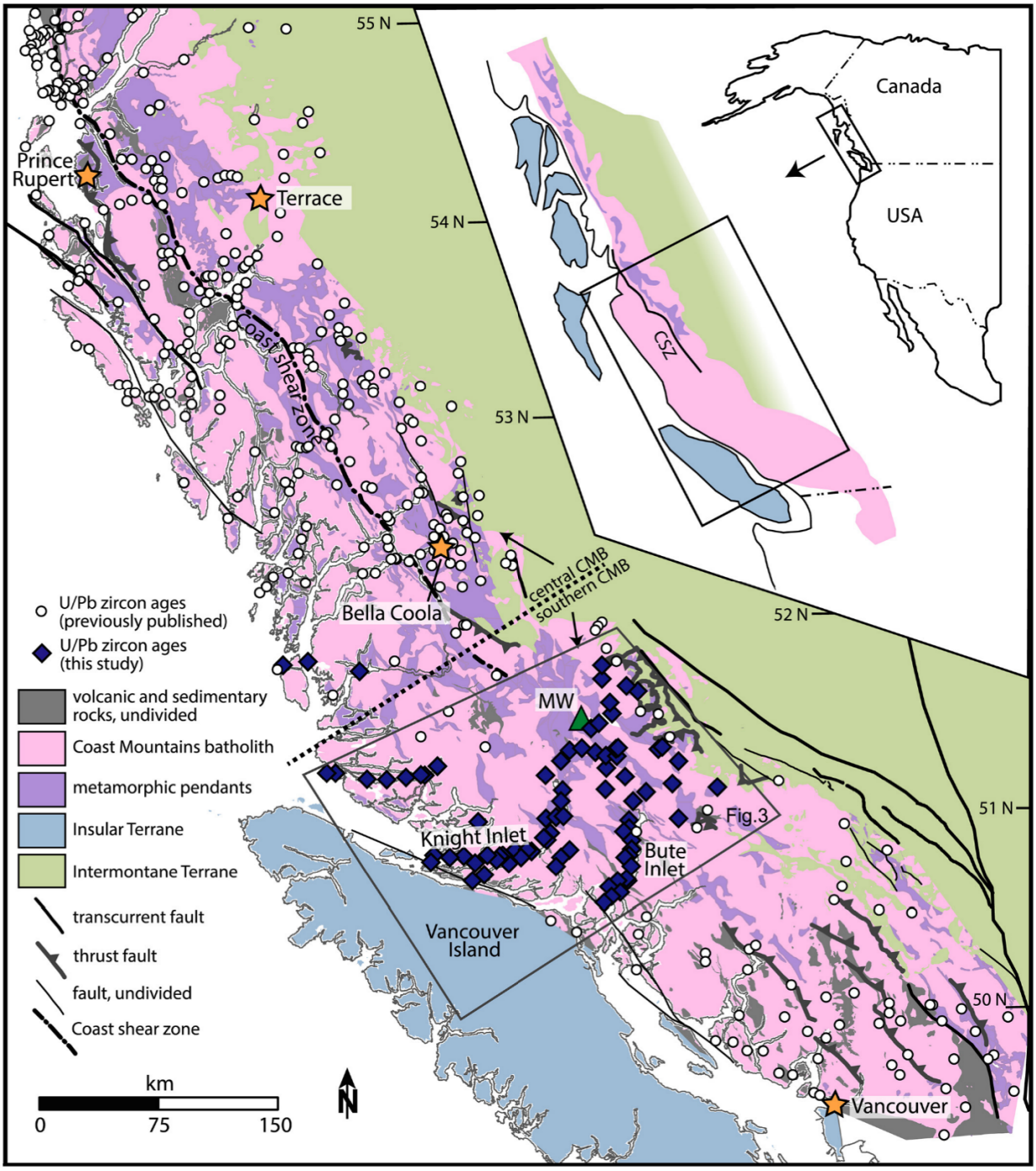


Figure 4.2. Generalized geology map of western British Columbia (Cecil et al., 2018). The Hinterland of Bute Inlet is mainly composed of the Coast Mountains batholith and metamorphic rocks.

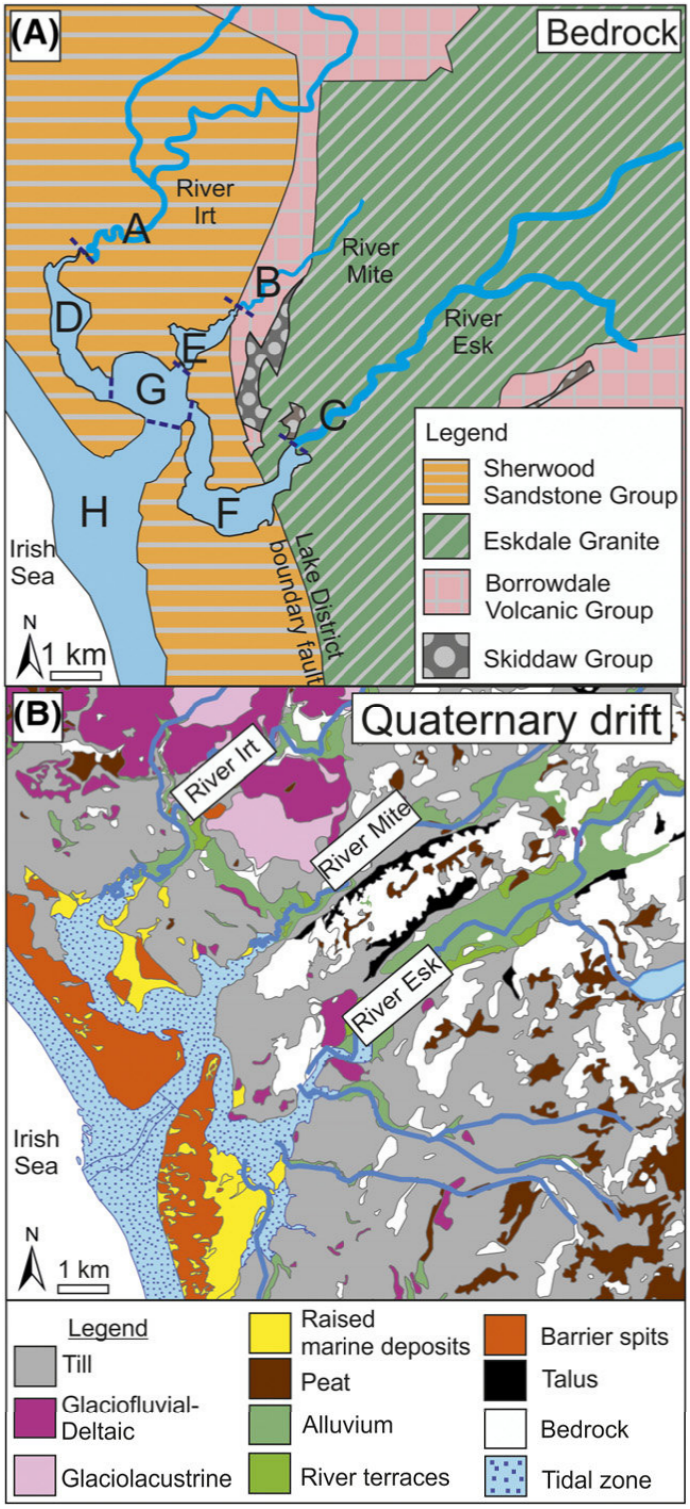


Figure 4.3. Geological setting of the Ravenglass Estuary, United Kingdom (Griffiths et al., 2019). A) Bedrock geology with estuarine zones lower Irt (A); lower Mite (B); lower Esk (C); inner Irt (D); inner Mite (E); inner Esk (F); central basin (G); and outer estuary (H). B) Quaternary drift deposits.

4.2 Materials and methods

This section provides a summary of the methods used in this chapter. A more detailed description of methodology can be found in Chapter 2.

4.2.1 Sediment sampling

Sediment samples from a total of 71 locations across Bute Inlet were collected during a month-long sampling campaign in May 2018 (see Figure 2.5 in chapter 2 for sample location map). Samples were collected from proximal to distal parts of the system covering mixed flat, sand flat, tidal bar, submarine channel thalweg, submarine channel terraces and distal lobe depositional sub-environments. Samples from exposed intertidal locations were collected on foot. A box corer deployed from a research ship was used to collect samples from submerged locations across Bute Inlet. This allowed an intact box core of the top 20cm of sediment to be retrieved. The top 2cm of sediment was then subsampled from the box core sample.

Surface sediment was collected from a total of 76 locations across Ravenglass Estuary (see Figure 2.6 in chapter 2 for sample location map) during a two-week sampling campaign in March 2018. Samples were taken from across the estuary, covering mud flat, mixed flat, sand flat, tidal bar and tidal inlet depositional sub-environments. Tidal channels were not sampled due to difficulty obtaining an undisturbed sediment sample from submerged sediment. This study focused on intertidal settings and did not sample barrier spits.

Depositional facies for samples collected across Bute Inlet and Ravenglass Estuary (Table 4.1) were defined using a combination of aerial photographs and field observations. A classification scheme based on sand content, proposed by Brockamp and Zuther (2004) was also used, where a sand flat has >90% sand, a mixed flat has 50-90% sand and a mudflat has 15-50% sand.

All samples were stored in a freezer (-20°C) until subsequent processing and analysis.

Depositional facies	Description	Sand Fraction (%)
Ravenglass Estuary		
Mud Flat	Clay to silt with moderate to high levels of bioturbation. Desiccation cracks common in areas fringing saltmarsh. Yellowish biofilms observed on surface of sediment.	15-50%
Mixed Flat	Silt to fine grained sand with variable levels of bioturbation. Clay draped ripples (formed during slack-water periods) present in locations proximal to main ebb-channel. Patchy yellowish biofilms observed on surface in some locations during low tide.	50-90%
Sand Flat	Fine to coarse grained sand with low bioturbation. Dunes and current ripples present on surface of sediment during low tide.	>90%
Tidal Bar	Fine to medium grained sand with no evidence of bioturbation. Well-developed ripples present on surface of sediment.	>90%
Tidal Inlet	Fine to medium grained sand. No evidence of bioturbation. Often displays shell lags and dunes.	>90%
Upper Foreshore	Medium grained sand. Occasionally contains shells. No bioturbation. Ripples are occasionally present.	>90%
Bute Inlet		
Mixed Flat	Silt with variable levels of bioturbation. Clay draped ripples (formed during slack-water periods) present in locations proximal to main ebb-channel. Patchy yellowish biofilms observed on surface in some locations during low tide.	50-90%
Sand Flat	Silt to very fine-grained sand with low bioturbation. Dunes and current ripples present on surface of sediment during low tide.	>90%
Tidal Bar	Very fine to fine grained sand with no evidence of bioturbation. Well-developed ripples present on surface of sediment.	>90%
Submarine channel thalweg	Silt to fine grained sand capped by 1cm thick mud layer. No evidence of bioturbation.	50-90%
Submarine channel terrace	Silt to very fine-grained sand displaying no internal layering or structures. No evidence of bioturbation.	15-50%
Distal lobe	Silt showing no structures or layering. No evidence of bioturbation.	15-50%

Table 4.1. Criteria used to assign depositional facies for samples collected in the field.

4.2.2 Sediment analysis

Grain size analysis was performed on all samples from Bute Inlet and Ravenglass Estuary using a Beckmann Coulter LS230 particle analyser (Beckman Coulter Inc., Brea, California, USA). The resulting grain size distribution data was used to determine mean grain size, clay fraction content (wt. % < 2µm) and grain sorting.

C*hlorophyll-a* concentration and total carbohydrate concentration (proxies for EPS content) were quantified for all samples from Bute Inlet and Ravenglass Estuary. Total carbohydrate was extracted from sediment using the method outlined in Chen et al. (2017). The total carbohydrate content was quantified using a phenol-sulphuric acid colorimetric assay, with glucose used as the standard solution (DuBois et al., 1956).

Chlorophyll-a was extracted from sediment using methanol. The absorbance of the sample extract and standard solutions was read in triplicates at 652, 665 and 750nm using a SpectraMax M3 Multi-Mode Microplate Reader (Molecular Devices, LLC, San Jose, California, USA). The *chlorophyll-a* content (µg/g) of the standard solutions and sample extracts were quantified using the equation modified from Porra et al. (1989).

Clay-coat grain coverage (% of the perimeter of a grain which is coated) was quantified for 15 samples from Bute Inlet and 15 samples from Ravenglass Estuary using the method adopted by Wooldridge et al. (2017a). This involved measuring the length of clay coats on 50 grains per sample via petrography.

Automated mineralogy (QEMSCAN) was performed on 6 samples from Bute Inlet and 5 samples from Ravenglass Estuary. QEMCAN analysis was performed using a FEI QEMSCAN 650F Scanning Magnetic Microscope (Thermo Fisher Scientific, Waltham, Massachusetts, USA).

SEM analysis was performed on 6 samples from Bute Inlet and 5 samples from Ravenglass Estuary. Sediment samples were mounted onto aluminium stubs and analysed using a TESCAN Vega 3LMU Scanning Electron Microscope (TESCAN, Brno, Czech Republic).

4.2.3 Mapping

ArcGIS Pro Version 3.2 was used to generate maps displaying sample locations and perform spatial analysis. The inverse distance weight (IDW) spatial analyst tool was used to produce grain size, sorting, chlorophyll-a content and total carbohydrate content distribution maps. Tile size was set to 128x128 pixels for all maps. IDW was selected as an interpolation tool as it avoids the generation of ridges or valleys of underrepresentive or extreme values (Watson and Phillip, 1985).

4.2.4 Pearson correlation coefficient analysis

Pearson correlation coefficient analysis was used to measure the linear relationship between two variables. Table 2.2 in Chapter 2 displays the numerical cut offs used in this study. P-values were calculated from R-values at a significance level of 0.05. P-values less than 0.05 suggest that the relationship is significant and that there is a less than 5% chance that the data trend has been produced by random chance.

4.3 Results

4.3.1 Textural analysis

Table 4.2 displays the grain size, sorting and clay content of all samples from Bute Inlet grouped by depositional facies. The highest grain size was associated with tidal bars (average mean grain size of 127.95µm). Sand flats had an average mean grain size of 72.15µm. Samples from mixed flats, submarine channel terraces and the submarine channel thalweg had an average mean grain size of silt (below 62µm). Figure 4.4 displays mean grain size mapped across Bute Inlet.

Grain sorting ranged from 4.983 (very poorly sorted) to 2.256 (poorly sorted). Sediment within the deltas were typically poorly sorted and sediment within the submarine channel and distal lobe were very poorly sorted (Figure 4.5).

Distal lobe and submarine cannel terraces had the highest average clay content (14.38% and 17.29%, respectively). Tidal bars and sand flats had the lowest clay content (<4%).

Table 4.3 displays the grain size, sorting and clay content of all samples from Ravenglass Estuary grouped by depositional facies. The highest grain size was associated with samples from the foreshore (average mean grain size of 314.35µm) and tidal inlet (average grain size of 261.42 µm). Sand flats had an average mean grain size of 261.62µm. Samples from mixed flats and mud flats had an average mean grain size of silt (below 62µm). Figure 4.6 displays mean grain size mapped across Ravenglass Estuary.

Grain sorting ranged from 5.218 (very poorly sorted) to 1.288 (well sorted). Sediment within the tidal inlet was well sorted, whereas sediment within the intertidal zone typically ranged from moderately to poorly sorted (Figure 4.7).

Sediment from mud and mixed flats had the highest average clay content (7.57% and 3.55%, respectively), whereas sediment from sand flats, the tidal inlet and tidal bars had a low clay content (<2%).

Sample number	Depositional Facies	Mean grain size (µm)	Grain sorting	Clay content (% weight less than 2µm)
2	Mixed Flat	34.00	3.32	5.50
8	Mixed Flat	42.63	3.35	4.90
11	Mixed Flat	31.80	3.27	6.40
12	Mixed Flat	19.44	3.46	7.80
16	Mixed Flat	47.49	3.03	4.60
40	Mixed Flat	13.11	3.44	10.30
41	Mixed Flat	17.34	3.38	8.70
43	Mixed Flat	14.29	4.11	12.70
44	Mixed Flat	12.64	4.16	13.30
45	Mixed Flat	23.25	3.32	7.20
Count		10.00	10.00	10.00
Minimum		12.64	3.03	4.60
Maximum		47.49	4.16	13.30
Average		25.60	3.48	8.14
Standard deviation		12.66	0.36	3.10
6	Sand Flat	55.85	3.06	3.90
7	Sand Flat	84.95	4.14	4.20
9	Sand Flat	73.79	3.04	3.20
10	Sand Flat	86.90	3.84	3.70
13	Sand Flat	70.86	2.48	3.10
15	Sand Flat	66.32	2.82	3.80
17	Sand Flat	77.63	3.23	3.50
42	Sand Flat	66.32	2.82	3.80
46	Sand Flat	66.73	3.06	3.80
Count		9.00	9.00	9.00
Minimum		55.85	2.48	3.10
Maximum		86.90	4.14	4.20
Average		72.15	3.17	3.67
Standard deviation		9.87	0.52	0.35
3	Tidal Bar	133.00	3.37	3.40
4	Tidal Bar	135.50	3.22	2.40
5	Tidal Bar	101.60	2.70	2.80
67	Tidal Bar	107.00	3.27	2.80
68	Tidal Bar	83.69	2.57	3.30
69	Tidal Bar	101.40	2.26	2.30
70	Tidal Bar	189.40	3.68	2.40
71	Tidal Bar	172.00	2.45	1.60
Count		8.00	8.00	8.00
Minimum		83.69	2.26	1.60
Maximum		189.40	3.68	3.40
Average		127.95	2.94	2.63
Standard deviation		37.03	0.51	0.58

Sample number	Depositional Facies	Mean grain size (µm)	Grain sorting	Clay content (% weight less than 2µm)
1	Channel Thalweg	18.76	4.19	9.70
22	Channel Thalweg	17.05	4.77	12.30
25	Channel Thalweg	15.42	4.06	11.80
26	Channel Thalweg	11.21	4.07	14.50
29	Channel Thalweg	24.05	3.97	8.90
30	Channel Thalweg	9.48	4.51	17.50
47	Channel Thalweg	30.86	3.57	7.10
48	Channel Thalweg	81.56	2.64	3.10
50	Channel Thalweg	15.72	3.78	10.60
52	Channel Thalweg	19.92	4.37	10.00
53	Channel Thalweg	30.00	3.72	7.30
56	Channel Thalweg	57.34	3.09	4.50
57	Channel Thalweg	241.40	2.70	1.50
58	Channel Thalweg	35.04	4.10	6.80
59	Channel Thalweg	60.51	3.62	4.50
60	Channel Thalweg	113.20	2.45	2.40
62	Channel Thalweg	20.57	4.12	9.70
65	Channel Thalweg	31.82	3.63	7.00
66	Channel Thalweg	23.29	4.61	9.90
Count		19.00	19.00	19.00
Minimum		9.48	2.45	1.50
Maximum		241.40	4.77	17.50
Average		45.12	3.79	8.37
Standard deviation		54.46	0.66	4.15
61	Terrace	7.83	4.83	21.10
14	Terrace	49.65	3.14	4.40
18	Terrace	12.88	4.70	14.20
19	Terrace	10.99	4.21	15.00
20	Terrace	14.16	4.98	13.90
23	Terrace	6.10	3.69	20.90
24	Terrace	6.00	3.78	21.80
27	Terrace	6.46	4.15	21.70
28	Terrace	6.19	4.02	22.40
31	Terrace	5.33	3.91	25.20
32	Terrace	4.68	3.87	27.40
33	Terrace	7.63	4.26	19.90
34	Terrace	21.16	4.24	9.90
35	Terrace	6.35	4.06	22.50
49	Terrace	8.58	4.04	17.00
51	Terrace	8.10	3.88	17.20
54	Terrace	101.40	2.26	2.30
55	Terrace	12.70	4.01	12.70
63	Terrace	7.12	3.96	19.30
64	Terrace	8.10	3.95	17.00
Count		20.00	20.00	20.00
Minimum		4.68	2.26	2.30
Maximum		101.40	4.98	27.40
Average		15.57	4.00	17.29
Standard deviation		22.49	0.58	6.44
21	Distal Lobe	14.30	4.78	13.60
36	Distal Lobe	33.13	3.34	7.00
37	Distal Lobe	9.53	4.34	17.10
38	Distal Lobe	7.16	4.19	20.20
39	Distal Lobe	11.08	4.26	14.00
Count		5.00	5.00	5.00
Minimum		7.16	3.34	7.00
Maximum		33.13	4.78	20.20
Average		15.04	4.18	14.38
Standard deviation		10.44	0.52	4.91

Table 4.2. Sediment textural properties by depositional facies across Bute Inlet.

Sample number	Depositional Facies	Mean grain size (µm)	Grain sorting	Clay content (% weight less than 2µm)
15	Mud Flat	27.45	5.28	8.80
20	Mud Flat	67.14	5.15	5.70
22	Mud Flat	25.37	3.85	6.70
25	Mud Flat	19.46	3.89	9.60
26	Mud Flat	22.58	4.16	8.40
29	Mud Flat	32.84	3.82	7.10
32	Mud Flat	45.52	4.03	5.00
34	Mud Flat	38.32	4.90	6.90
39	Mud Flat	41.33	4.11	5.60
50	Mud Flat	37.45	3.63	6.00
51	Mud Flat	26.11	4.32	8.10
52	Mud Flat	38.61	3.75	5.20
53	Mud Flat	15.54	4.07	11.40
54	Mud Flat	18.76	4.53	9.60
55	Mud Flat	17.39	4.83	10.00
56	Mud Flat	23.39	3.84	6.60
57	Mud Flat	44.87	4.04	5.30
58	Mud Flat	42.09	4.01	5.50
63	Mud Flat	15.18	4.30	12.30
Count		19.00	19.00	19.00
Minimum		15.18	3.63	5.00
Maximum		67.14	5.28	12.30
Average		31.55	4.24	7.57
Standard deviation		13.43	0.48	2.21
1	Mixed Flat	52.49	3.47	4.50
2	Mixed Flat	59.82	3.39	2.00
13	Mixed Flat	62.03	3.837	2.2
8	Mixed Flat	53.06	3.02	2.00
9	Mixed Flat	40.10	3.15	2.30
14	Mixed Flat	54.18	3.35	2.20
16	Mixed Flat	34.00	3.24	2.70
19	Mixed Flat	56.82	3.99	4.90
21	Mixed Flat	53.09	3.43	4.90
27	Mixed Flat	44.98	3.83	4.80
30	Mixed Flat	70.68	4.95	4.70
35	Mixed Flat	51.93	3.94	4.60
40	Mixed Flat	106.60	2.47	3.00
49	Mixed Flat	67.19	3.23	3.40
59	Mixed Flat	71.97	3.75	3.90
61	Mixed Flat	64.90	5.19	4.70
Count		16.00	16.00	16.00
Minimum		34.00	2.47	2.00
Maximum		106.60	5.19	4.90
Average		58.99	3.64	3.55
Standard deviation		16.43	0.68	1.18
11	Tidal Bar	194.20	2.13	2.80
12	Tidal Bar	213.20	1.43	0.70
17	Tidal Bar	199.60	1.38	1.00
18	Tidal Bar	190.20	1.78	1.50
23	Tidal Bar	447.00	2.20	1.20
38	Tidal Bar	228.80	2.06	1.30
64	Tidal Bar	351.70	1.41	0.00
73	Tidal Bar	218.00	1.47	1.10
74	Tidal Bar	218.90	2.40	2.60
75	Tidal Bar	200.30	2.38	3.10
10	Tidal Bar	222.40	1.46	1.10
Count		11.00	11.00	11.00
Minimum		190.20	1.38	0.00
Maximum		447.00	2.40	3.10
Average		244.03	1.83	1.49
Standard deviation		80.63	0.41	0.95

Sample number	Depositional Facies	Mean grain size (µm)	Grain sorting	Clay content (% weight less than 2µm)
3	Sand Flat	192.30	1.29	0.00
7	Sand Flat	221.40	3.17	3.20
24	Sand Flat	466.00	2.64	1.70
28	Sand Flat	230.10	2.28	2.00
31	Sand Flat	203.50	1.40	1.00
33	Sand Flat	569.50	3.83	1.10
36	Sand Flat	139.00	1.88	2.00
37	Sand Flat	158.70	2.40	2.30
41	Sand Flat	256.10	2.04	1.50
42	Sand Flat	160.90	1.99	2.00
48	Sand Flat	424.90	2.30	1.20
60	Sand Flat	437.20	2.81	1.80
62	Sand Flat	241.20	1.79	1.10
65	Sand Flat	168.70	1.36	1.10
70	Sand Flat	162.30	1.58	1.60
71	Sand Flat	189.40	1.45	1.40
72	Sand Flat	305.60	2.04	1.30
76	Sand Flat	182.40	1.88	1.80
Count		18.00	18.00	18.00
Minimum		139.00	1.29	0.00
Maximum		569.50	3.83	3.20
Average		261.62	2.12	1.56
Standard deviation		126.72	0.67	0.67
6	Tidal Inlet	282.00	1.37	0.00
43	Tidal Inlet	286.20	1.53	0.80
44	Tidal Inlet	350.70	1.51	0.00
45	Tidal Inlet	439.20	1.43	0.50
46	Tidal Inlet	167.50	1.37	1.30
47	Tidal Inlet	165.90	1.42	1.50
66	Tidal Inlet	197.20	1.64	1.10
67	Tidal Inlet	191.50	1.36	1.10
68	Tidal Inlet	247.40	1.40	0.90
69	Tidal Inlet	286.60	1.37	0.60
Count		10.00	10.00	10.00
Minimum		165.90	1.36	0.00
Maximum		439.20	1.64	1.50
Average		261.42	1.44	0.78
Standard deviation		87.18	0.09	0.51
4	Upper foreshore	339.60	1.37	0.70
5	Upper foreshore	289.10	2.82	0.90
Count		2.00	2.00	2.00
Minimum		289.10	1.37	0.70
Maximum		339.60	2.82	0.90
Average		314.35	2.09	0.80
Standard deviation		35.71	1.03	0.14

Table 4.3. Sediment textural properties by depositional facies across Ravenglass Estuary.

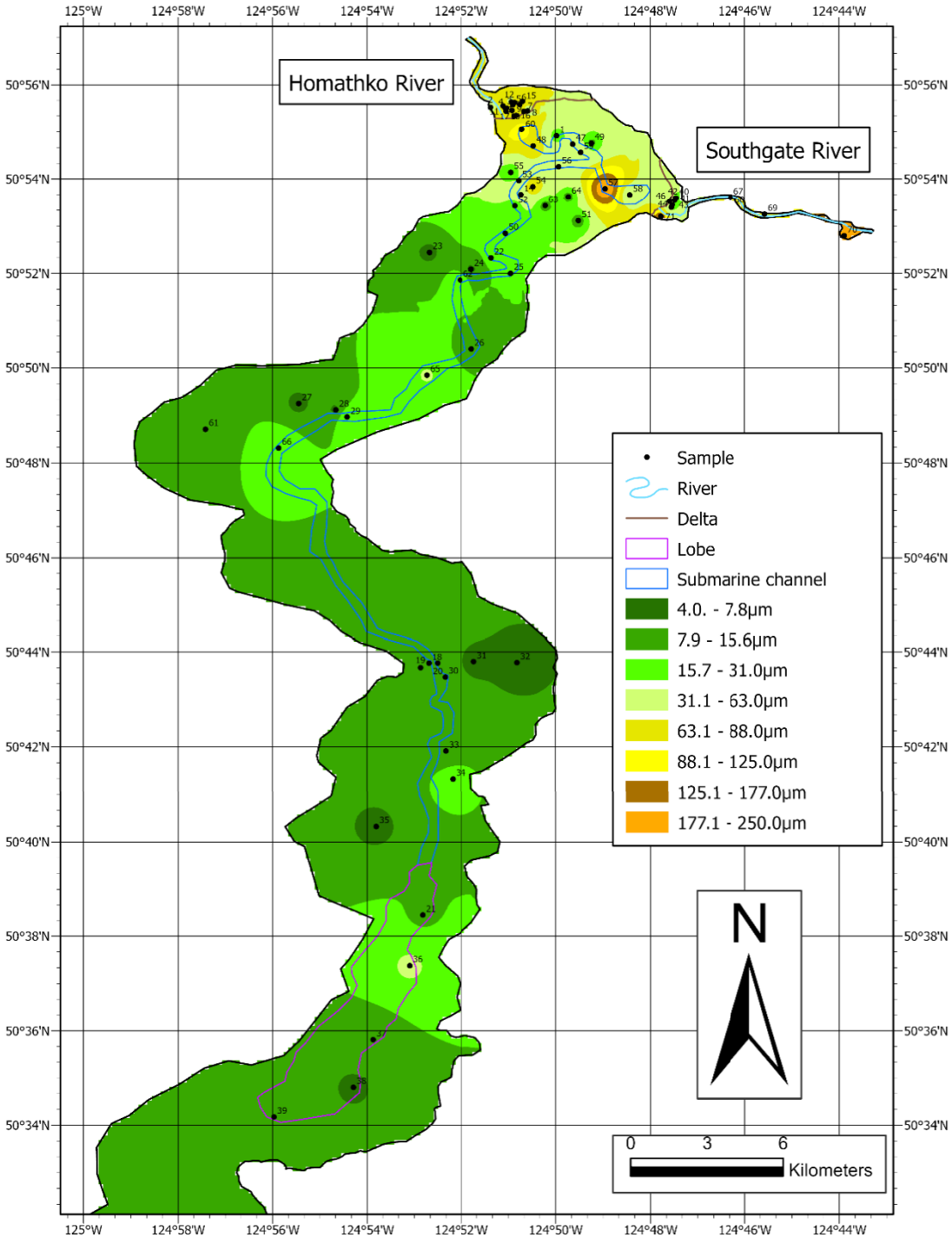


Figure 4.4. Mean grain size across Bute Inlet, B.C, Canada. This map was produced in ArcGIS Pro using the IDW spatial analysist tool. Tile size was 128x128 pixels.

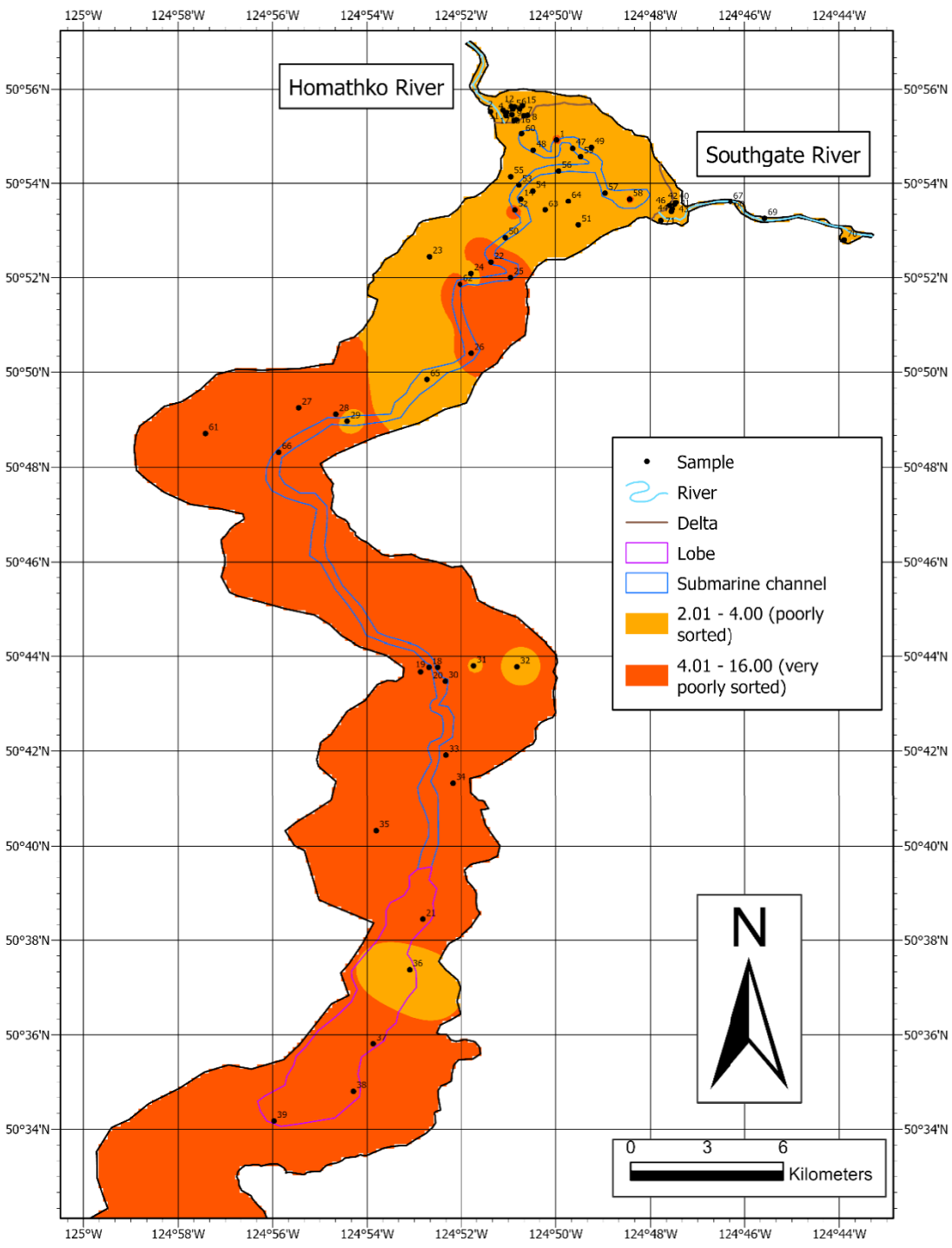


Figure 4.5. Grain sorting across Bute Inlet, B.C, Canada. This map was produced in ArcGIS Pro using the IDW spatial analysist tool. Tile size was 128x128 pixels.

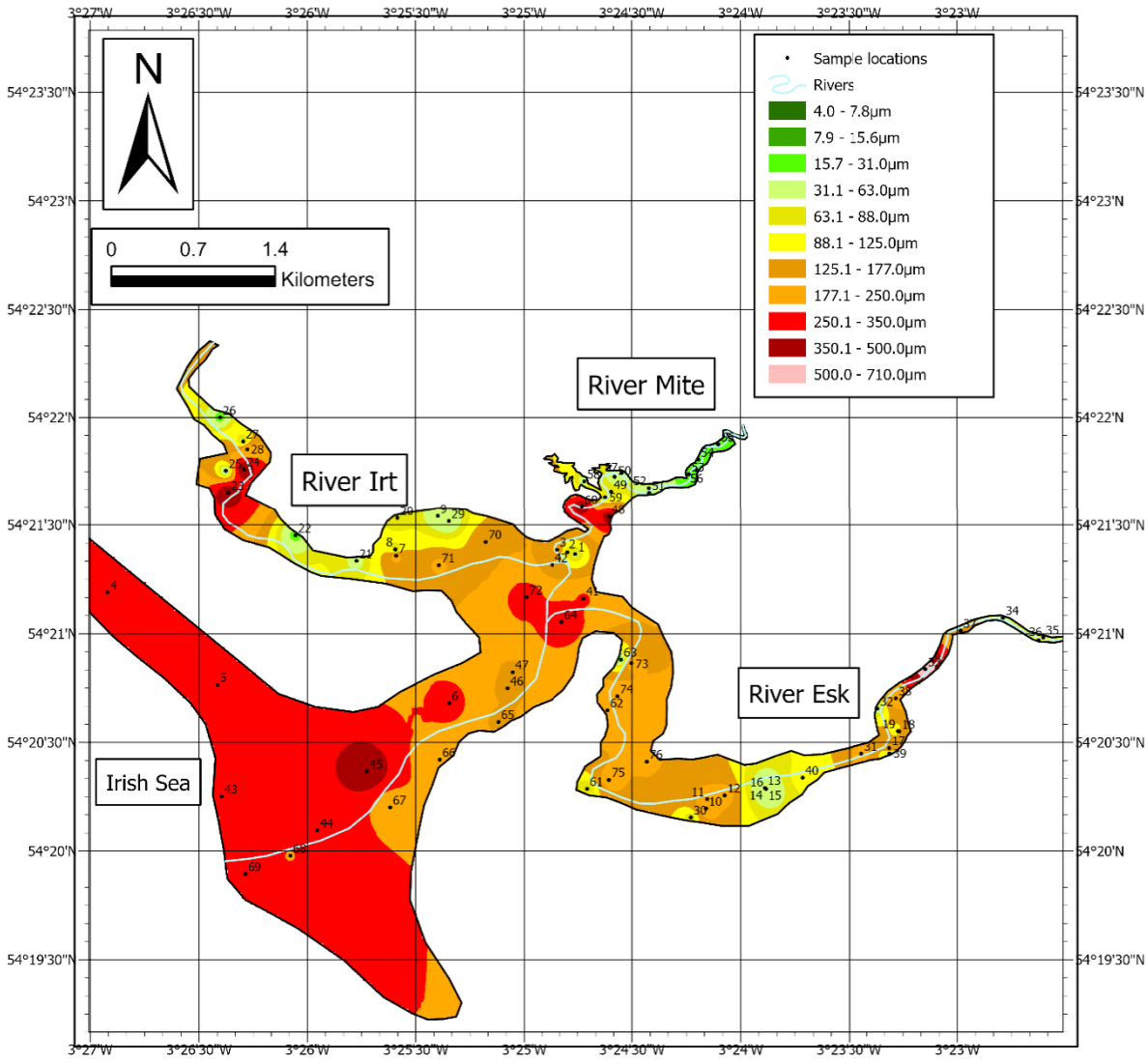


Figure 4.6. Grain size across Ravenglass Estuary. This map was produced in ArcGIS Pro using the IDW spatial analysist tool. Tile size was 128x128 pixels.

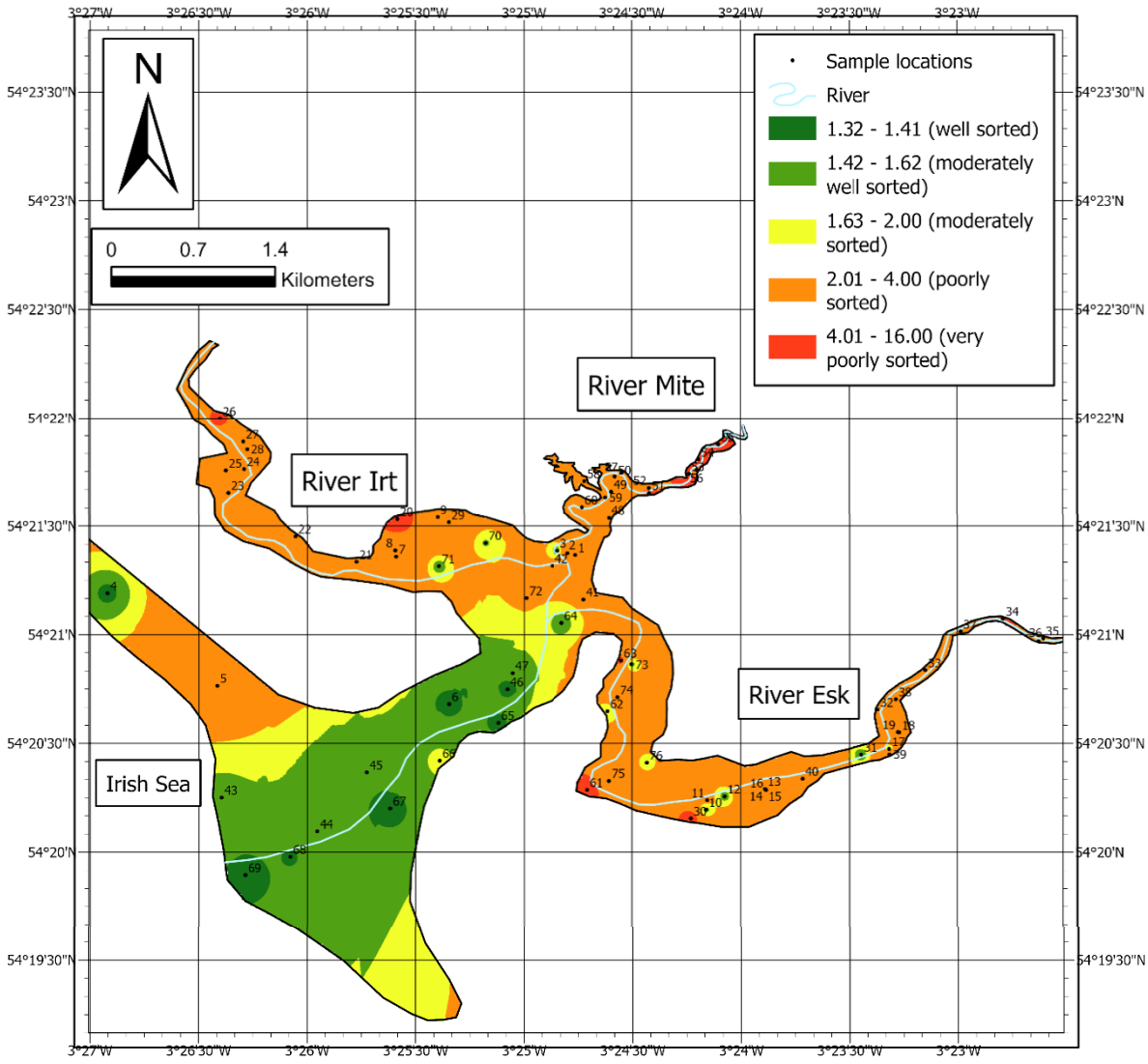


Figure 4.7. Grain sorting across Ravenglass Estuary. This map was produced in ArcGIS Pro using the IDW spatial analysist tool. Tile size was 128x128 pixels.

4.3.2 Mineralogy

QEMSCAN analysis was performed on 1 sample from each depositional facies in Bute Inlet. QEMSCAN analysis indicated bulk mineralogy across Bute Inlet (Table 4.4) is dominated by quartz (17-25%), K-feldspar (3-6%) and plagioclase feldspar (25-31%). Around 26-38% of the bulk mineralogy consist of clay minerals, which include chlorite (2-5%), illite (1-6%), kaolinite (4-14%) and smectite (12-20%). Overall, smectite is the most abundant clay mineral present in Bute Inlet. Mixed flat and tidal bar depositional facies typically have a higher quartz and lower clay mineral content, compared to distal lobe and mixed flat depositional facies. Biotite is present in variable amounts ranging from 3-10%.

QEMSCAN analysis was performed on 1 sample from a mudflat, 1 sample from a mixed flat, 1 sample from a sand flat, 1 sample from a tidal bar and 1 sample from a tidal inlet. Bulk mineralogy across Ravenglass Estuary (Table 4.4) is dominated by quartz (64-79%), K-feldspar (5-7%) and plagioclase feldspar (4-6%). Around 4-15% of the bulk mineralogy consist of clay minerals, which include chlorite (1-2%), illite (2-9%), kaolinite (1-3%) and smectite (~1%). Overall, Illite is the most abundance clay mineral present across Ravenglass Estuary. Sand flat and tidal bar depositional facies typically have a higher quartz and lower clay mineral content, compared to mud flat and mixed flat depositional facies.

Depositional Facies	Quartz (%)	Plagioclase Feldspar (%)	K-Feldspar (%)	Biotite (%)	Chlorite (%)	Illite (%)	Smectite (%)	Kaolinite (%)
BUTE INLET								
Mixed flat (Sample 8)	20%	25%	4%	10%	4%	1%	18%	6%
Sand flat (Sample 6)	23%	31%	4%	3%	2%	1%	20%	4%
Tidal bar (Sample 5)	25%	28%	6%	5%	3%	1%	19%	4%
Submarine channel thalweg (Sample 29)	20%	25%	4%	9%	3%	1%	17%	7%
Submarine channel terrace (Sample 31)	21%	28%	5%	4%	2%	1%	20%	6%
Distal lobe (Sample 36)	17%	25%	3%	5%	5%	6%	12%	14%
RAVENGLASS ESTUARY								
Mud flat (Sample 29)	64%	6%	6%	1%	2%	9%	1%	3%
Mixed flat (Sample 40)	74%	5%	7%	1%	2%	4%	1%	2%
Sand flat (Sample 33)	79%	4%	5%	1%	1%	2%	1%	1%
Tidal bar (Sample 18)	79%	5%	7%	<1%	1%	2%	<1%	1%
Tidal inlet (Sample 66)	75%	6%	5%	1%	1%	2%	1%	1%

Table 4.4. Bulk mineralogy measured by QEMSCAN in Bute Inlet and Ravenglass Estuary (11 samples).

4.3.3 EPS analysis

Total carbohydrate content and chlorophyll-a content were used as proxies for EPS abundance.

The concentration of total carbohydrate in surface sediment across Bute Inlet (Figure 4.8) ranged from below the limit of detection (BLOD) up to 248µg per gram of sediment (dry weight). The highest EPS concentration was found in sediments taken from the distal lobe (Figure 4.8).

The concentration of *chlorophyll-a* present in surface sediment across Bute Inlet (Figure 4.9) ranged from 10 - 82µg per gram of sediment (dry weight). *Chlorophyll-a* content was highest in the distal lobe (Figure 4.9).

The concentration of total carbohydrate presents in sediment samples ranged from below the limit of detection up to 494µg per gram of sediment (dry weight) across Ravenglass Estuary (Figure 4.10). The highest EPS concentration is present in samples derived from intertidal areas, such as mud and mixed flats and the lowest EPS concentration is associated with sediment found in more seaward areas such as the tidal inlet.

The concentration of *chlorophyll-a* present in surface sediment across Ravenglass Estuary (Figure 4.11) ranges from below the limit of detection to >60µg per gram of sediment (dry weight). The highest *chlorophyll-a* concentration was present in samples derived from mud and mixed flats.

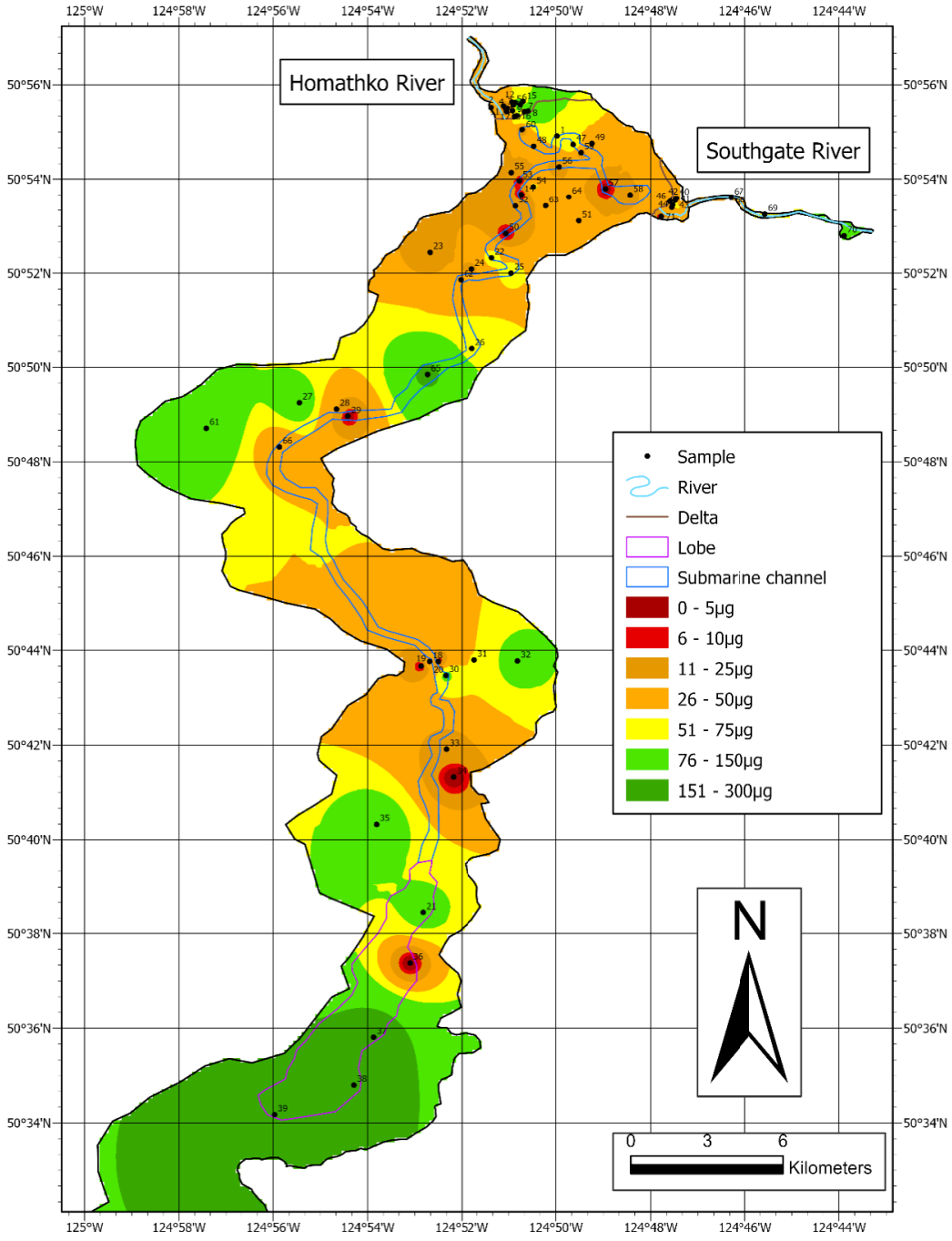


Figure 4.8. The concentration of EPS present in surface sediment across Bute Inlet, B.C, Canada. This map was produced in ArcGIS Pro using the IDW spatial analysist tool. Tile size was 128x128 pixels.

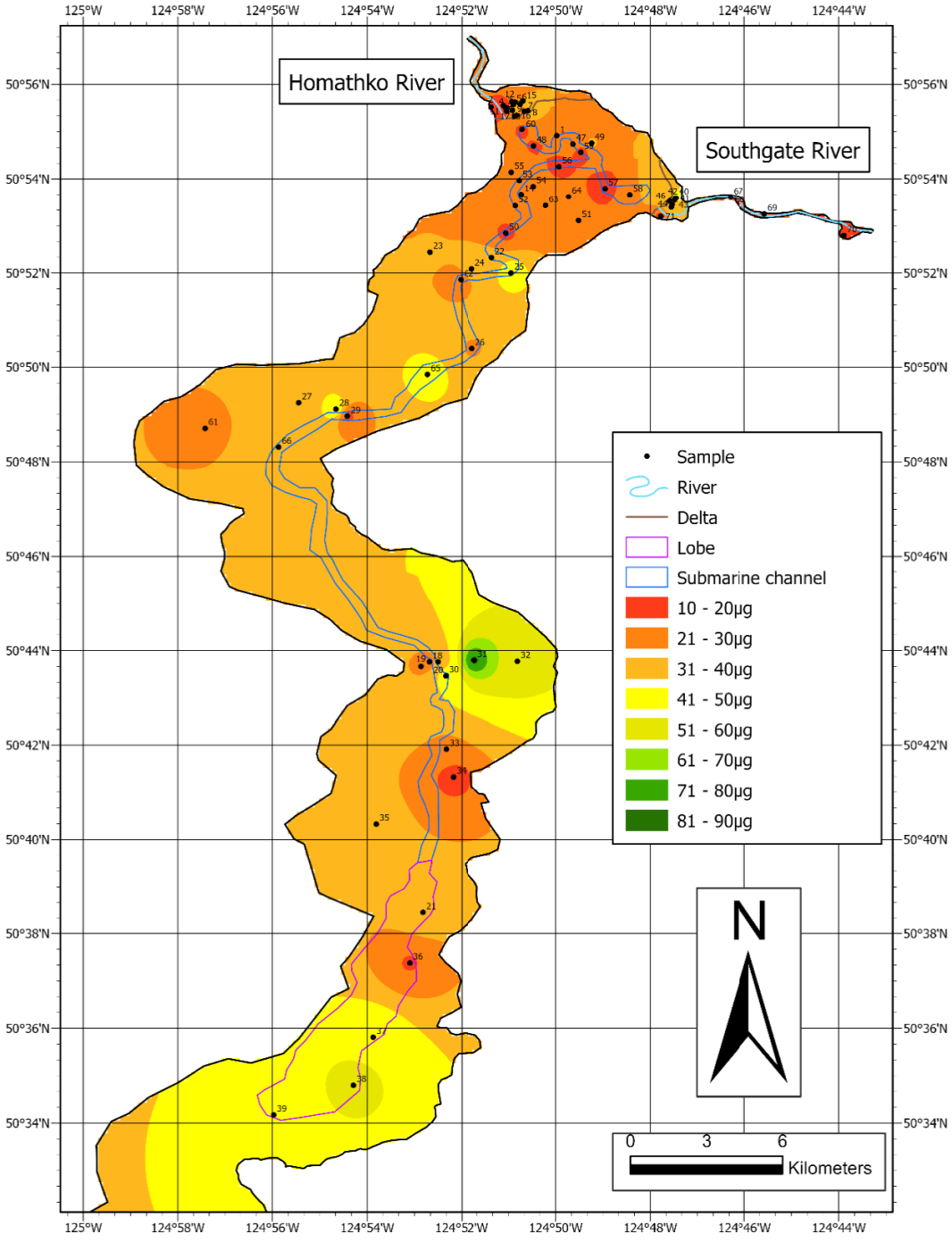


Figure 4.9. The concentration of *chlorophyll-a* present in surface sediment across Bute Inlet, B.C, Canada. This map was produced in ArcGIS Pro using the IDW spatial analysist tool. Tile size was 128x128 pixels.

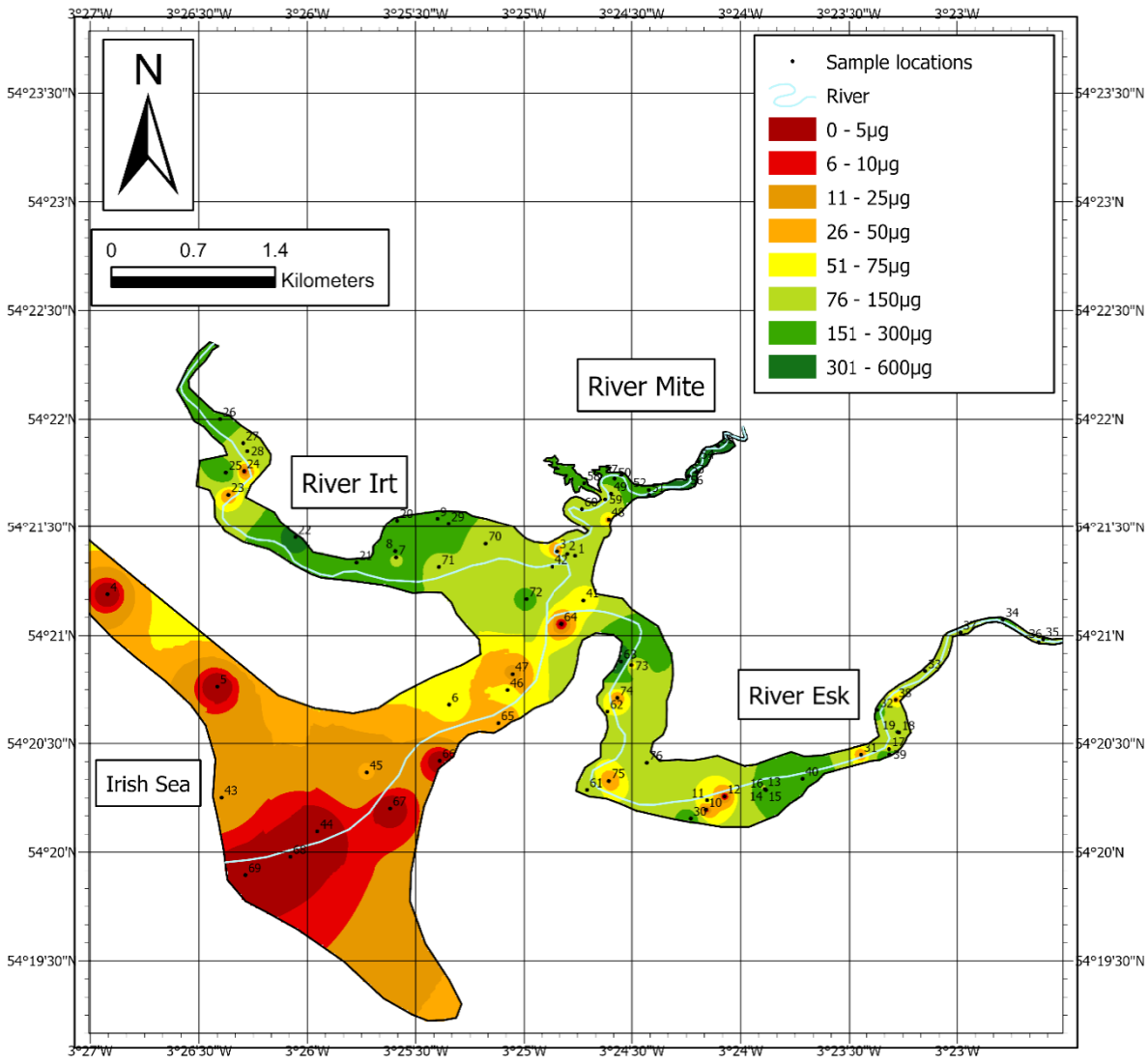


Figure 4.10. The concentration of EPS present in surface sediment across Ravenglass Estuary, UK. This map was produced in ArcGIS Pro using the IDW spatial analysist tool. Tile size was 128x128 pixels.

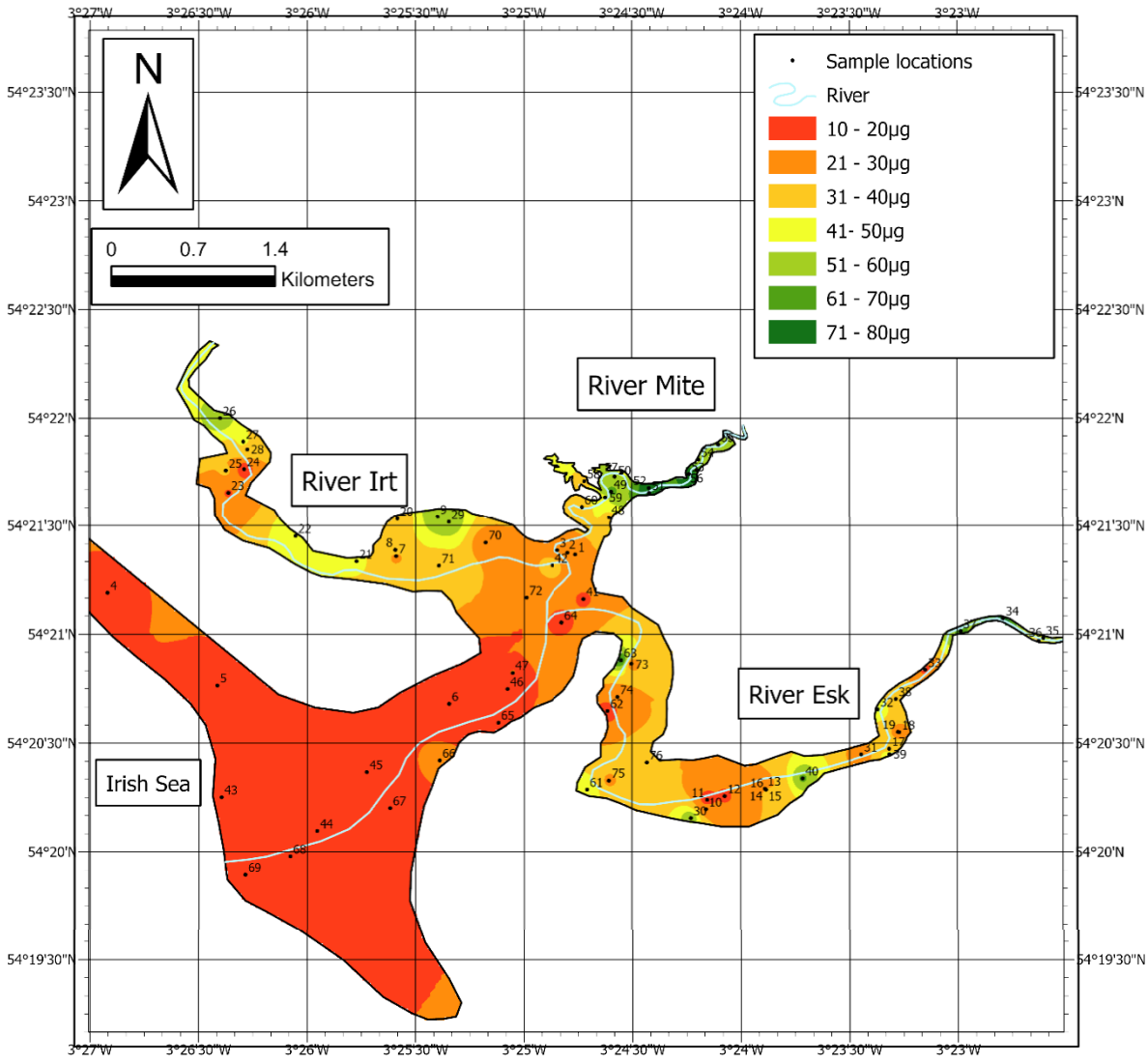


Figure 4.11. The concentration of *chlorophyll-a* present in surface sediment across Ravenglass Estuary, UK. This map was produced in ArcGIS Pro using the IDW spatial analysist tool. Tile size was 128x128 pixels.

4.3.4 Clay-coat coverage

Average grain clay-coat coverage in Bute Inlet was low and ranged from 7 to 23% (Figure 4.12). The highest levels of grain clay-coat coverage was observed in sediment samples from the distal lobe.

Clay coats present in sediment from the Southgate mixed flat range from continuous to discontinuous (Figure 4.14B). Grains coated by clay lamina style coatings were also observed in sediment from the submarine channel thalweg, halfway down the system (Figure 4.14C).

Average grain clay-coat coverage ranged from 13 to 92% across Ravenglass Estuary, with the highest clay-coat coverage present in sediment samples from mud and mixed flats (Figure 4.13). A range of clay-coat morphologies (Figure 4.15A-F) were observed in sediment from Ravenglass Estuary, including clay bridges, clay flocs and discontinuous coats. Discontinuous coats are mainly observed in sediment from mud flats (Figure 4.15A). Clay bridges, clay flocs and discontinuous coatings more common in sediment from sand and mixed flats (Figure 4.15B and Figure 4.15C). Aggregates of fine-grained quartz grains within a clay bridging network were observed in sediment from the tidal inlet (Figure 4.15E).

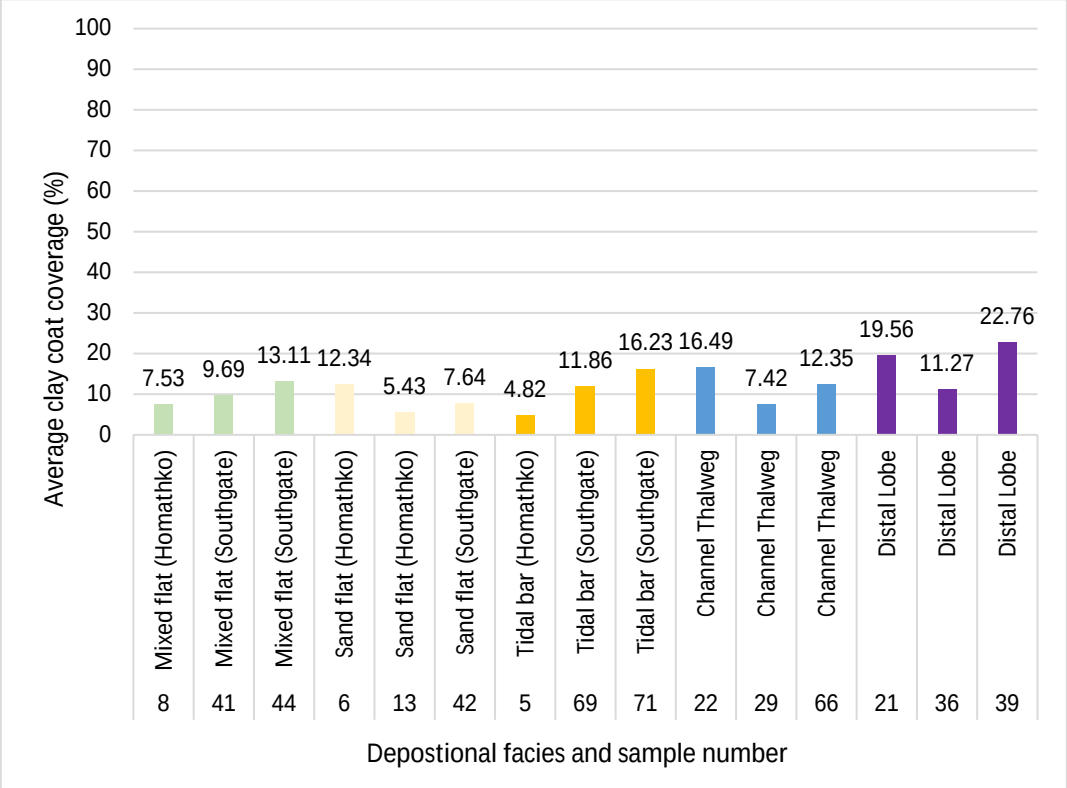


Figure 4.12. Average clay coat coverage of samples from Bute Inlet coloured by depositional facies.

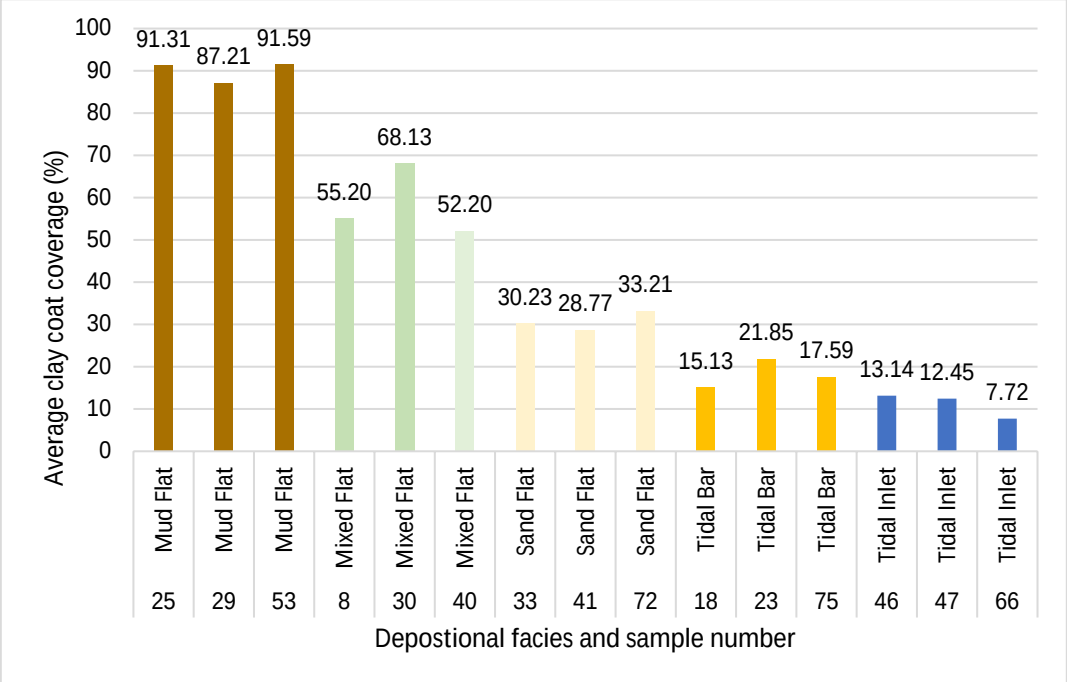


Figure 4.13. Average clay coat coverage of samples from Ravenglass Estuary coloured by depositional facies.

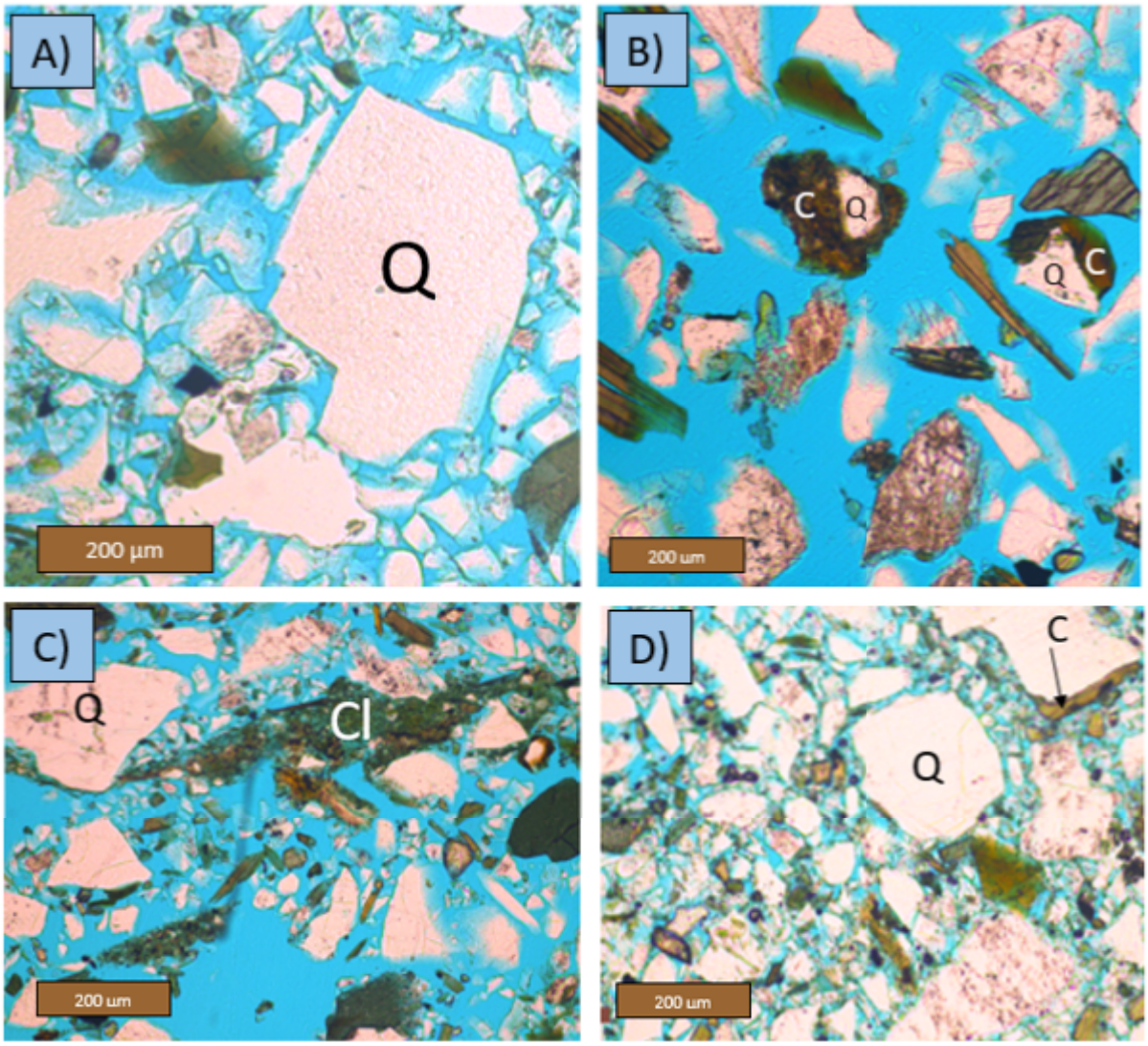


Figure 4.14. Clay coat morphologies across Bute Inlet. A) Clean texturally immature sediment from Homathko sand flat, sample 13. B) Continuous and discontinuous clay coats in sediment from Southgate mixed flat, sample 41. C) Clay lamina partially coating quartz in sediment from channel thalweg, sample 22. D) Discontinuous clay coats in sediment from distal lobe, sample 36. Q = Quartz, Cl = Clay lamina, C = clay coating.

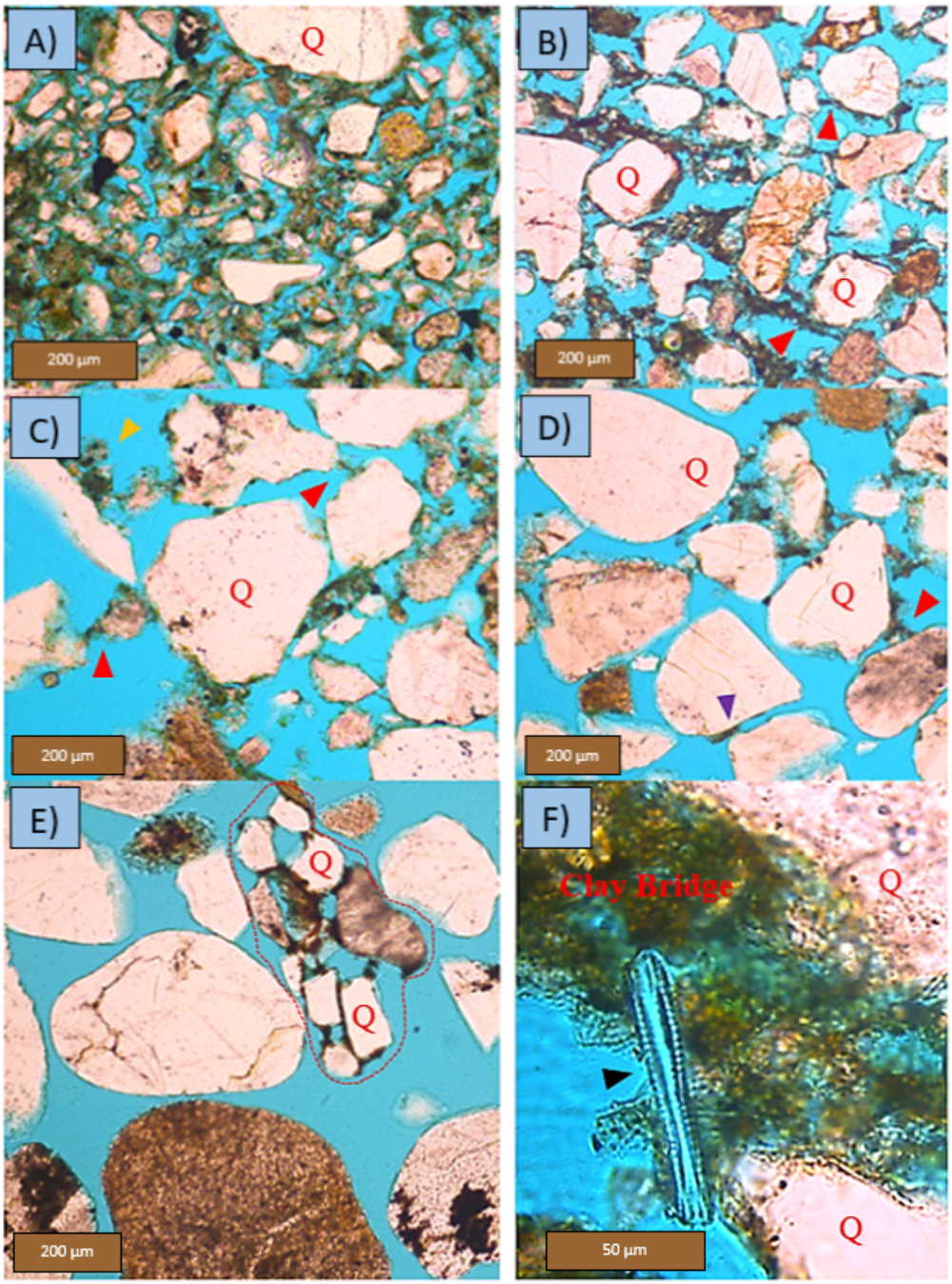


Figure 4.15. Clay coat morphologies across Ravenglass Estuary. A) discontinuous coats in sample 25 (mud flat). B) Clay bridging (red triangle) quartz grains (Q) in sample 8 (mixed flat). C) Clay floc (yellow triangle) in sample 41 (sand flat). D) Discontinuous clay coats (purple triangle) and clay bridge (red triangle) in sample 18 (tidal bar). E) Aggregate of fine-grained quartz within clay bridging network (red dashed line) in sample 66 (tidal inlet). F) Diatom (black triangle) encased by clay bridge in sample 29 (mud flat).

4.3.5 SEM analysis

SEM analysis was performed to image bio-sediment interactions at the grain scale. SEM images of Bute Inlet sediment show EPS stalks between grains with minor levels of clay mineral attachment (Figure 4.16A and B). Intact diatoms (*Thalassiosira Sp.)* attached to quartz grains and clay bridges are present in sediment from the distal lobe (Figure 4.17).

SEM images show fibrous EPS stalks bridging quartz grains, with clay particles attached to EPS bridges in sediment from Ravenglass Estuary (Figure 4.18). Diatoms were observed attached to sediment from intertidal depositional sub-environments across Ravenglass Estuary (Figure 4.19).

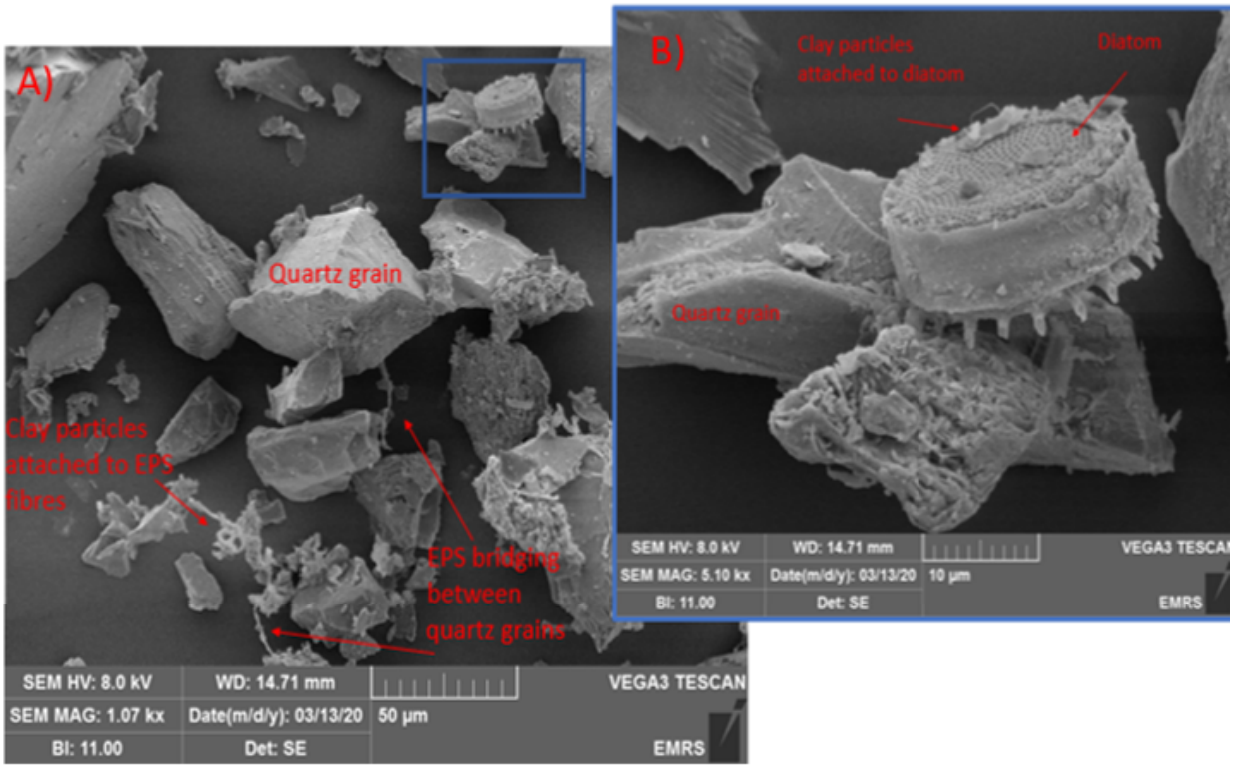


Figure 4.16. SEM images of sediment from Homathko sand flat, Bute Inlet. A) Clay-coated sediment with EPS strands bridging quartz grains. B) Clay-coated diatom attached to quartz grain.

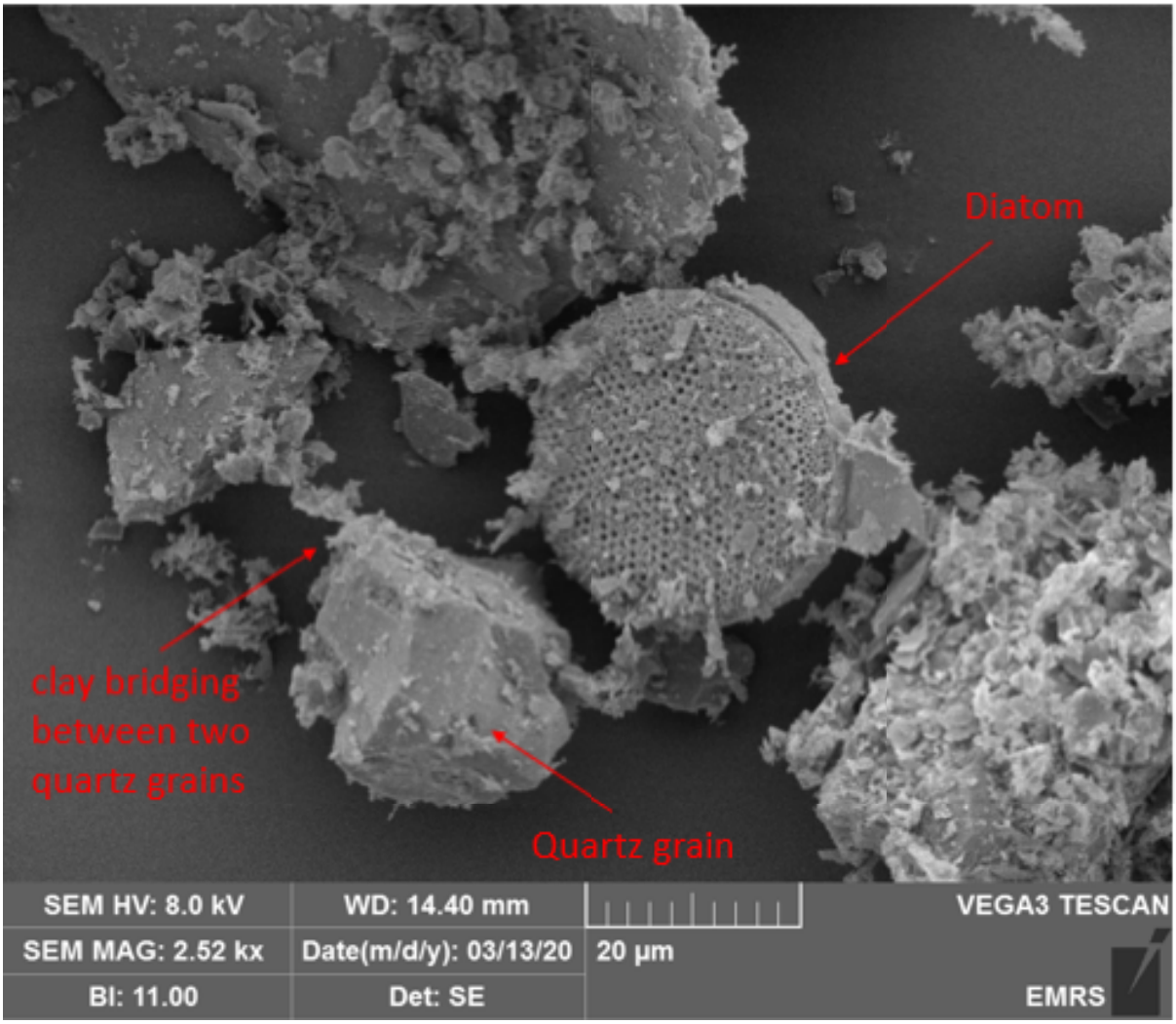


Figure 4.17. SEM image of sediment from distal lobe, Bute Inlet.

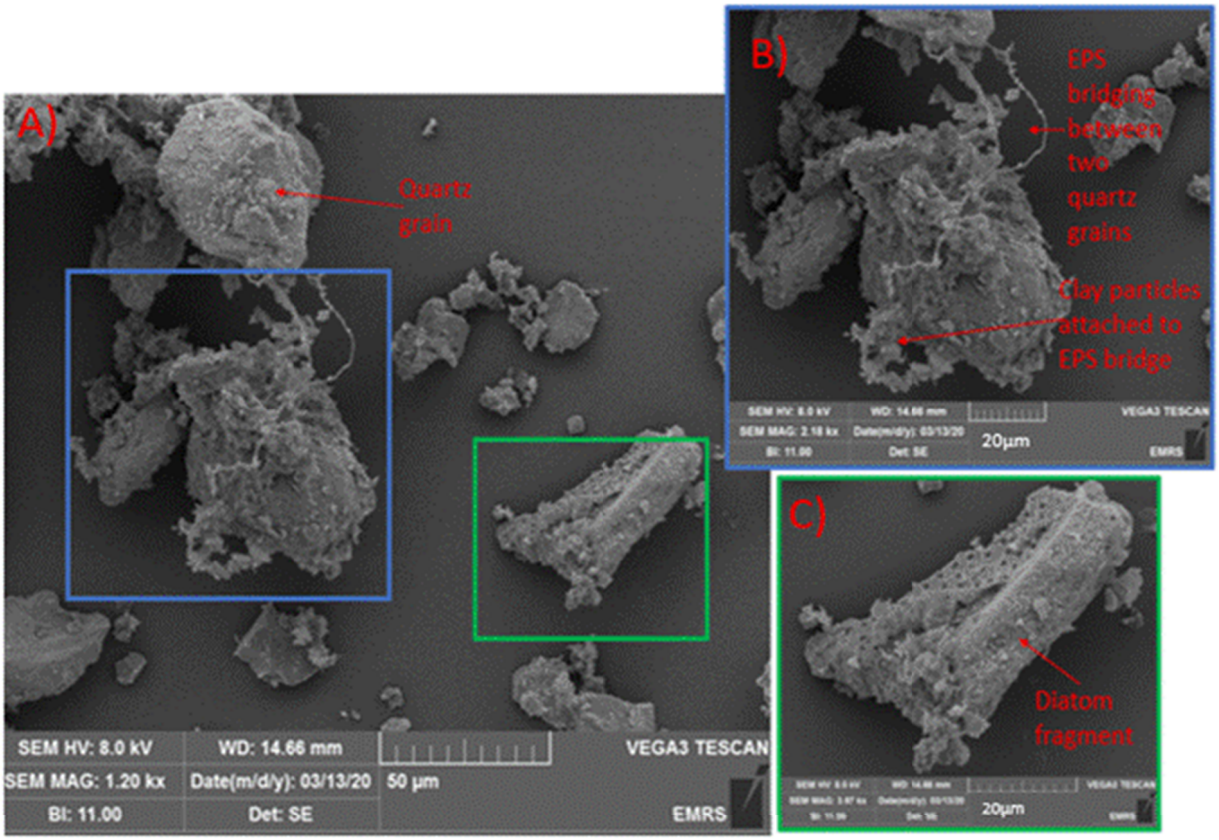


Figure 4.18. SEM image of sediment from mixed flat, Ravenglass Estuary. A) Clay-coated sediment with EPS bridges. B) Clay and EPS-coated quartz grain. C) Clay-coated diatom.

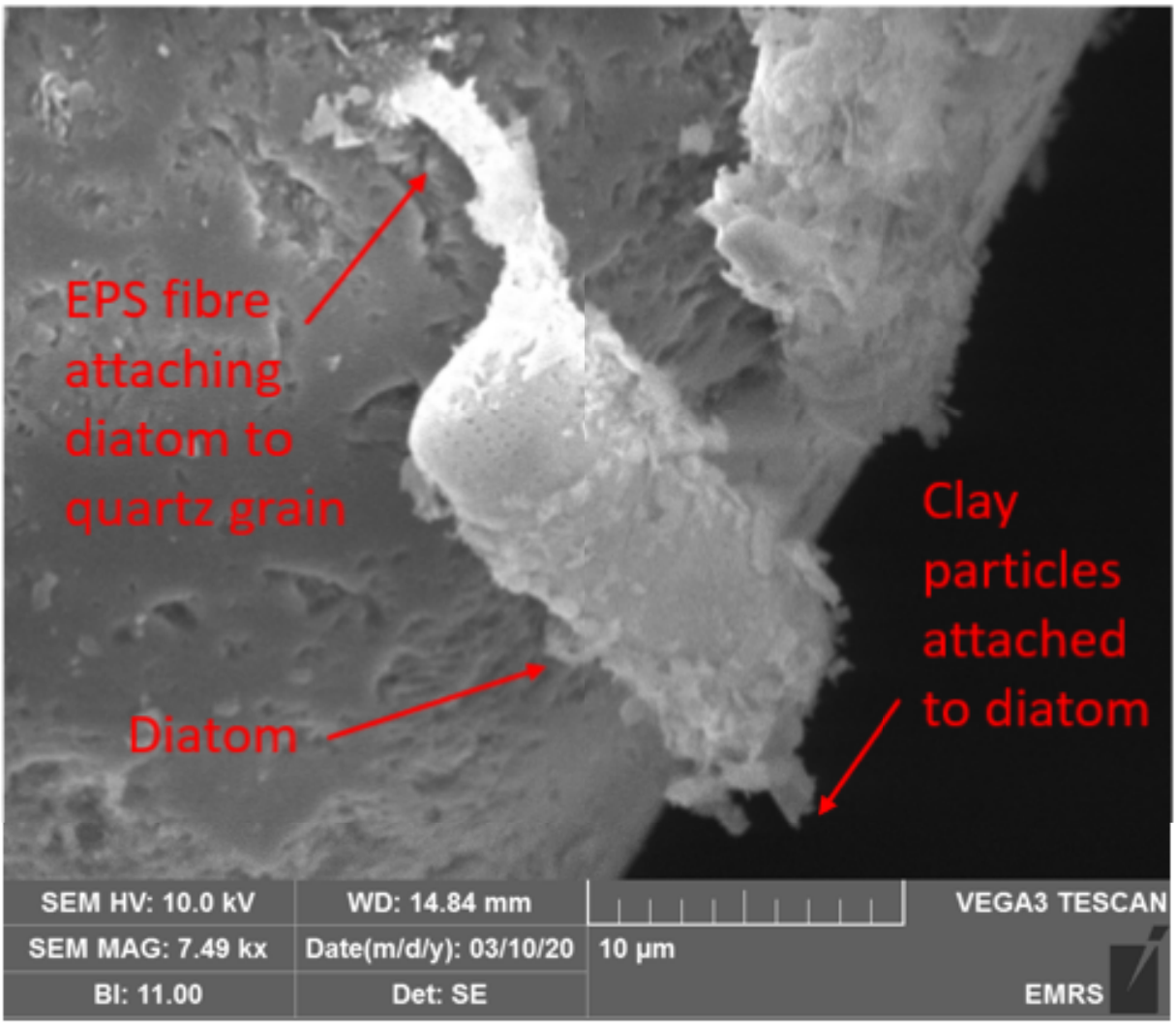


Figure 4.19. SEM image of diatom attached to sediment from tidal bar, Ravenglass Estuary.

4.4.1 Bute Inlet statistical analysis

Pearson correlation co-efficient analysis was performed on a subset of 15 samples from Bute Inlet to visualize the relationship between variables. Only 15 samples had data for all of the variables, therefore the statistical analysis results presented are limited by a low number of samples.

Cross plots of each of the tested variables from Bute Inlet can be found in Figure 4.20 to Figure 4.34. Table 4.5 displays the R-value and corresponding P-value for each pair of tested variables.

Average clay coat grain coverage had a significant positive relationship (Table 4.5) with clay fraction content (R-value of 0.619, P-value of 0.014). This suggests that as the volume of clay-sized material increases in sediment, the abundance of clay-coated grains increases. This is likely to be due to more clay-sized material allowing a large number of quartz grains to be coated.

Average clay coat grain coverage also had a significant positive relationship (Table 4.5) with sorting values (R-value of 0.546, P-value of 0.035). An increase in sorting values reflect a decrease in sorting, where 1.32 is equivalent to well sorted and 4.00 is equivalent to very poorly sorted. This means that in Bute Inlet, average clay coat grain coverage increases with decreasing sorting. All samples from Bute Inlet ranged between very poor to poorly sorted.

Average clay coat grain coverage showed no significant positive relationship (P-values greater than 0.05) with total carbohydrate content, mean grain size and *chlorophyll-a* content (Table 4.5). Overall, average clay coat coverage in Bute Inlet was low. This made it difficult to determine what variables affected average clay coat coverage.

Total carbohydrate content had a significant positive relationship (Table 4.5) with *chlorophyll-a* content (R-value of 0.629, P-value of 0.012). These two variables are considered proxies for EPS content. Both total carbohydrate and chlorophyll-a showed no significant correlation (P-values greater than 0.05) to mean grain size, sorting, clay fraction or average clay coat coverage (Table 4.5).

Mean grain size had a significant negative relationship (Table 4.5) with sorting (R-value of -0.795, P-value of <0.001). As mentioned above, an increase in sorting values reflect a

decrease in sorting, where 1.32 is equivalent to well sorted and 4.00 is equivalent to very poorly sorted. This means that in Bute Inlet, sorting increases as grain size increases.

Mean grain size also had a significant negative relationship (Table 4.5) with clay fraction content (R-value of -0.825, P-value of <0.001). In sedimentary systems, the volume of clay content typically decreases as grain size increases due to the separation of different grain size fractions.

Mean grain size showed no significant correlation (P-values greater than 0.05) to average clay coat coverage, total carbohydrate content and chlorophyll-a content (Table 4.5).

Clay fraction content had a significant positive relationship (Table 4.5) with sorting values (R-value of 0.932, P-value of <0.001). An increase in sorting values reflect a decrease in sorting. This means that in Bute Inlet sorting decreased as the volume of clay content increased.

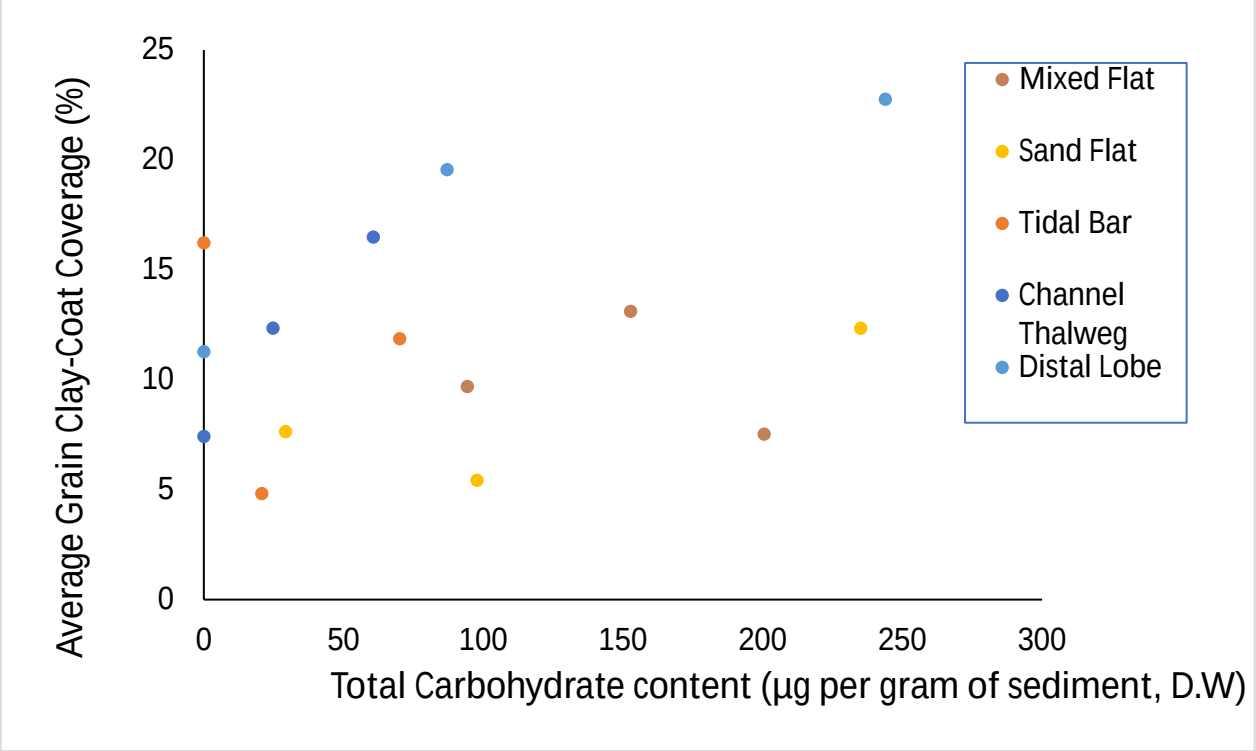


Figure 4.20. Total Carbohydrate content vs average clay-coat coverage in Bute Inlet. N=15.

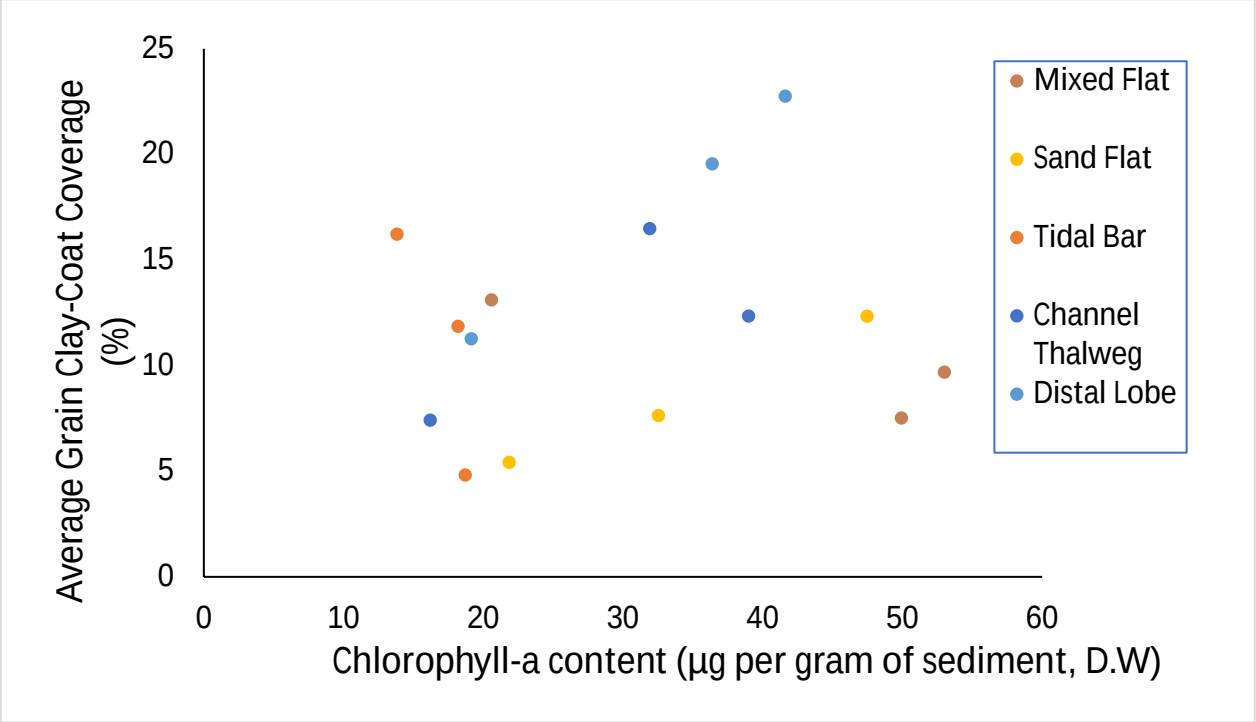


Figure 4.21. Chlorophyll-a content vs average clay-coat coverage in Bute Inlet. N=15.

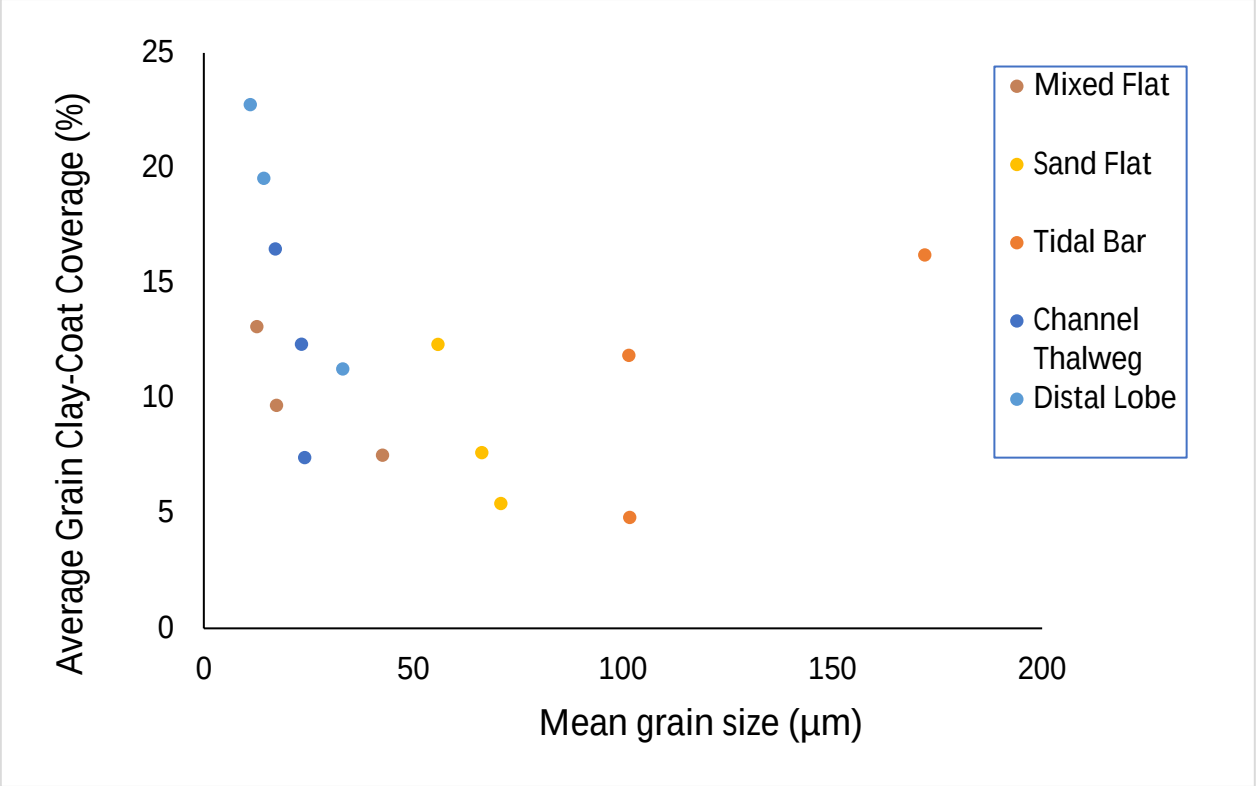


Figure 4.22. Mean grain size vs average clay-coat coverage in Bute Inlet. N=15.

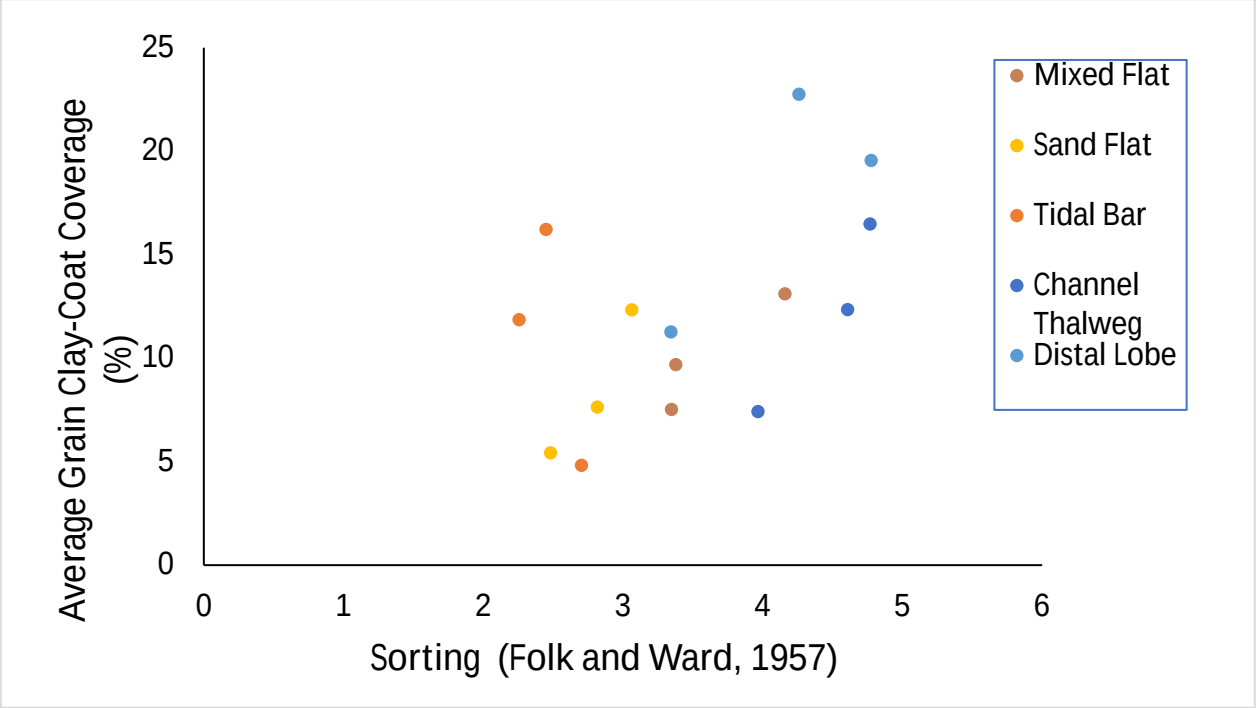


Figure 4.23. Sorting vs average clay-coat coverage in Bute Inlet. N=15.

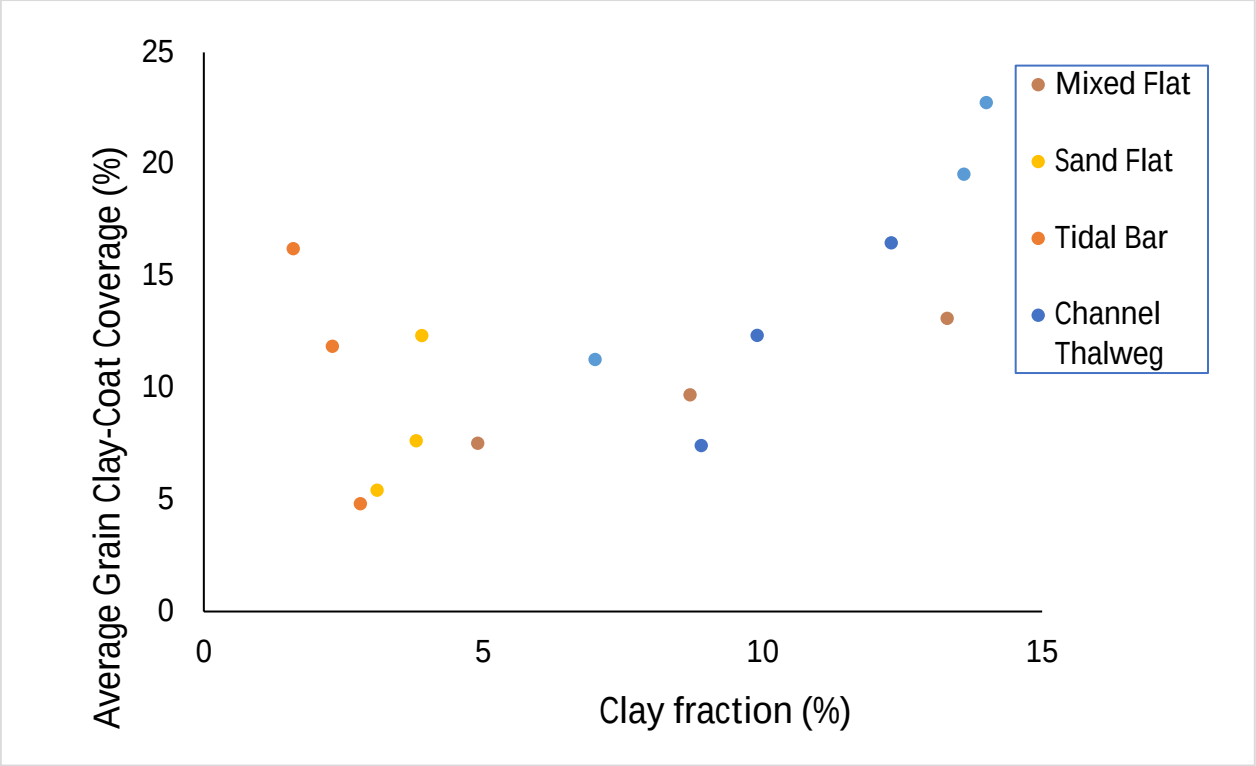


Figure 4.24. Clay fraction vs average clay-coat coverage in Bute Inlet. N=15.

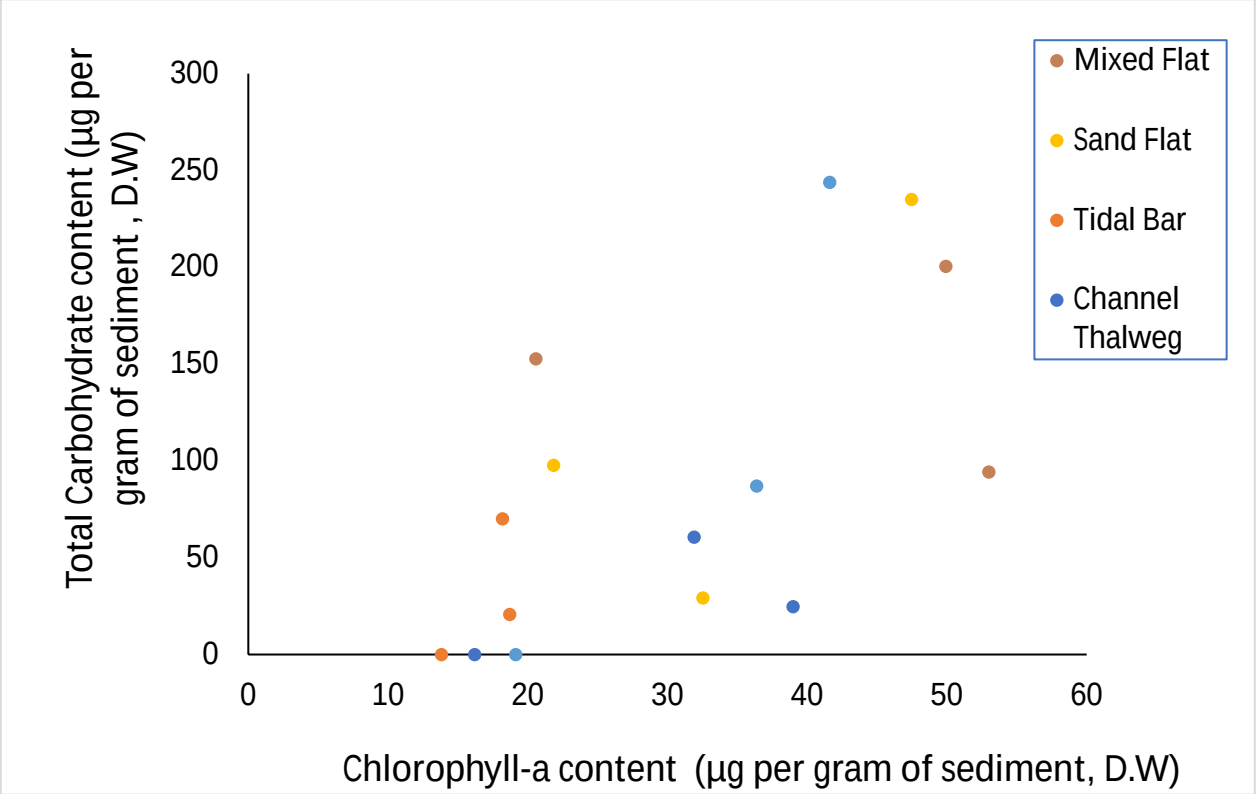


Figure 4.25. Chlorophyll-a content vs total carbohydrate content in Bute Inlet. N=15.

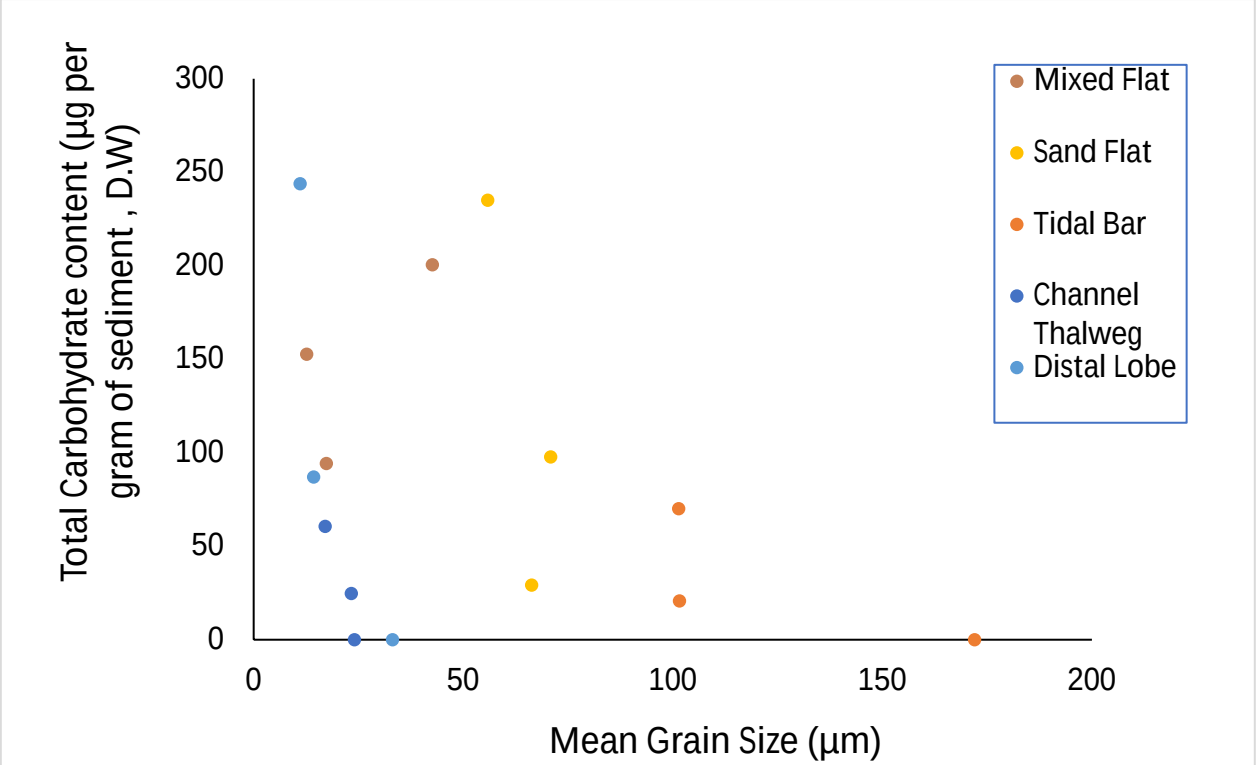


Figure 4.26. Mean grain size vs total carbohydrate content in Bute Inlet. N=15.

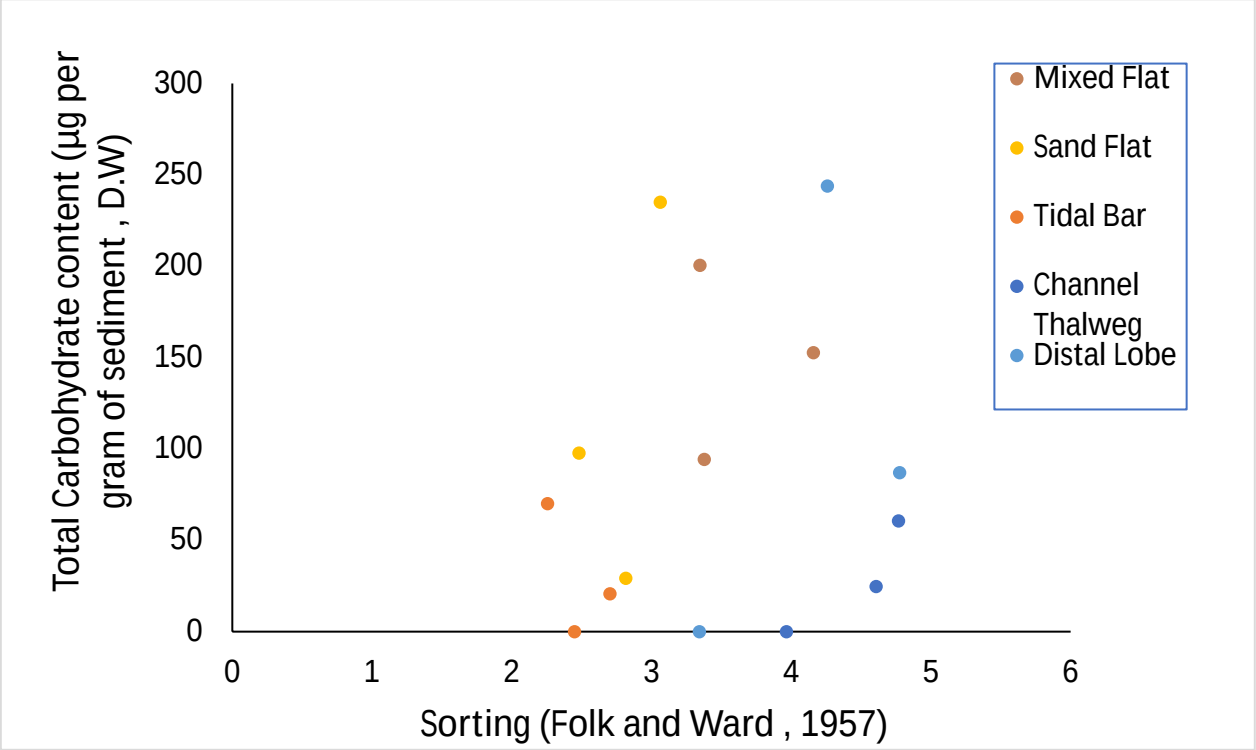


Figure 4.27. Sorting vs total carbohydrate content in Bute Inlet. N=15.

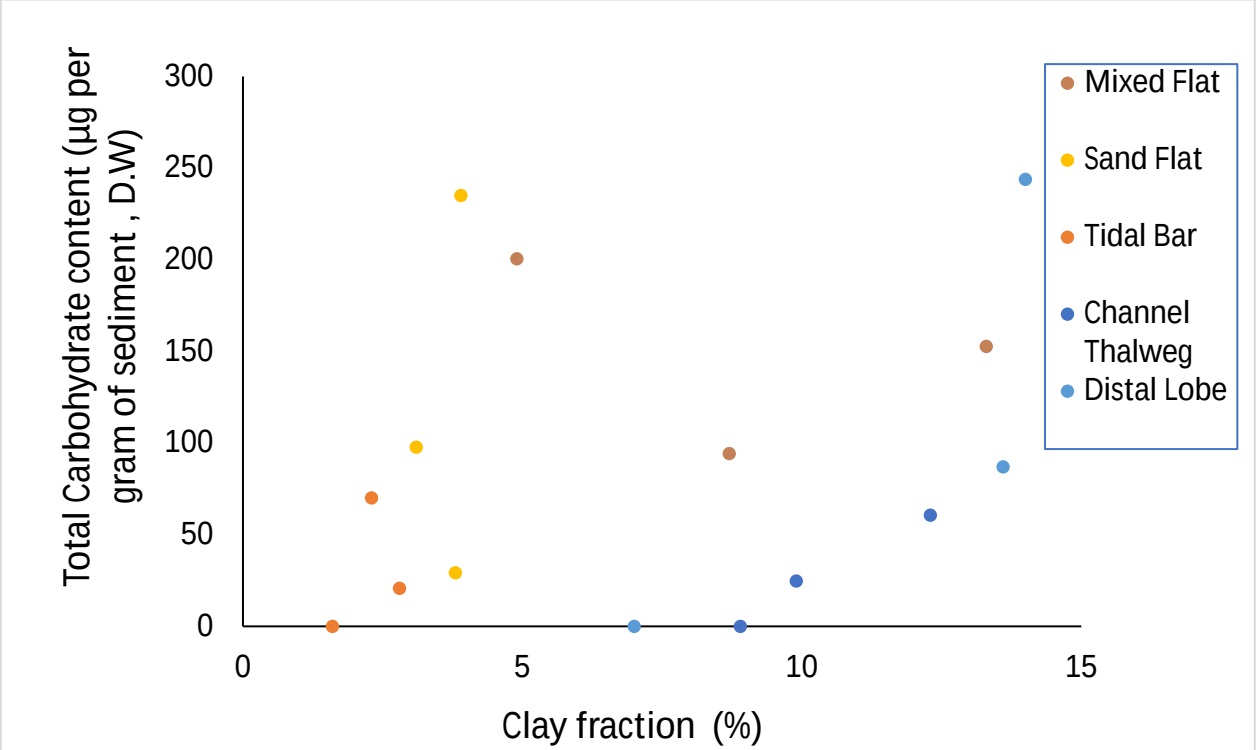


Figure 4.28. Clay fraction vs total carbohydrate content in Bute Inlet. N=15.

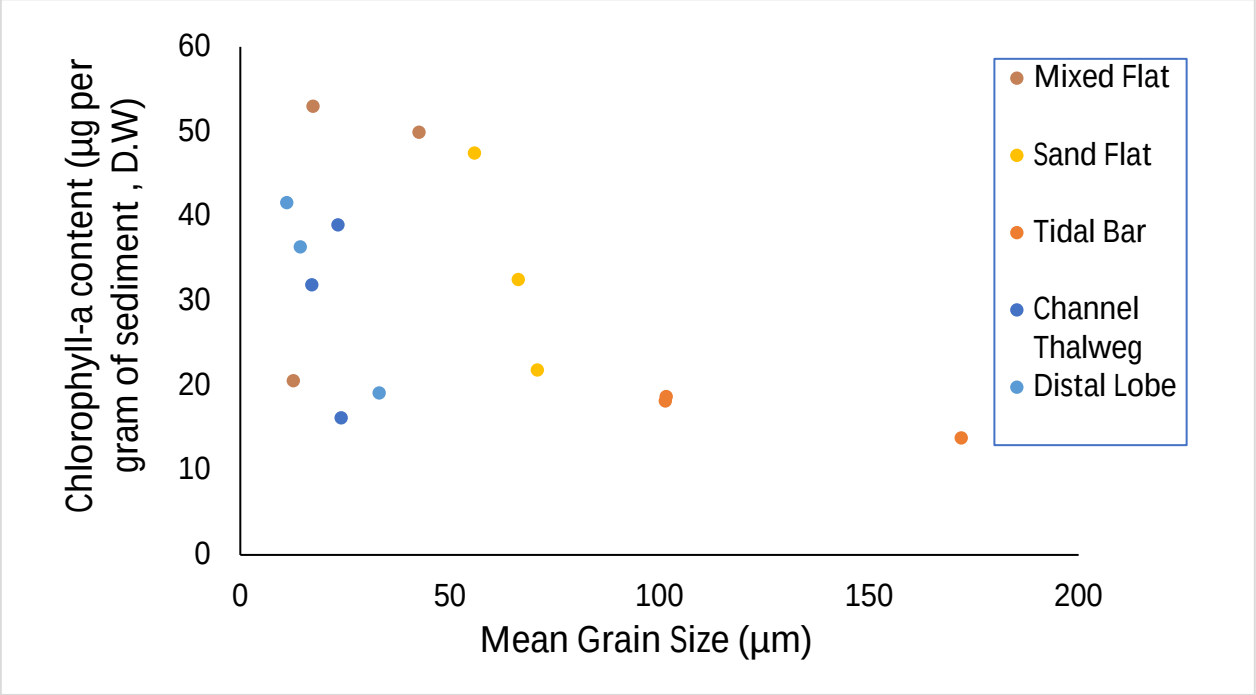


Figure 4.29. *Chlorophyll-a* vs mean grain size in content in Bute Inlet. N=15.

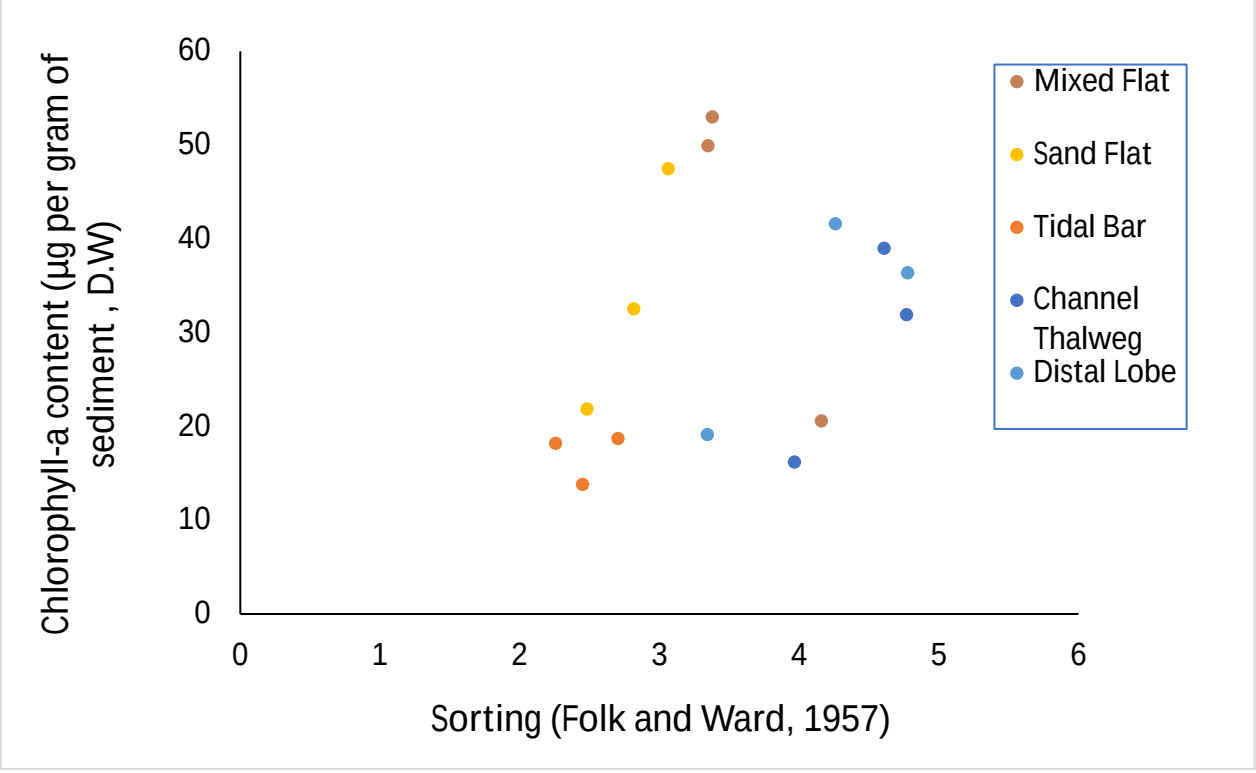


Figure 4.30. *Chlorophyll-a* vs sorting in content in Bute Inlet. N=15.

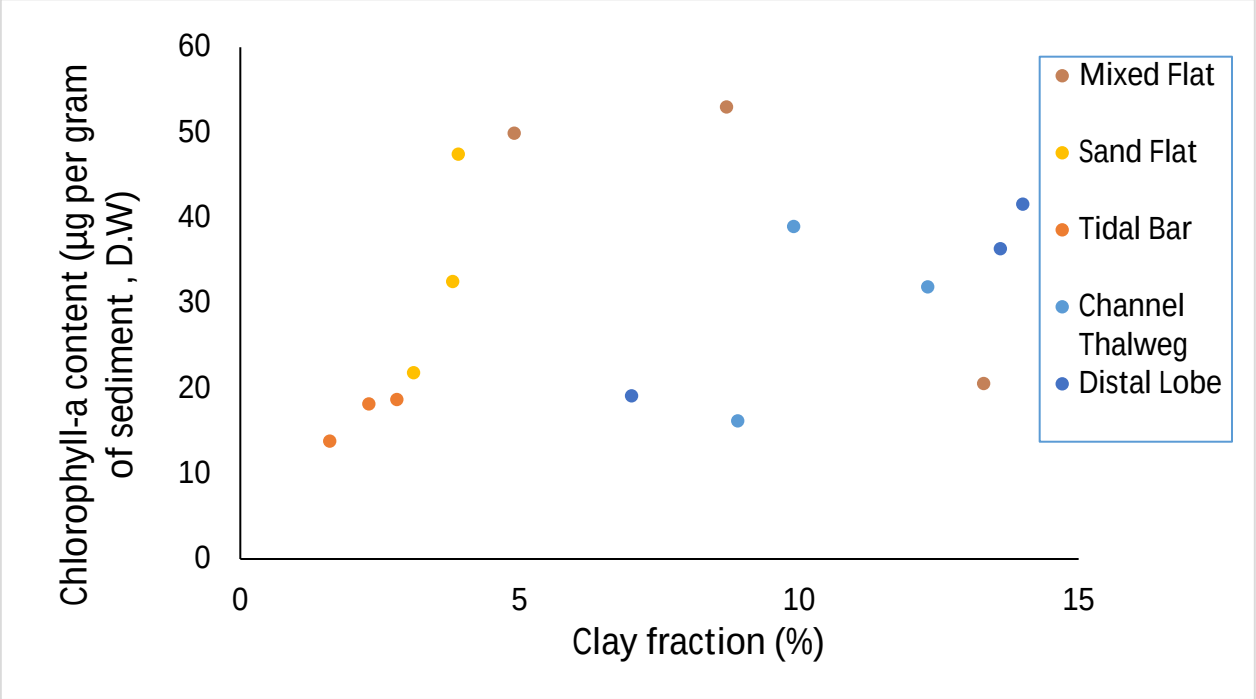


Figure 4.31. *Chlorophyll-a* vs clay fraction in content in Bute Inlet. N=15.

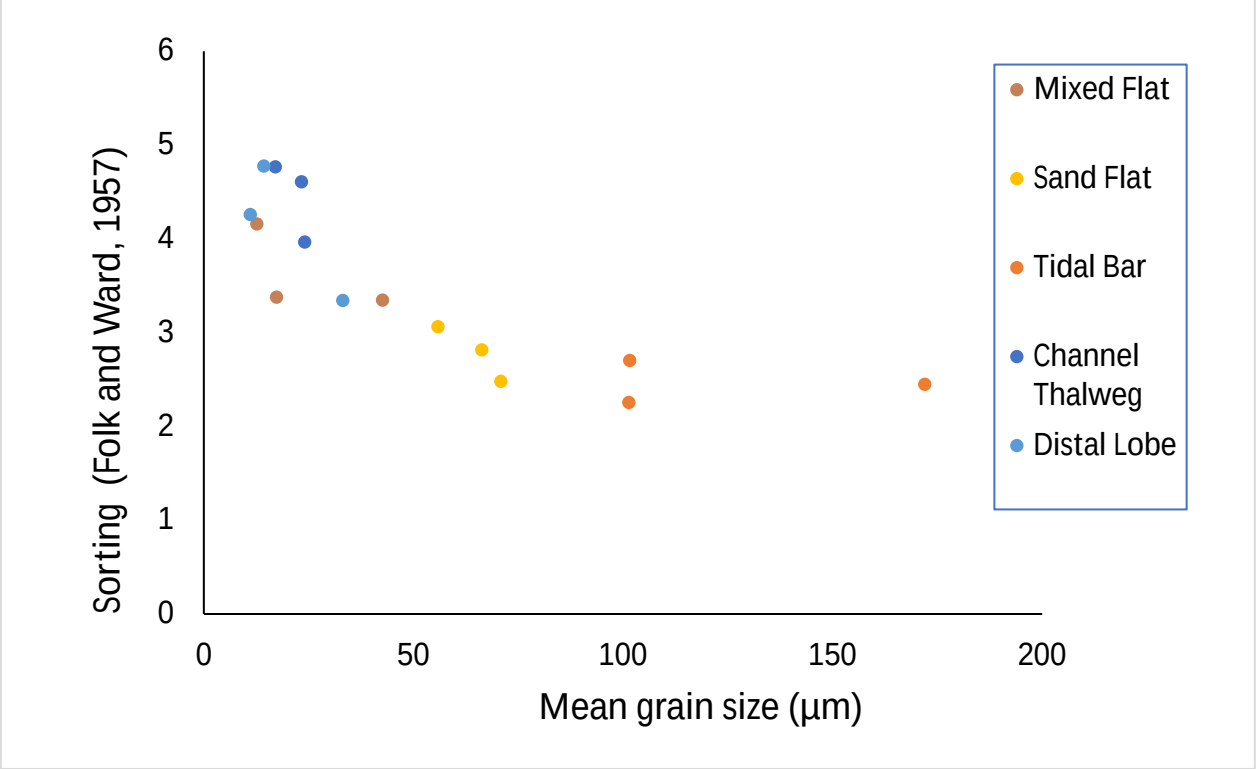


Figure 4.32. Mean grain size vs sorting in content in Bute Inlet. N=15.

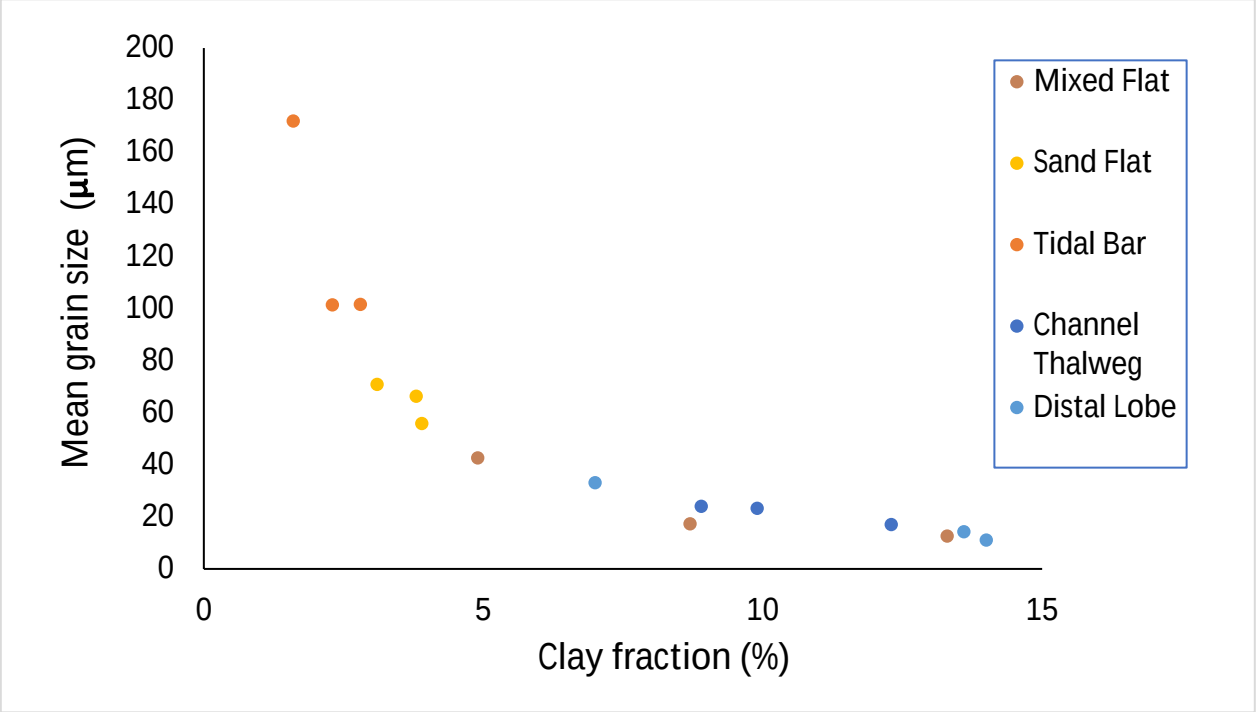


Figure 4.33. Mean grain size vs clay fraction in content in Bute Inlet. N=15.

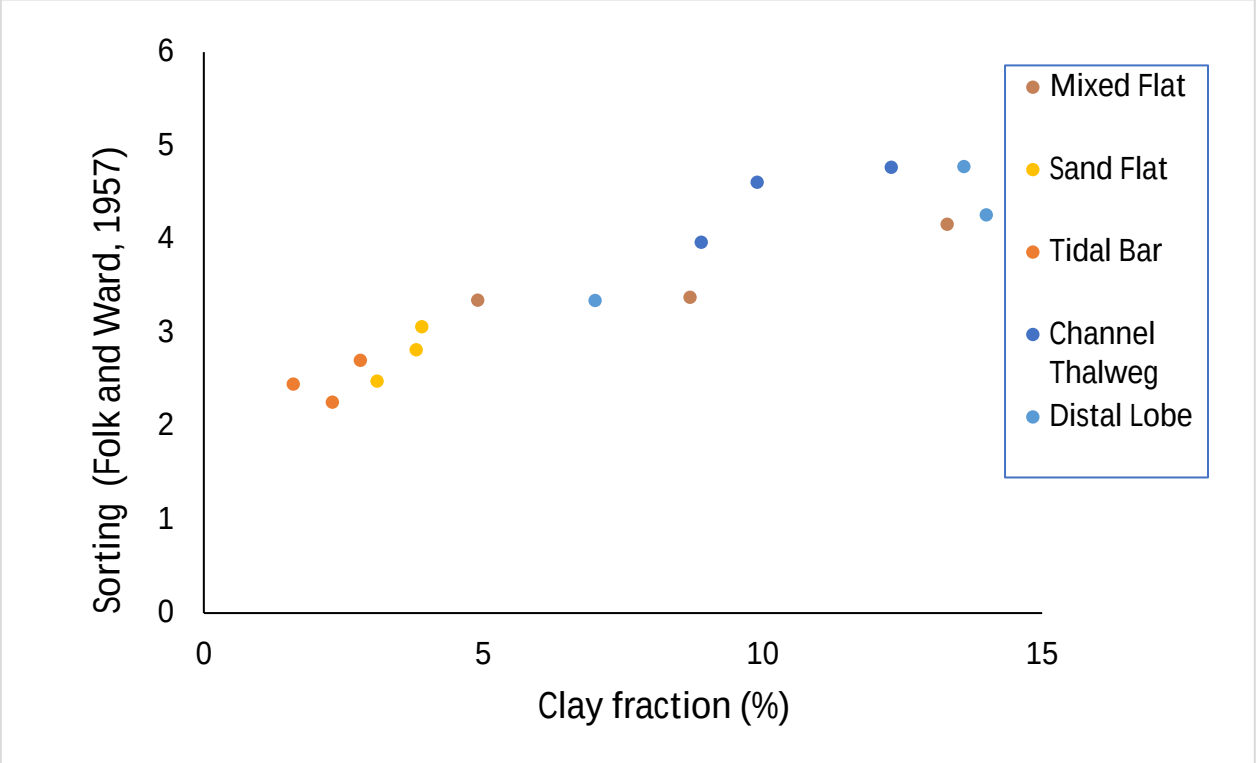


Figure 4.34. Sorting vs clay fraction in content in Bute Inlet. N=15

Pearson R value (P-value)	Average clay-coat grain coverage	Total carbohydrate content	Chlorophyll-a content	Mean grain size	Sorting	Clay fraction
Average clay-coat grain coverage	X	0.313 (0.256)	0.174 (0.535)	-0.217 (0.437)	0.546 (0.035)	0.619 (0.014)
Total carbohydrate content	0.313 (0.256)	X	0.629 (0.012)	-0.338 (0.218)	0.140 (0.619)	0.247 (0.375)
Chlorophyll-a content	0.174 (0.535)	0.629 (0.012)	X	-0.494 (0.061)	0.320 (0.245)	0.272 (0.327)
Mean grain size	-0.217 (0.437)	-0.338 (0.218)	-0.494 (0.061)	X	-0.795 (<0.001)	-0.825 (<0.001)
Sorting	0.546 (0.035)	0.140 (0.619)	0.320 (0.245)	-0.795 (<0.001)	X	0.932 (<0.001)
Clay fraction	0.619 (0.014)	0.247 (0.375)	0.272 (0.327)	-0.825 (<0.001)	0.932 (<0.001)	X

Table 4.5. Correlation matrix for Bute Inlet. P-values for each R-value are in brackets. P-values below 0.05 (significant) are in black text and P-values higher than 0.05 (non-significant) are in red text. Positive correlations are in green boxes, whereas negative correlations are in orange boxes. White boxes represent R-values between 0 and 0.2.

4.4.2 Ravenglass Estuary statistical analysis

Pearson correlation co-efficient analysis was performed on a subset of 15 samples from Ravenglass Estuary to visualize the relationship between variables. Only 15 samples had data for all of the variables tested which limited the reliability of the statistical analysis.

Figure 4.35 to Figure 4.49 contain cross plots of each of the tested variables from Ravenglass Estuary. Table 4.6 displays the R-value and corresponding P-value for each pair of tested variables.

Average clay coat grain coverage had a significant positive relationship (Table 4.6) with clay fraction content (R-value of 0.884, P-value of <0.001). This suggests that as the volume of clay-sized material increases in sediment, the abundance of clay-coated grains increases. As mentioned above, is likely to be due to more clay-sized material allowing a large number of quartz grains to be coated.

Average clay coat grain coverage also had a significant positive relationship (Table 4.6) with sorting values (R-value of 0.896, P-value of <0.001). An increase in sorting values reflect a decrease in sorting, where 1.32 is equivalent to well sorted and 4.00 is equivalent to very poorly sorted. This means that in Ravenglass Estuary, average clay coat grain coverage increases with decreasing sorting.

Average clay coat grain coverage showed a significant positive relationship (Table 4.6) with *chlorophyll-a* content (R-value of 0.783, P-value of <0.001) and total carbohydrate content (R-value of 0.854, P-value of <0.001). Total carbohydrate content and chlorophyll-a content are proxies for EPS content. This means that as EPS content increase, clay coat coverage also increases across Ravenglass Estuary.

Average clay coat coverage had a significant negative correlation with mean grain size (R-value of -0.602, P-value of 0.018). This is likely due to a decrease in clay content as grain size increase, which limits the amount of clay available to coat grains.

Total carbohydrate content had a significant positive relationship (Table 4.6) with *chlorophyll-a* content (R-value of 0.818, P-value of <0.001). Both total carbohydrate and *chlorophyll-a* content showed a significant positive relationship with clay fraction content (R-value of 0.747, P-value of 0.001 and R-value of 0.715, P-value of 0.003, respectively). This may be due to an increase in clay content typically being found in lower energy, quieter environments which are more preferential for EPS producing microorganisms (Stal, 2003) compared to higher energy environments which have a lower clay content. Chlorophyll-a showed a significant negative correlation with mean grain size (R-value of -0.643, P-value of 0.002) which supports this hypothesis. However, total carbohydrate content showed no significant relationship with mean grain size (P-value greater than 0.05).

Both total carbohydrate content and chlorophyll-a content showed a significant positive relationship with sorting (R-value of 0.726, P-value of 0.002 and R-value of 0.776, P-value of <0.001, respectively). As mentioned above, an increase in sorting values reflect a decrease in sorting, where 1.32 is equivalent to well sorted and 4.00 is equivalent to very poorly sorted. This means that in Ravenglass Estuary, EPS content increases as sorting increases.

Mean grain size had a significant negative relationship (Table 4.6) with sorting (R-value of -0.540, P-value of 0.034). As mentioned above, an increase in sorting values reflect a decrease in sorting. This means that in Ravenglass Estuary, sorting increases as grain size increases.

Mean grain size also had a significant negative relationship (Table 4.6) with clay fraction content (R-value of -0.635, P-value of 0.011) which is likely related to the separation of different grain size fractions during deposition.

Clay fraction content had a significant positive relationship (Table 4.6) with sorting values (R-value of 0.780, P-value of <0.001). An increase in sorting values reflect a decrease in sorting. This means that in Ravenglass Estuary sorting decreased as the volume of clay content increased.

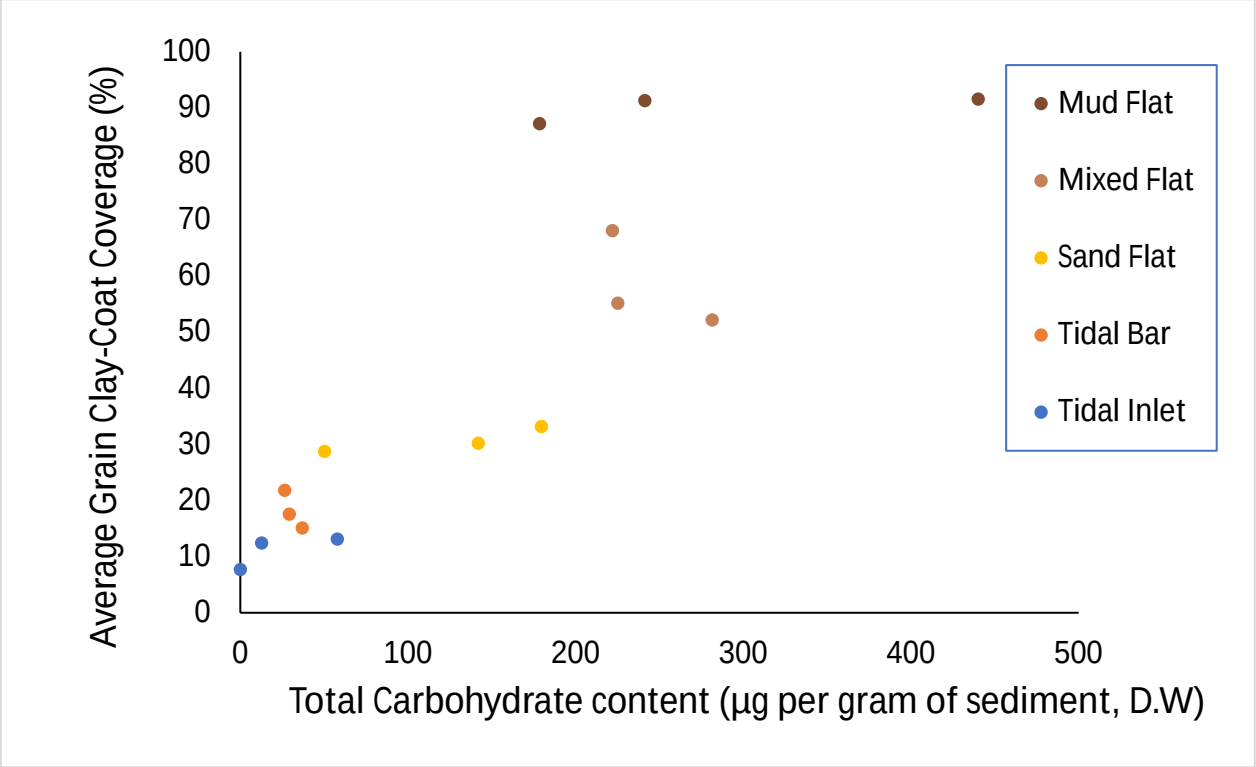


Figure 4.35. Total Carbohydrate content vs average clay-coat coverage in Ravenglass Estuary. N=15.

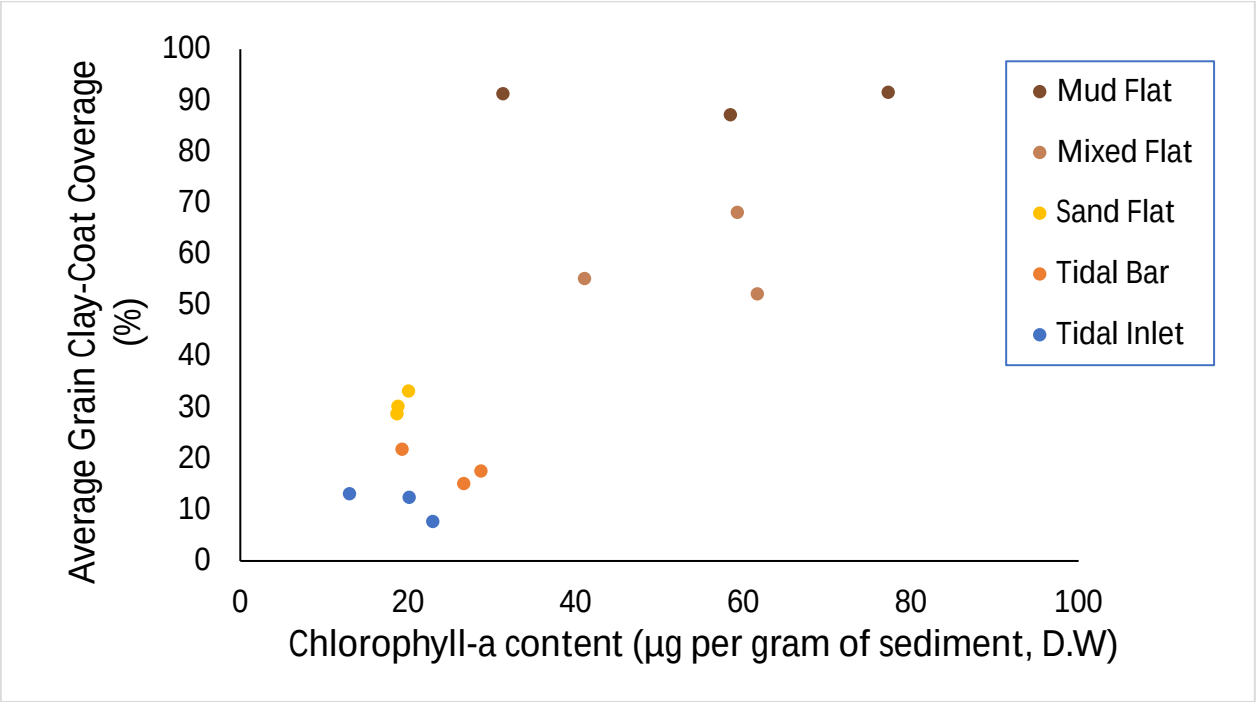


Figure 4.36. Chlorophyll-a content vs average clay-coat coverage in Ravenglass Estuary. N=15.

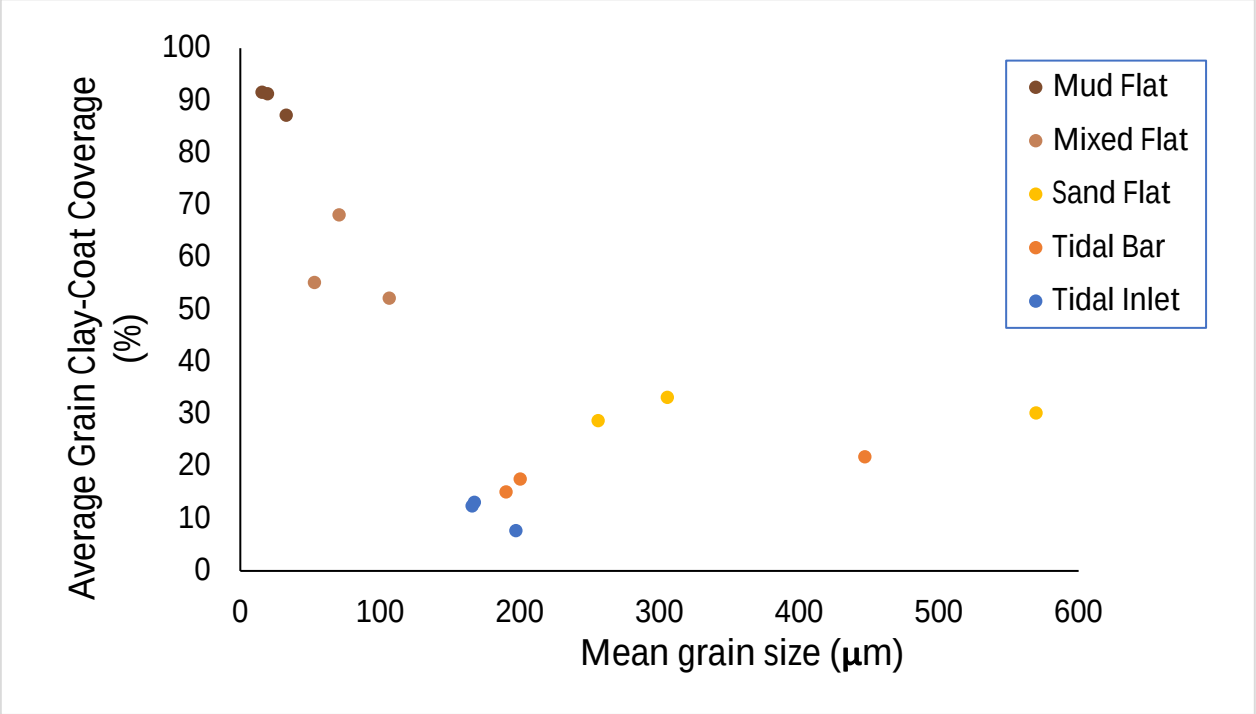


Figure 4.37. Mean grain size vs average clay-coat coverage in Ravenglass Estuary. N=15.

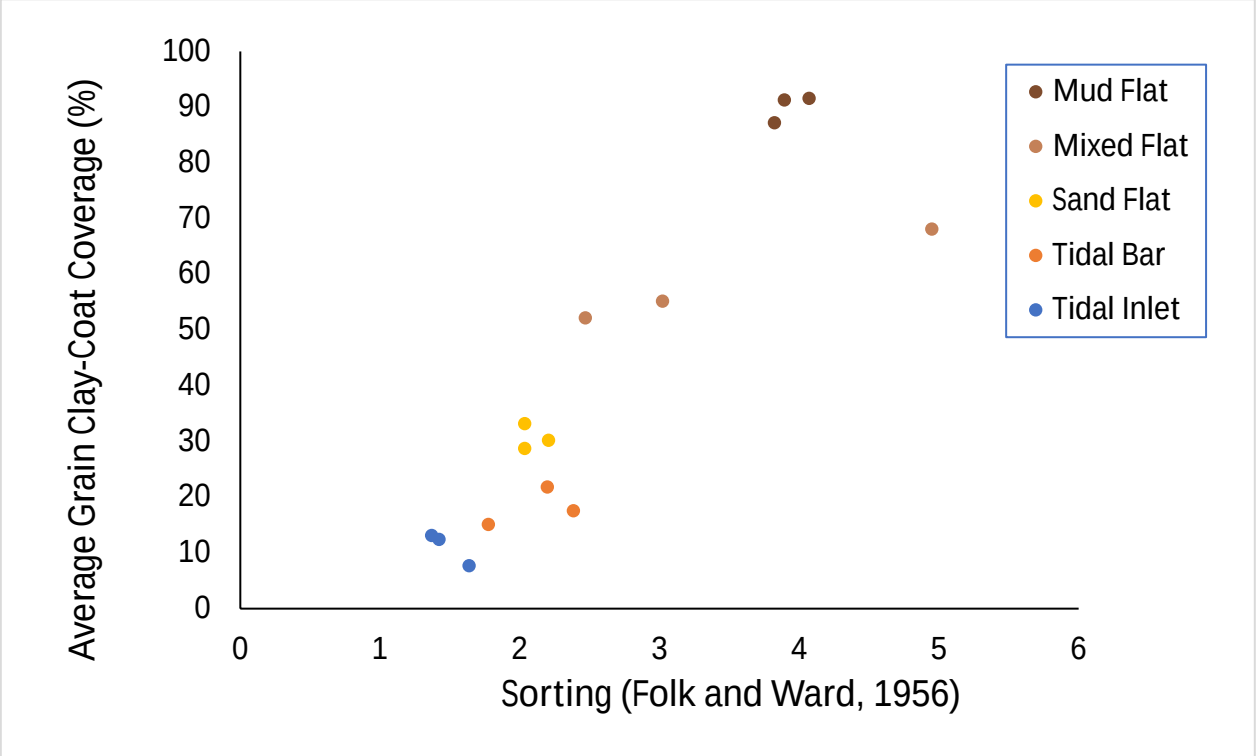


Figure 4.38. Sorting vs average clay-coat coverage in Ravenglass Estuary. N=15.

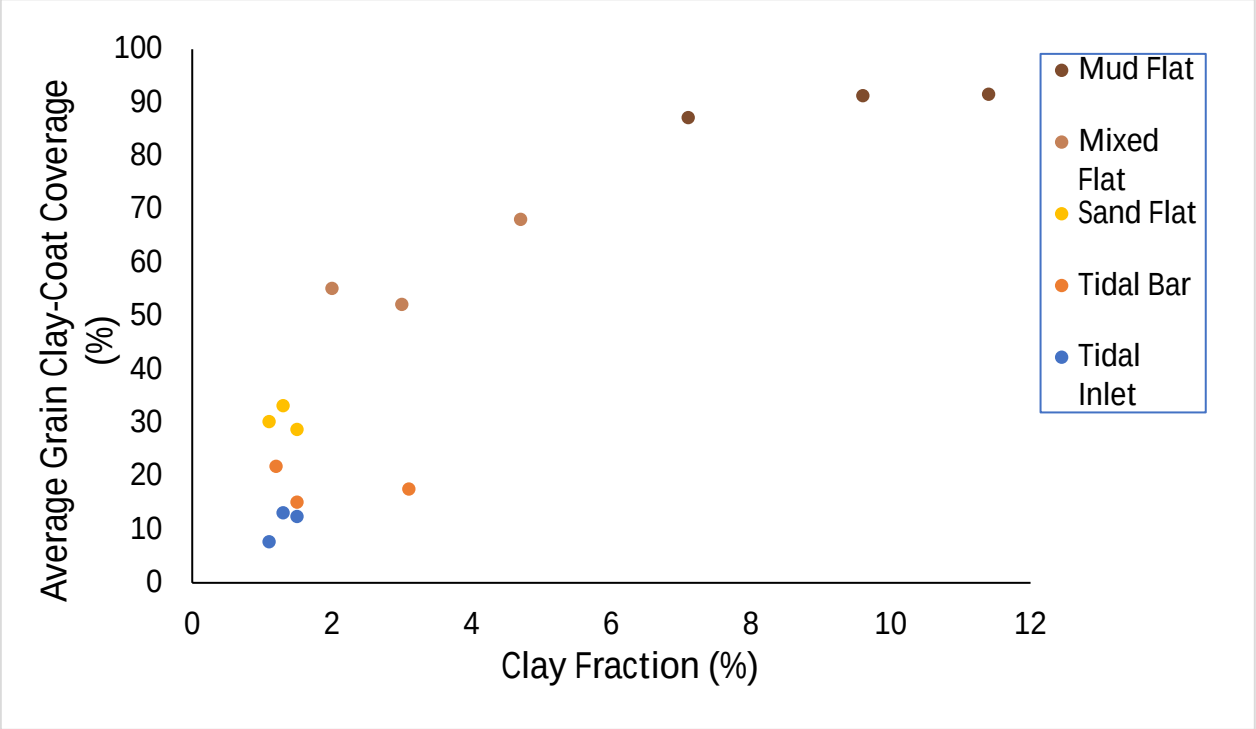


Figure 4.39. Clay fraction vs average clay-coat coverage in Ravenglass Estuary. N=15.

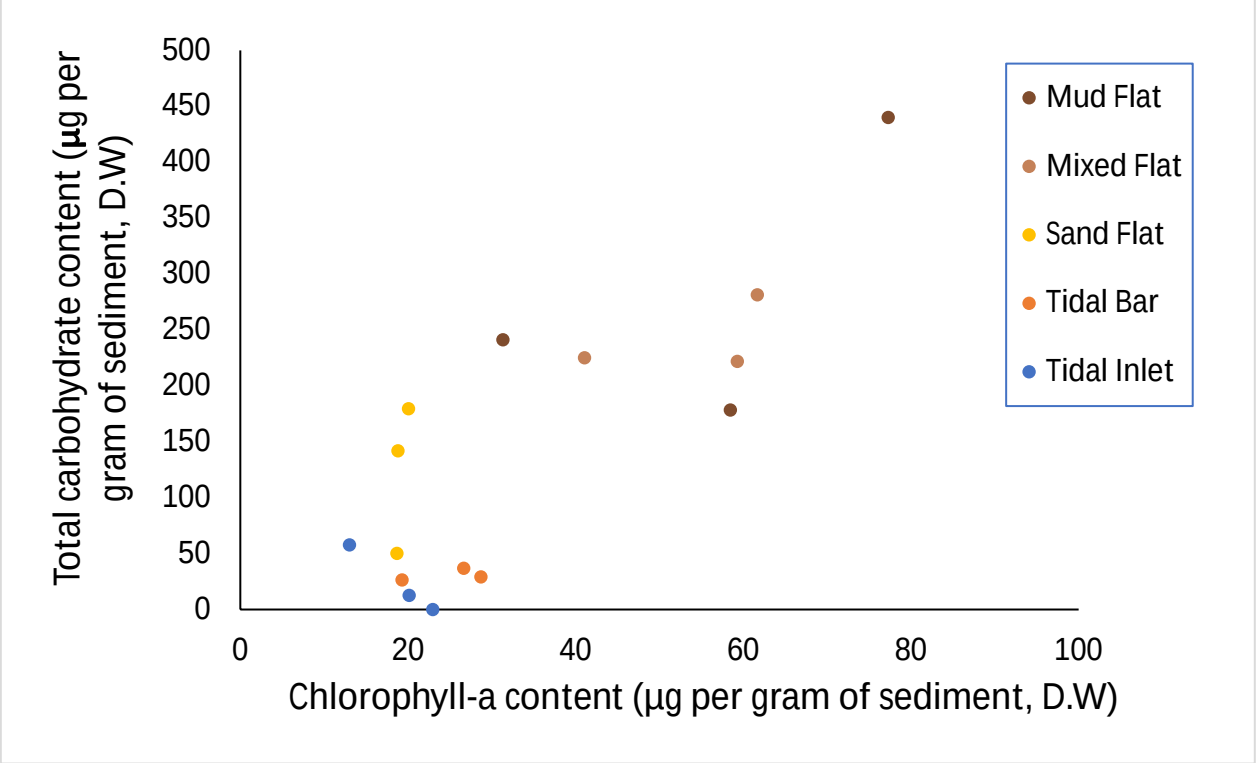


Figure 4.40. Chlorophyll-a content vs total carbohydrate content in Ravenglass Estuary. N=15.

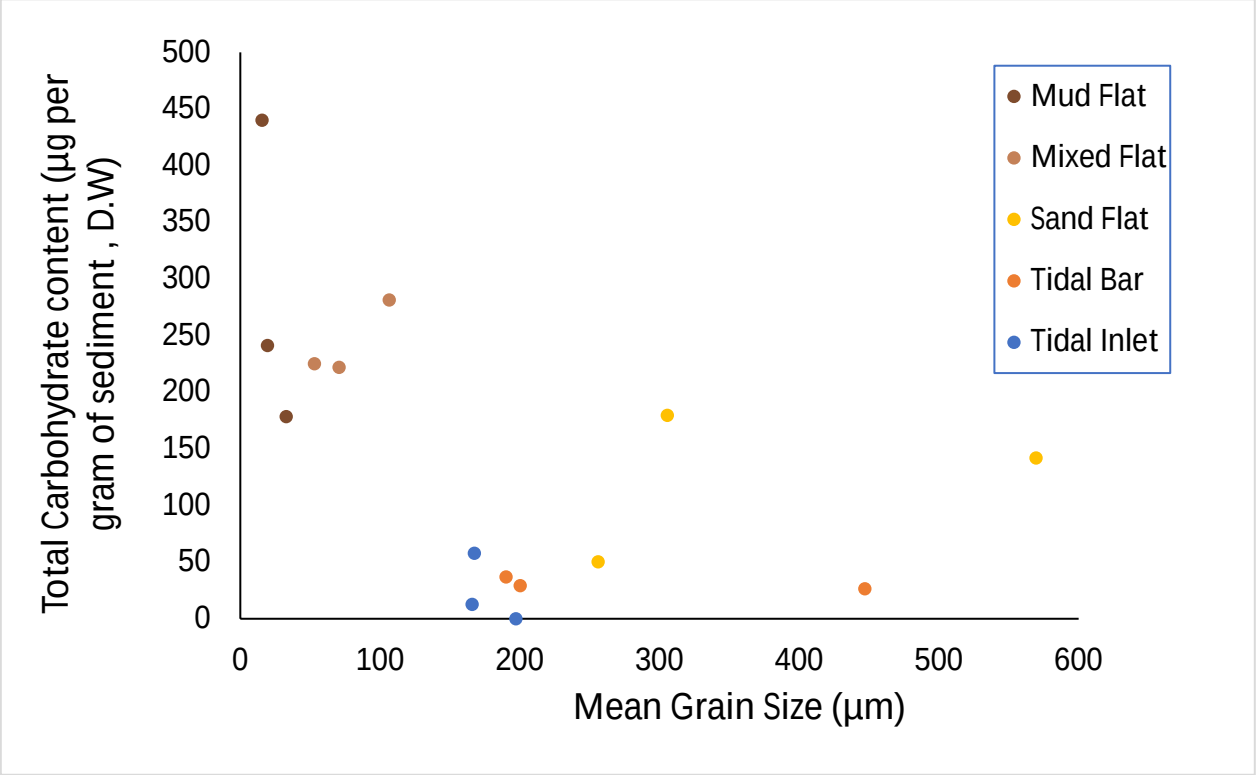


Figure 4.41. Mean grain size vs total carbohydrate content in Ravenglass Estuary. N=15.

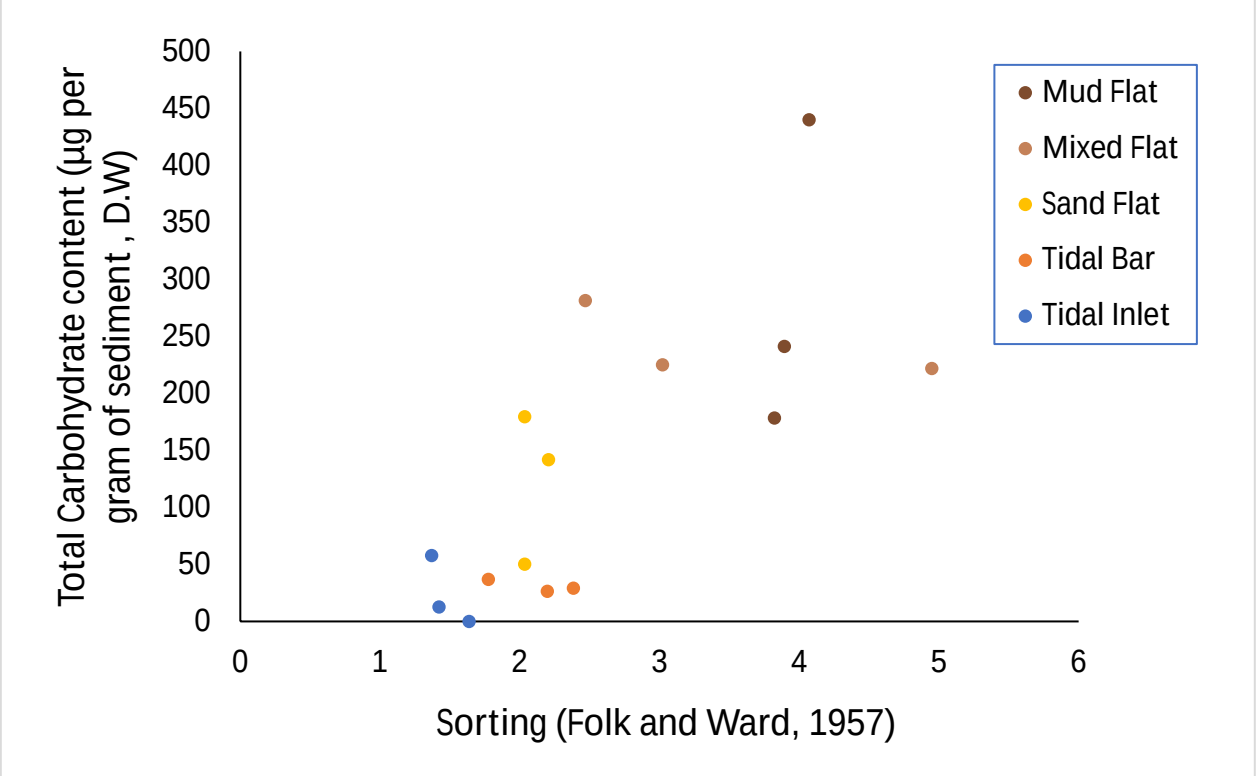


Figure 4.42. Sorting vs total carbohydrate content in Ravenglass Estuary. N=15.

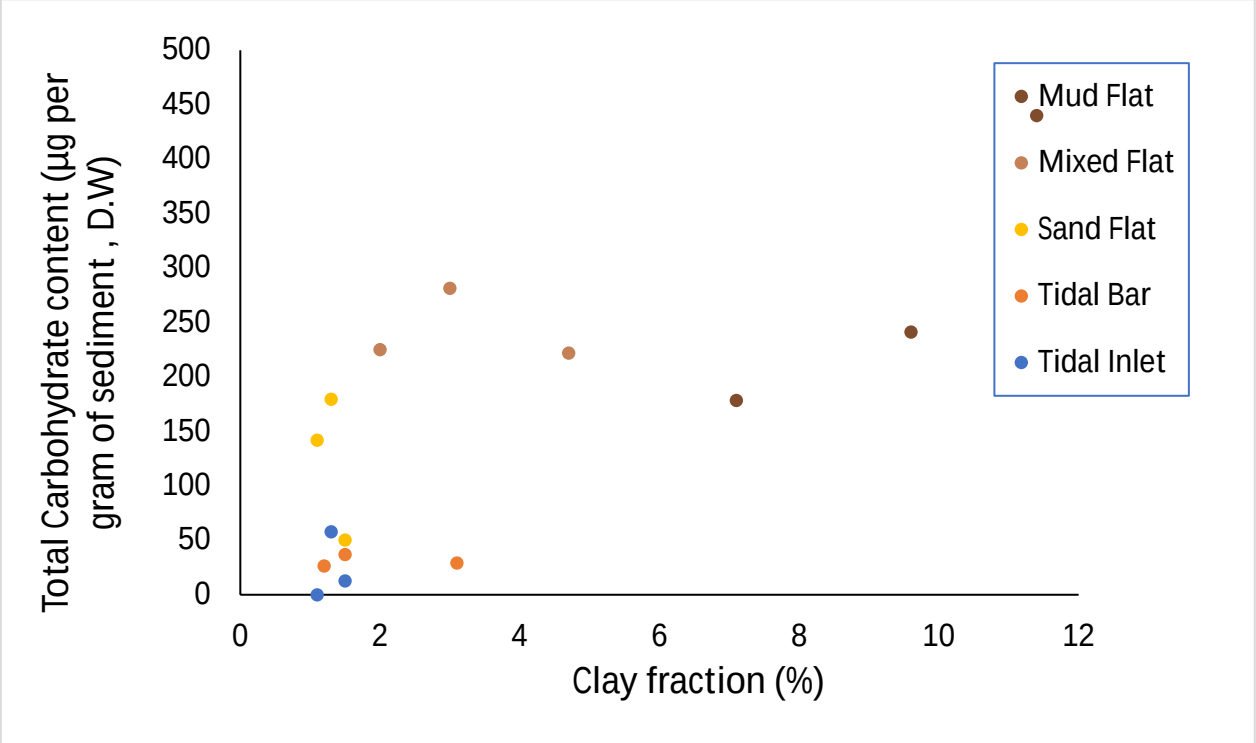


Figure 4.43. Clay fraction vs total carbohydrate content in Ravenglass Estuary. N=15.

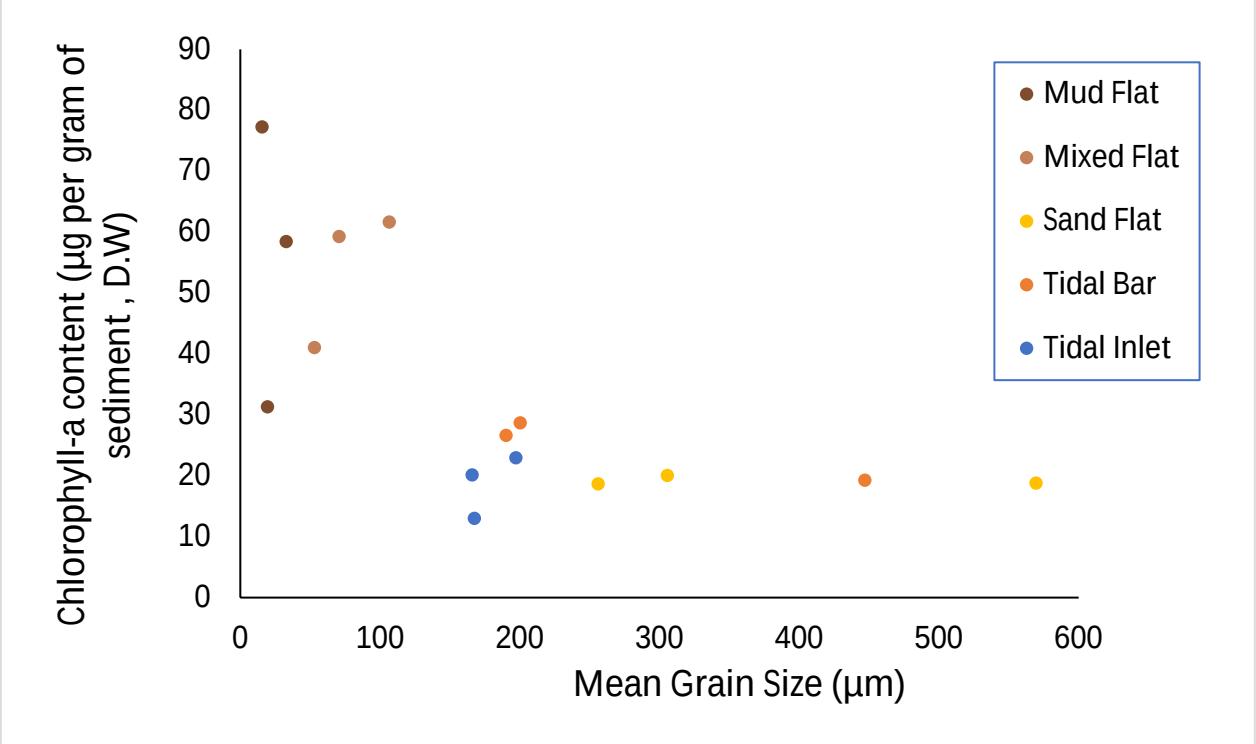


Figure 4.44. *Chlorophyll-a* vs mean grain size in content in Ravenglass Estuary. N=15.

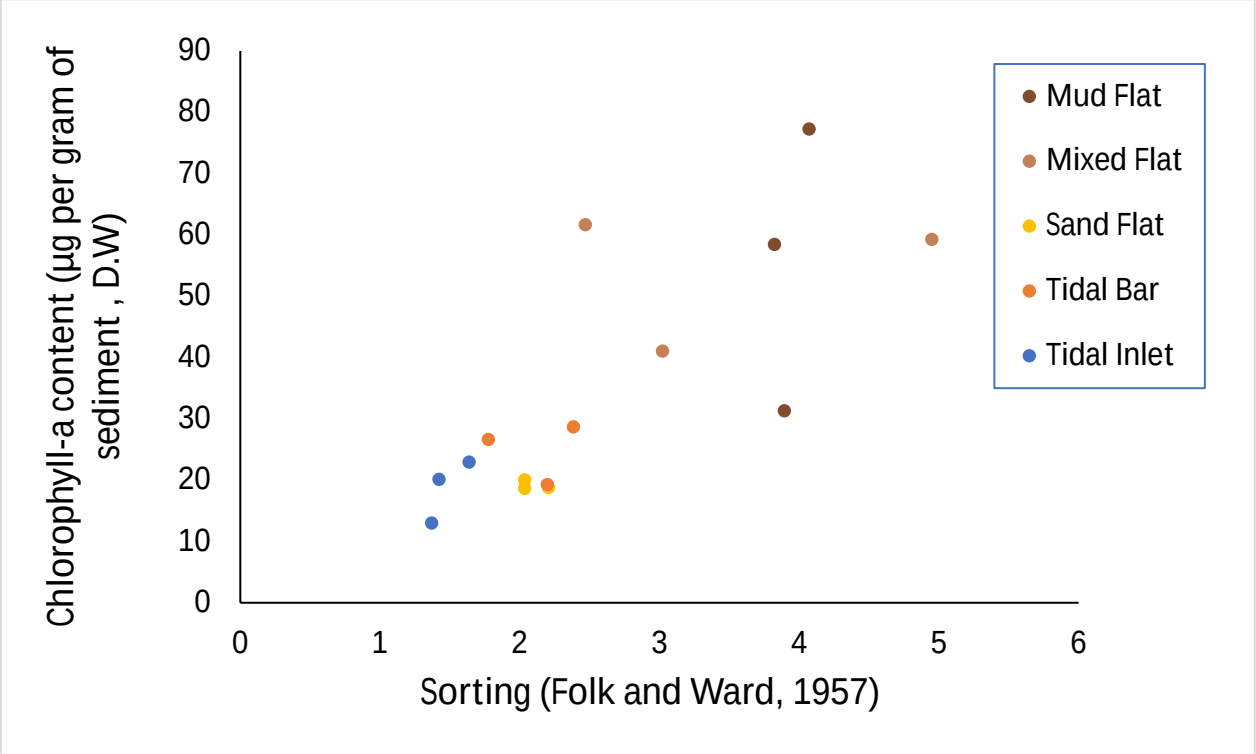


Figure 4.45. *Chlorophyll-a* vs sorting in content in Ravenglass Estuary. N=15.

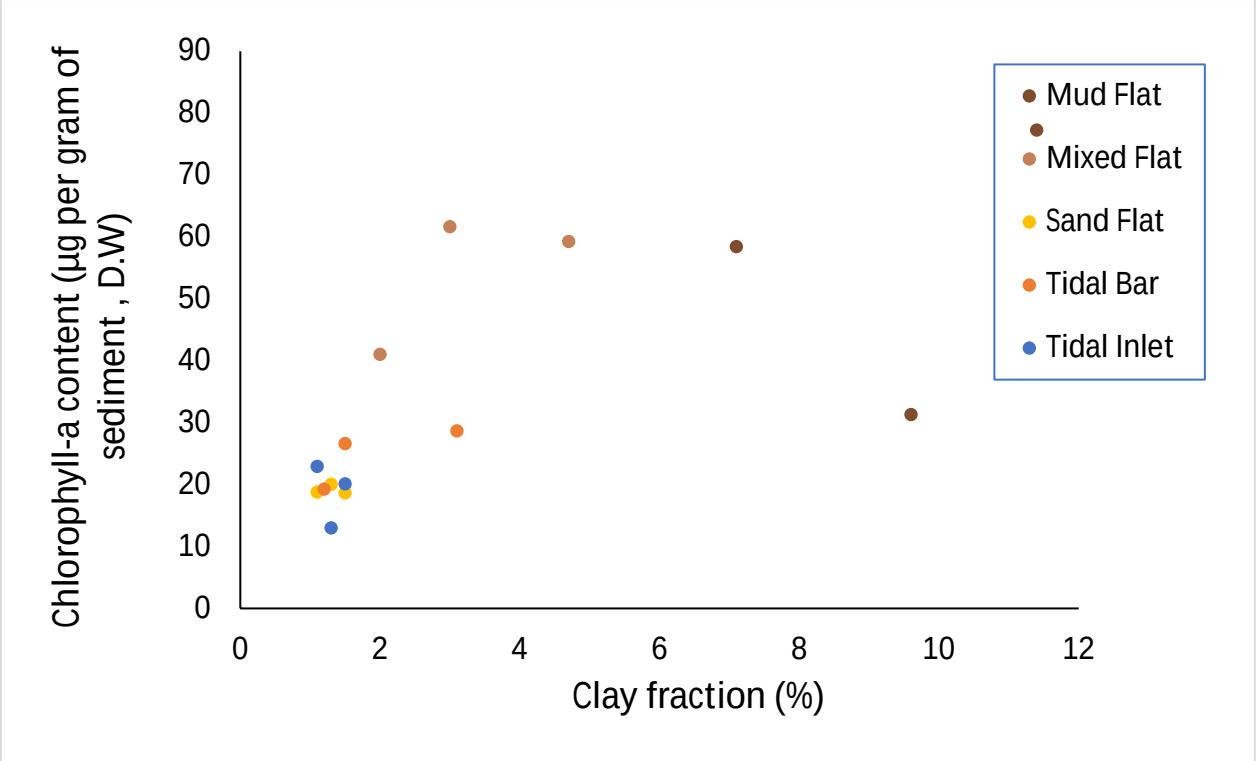


Figure 4.46. *Chlorophyll-a* vs clay fraction in content in Ravenglass Estuary. N=15.

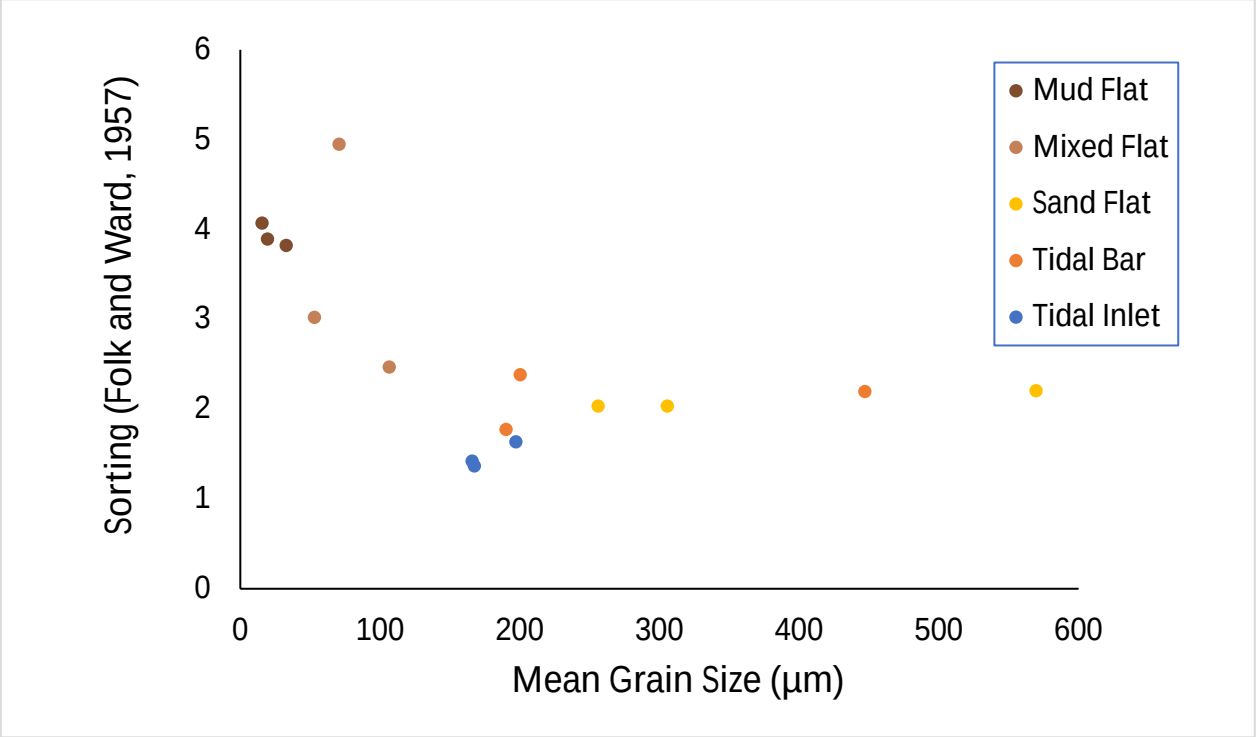


Figure 4.47. Mean grain size vs sorting in content in Ravenglass Estuary. N=15.

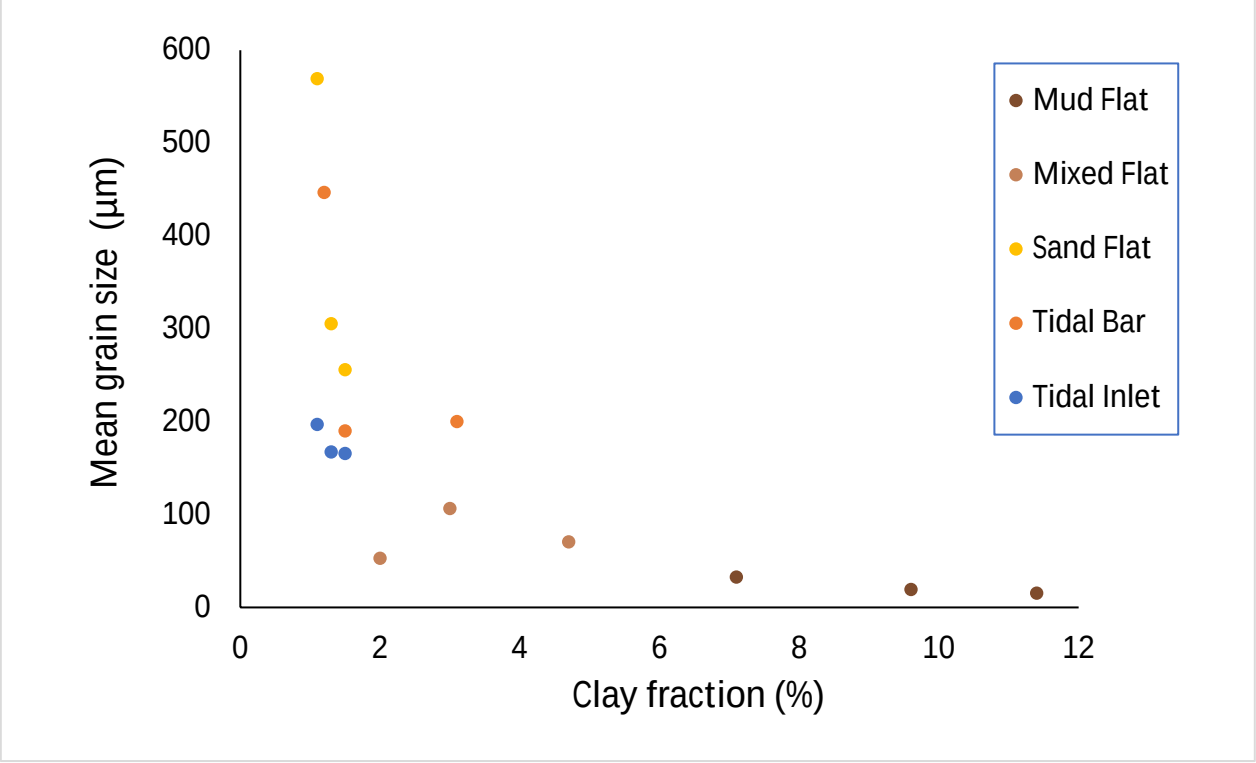


Figure 4.48. Mean grain size vs clay fraction in content in Ravenglass Estuary. N=15.

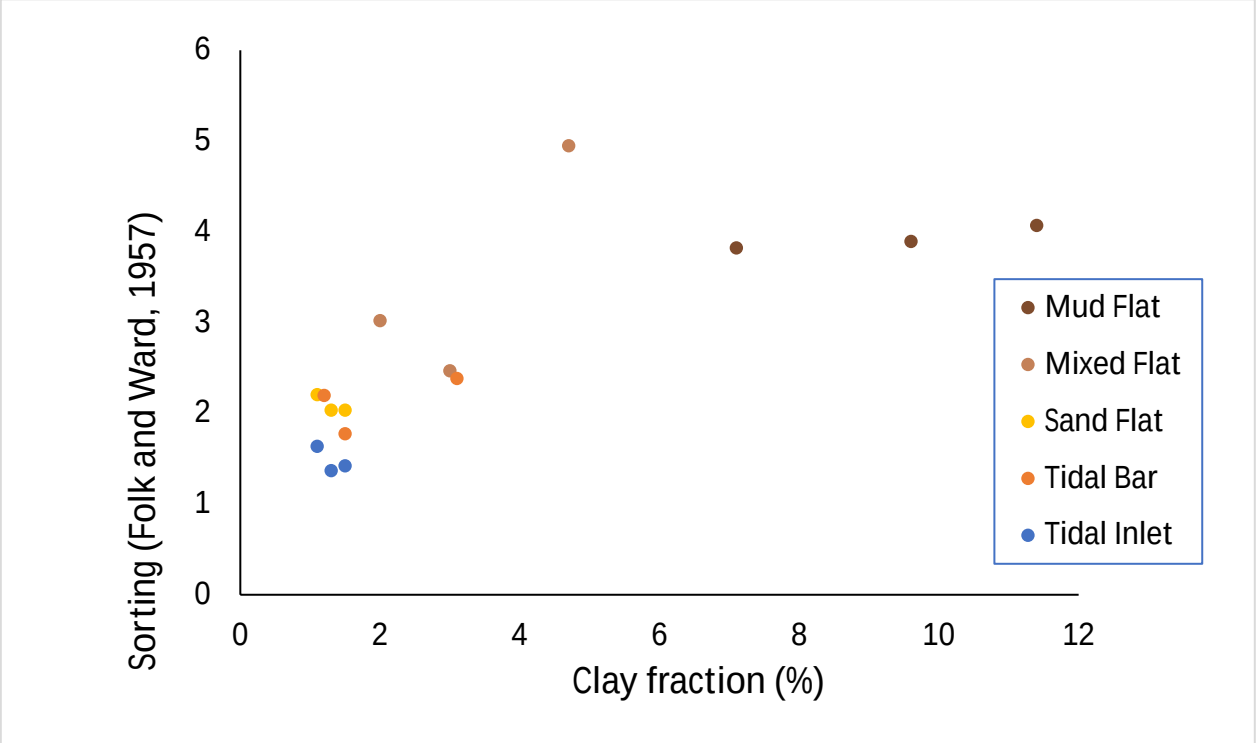


Figure 4.49. Sorting vs clay fraction in content in Ravenglass Estuary. N=15.

Pearson R value (P-value)	Average clay-coat grain coverage	Total carbohydrate content	Chlorophyll-a content	Mean grain size	Sorting	Clay fraction
Average clay-coat grain coverage	X	0.854 (<0.001)	0.783 (<0.001)	-0.602 (0.018)	0.896 (<0.001)	0.884 (<0.001)
Total carbohydrate content	0.854 (<0.001)	X	0.818 (<0.001)	-0.484 (0.068)	0.726 (0.002)	0.747 (0.001)
Chlorophyll-a content	0.783 (<0.001)	0.818 (<0.001)	X	-0.643 (0.002)	0.776 (<0.001)	0.715 (0.003)
Mean grain size	-0.602 (0.018)	-0.484 (0.068)	-0.643 (0.002)	X	-0.540 (0.034)	-0.635 (0.011)
Sorting	0.896 (<0.001)	0.726 (0.002)	0.776 (<0.001)	-0.540 (0.034)	X	0.780 (<0.001)
Clay fraction	0.884 (<0.001)	0.747 (0.001)	0.715 (0.003)	-0.635 (0.011)	0.780 (<0.001)	X

Table 4.6. Correlation matrix for Ravenglass Estuary. P-values for each R-value are in brackets. P-values below 0.05 (significant) are in black text and P-values higher than 0.05 (non-significant) are in red text. Positive correlations are in green boxes, whereas negative correlations are in orange boxes.

4.5 Discussion

This Chapter focused on the research theme “The origin and distribution of precursor clay-coated grains in shallow marine and deep-water turbidite systems”. The key research questions addressed in this chapter were:

- How is EPS distributed across modern shallow marine and deep-water turbidite system analogues?
- Is there a relationship between EPS content and clay coat coverage in modern shallow marine and deep-water turbidite system analogues?
- What are the textural and depositional controls on clay coat formation in modern shallow marine and deep-water turbidite system analogues?
- How are precursor clay-coated grains formed in modern shallow marine and deep-water turbidite system analogues?

4.5.1 Distribution of EPS across shallow marine and deep-water turbidite systems

One of the main research questions of this chapter was “how is EPS distributed across modern shallow marine and deep-water turbidite system analogues?”. Total carbohydrate content and chlorophyll-a content were used as proxies for EPS abundance in this study.

The highest EPS concentration in Bute Inlet was found in sediments taken from the distal lobe. A study of organic matter distribution across Bute Inlet concluded that organic matter is mainly sourced from the proximal shallow marine section of the system and transported to the lobe (Hauge et al., 2021). EPS measured in the distal lobe likely reflect EPS produced in shallow marine conditions which has been transported to the distal lobe via turbidity currents. However, EPS could also be produced in deep water settings by planktonic microorganisms within the water column. Future studies of EPS distribution within deep water systems should aim to distinguish where EPS present in distal lobes is predominantly transported from shallow marine settings or sourced from the overlying water column.

The highest content of EPS across Ravenglass Estuary was associated with mud flats and mixed flats. Statistical analysis indicates EPS content has a significant positive correlation with clay content and sorting. EPS within Ravenglass Estuary is known to be

mainly produce by epilithic diatoms (Wooldridge et al., 2017a). The increase in EPS content with increasing clay content likely reflects the higher abundance of clay minerals in lower energy environment which experience less disturbance (e.g. mudflat) which are more preferential for diatoms (Stal, 2003).

4.5.2 Relationship between clay coat coverage and EPS across shallow marine and deep-water turbidite systems

Within Bute Inlet, there was no statistical relationship between average clay coat coverage and total carbohydrate and *chlorophyll-a* content (proxies for EPS content). This suggests clay coated grains present in Bute Inlet do not form in association with biofilms. Clay coat grain coverage in Bute was significantly lower than Ravenglass Estuary. Yet both systems had a similar range of total carbohydrate content (EPS). This indicates another factor other than EPS content is responsible for the low level of clay coated grains observed in Bute Inlet.

The clay-lamina style-coatings observed in sediment samples from the channel thalweg in Bute Inlet are interpreted as being formed by the erosion and subsequent transportation of alternating layers of clay and sand rich deposits from the proximal part of the system via monthly turbidity currents. However, these sediments contain a high proportion of clay and would be considered non reservoir facies in ancient analogues.

In Ravenglass Estuary, average clay coat coverage showed a significant positive correlation with both chlorophyll-a content and total carbohydrate content. Clay minerals were also seen attached to EPS stalks in sediment from Ravenglass Estuary via SEM analysis. Overall, this indicates that biofilms play a key role in the formation of clay coated grains in shallow marine environments, supporting the hypothesis put forward by Wooldridge et al (2017a). Aggregates of fine sand grains within a clay bridging network are present in sediment from the tidal inlet. These aggregates likely represent fine grained material eroded from intertidal sub-environments that have been transported seaward. This may suggest clay coated grains formed in intertidal environments are durable enough to withstand sediment transportation seaward. Future studies should investigate how durable clay coats are and if clay coated grains have been recorded in shelf depositional settings.

The high abundance of clay-coated grains in Ravenglass Estuary vs the low abundance of clay-coated grains in Bute Inlet is likely due to several factors. One of these factors is the sediment source and mineralogy. Sediment present in Bute Inlet was found to have an arkosic composition, dominated by plagioclase feldspar, whereas sediment from Ravenglass Estuary was found to be largely quartz rich. No previous studies have considered the control of detrital mineralogy (arkose vs quartz rich) on the formation of clay-coated grains, which presents and interesting avenue for future research.

Sediment residence and transportation is another feature which may explain the variation in clay-coat abundance between Bute Inlet and Ravenglass Estuary. Dowey et al (2012) suggested sediment which resides in intertidal conditions for a long period of time is more likely to contain clay-coated grains, compared to sediment which is transported into deeper marine settings relative soon after initial deposition. Sediment within Ravenglass Estuary has a long residence time within shallow intertidal conditions, whereas sediment in Bute Inlet is transported to the fjord floor relatively soon after initial deposition via monthly turbidity currents (Prior et al., 1987).

Lastly, sediment maturity may explain the high clay-coat coverage and abundance present in Ravenglass Estuary and the low clay-coat coverage and abundance in Bute Inlet. Petrographic analysis of sediment from Bute Inlet revealed sediment was largely immature with some fresh feldspar grains subject to minimum alteration. In contrast, sediment from Ravenglass Estuary is significantly more mature and is generally well rounded as a result of reworking along the coast and thus has many embayments on the surface of quartz grains, which is likely to promote the formation of clay-coated grains.

4.5.3 Textural controls and depositional controls on clay coat formation in modern shallow marine and deep-water turbidite system analogues

Bute inlet has significantly lower levels of average clay coat coverage compared to Ravenglass Estuary. Therefore, the relationships between clay coat coverage and textural and depositional controls described for Bute Inlet are limited and may not be reliable. Future studies should focus on any other deep water turbidite systems (modern or ancient) which are associated with a higher proportion of clay coated grains.

In Ravenglass Estuary, average clay coat grain coverage had a significant positive relationship with clay fraction content and a negative correlation with mean grain size. Average grain clay-coat coverage ranged from 13 to 92% across Ravenglass Estuary, with the highest clay-coat coverage present in sediment samples from mud and mixed flats. Mixed flat and mud flat facies in ancient systems would typically be considered non reservoir due to a high content of detrital mud. Therefore, a threshold exists where enough clay material is required to coat quartz grains but not too much to inhibit pore space. Facies which likely meet these criteria are tidal bar and sand flats.

4.5.4 The formation of precursor clay-coated grains in modern shallow marine and deep-water turbidite system analogues

In Ravenglass Estuary, average clay coat coverage was highest in areas with the highest EPS content such as mixed flats and mud flats. SEM analysis of sediment from Ravenglass Estuary showed clay particles are often attached to EPS strands secreted by diatoms. This shows that EPS acts as a binding material for clay particles on the surface of quartz grains. The clay coat synthesis experiments outlined in Chapter 3 found an increase in clay coat coverage with increasing EPS content where clay content was kept constant. However, clay coated grains were also formed in abiotic clay coat synthesis experiments which had no EPS present. Overall, EPS within shallow marine systems likely assists the formation of clay coats by acting as a binding agent between clay particles and quartz grains. However, EPS is not absolutely essential for the formation of clay coated grains and clay coated grains can form in the absence of EPS.

The presence of clay coated grains within Bute Inlet was low which makes it an unsuitable case study to try to understand how clay coated grains form in deep marine settings. Future studies should consider modern or ancient deep water case studies with a higher abundance of clay coated grains.

4.6 Conclusion

Clay-coated grains observed in modern analogue systems are acknowledged as representing precursors to chlorite-coated grains present in ancient deeply buried sandstone reservoirs (Jones, 2017; Wooldridge et al., 2017a; Wooldridge et al., 2018). Understanding the formation of clay-coated grains in modern analogue systems is pivotal to understanding and predicting the spatial distribution of clay-coated grains in ancient subsurface siliciclastic reservoirs.

This study found that deep water turbidite systems (Bute Inlet) contain a lower abundance of clay coated grains compared to shallow marine environments (Ravenglass Estuary).

This study found a strong relationship existed between clay coat coverage and total carbohydrate content and *chlorophyll-a* content (proxies for EPS) in Ravenglass Estuary. This indicates that as EPS content increases, clat coat coverage also increases. Total carbohydrate content and chlorophyll-a content also had a strong relationship with clay fraction across Ravenglass Estuary. The increase in clay coat coverage observed with an increase in EPS content may be purely due to a higher clay content (higher EPS content is typically found in areas with high clay content). The clay coat synthesis experiments outlined in chapter 3 found an increase in clay coat coverage with increasing EPS content where clay content was kept constant. Additional clay coat synthesis laboratory experiments should be carried out in the absence of EPS, where the clay content % is increased. This will help confirm if a higher clay content or higher EPS content is responsible for higher clay coat coverage in modern day analogues such as Ravenglass Estuary.

Chapter 5. The transformation of precursor clay coats during diagenesis

ABSTRACT: Clay coats, especially chlorite clay coats, inhibit the precipitation of quartz cement during diagenesis. This process preserves primary porosity, which increases the storage capacity of a reservoir. Chlorite clay coats are commonly formed via the transformation of precursor clay mineral coats, with increasing temperature and pressure during diagenesis. The transformation process involved in converting precursor clay coats to chlorite coats is complex and not fully understood.

This study investigates the transformation of modern-day clay-coated grains from Ravenglass Estuary through a series of temperature and pressure chamber experiments. Clay-coated grains present in Ravenglass Estuary are thought to represent precursors to chlorite-coated grains present in ancient sandstone reservoirs. Therefore, understanding how modern-day clay-coated grains transform during pressure chamber experiments provides an insight into the processes responsible for the formation of chlorite-coated grains in subsurface reservoirs. Understanding the formation of chlorite clay coats will improve the prediction of their distribution in subsurface reservoirs.

Unconsolidated sediment was placed in a hydrothermal pressure chamber at temperatures of 60, 90, 150 and 250°C with a set pressure of 10MPa. These temperatures were selected as published studies indicated that quartz overgrowth formation in natural reservoirs typically occurs between 60 and 150°C (Girard et al., 2001: Xi et al., 2015; Chen et al., 2024). An extreme temperature of 250°C was selected for experimental purposes to test how clay coats and quartz overgrowths interact at high geothermal temperatures.

The sediment samples were subject to SEM, thin section and QEMSCAN (automated mineralogy) analysis to determine changes in clay coat morphology and mineralogy with increasing temperature.

Average clay-coat coverage increased from 18% (starting surface material) to 22% during the 60°C pressure chamber experiment. No further increase in clay-coat

coverage was observed with increasing temperature (90, 150, 250°C experiments).SEM and EDS analysis of samples from the 60 and 90°C hydrothermal pressure chamber experiments indicate the presence and formation of authigenic needle-like mineral coats with an iron rich composition. Frost like authigenic clay mineral coatings were observed in samples from the 150 and 250°C pressure chamber experiments. These frost-like mineral coats had a composition similar to authigenic chlorite. Sodium silicate mineral coats, with a rosette morphology, similar to authigenic chlorite were formed in the hydrothermal pressure chamber experiments at 150 and 250°C.

This study confirms that authigenic chlorite can form from precursor clay coats taken from modern day analogues such as Ravenglass Estuary at temperatures of 150°C and above. The rearrangement of detrital clay mineral coats appears to occur at temperatures between ambient and 60°C, with no further increase in clay-coat coverage with increasing temperature.

5.1 Introduction

In subsurface sandstone reservoirs, quartz overgrowths are the main diagenetic phase responsible for the reduction of porosity and permeability, which drastically reduces the volume of recoverable hydrocarbons (King, 1992; Bloch et al., 2002; Lander et al., 2008). Various coatings developed on the surface of detrital quartz grains, including authigenic microcrystalline quartz (Ramm and Bjørlykke, 1994; Aase et al., 1996) and more commonly clay coats (Bloch et al., 2002; Anjos et al., 2003) inhibit the precipitation of diagenetic quartz cement during burial.

Chlorite is the most common authigenic clay mineral associated with inhibiting the formation of diagenetic quartz cement (Bloch et al., 2002; Dowey et al., 2012; Cao et al., 2018). However, smectite, mixed-layer illite/smectite, illite, and mixed layer chlorite/smectite clay coatings also inhibit the formation for quartz overgrowths (Pittman et al., 1992; Storvoll et al., 2002; Haile et al., 2015).

Chlorite coats prevent the formation of quartz overgrowths by blocking nucleation sites on the surface of detrital grains, where the key factor controlling the inhibition of quartz cementation is the completeness of coats (Billault et al., 2003; Lander et al., 2008).

Previous studies of chlorite-coated grains in reservoirs indicate a precursor clay mineral such as berthierine or smectite is essential for chlorite coat formation, where chlorite forms through the thermal alteration of the precursor clay mineral with increasing temperature and pressure (Ehrenberg, 1993; Ryan and Reynolds, 1996; Anjos et al., 2003). Authigenic chlorite may also form due to direct precipitation from a solution, in the absence of a precursor clay coat via the dissolution and recrystallization of detrital grains or volcanic rock fragments (Humphrey et al.,1989; Haile et al., 2015).

Authigenic smectite and chlorite have been grown on clean feldspar and quartz grains under controlled laboratory conditions in a series of high temperature (100-150°C) hydrothermal pressure chamber experiments conducted by Haile et al. (2015).

Artificial chlorite-coated grains, similar to naturally occurring chlorite-coated grains have also been synthesised by placing berthierine-coated lithified sandstones from the Oseberg field, Norwegian Continental Shelf in a hydrothermal pressure chamber, during an experimental study carried out by Aagaard et al. (2000). Little research has been conducted on the transformation of precursor clay-coated sediment during lithification and diagenesis.

The focus of this study is to determine whether authigenic grain coating chlorite can be synthesised from modern day clay-coated sediment using a hydrothermal pressure chamber. This study aims to further understand the stages involved in the transformation of precursor clay coats during burial and diagenesis, which cannot be uncovered using traditional approaches which involve studying chlorite-coated grains in ancient sandstone reservoirs.

5.1.1 Research theme and questions

Chapter 3 focused on testing the relationship between grain clay coat formation and biofilms using a series of abiotic and biotic laboratory experiments. Clay coat grain

coverage was found to increase as the concentration of EPS increased. This indicates that biofilms enhanced the formation of clay coated grains in the laboratory experiments by forming an adhesive surface on quartz grains.

Chapter 4 studied the interaction of EPS and clay coats in two modern analogue settings (Bute Inlet, British Columbia and Ravenglass Estuary, UK). A lack of clay coated grains were observed in Bute Inlet (a deep-water turbidity system). Clay coated grains were heterogenous distributed across Ravenglass Estuary. Clay-coat grain coverage was highest in mud and mixed flats and lowest in the tidal inlet. Clay coat grain coverage in Ravenglass Estuary showed a significant positive relationship with EPS concentration. Ravenglass Estuary is thought to serve as a modern-day analogue for ancient shallow marine clay coated reservoirs (Wooldridge et al., 2017).

This chapter aims to study how clay coated sediment from Ravenglass Estuary transforms under temperature and pressure via a series of hydrothermal pressure chamber experiments designed to represent burial and diagenesis.

This Chapter focuses on the research theme “The transformation of precursor clay-coated grains during burial and diagenesis” which is fully outlined in chapter 1.7.2. The key research questions to be addressed in this chapter are:

- How do precursor clay mineral coats transform during diagenesis to form authigenic clay mineral coats?
- Are authigenic clay coats formed during pressure chamber experiments comparable to authigenic clay coats present in natural settings?

5.2 Materials and methods

This section provides a summary of the methods used in this chapter. A more detailed description of methodology can be found in Chapter 2.

5.2.1 Sediment sampling

Bulk surface sediment (top 2 cm) was collected from a tidal bar located on the arm of the River Esk (Latitude 54.338797, Longitude -3.410097) in Ravenglass Estuary (Figure 5.1). A tidal bar was selected as a study site due to previous studies indicating that tidal bars within estuarine conditions have a clay content which is sufficient to form clay coats and not too high to result in pore filling clay (Virolle et al., 2019). Ravenglass is a shallow, well mixed, macro-tidal estuary in northwest England, UK. The estuary has a quartzo-feldspathic rich sediment source which is similar to many ancient chlorite-coated sandstone reservoirs, such as tidally influenced reservoir units of the Early Jurassic Tilje Formation, Smørbukk Field, Halten Terrace, mid-Norway (Martinius et al., 2005). Clay-coated grains have been well studied in sediment from Ravenglass Estuary with previous studies hypothesising that clay-coated grains represent precursors to chlorite-coated grains found in ancient sandstone reservoirs (Jones, 2017; Wooldridge et al., 2017a).

5.2.2 Experiment set up

Experiments were set up as depicted in Figure 2.16 in Chapter 2. Experiments were run under closed conditions, where samples were subjected to cooling and subsampling after each experimental run. Each experiment was run for 3 days. The experiments were limited to a maximum of 10MPa (equivalent to roughly 500m of burial). The focus of this study is the effect that increasing temperature has on the transformation of precursor clay-coated grains. A total of four experiments were carried out with temperatures of 60°C, 90°C, 150°C and 250°C. A control sample consisted of surface sediment from the tidal bar in Ravenglass Estuary which was not exposed to any pressure or temperature changes.

The starting sediment samples were placed into a steel mesh bag and added to the pressure chamber vessel, along with 5 grams of silica beads. Synthetic formation water was prepared for each experiment by mixing 10ml of Na_2CO_3 with 90ml of deionised water to form a 0.1M solution. The formation water composition used in the pressure chamber experiments was selected based on the composition of formation waters for

Jurassic sandstone reservoirs in the North Sea and Halten Terrace (Egeberg and Aagaard, 1989; Aagaard et al., 1992).

This study focused on clastic sediment where silica for quartz cement is mainly formed via the interaction of silica saturated diagenetic fluids and detrital quartz grains (Bloch et al., 2002). Studies of carbonate lithologies indicate that quartz cement is mainly formed via the interaction of biogenic silica dissolution (e.g., the dissolution of sponge spicules) and the interaction of clay minerals (Ohiara et al., 2023).

5.2.3 Thin section analysis

Thin sections were prepared for the pre-experiment and post-experiment sediment samples by Independent Petrographic Services (Aberdeen, United Kingdom). Thin sections were analysed at low and high magnification to record clay-coat coverage and morphology. The clay-coat grain coverage was quantified via the method used by Wooldridge et al. (2017a). Clay coat morphologies were described using the scheme set out in Chapter 2 in Table 2.1.



Figure 5.1. Map showing location of sampling site, Ravenglass Estuary, UK (map generated in ArcGIS Pro version 3.1).

5.2.4 Automated mineralogy

Thin sections were carbon-coated and subjected to automated mineralogy (QEMSCAN) analysis to determine the mineralogy of clay-coated grains and identify any changes in mineralogy with increasing temperature. QEMCAN analysis was performed using a FEI QEMSCAN 650F Scanning Magnetic Microscope (Thermo Fisher Scientific, Waltham, Massachusetts, USA) at CGG Robertson, Llandudno.

5.2.5 SEM and EDS analysis

SEM analysis was performed using a TESCAN Vega 3LMU Scanning Electron Microscope (TESCAN, Brno, Czech Republic) at Newcastle University Medical School. Experiment samples and a control sample were mounted onto aluminium stubs, dried and gold-coated prior to SEM analysis to image clay-coat morphologies. Energy Dispersive X-Ray Spectroscopy (EDS) was performed to provide an indication of the likely mineralogy of clay coats. EDS is an analysis which is used to determine the surface elemental composition of a sample. The elemental data can then be used to infer the likely mineral of a sample by considering the elemental composition of different rock forming minerals. In this study, point EDS analysis was used which involves analysing a specific point on an individual grain or crystal. This method was chosen to determine the mineralogy of individual authigenic cement within the samples.

5.2.5 Geochemical modelling

Geochemical modelling was conducted, based on solubility indices, the starting material composition, and the experimental conditions (temperature and pressure). Modelling was carried out to predict the minerals likely to form during the different pressure chamber experiments. Further details of the method used for geochemical modelling can be found in Chapter 2.11.1.

5.3 Results

5.3.1 Surface sediment

Thin section (Figure 5.2) and SEM analysis (Figure 5.3A) of the starting material indicate that clay-coats were present in the form of clay bridges, clumped and discontinuous coatings attached to quartz grains. EDS signatures of clay minerals suggest an iron, magnesium and aluminium rich composition (Figure 5.3B). QEMSCAN analysis revealed the starting material (Figure 5.4 and Table 5.1) had a bulk mineralogy dominated by quartz (80%), K-feldspar (7%) and plagioclase feldspar (5%). Clay minerals made up 5% of the bulk mineralogy with precursor clay coats consisting of a mixture of illite (2%), smectite (1%), kaolinite (1%) and chlorite (1%). The sediment was found to have an average clay-coat grain coverage of 18% (Table 5.1).

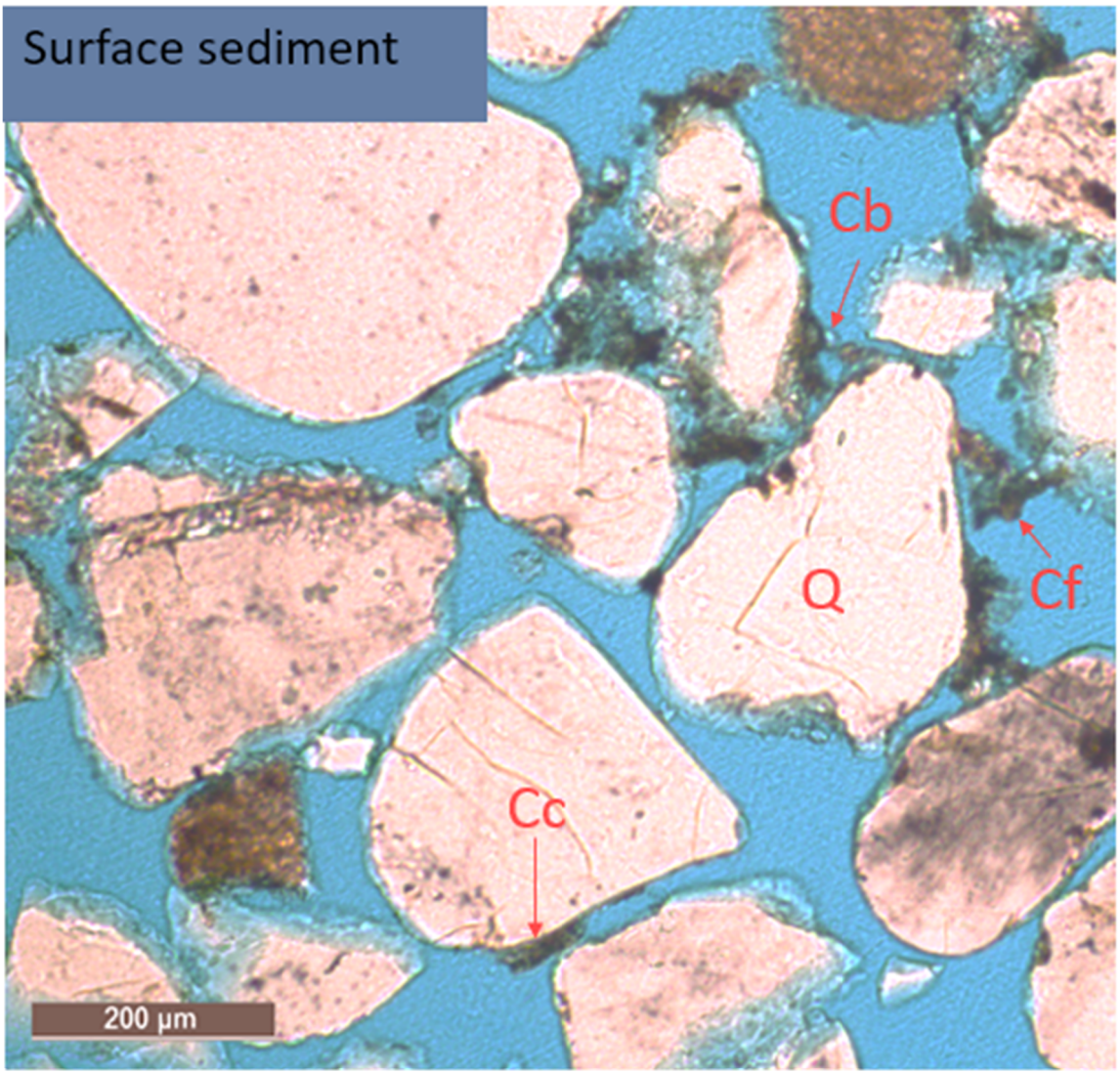


Figure 5.2. Thin section of starting material used in the pressure chamber experiments. Q = quartz, Cc = clay coating, Cb = clay bridge, Cf = clumped clay coat.

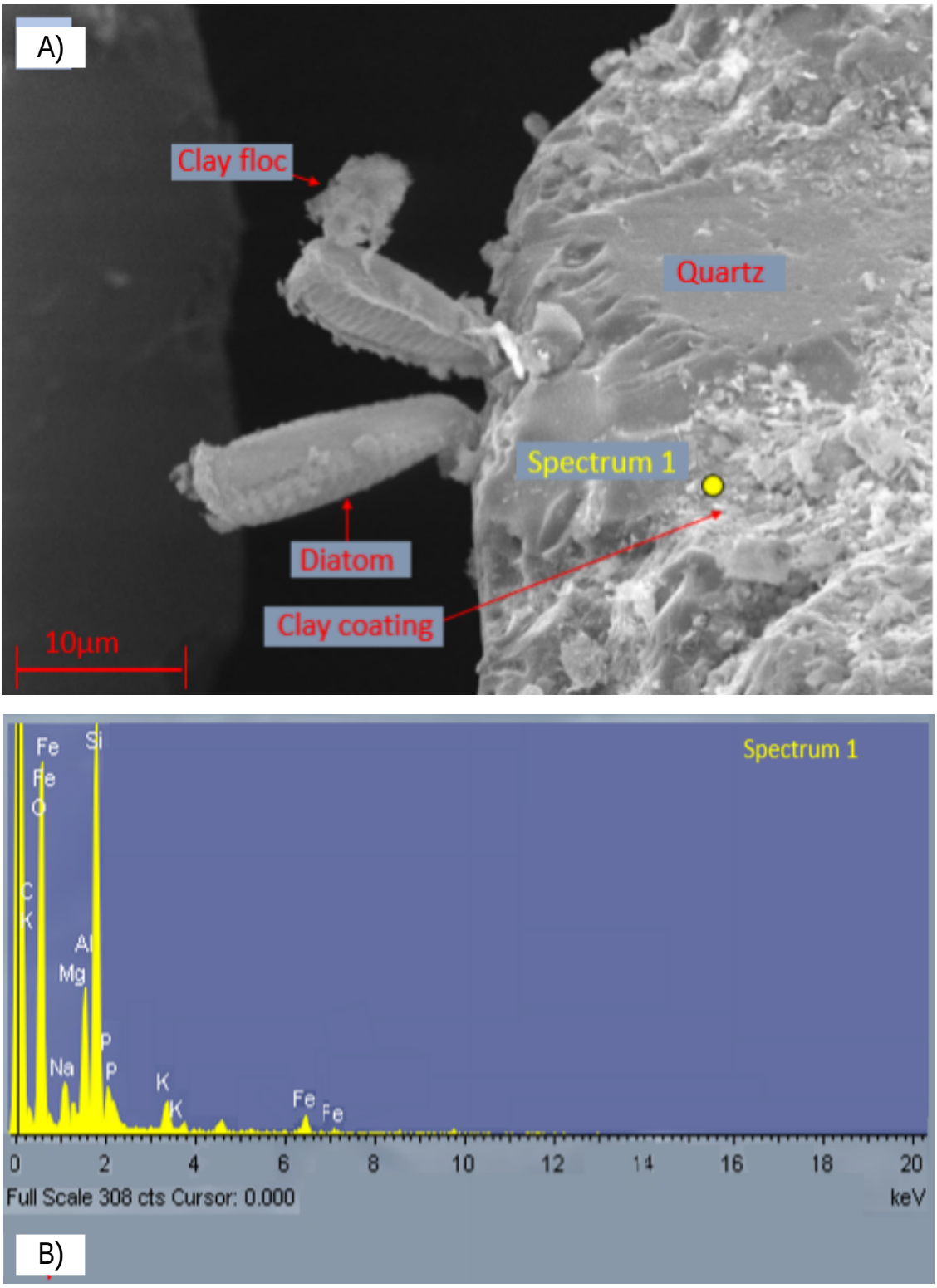


Figure 5.3. A) SEM and B) EDS signature of clay-coated material used in the pressure chamber experiments.

Sample	Bulk mineralogy							Clay coat coverage (%)
	Quartz (%)	K-Feldspar (%)	Plagioclase Feldspar (%)	Illite (%)	Smectite (%)	Kaolinite (%)	Chlorite (%)	
Surface	80%	70%	5%	2%	1%	1%	1%	18%
60°C, 10MPa	79%	6%	7%	2%	<1%	1%	1%	21%
90°C, 10MPa	82%	7%	4%	1%	<1%	1%	1%	20%
150°C, 10MPa	79%	7%	5%	2%	1%	1%	1%	23%
250 °C, 10MPa	81%	4%	6%	1%	1%	1%	1%	21%

Table 5.1. Summary of bulk mineralogy and average clay coat coverage.

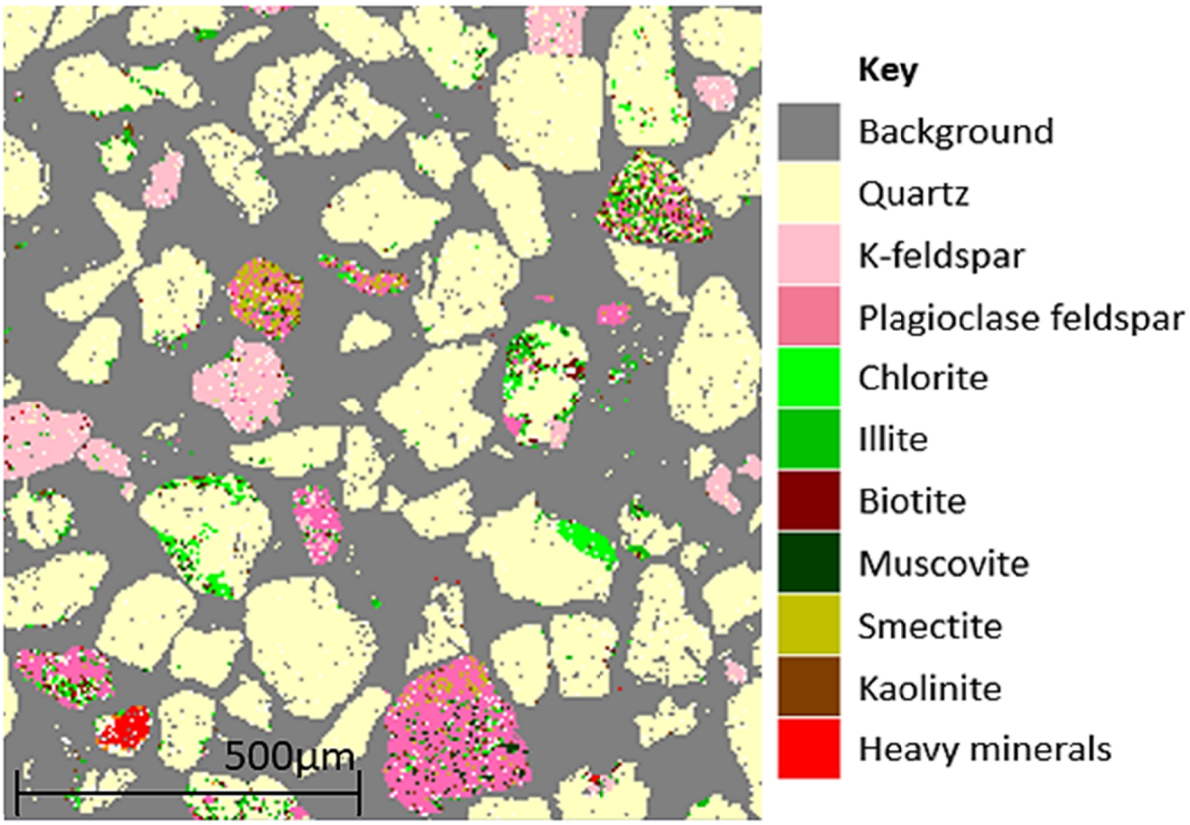


Figure 5.4. QEMSCAN image of the starting material used in pressure chamber experiments.

5.3.2 60°C, 10MPa Experiment

SEM analysis of sediment from the 60°C pressure chamber experiments (Figure 5.5A) reveals the presence of long needle like mineral coats, developed on the surface of quartz grains, with an EDS composition (Figure 5.5B) which is rich in iron. QEMSCAN analysis (Figure 5.6) indicates little to no significant change in bulk mineralogy compared to the starting material (Table 5.1). Average clay-coat coverage increased from 18% (starting surface material) to 21% during the 60°C pressure chamber experiment (Table 5.1).

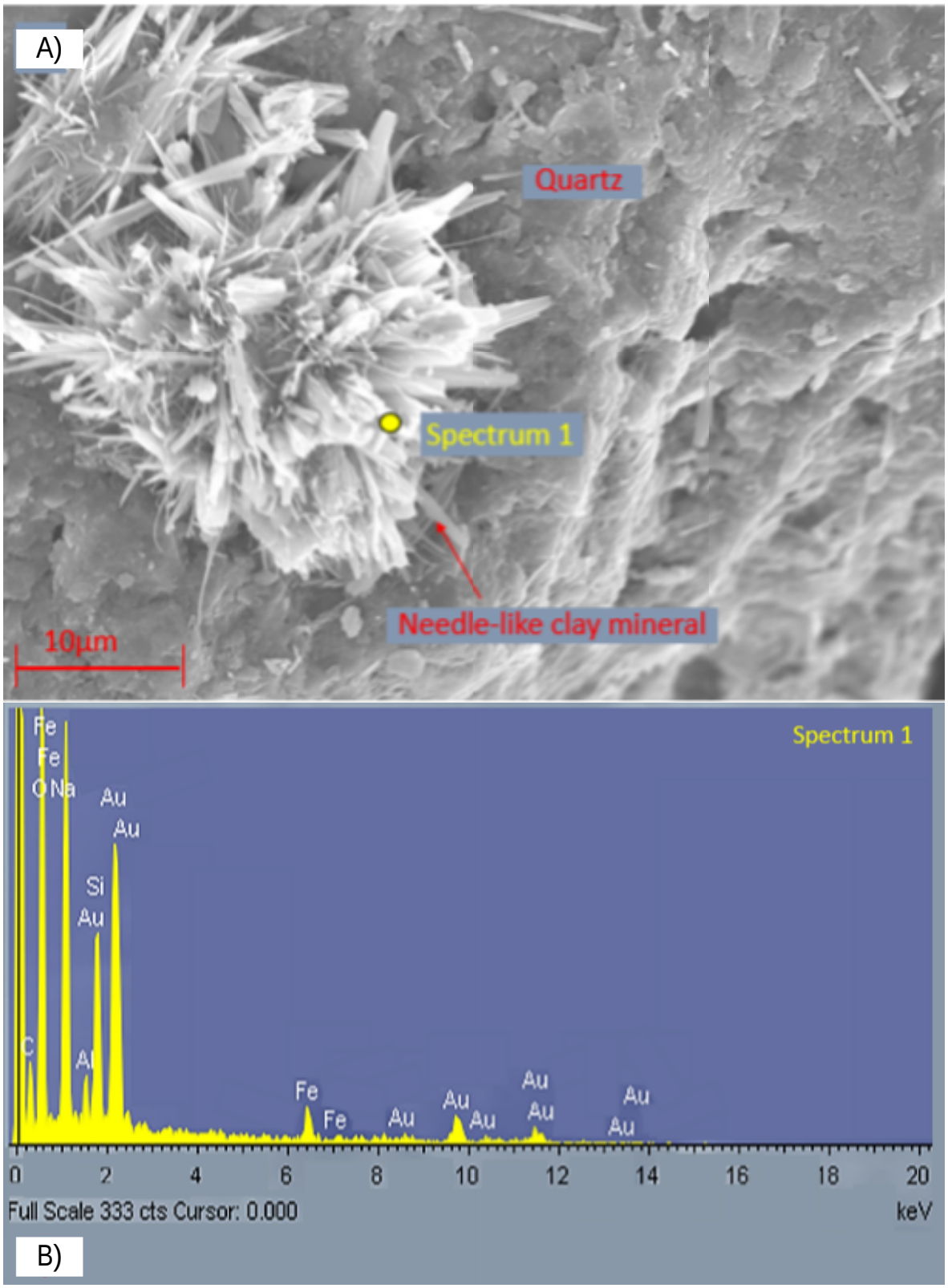


Figure 5.5. A) SEM and B) EDS signature of the 60°C pressure chamber experiment sample.

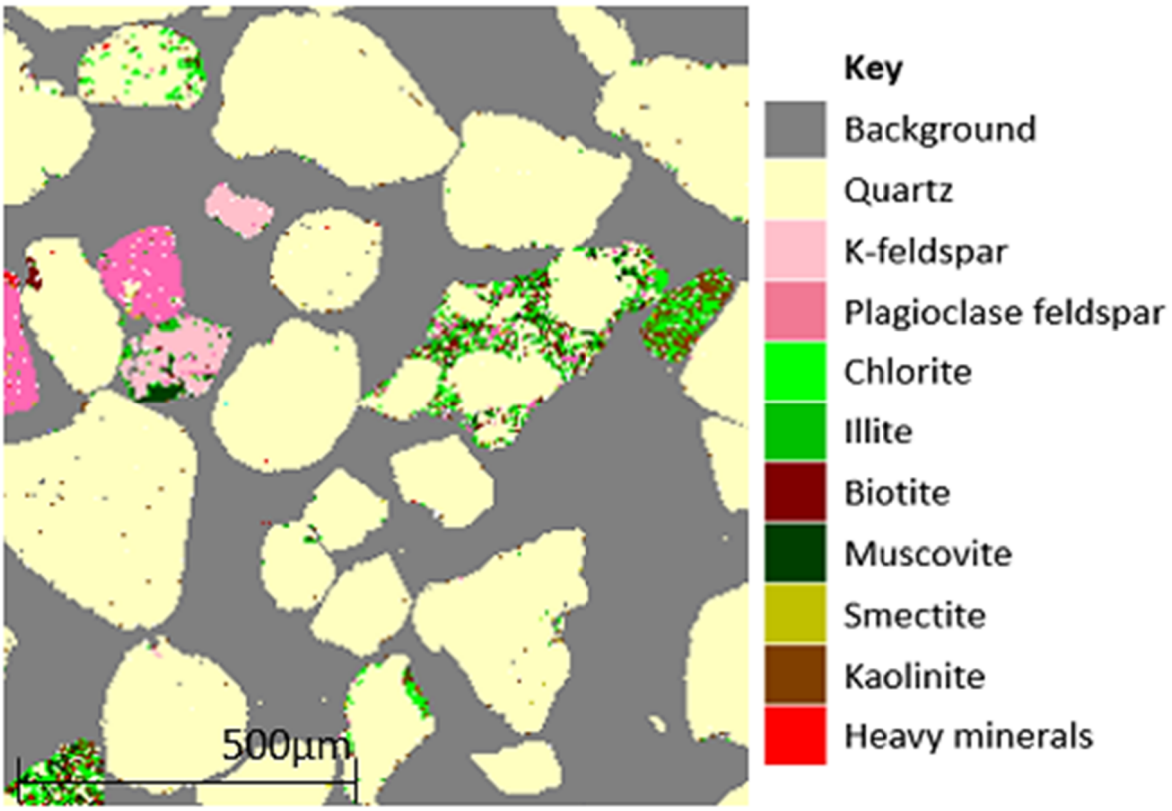


Figure 5.6. QEMSCAN image of the 60°C pressure chamber experiment sample.

5.3.3 90°C, 10MPa experiment

SEM analysis of the sediment from the 90°C pressure chamber experiment (Figure 5.7A) shows the same needle-like mineral coats as observed in the 60°C experiments and the detrital clay clumped coats. EDS analysis (Figure 5.7B) of detrital clay clumped coat indicate an iron, aluminium and magnesium rich composition.

QEMSCAN analysis (Figure 5.8) indicates little change in bulk mineralogy compared to the starting material (Table 5.1). Average clay-coat grain coverage (%) of sediment from the 90°C pressure chamber experiment showed little to no change from the average clay-coat coverage observed in the 60°C pressure chamber experiment (Table 5.1).

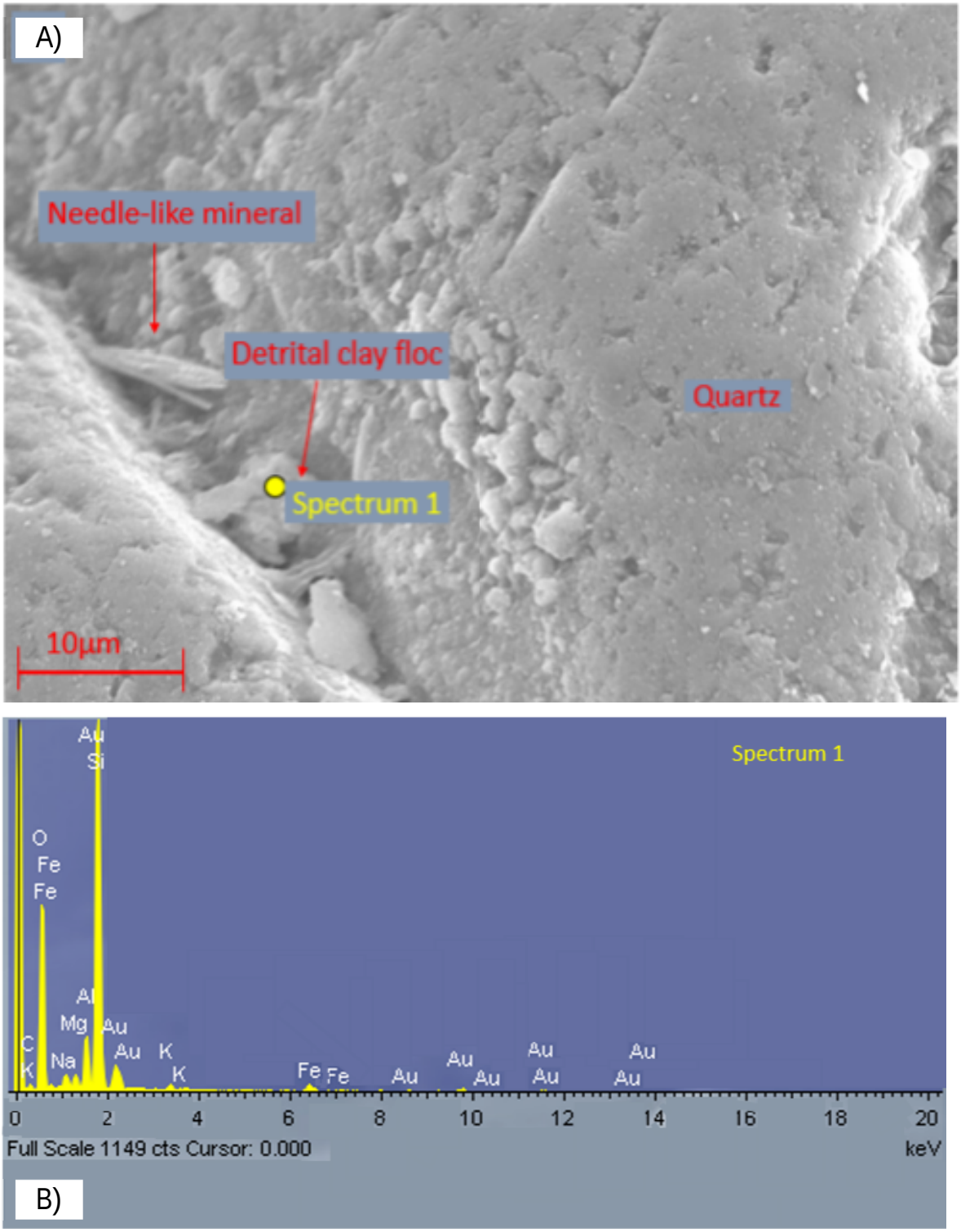


Figure 5.7. A) SEM and B) EDS signature of the 90°C pressure chamber experiment sample.

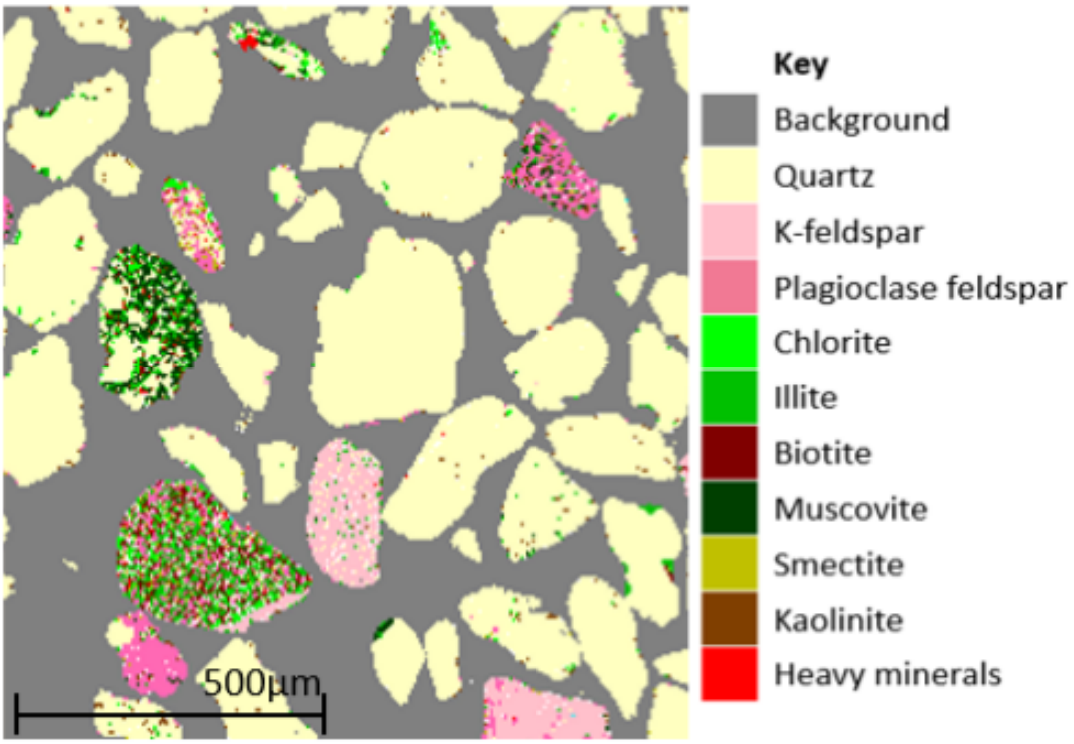


Figure 5.8. QEMSCAN image of the 90°C pressure chamber experiment sample.

5.3.4 150°C, 10MPa experiment

SEM analysis of the samples from the 150°C experiment indicates the presence of neoformed mineral coats on the surface of quartz grains, with a frost like morphology, consisting of interlocking individual crystals which are less than 1nm long (Figure 5.9A). EDS performed on the frost-like mineral coats (Figure 5.9B) indicates an iron, magnesium and aluminium content which is similar to authigenic chlorite. Quartz overgrowths appear to have formed in areas on the surface of detrital quartz grains which are not coated with the frost like clay coating. Needle like iron rich minerals, similar to those present in samples from the 60 and 90°C pressure chamber experiments were also observed. The QEMSCAN analysis indicates no significant change in clay or bulk mineralogy (Table 5.1). The average clay-coat grain coverage (%) of sediment from the 150°C pressure chamber experiment was similar to the average clay-coat coverage observed in the 90°C and 60°C pressure chamber experiments (Table 5.1).

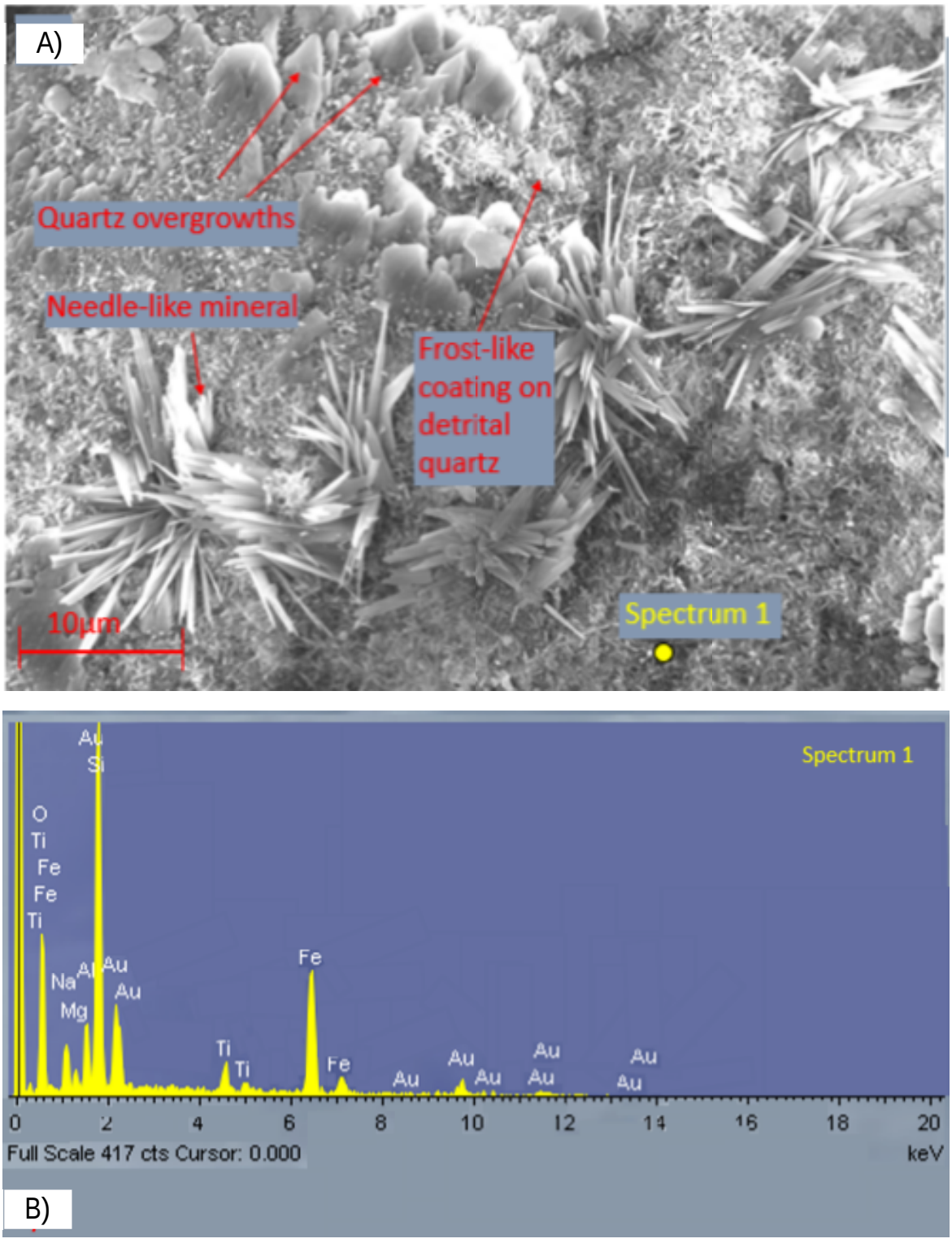


Figure 5.9. A) SEM and B) EDS signature of the 150°C pressure chamber experiment sample.

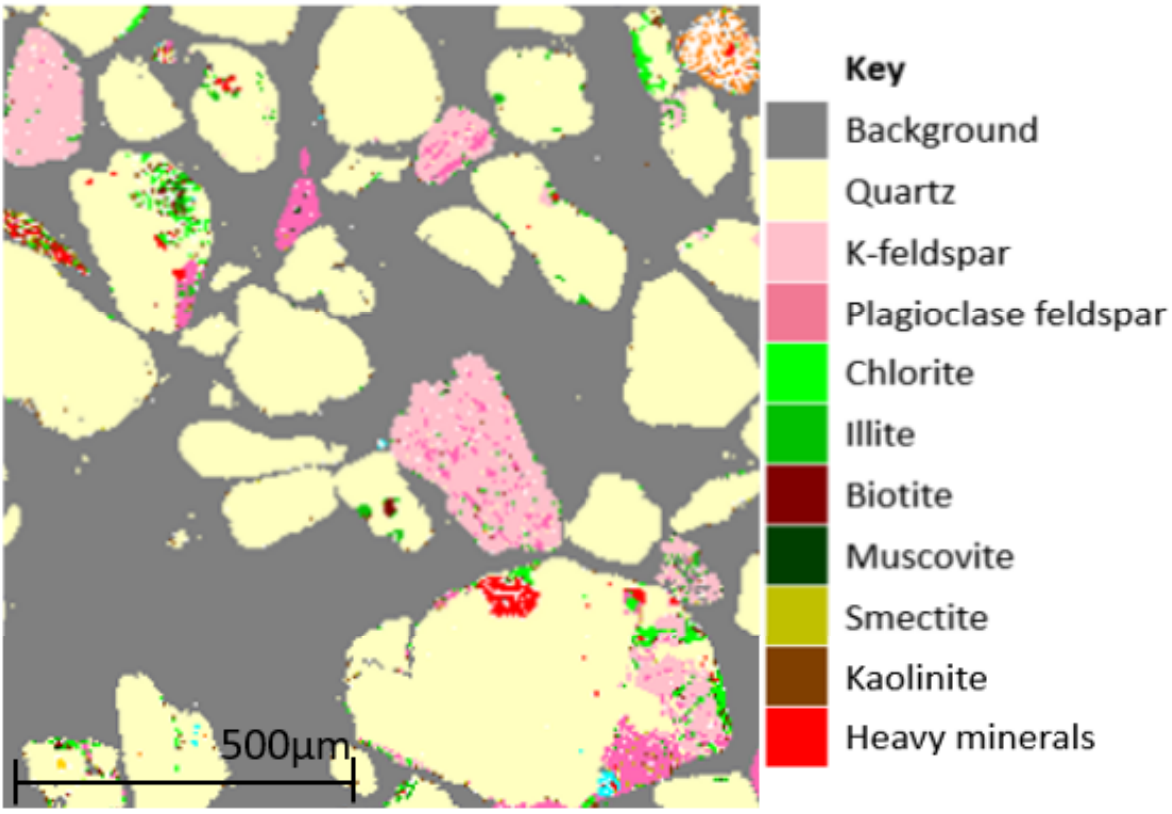


Figure 5.10. QEMSCAN image of 150°C pressure chamber experiment sample.

5.3.5 250°C, 10MPa experiment

SEM analysis of the sediment from the 250°C pressure chamber experiment (Figure 5.11A) indicates the presence of the same needle-like minerals, present in samples from the 60, 90 and 150°C pressure chamber experiments. Frost-like clay mineral coatings, present in the 150°C pressure chamber experiment were also observed.

The sample from the 250°C pressure chamber experiment also contained mineral coats with a rosette morphology (Figure 5.11A), similar in morphology to authigenic chlorite found in ancient sandstone reservoirs (Ehrenberg, 1993: Schmid et al., 2004). Repeat EDS analysis (Figure 5.11B) of the rosette mineral indicate a high content of calcium and sodium with very little magnesium, iron and aluminium. The low magnesium, iron and aluminium content indicates the rosette mineral observed in the sample is not chlorite.

The QEMSCAN analysis (Figure 5.12) indicates no significant change in clay or bulk mineralogy from the starting surface material (Table 5.1). The average clay-coat grain coverage (%) of the sediment from the 250°C pressure chamber experiment showed no to little change to the average clay-coat coverage observed in the 150, 90 and 60°C pressure chamber experiments (Table 5.1).

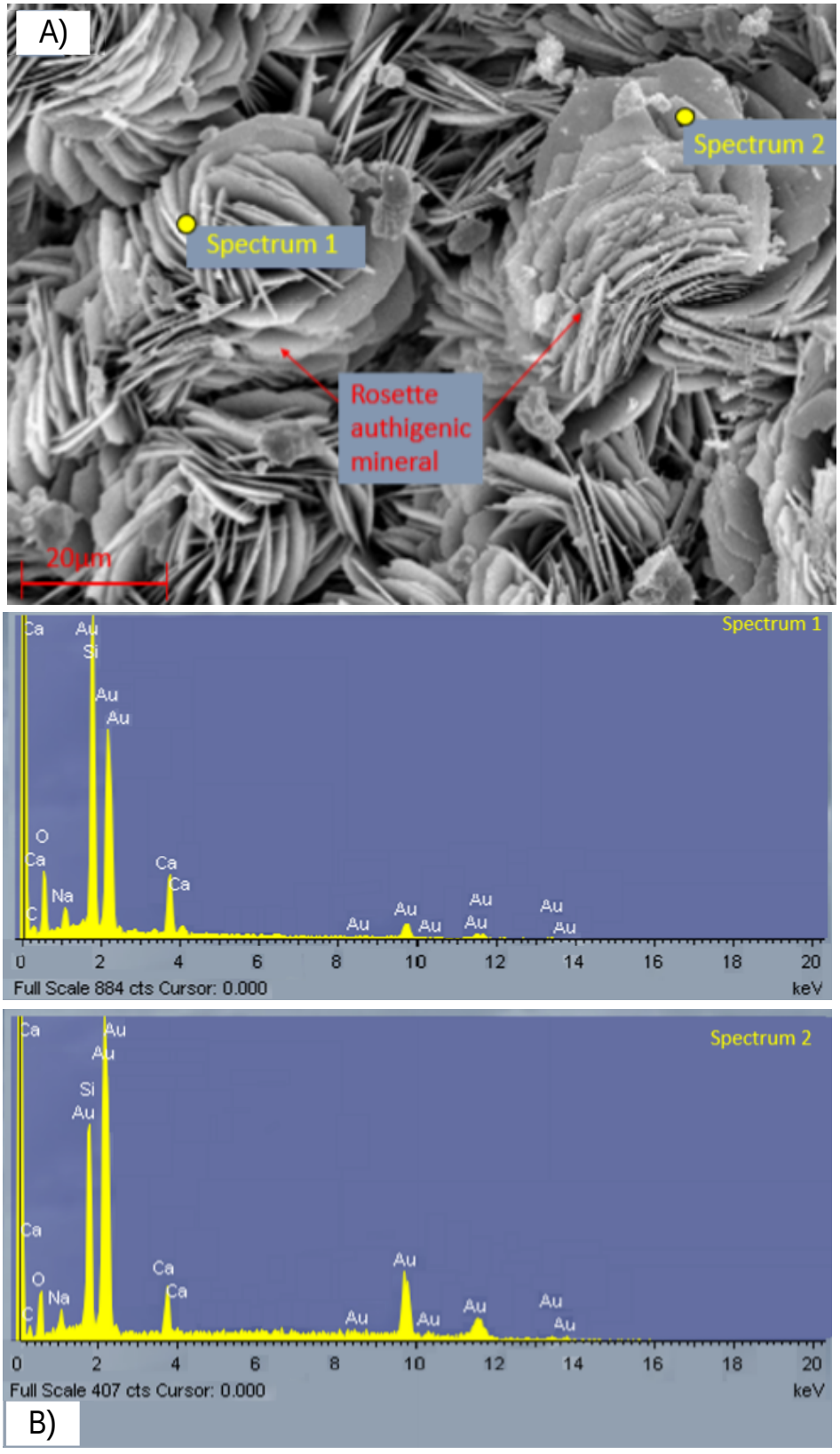


Figure 5.11. A) SEM and B) EDS signatures of rosette mineral formed in 250°C pressure chamber experiment.

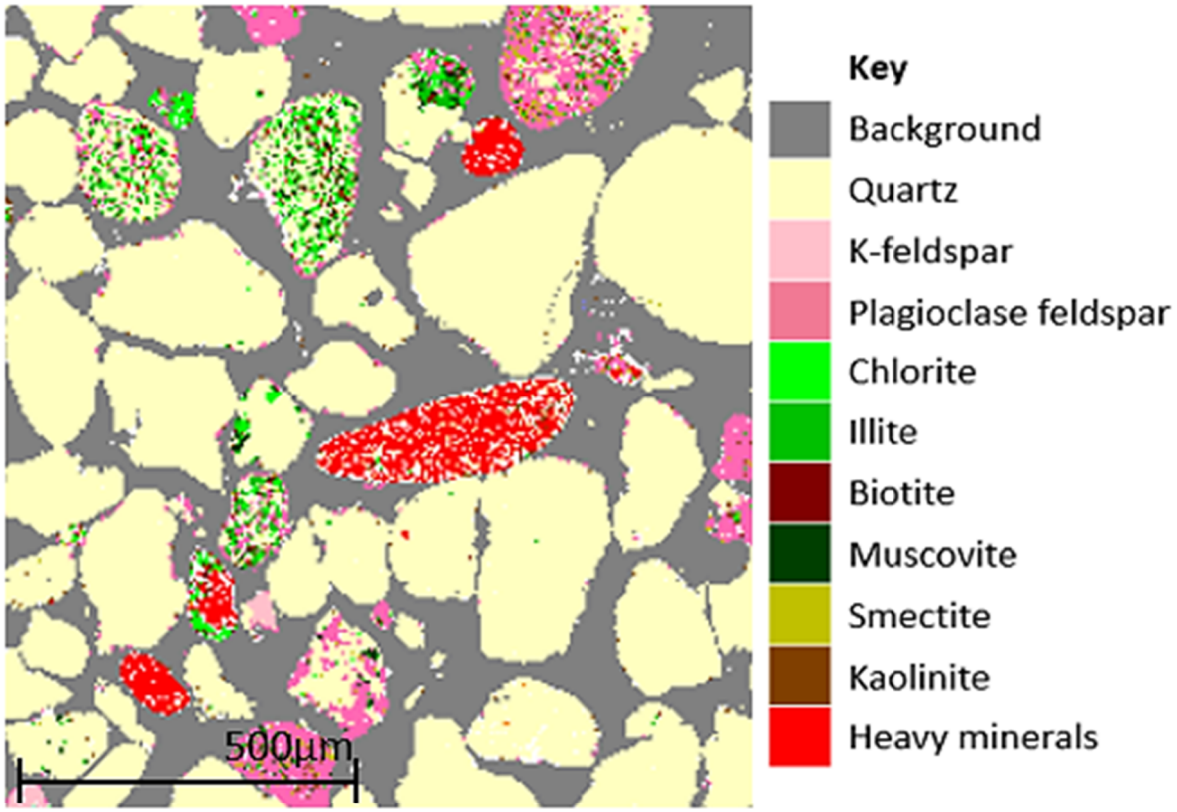


Figure 5.12. QEMSCAN image of 250°C pressure chamber experiment sample.

5.3.6 Geochemical modelling

Saturation indices (SI) were calculated using the minerology of the starting materials, background solution, and the experimental conditions to determine if the conditions were favourable for the formation of new mineral phases. For the models the solution chemistry was held in equilibrium with the most abundant mineral phases identified by QEMSCAN (anorthite, adularia, chlorite 7A, illite, and amorphous silica). A log SI value great than zero indicate the conditions are thermodynamically favorable for the formation of that phase, equaling zero the system is in equilibrium, and less than zero the conditions are unfavorable for the formation of the given phase. Typically, phases are assumed to be in equilibrium if within ± 1 Log SI of zero, due to modeling uncertainty. Broadly speaking the minerals log SI values greater than zero fall into five classes: pure silica silicates, silicates, carbonates, clays, and zeolites.

From 60 to 250°C the Log SI for chalcedony, cristobalite and quartz all were greater than zero, with quartz having the highest Log SI across the modelled experimental range (Figure 5.13A). All silica phases show a decrease in their Log Si with increasing temperature and only quartz has a Log SI exceeding 1 (only at 60°C). The relatively low log SI values (with nearly all values within 1 Log SI of zero) indicate a low probability for the formation of pure silicate phases.

Across the silicate mineral phases, tremolite ($Ca_2Mg_5Si_8O_{22}(OH)_2$) had a log SI that exceed both talc ($Mg_3Si_4O_{10}(OH)_2$) and magadiite by 9 orders of magnitude at 60 °C and exceeded magadiite until the experimental temperature exceeded 150 °C (Figure 5.13B). However, the results from the EDS spectra across all experimental settings show that for only 1 of the 11 spectra, Mg has a Mg to Ca ratio greater than 1 making the formation of tremolite unlikely. Across experiments (60-250°C), Magadiite ($NaSi_7O_{13}(OH)_3{:}3H_2O$) Log SI increased from 4.6 to 8.41 with increasing temperature. A total of 27 of 45 EDS spectra indicated Si in the absence of Al, which is a strong indicator of the formation of silicate minerals. Of those 27 spectra, ten spectra also had Na which gives circumstantial evidence for the formation of magadiite. Magadiite is a white hydrous sodium silicate mineral, which commonly precipitates from alkali brines and is thought to serve as a precursor to bedded chert (Eugster, 1967). Additionally, magadiite has also been found in altered volcanic rocks located in Trinity County, California (McAtee et al., 1968). The Na_2Ca_3 background solution and abundance of volcanically derived feldspars indicate that similar conditions were present in the experiments to where magadiite forms in the natural environment. Magadiite usually forms as thin platy crystals, which may aggregate to form spherulites with internal layering. Magadiite present in sediment from the northern bank of Lake Chad (Sebag et al., 2000) is similar in morphology and composition to the unidentified mineral formed in the high temperature pressure chamber experiments (Figure 5.15). Therefore, the rosette mineral formed in the high temperature pressure chamber experiments is likely a sodium silicate, possible magadiite.

Aragonite, calcite, and dolomite all had log SI values greater than zero for experiments with temperatures lower than 150 °C (Figure 5.14A). Of the 22 EDS spectra with C, only 7 also indicated the presence of Ca. Additionally, 5 of those 7 were from experiments

exceeding 150 °C, indicating that the carbonate minerals found were more likely detrital than having formed during the experiments.

The Log SI values were positive for kaolinite, Ca montmorillonite and chlorite 14A-Mg across the entire experimental temperature range (Figure 5.14B). Ca montmorillonite had the lowest Log SI and decreased from 1.26 at 60°C to 0.86 at 250°C. Chlorite 14A-Mg, had the highest Log SI at 60°C of the clay minerals but show an increase in solubility with increasing temperature, similar to Ca montmorillonite. In contrast to the other two clays, kaolinite's Log SI increased with increasing temperature and kaolinite had the highest Log SI of the clay minerals between 150 and 250°C. The models indicate that there is a transition in the most thermodynamically favourable clay species to form with increasing temperature which could correspond to an important transition point for clay coat formation.

The final class of minerals predicted to form during the experiments was zeolites, which are commonly known to form during the diagenesis and metamorphosis of feldspathic sedimentary systems, particularly when alkaline fluids are present (Gottardi, 1989; Wang et al., 2023). Three zeolites had Log SI values greater than 0 indicating that they were favourable to form (Figure 5.14C). At 60°C leonhardite ($Ca_2Al_4Si_8O_{24}$:$7H_2O$) has the highest Log SI at 15.3, however, leonhardite is the dehydrated form of laumontite ($CaAl_2Si_4O_{12}$:$4H_2O$) and is unlikely to be present in an aqueous system. Laumontite is a zeolite commonly found in many clastic reservoirs and even used as an indicator of low to intermediate diagenesis (Ullmer-Scholle, 2014). Laumontite had a positive but decreasing Log SI from 60 to 150°C, which is the commonly agreed temperature range over which laumontite is stable in environmental systems (Jove and Hacker, 1997). The final zeolite predicted to form was pyrophyllite ($Al_2Si_4O_{10}(OH)_2$), which was the only zeolite with increasing stability with increasing temperature. Despite being commonly predicted in SI modelling, pyrophyllite is typically only viewed to be formed at temperatures above 200°C (Nieto et al., 2020).

One short coming to this geochemical modelling approach was the lack of minerals containing iron, which was observed to be 1.12 to 12.9% by mass percent in 17 of 45 spot locations analyzed by EDS. The lack of initial minerals containing iron as

constituents means that iron and iron phases were not considered in the system that was modelled and could mean that phases that formed were not considered.

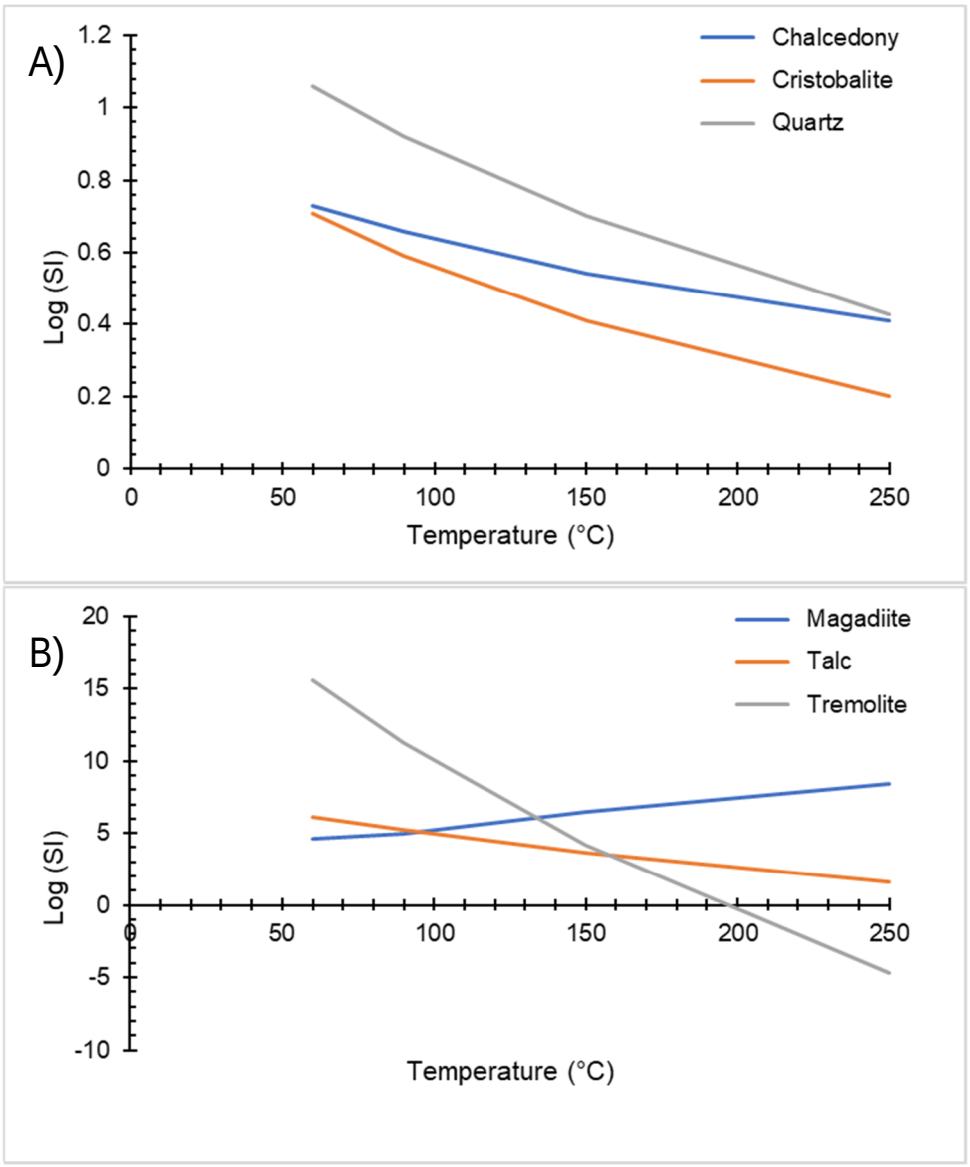


Figure 5.13. Saturation indices of A) pure silica silicates and B) silicates that could have formed during the experiments.

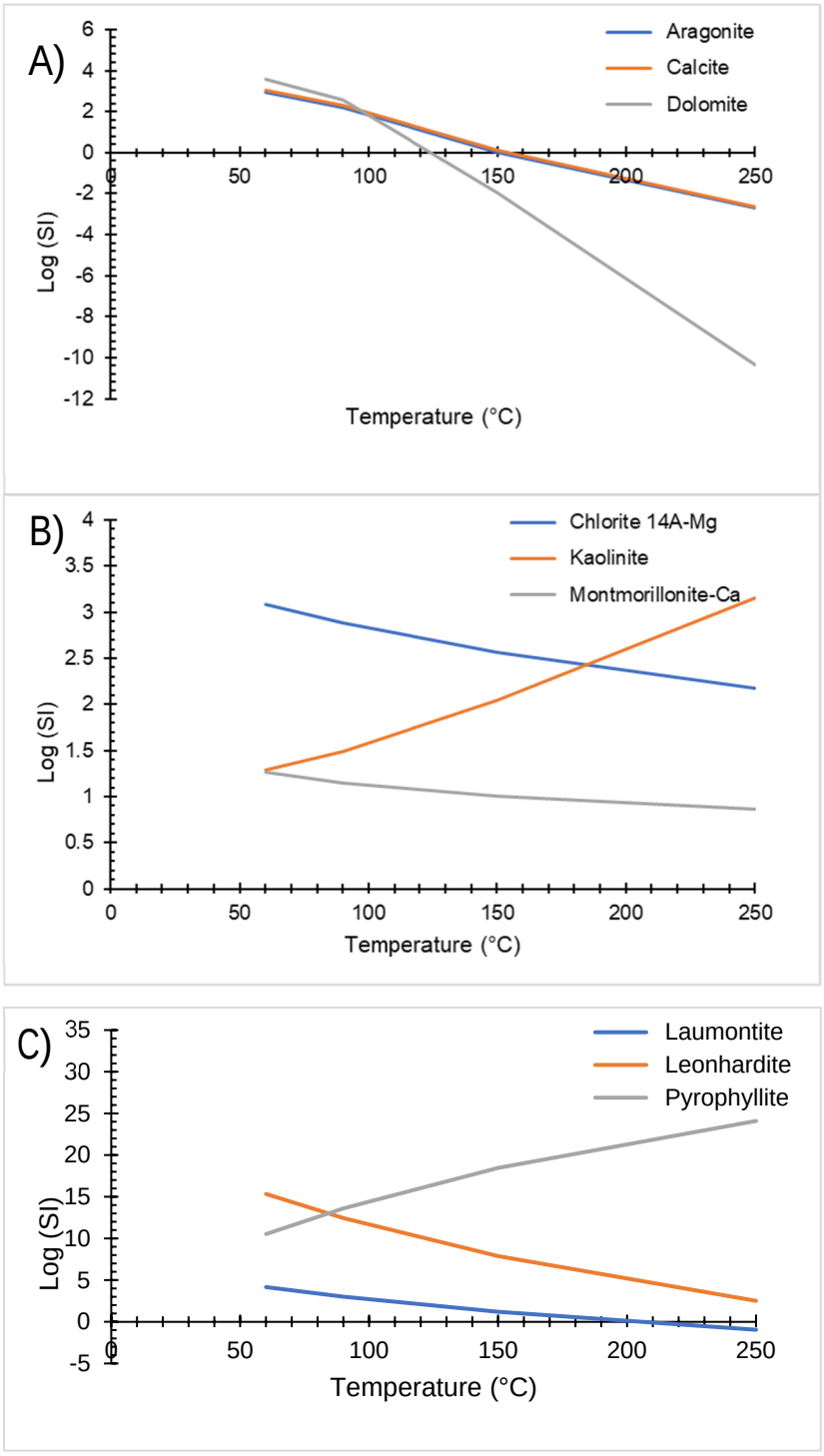


Figure 5.14. Saturation indices of A) carbonates, B) clays, and C) zeolites that could have formed during the experiments.

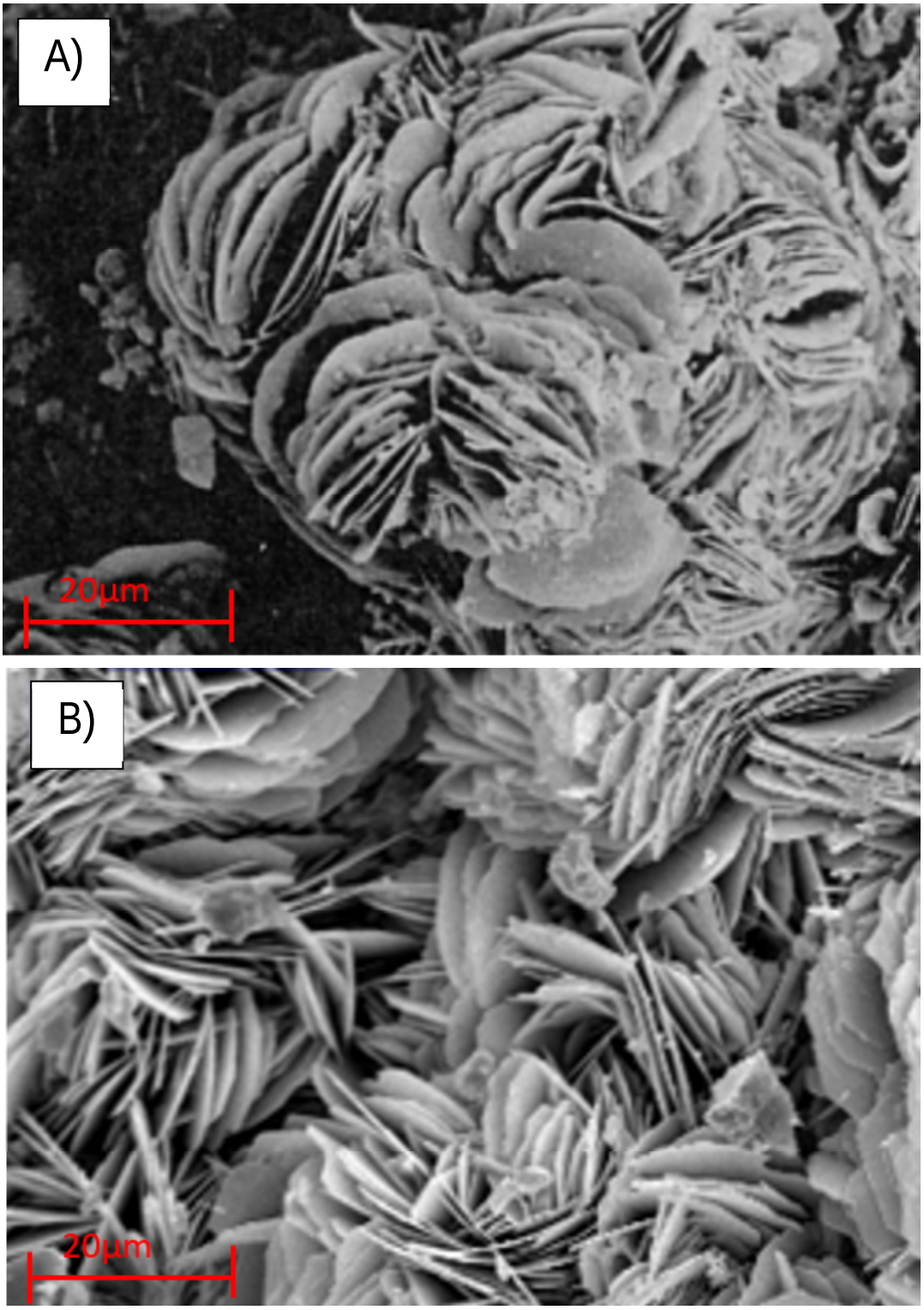


Figure 5.15. A) Magadiite present in Lake Chad sediment (Sebag et al., 2001) B) Sodium silicate formed during 250°C pressure chamber experiment.

5.4 Discussion

This Chapter focused on the research theme “The transformation of precursor clay-coated grains during burial and diagenesis” which is fully outlined in chapter 1.7.2. The key research questions addressed in this chapter were “How do precursor clay mineral coats transform during diagenesis to form authigenic clay mineral coats?” and “Are authigenic clay coats formed during pressure chamber experiments comparable to authigenic clay coats present in natural settings?”.

5.4.1 The transformation of precursor clay-coats

The frost-like mineral formed in the mid and high temperature experiments (150°C and 250°C) has been interpreted as authigenic chlorite based on EDS and QEMSCAN analysis. The authigenic mineral with the rosette morphology was initially thought to be chlorite based on morphology, where chlorite similar in appearance and morphology was formed in other pressure chamber experiments (Aagaard et al., 2000; Haile et al., 2015). However, the EDS analysis of this mineral indicates a composition which is dominated by calcium, sodium and silica with little to no iron and magnesium. The rosette mineral may be a calcium silicate or gypsum formed as a biproduct of the pressure chamber experiment.

The QEMSCAN analysis indicates that authigenic coats present in samples from the 150 and 250°C experiments often appear to have a chlorite outer rim and feldspar inner rim. This indicates that chlorite formed via the transformation of feldspars, where chlorite grows outwards from feldspar crystals. Feldspar typically transforms to form illitic clay and kaolinite during diagenesis (Haile et al., 2015) and not chlorite. However, the transformation of detrital feldspar to form authigenic chlorite observed in this study has also been identified in Upper Proterozoic sandstones from southern Sweden (Morad and AlDahan, 1987).

5.4.2 Comparison of clay coats formed in pressure chamber experiments and natural chlorite-coated sandstone reservoirs.

The temperature and basic chemistry of formation water used during the pressure chamber experiments was similar to those present in natural systems, such as the North Sea. However, this study is limited by the variables of time and pressure, as diagenesis of sandstones in natural settings usually occurs over a long period of geological time and greater pressures. Some of the key finding from his study are still applicable to ancient chlorite-coated reservoirs.

Authigenic clay mineral coats formed in the pressure chamber experiments ran at 60,90 and 150°C had a similar iron rich mineralogy to chlorite coats present in natural sandstone reservoir.

The morphology of authigenic clay coats in the pressure chamber experiments, captured via SEM, ranged from frost like coatings to needle authigenic crystal coatings. Chlorite coats in natural sandstone reservoirs typically have a rosette morphology.

This study demonstrates that chlorite minerals may form from precursor clay minerals such as those found in modern analogues such as Ravenglass Estuary via high temperature pressure chamber experiments (150-250°C). Understanding how precursor clay coats form, and what factors control their distribution is key to predicting the distribution of chlorite-coated grains in the subsurface.

5.5 Conclusion

Chlorite clay coats preserve primary porosity by inhibiting the formation of quartz overgrowths, during burial and diagenesis (Bloch et al., 2002; Anjos et al., 2003; Dowey et al., 2012; Cao et al., 2018). Therefore, understanding the stages involved in the formation of chlorite-coated grains is essential for predicting their distribution in the subsurface.

Clay-coated grains present in Ravenglass Estuary and other modern analogues represent precursors to chlorite-coated grains present in ancient deeply buried sandstone reservoirs (Jones, 2017; Wooldridge et al., 2017a; Wooldridge et al., 2018).

Therefore, carrying out pressure chamber experiments on modern day sediment allows the stages involved during the formation of chlorite-coated grains to be identified and studied in detail which is not possible through analysing chlorite-coated grains in ancient samples alone.

During the pressure chamber experiments, detrital clay coats present in sediment form Ravenglass Estuary was transformed to authigenic clay coats when subjected to an increase in temperature and pressure. The resulting authigenic clay coats had a similar mineralogy to chlorite present in ancient sandstone reservoir but did not exhibit a rosette morphology which is typically observed in chlorite in ancient samples. The arrangement of detrital clay minerals to start to form authentic clay coats appeared to occur in the 60°C pressure chamber experiment. The authigenic clay coats produced in samples from Ravenglass Estuary during the pressure chamber experiments could represent similar authigenic clay coats to those found in antient chlorite coated sandstone reservoirs.

Future studies should focus on running more realistic pressure chamber experiments with higher pressures equivalent to roughly 2-3km burial depth for longer periods of time to gain a more accurate representation of the transformation of detrital clay coats during diagenesis.

Chapter 6. Chlorite clay-coated grains and their effect on reservoir quality in Mid Jurassic Brent Group reservoirs, northern North Sea

ABSTRACT: In sandstone reservoirs, quartz cement is the main diagenetic phase responsible for the loss of porosity and permeability. Clay coats, particularly chlorite coats, are known to maintain primary porosity by inhibiting the precipitation of diagenetic quartz overgrowths. The depositional and diagenetic controls on the subsurface distribution of chlorite-coated grains remains unconstrained. This makes identifying and exploiting sandstone bodies with high porosities (associated with the presence of chlorite-coated grains) extremely difficult. The presence of chlorite clay-coats and their effect on the reservoir quality of the Rannoch Formation and Etive Formation (Mid Jurassic Brent Group) was studied by analysing samples from three cored wells in Quad 211, Block 18.

A total of 33 thin sections were analysed to establish grain size, sorting, quartz overgrowth abundance, clay-coat coverage and clay-coat abundance. Additional Helium porosity and horizontal permeability data was acquired from the BGS for corresponding thin sections.

Overall, the potential reservoir quality was highly variable within each facies. Statistical analysis suggests that total authigenic cement is the main control on porosity and permeability.

Overall, chlorite clay coat coverage was low and chlorite coated grains did not exert a major control on reservoir quality. Statistical analysis show quartz overgrowth % had no significant relationship with average clay coat coverage or clay coat abundance.

SEM analysis revealed a trace amount of thin flaky detrital Illite/smectite coats are present. These Illite/smectite coats are regarded to be the precursor phase to authigenic chlorite coats.

The workflow utilised in this study should be applied to an ancient case study with a higher content of chlorite coated grains. This would allow the distribution of clay coated grains in modern analogues such as Ravenglass Estuary to be compared to the subsurface distribution of chlorite coated grains in an ancient case study.

6.1 Introduction

Porosity and permeability are the two factors which govern reservoir quality. Porosity controls the hydrocarbon storage potential of a reservoir. Whereas permeability controls the rate at which hydrocarbons can be extracted. Porosity and permeability are typically controlled by a combination of depositional and diagenetic processes.

In sandstone reservoirs, quartz cement is the main diagenetic phase responsible for the loss of porosity and permeability (Kantorowicz, 1990; Bloch et al., 2002). During the early and late diagenesis quartz overgrowths typically fill pore space and block pore throats which limits the economic viability of a reservoir. However, the presence of clay coatings (authigenic clay coats; commonly chlorite coats) on detrital quartz grains inhibits the formation of the quartz overgrowths and cement during burial and diagenesis by blocking the nucleation sites of detrital quartz grains (Bloch et al., 2002; Billault et al., 2003; Lander et al., 2008). Diagenetic models of quartz cementation suggest the main factor controlling the efficiency of clay coats in inhibiting quartz cement is coat completeness (Lander et al., 2008). Consequently, chlorite clay-coated reservoirs retain a higher proportion of primary porosity during deep burial compared to cleaner, non-clay-coated reservoirs. For example, reservoir units of the Lower Cretaceous Tuscaloosa Formation, in the Cranfield Field, Mississippi, U.S.A, have highly variable porosities, which is largely controlled by the presence or absence of chlorite clay-coated grains (Lu et al., 2013). Although far less common in sandstone reservoirs, other clay mineral coats (such as illite and smectite) also preserve porosity and permeability via a similar mechanism to chlorite coats (Storvoll et al., 2002; Taylor et al., 2010).

Authigenic chlorite, when present in high quantities (above 15%), has a detrimental effect on reservoir quality by reducing the diameter of pore throats (Pay et al., 2000). Although the relationship between chlorite coats and porosity can be both positive and negative, they are generally found to have an improving effect on reservoir quality (Dowey et at., 2012; Cao et al., 2018). The controls on the distribution and mechanisms that lead to chlorite clay-coat formation are still unknown. This inhibits our ability to predict the distribution of high porosity, chlorite-coated sandstone reservoirs.

Chlorite (general chemical formula: (Mg,Al,Fe)6 [(Si,Al)4O10](OH)8)) is a 2:1:1 clay mineral, usually iron or magnesium rich, commonly formed by thermal alteration of

precursor clay minerals during diagenesis at temperatures greater than 60–70°C (Worden and Morad, 2003). Berthierine was identified as the likely precursor to iron-rich chlorite-coated grains present in Lower Jurassic sandstone reservoirs on the Norwegian Continental Shelf (Ehrenberg, 1993). This was based on the progressive increase in chlorite with depth, where the shallowest samples consist of a mixed layer chlorite-serpentine clay (thought to be berthierine) which becomes less abundant with increasing burial.

In the Central Graben, UK North Sea, smectite has been proposed as a precursor for grain-coating chlorite, due to authigenic chlorite having similar chemical and morphological characteristics to smectite (Humphreys et al., 1989). However, for chlorite formation from a smectite precursor, either a source of aluminium or loss of silica is required (Chang et al., 1986).

Chlorite may also form via the dissolution and recrystallization of volcanic rock fragments and iron and magnesium-rich detrital grains (Pay et al., 2000; Anjos et al., 2003; Dowey et al., 2012). For example, chlorite present in Lower Cretaceous reservoir units of the Britannia Field, North Sea, UK is reported as being sourced from the underlying Jurassic Forties Igneous Province (Blackbourn and Thompson, 2000).

This study aims to assess the depositional and diagenetic controls on the distribution of chlorite clay-coated grains in a shallow marine-estuarine setting. The Mid Jurassic Brent Group (Northern North Sea, Quad 211, Block 18) was selected as a case study due to the depositional evolution of the Brent Group being well constrained. Furthermore, an extensive reservoir quality dataset is available for much of the area.

Studying the distribution of chlorite clay-coated grains in an extensively explored formation provided vital information on the distribution of chlorite clay-coated grains. This will enhance the predictability and modelling of reservoir quality of chlorite-coated reservoirs in underexplored areas.

6.1.1 Regional geology

The Brent Group is a key reservoir horizon that stretches across the northern North Sea from 60.5°N to 61.6°N and onwards to the neighbouring Norwegian Continental Shelf (Went et al., 2013). Figure 6.1 displays a synthetic stratigraphy for the North Sea Basin (Patruno et al., 2021).

The deposition of the Brent Group took place during the Mid Jurassic in the northern section of the Viking Graben (Rattey and Hayward, 1993). The Brent Group consist of mainly continental, deltaic or shallow marine siliciclastic deposits. The Brent Group in the Northern North Sea overlies the Dunlin Group and is overlain by the Heather Formation.

During the Middle Jurassic, the Northern North Sea experienced a period of mantle plume thermal doming and regional uplift which led to enhanced sediment erosion and the progradation of the Brent Delta (Patruno et al., 2021).

The reservoir units of the Mid Jurassic Brent Group can be split into five regionally correlatable lithostratigraphic divisions: The Broom, Etive, Ness and Tarbert Formations.

This study focuses exclusively on the Rannoch and Etive Formations present in three wells from the Don (well 211.18-N4 and well 211/18a-N7) and Don SW fields (well 211/18a-22). The Don and Don SW fields are located towards the western edge of the North Viking Graben and are bound by the Halibut High to the west (Figure 6.2). Oil has been produced from the Brent Group which is located at depths between ~3350m and 3500m (Morrison et al., 1991). The study area contains a series of NNW-SSE and NE-SW trending faults (Figure 6.2).

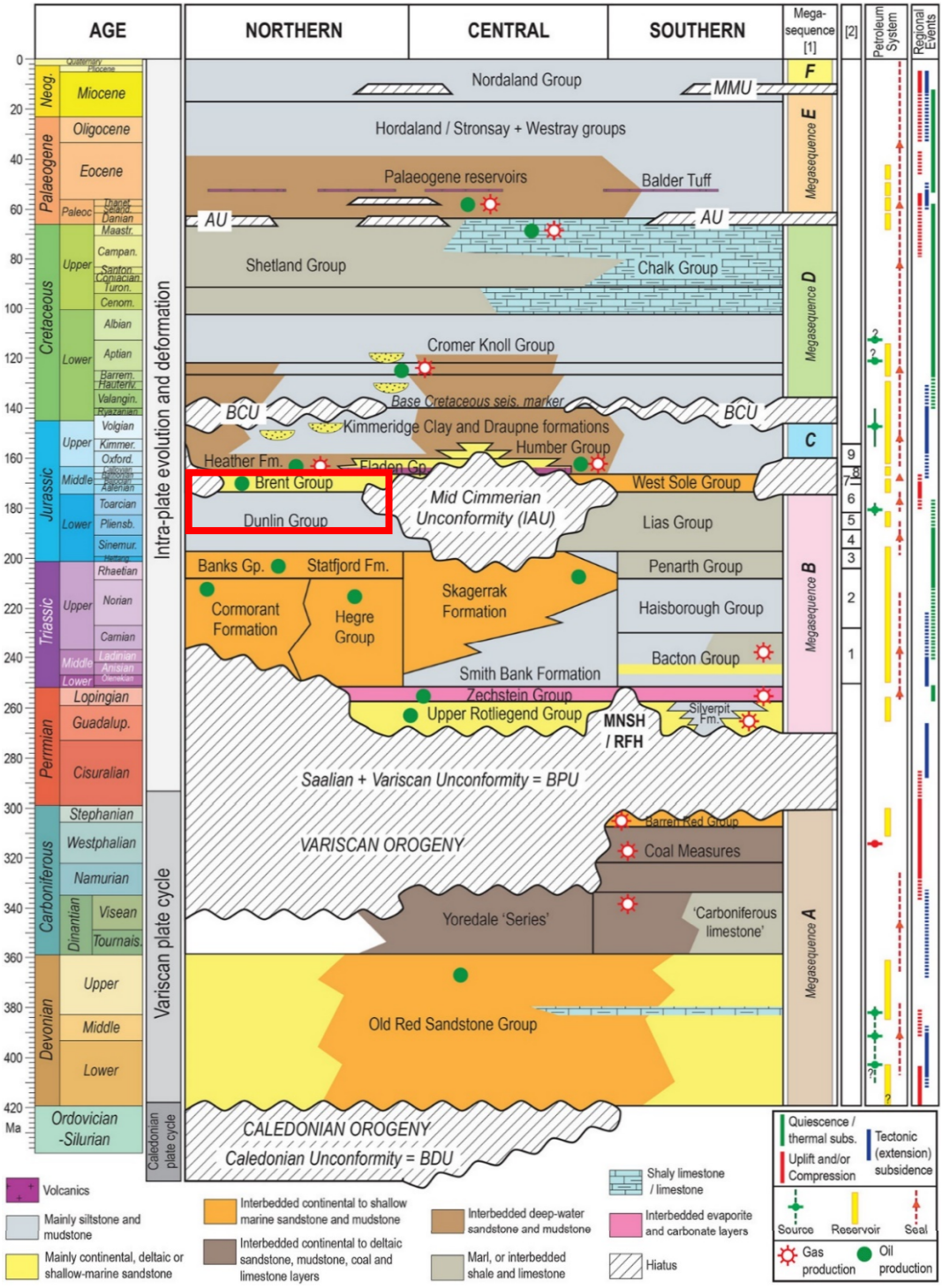


Figure 6.1. Synthetic stratigraphy for the North Sea Basin (Patruno et al., 2021). The Brent Group within the Northern North Sea (the focus of this study) is highlighted by a red box. The Brent Group within the Northern North Sea is associated with continental, deltaic or shallow marine deposits.

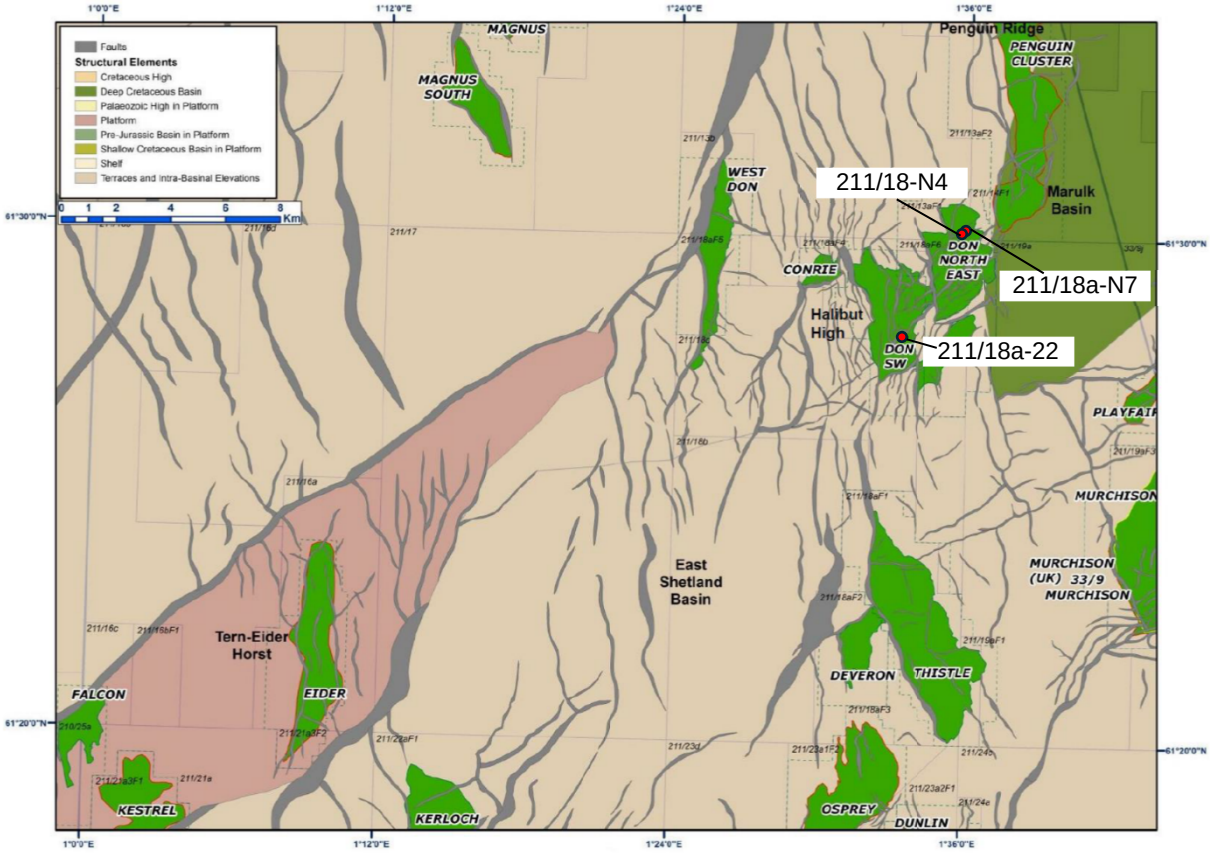


Figure 6.2. Map of regional structural elements across the Northern North Sea (EnQuest, 2021). Red dots show the location of the three study wells.

6.1.2 Research theme and questions

This chapter aims to see if the observations made in previous chapters can be applied to an ancient case study.

Chapter 4 studied the distribution of precursor clay coats in two modern analogue settings, Bute Inlet, British Columbia and Ravenglass Estuary, UK. Clay coat coverage was low within Bute Inlet (a deep-water turbidity system) which made it difficult to understand how clay coated grains form and what controls their distribution.

Clay coat coverage was higher in Ravenglass Estuary (shallow marine modern analogue). Clay coat coverage varied across Ravenglass Estuary depending on depositional sub environment. This made Ravenglass Estuary a good case study to research the different controls on the distribution of clay coated grains.

A shallow marine ancient case study (the Middle Jurassic Brent Group) was selected to investigate how the distribution of clay coated grains in Ravenglass Estuary compares to a subsurface example.

Chapter 3 and chapter 4 found that clay coat grain coverage increases with increasing EPS content. Clay coat coverage and EPS content within Ravenglass Estuary was highest in intertidal sub depositional environments such as mixed flats and mud flats. Mud flats and mixed flats are typically considered non reservoir due to a high detrital clay content. The results from Chapter 4 indicate that sand flats and tidal bars have a higher EPS content and higher clay coat coverage compared to upper shoreface deposits. Based on these results, intertidal sub depositional environments such as sand flats and tidal bars within the Middle Jurassic Brent Group are predicted to have the most optimum clay content to form clay coats and not form a pore filling clay matrix.

This Chapter focuses on the research theme “The origin and distribution of clay-coated grains in ancient sandstone reservoirs” which is fully outlined in Chapter 1.7.3. The key research questions to be addressed in this chapter are:

- What are the textural and depositional controls on the formation of clay-coated grains in the ancient reservoir case study?
- What is the origin of clay-coated grains present in the ancient sandstone reservoir case study?

- How does the distribution of chlorite coats in the ancient case study compare to the distribution of precursor clay coats in the shallow marine modern analogue system?

6.2 Materials and methods

This section provides a summary of the methods used in this chapter. A more detailed description of methodology can be found in Chapter 2.

6.2.1 Wells and data sets

Approximately 240m of core from three wells (211/18a-22, 211/18a-N7 and 211/18-N4), located in the Don and SW Don fields, was logged a scale of 1:100 to identify and assign sedimentary facies. A total of 33 thin sections (10 from Rannoch Formation and 23 from the Etive Formation), covering all facies in the three cored wells was analysed for detrital and authigenic mineralogy, grain size and sorting, chlorite clay-coat coverage and potential reservoir quality.

Chlorite clay-coat grain coverage was estimated using the method adopted by Wooldridge et al. (2017a). Clay-coat abundance (% of grains which display clay coatings) was also calculated via point counting (50 grains).

Additional conventional core analysis (CCA) data (Helium porosity and Horizontal Permeability), Scanning Electron Microscopy (SEM) imaging, textural (grain size and sorting) and mineralogy data (captured via point counting) were obtained from the National Geoscience Data Centre (Natural Environment Research Council item ID: 123897).

XRD results for two samples from well 211/18a-22 (one estuarine channel sample and one upper shoreface sample) from the National Geoscience Data Centre (Natural Environment Research Council, item ID: 123897) were also available.

6.2.2 Pearson's correlation coefficient analysis

Pearsons's correlation coefficient analysis was used to test the relationship between two variables. Table 2.2 in Chapter 2 provides the cut offs used in this study. P-values were calculated from R-values at a significance level of 0.05.A P-values describes how likely it is that an observed data trend has occurred by random chance (i.e. that a null hypothesis is true). In this study, P-values less than 0.05 suggest that the relationship is significant and that there is a less than 5% chance that the data trend has been produced by random chance.

6.3 Results

6.3.1 Facies and interpretations

Seven facies were assigned through three cores, based on texture (grain size, clay content, sorting), sedimentary structures, bioturbation, bed thickness and contacts, trace and fossil content. In this study facies were assigned to capture the relationship between facies, clay-coat coverage and potential reservoir quality. A core description chart at 1:50 scale for the wells 211/18a-22, 211/18a-N7 and 211/18-N4 can be found in appendices C,D and E, respectively.

Estuarine Channel

Estuarine channel deposits were characterized as fine to coarse grained sand with a sorting of poor to good. Detrital clay content is typically low (<20%) and clay was typically restricted to clay laminations (Figure 6.3). This facies shows little/ no evidence of bioturbation. Cross stratification is common in coarser grained sandstones (Figure 6.3), whilst finer grained deposits comprise parallel lamination. Erosive bed bases are common. This facies is composed of 1-7m thick typically upward fining beds and bedstacks. A total of eleven thin sections were available from estuarine channel deposits.

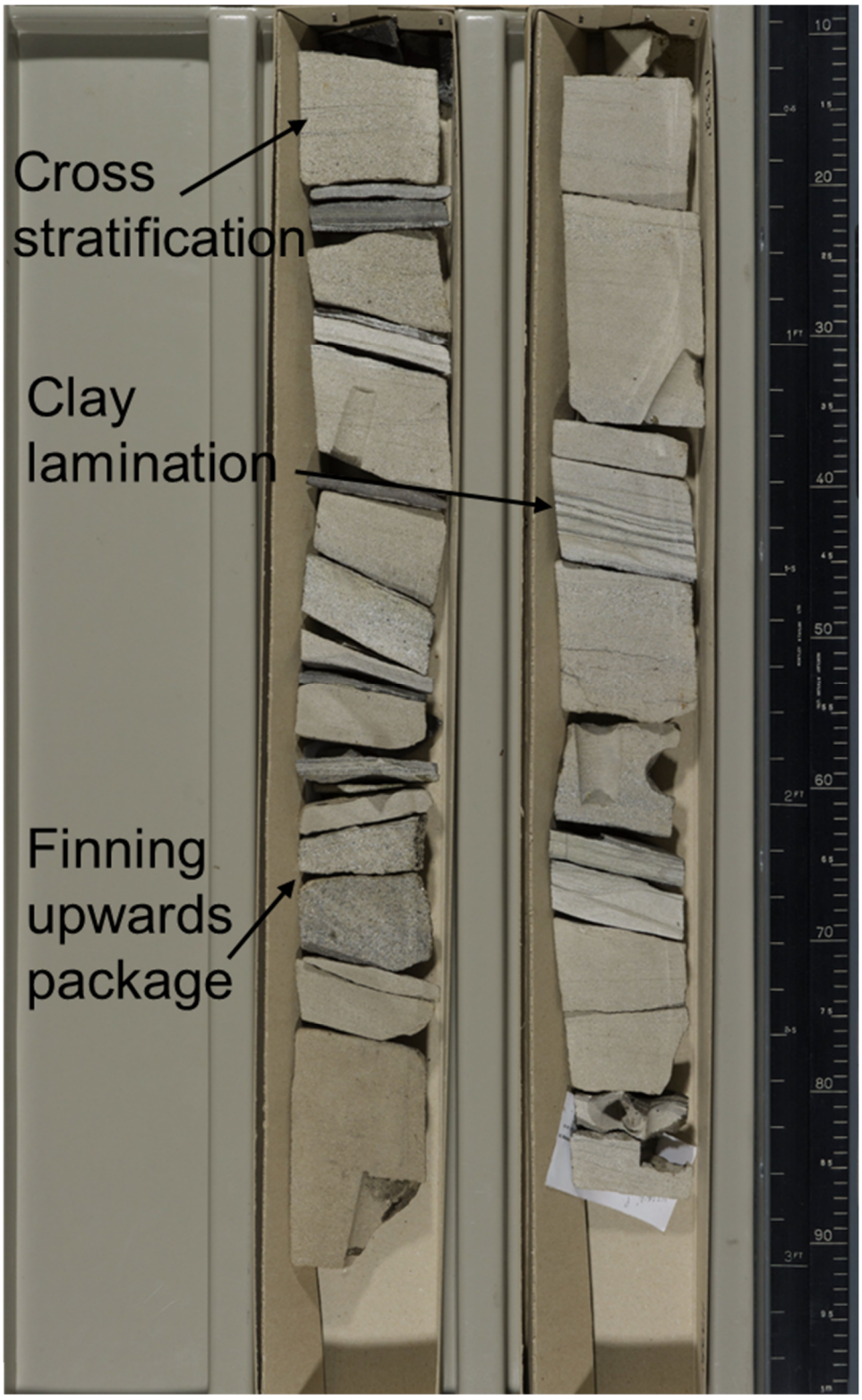


Figure 6.3. Example of estuarine channel deposits between 3453.99m and 3455.82m, well 221/18a-22.

Upper shoreface

Upper shoreface deposits were characterized as fine to coarse grained sand with moderate to good sorting. Upper shoreface deposits typically had low clay content (<10%). Bioturbation is rare and comprises vertical burrows about 50mm wide, 1cm long. Bed boundaries were not clearly defined. Upper shoreface deposits were recorded in all wells (Figure 6.4). A total of seven thin sections were available from upper shoreface deposits.

Lower shoreface

Lower shoreface deposits are characterized as very fine to fine grained sand and siltstone with good levels of sorting. Planar and hummocky cross stratification were common and defined by colour, mica content and grain size differences (Figure 6.5). Horizontal and vertical burrows are present but rare. Horizontal burrows are typically elongated, 1cm in diameter, sand-filled and they crosscut the core parallel to bedding. Vertical traces are discordant to bedding, 50mm in diameter and 1cm long. Bed thickness ranges from 2 to 5cm. Lower shoreface deposits were recorded in all wells and mainly constitutes the Rannoch Formation. A total of nine thin sections were available from lower shoreface deposits.

Lagoon

Light to dark grey mudstones and siltstones. Bioturbation is abundant and commonly obscures bedding (Figure 6.6). Trace fossils identified include Thalassinoides, Diplocraterion, Teichichnus and Asterosoma. The high bioturbation content and fine-grained nature along with the dark grey colour suggest a relatively low energy sheltered environment with high organic carbon content. Lagoonal deposits are present in all wells and most abundant in 211/18-N4. No petrographic samples were available from the lagoon facies.

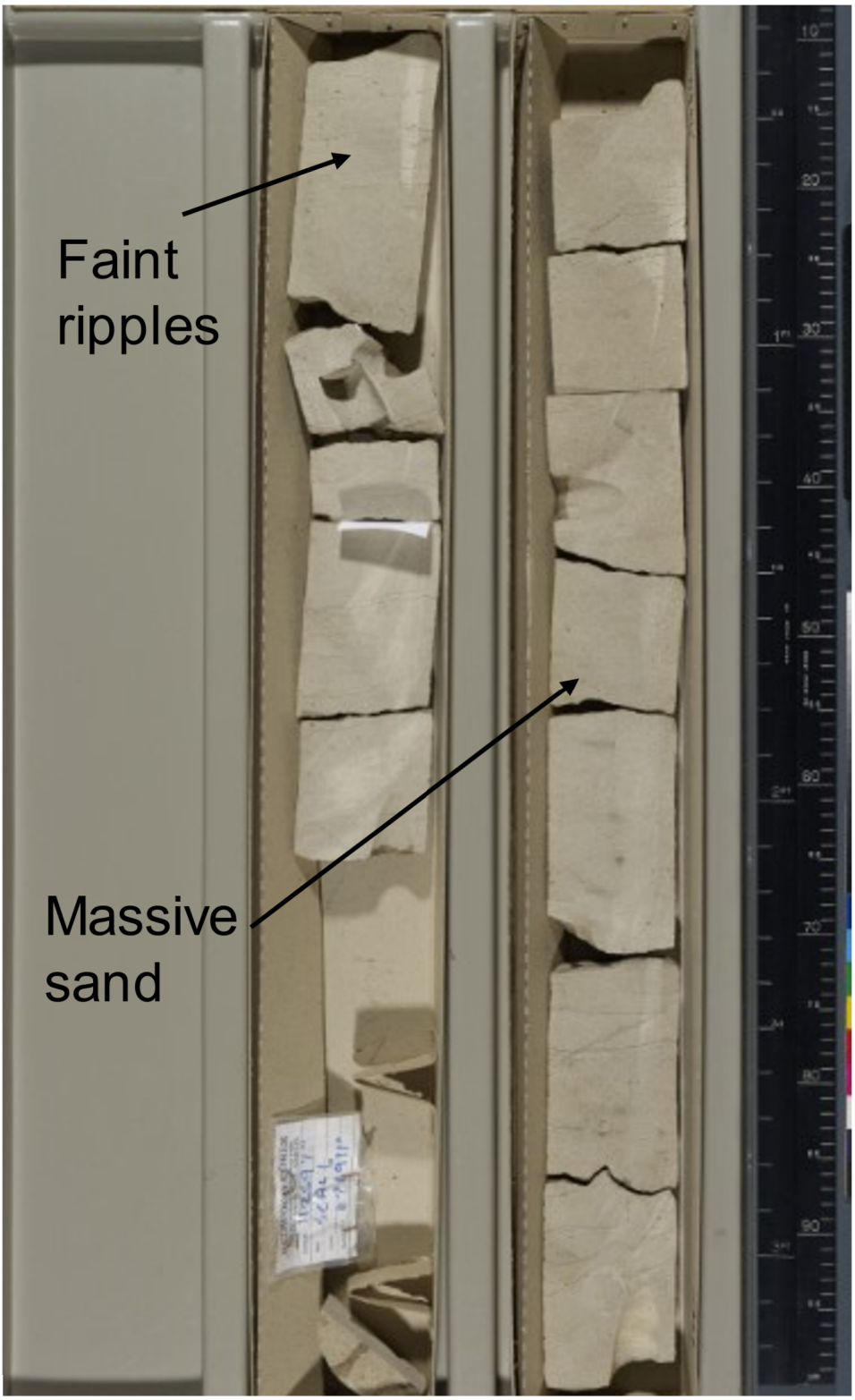


Figure 6.4. Example of upper shoreface deposits between 3433.27m and 3435.10m, well 221/18a-22.



Figure 6.5. Example of lower shoreface deposits between 3539.95m and 3541.78m, well 221/18a-22.



Figure 6.6. Example of lagoonal deposits between 3427.78m and 3429.61m, well 221/18a-22.

Barrier

Fine to coarse grained sandstones with a moderate to good level of sorting. Detrital clay content is typically low (<5%). Minor level of bioturbation (Figure 6.7) with some rootlets were observed. The presence of rootlets is evidence of subaerial exposure. This facies is restricted to well 211/18a-22 and well 211/18-N4. A total of four thin sections were available from barrier deposits.

Distal shoreface

Fine to coarse grained sand with moderate to good sorting. Beds are cm-thick and bounded by sharp top and bases. Argillaceous content is low (<10%). Bioturbation is variable (Figure 6.8). The distal shoreface deposits were recorded in only one well (211/18-N4). A total of two thin sections were available from distal shoreface deposits.

Swamp

Swamp deposits consisted of thin coal horizons (less than 1m thick). Rootlets were often seen in the beds directly below coal horizons (Figure 6.9). No petrographic samples were available from swamp deposits.

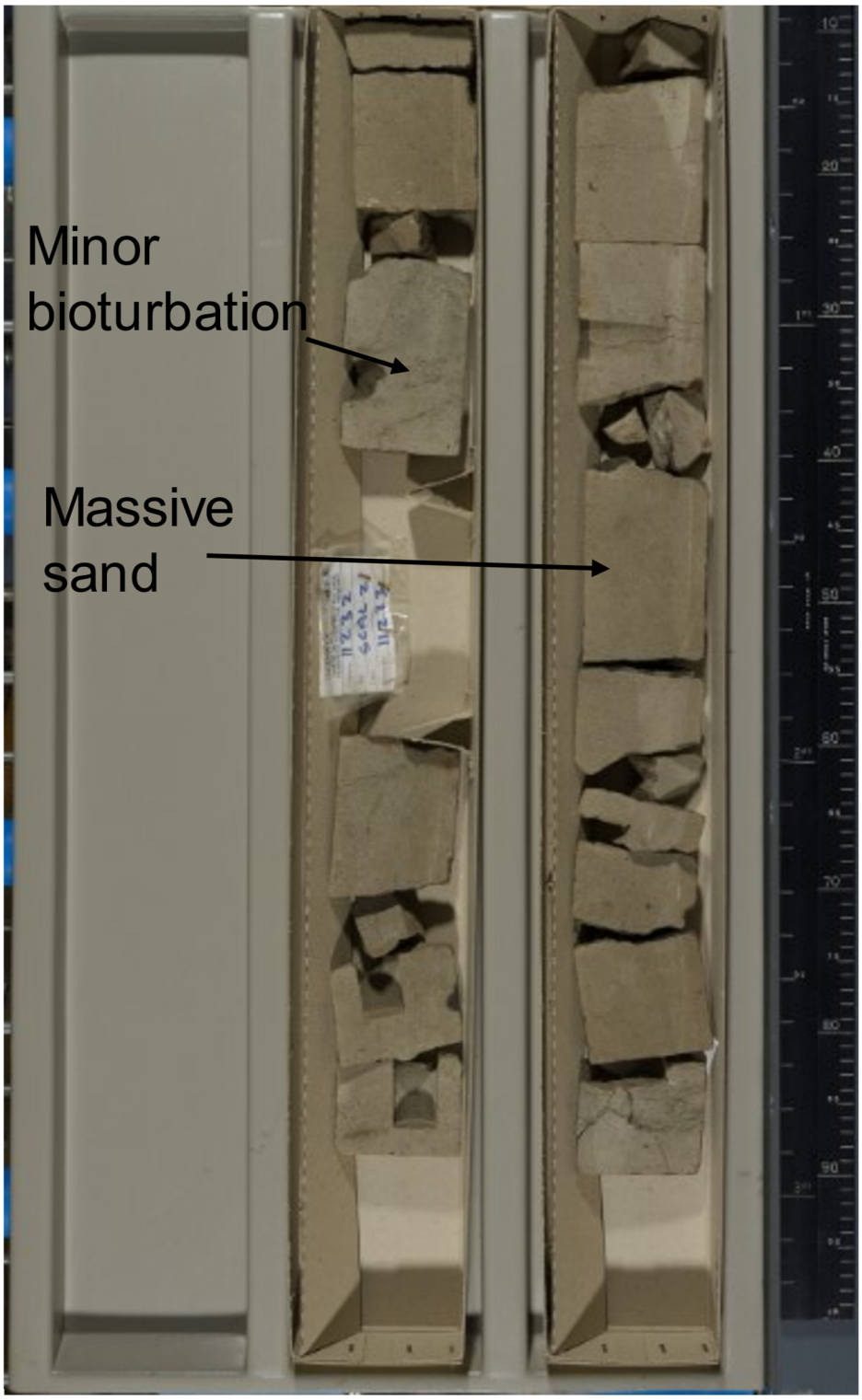


Figure 6.7. Example of barrier deposits between 3422.29m and 3424.12m, well 221/18a-22.

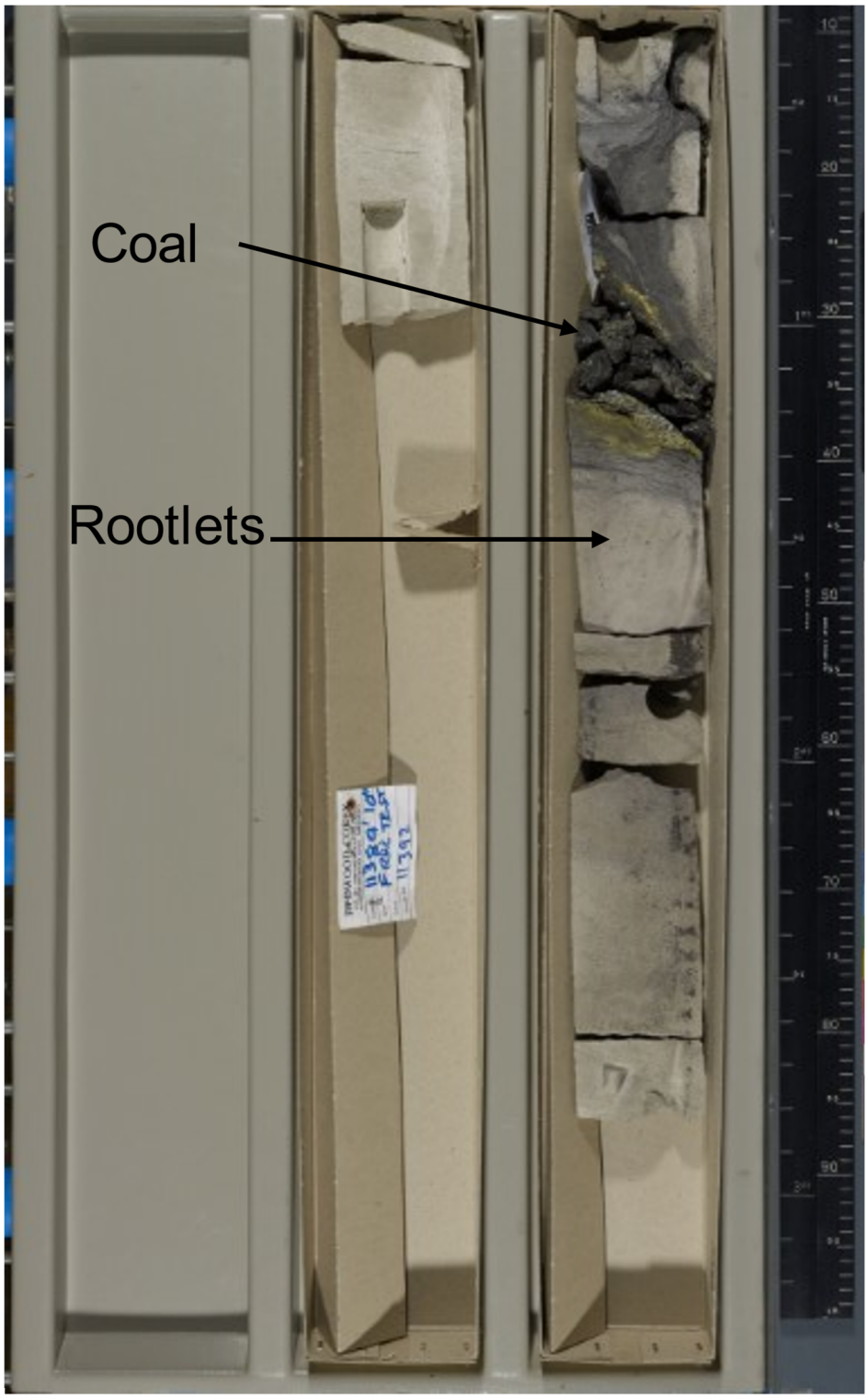


Figure 6.8. Example of swamp deposits between 3470.45m and 3472.28m, well 221/18a-22.

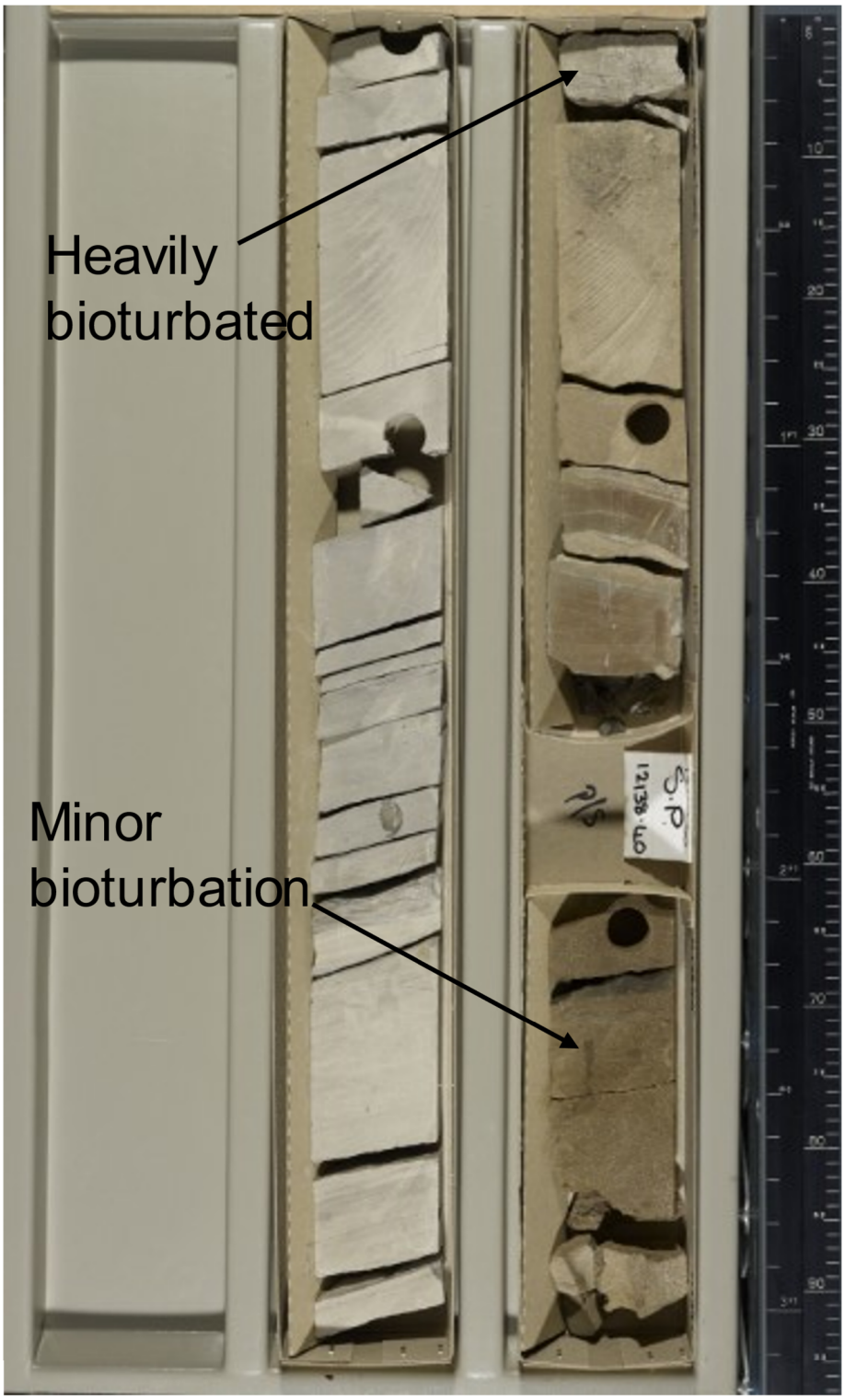


Figure 6.9. Example of distal shoreface deposits between 3699.05m and 3700.88m, well 221/18-N4.

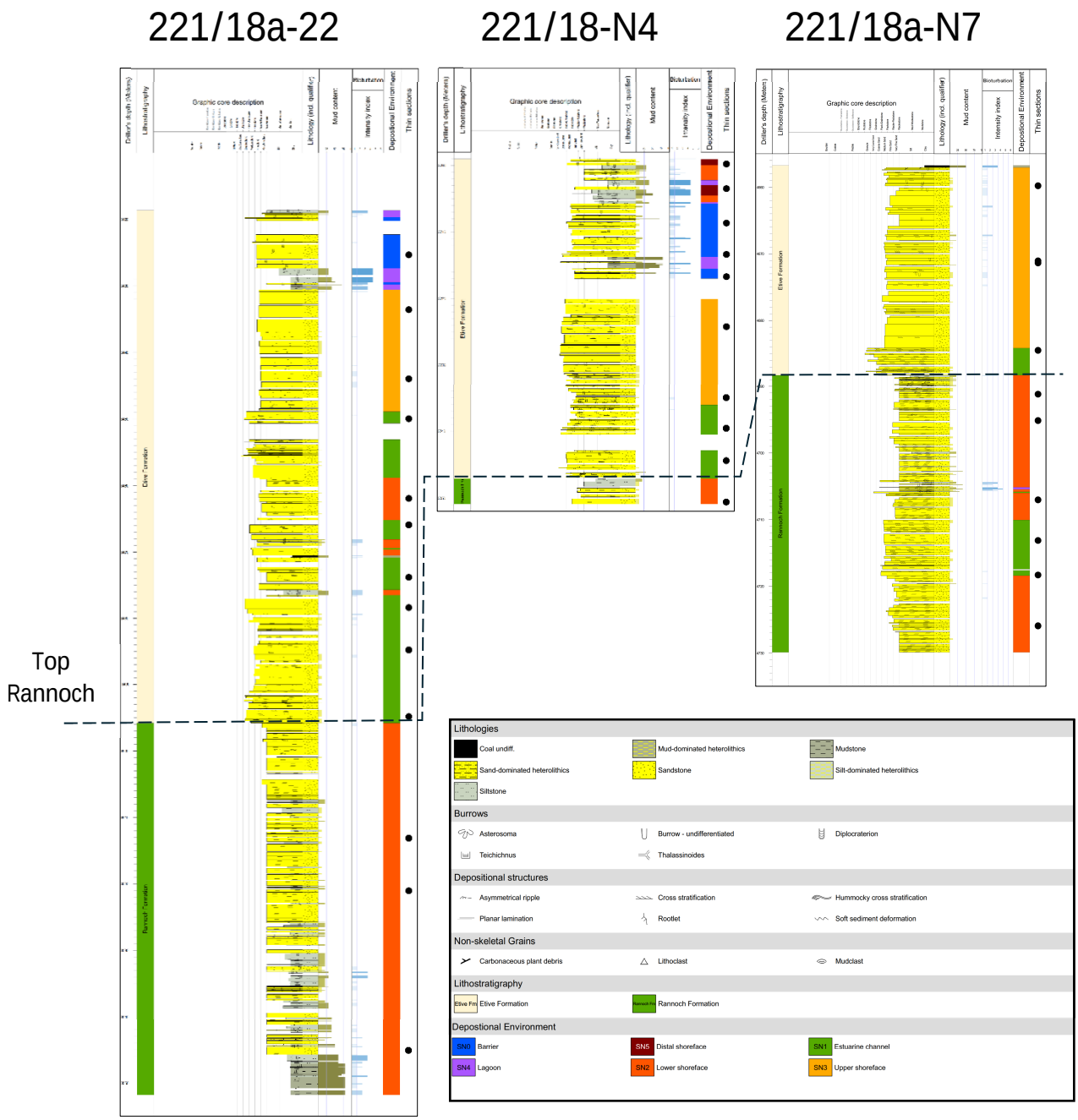


Figure 6.10. Core log for wells in Block 211/18. 1:200 scale. See appendices C, D and E for full logs.

6.3.2 Texture and mineralogy

Table 6.1 displays all data for the 33 thin section samples. Samples ranged from very fine sand to coarse sand. Sorting ranges from poor to good.

Quartz is the most abundant detrital framework grain and ranges from 38% up to 69% (polycrystalline and monocrystalline). Lithics are present in a minor amount (<5%). K-feldspar ranges from 1% to 15% and plagioclase feldspar ranges from <1% to 5%.

Detrital clay is present as a pore filling matrix and ranges from 0% up to 20%. All deposits have a similar detrital mineralogy ranging from arkose to subarkose in composition (Figure 6.12).

Total authigenic cement ranges from 2% up to 25%. The main authigenic cements are quartz overgrowths (0% - 15%), kaolinite (0% to 11%) and Fe calcite (0% to 21%). There were also minor amounts of siderite (up to 1%), albite (up to 1%) and illite (up to 2%).

Authigenic clay coats (Figure 6.11) made up <1% of the bulk mineralogy of each sample and are primarily chloritic in composition.

Secondary pores formed via the dissolution of unstable and liable grains such as feldspars and lithics.

There are also traces of hydrocarbons in the form of bitumen in some samples.

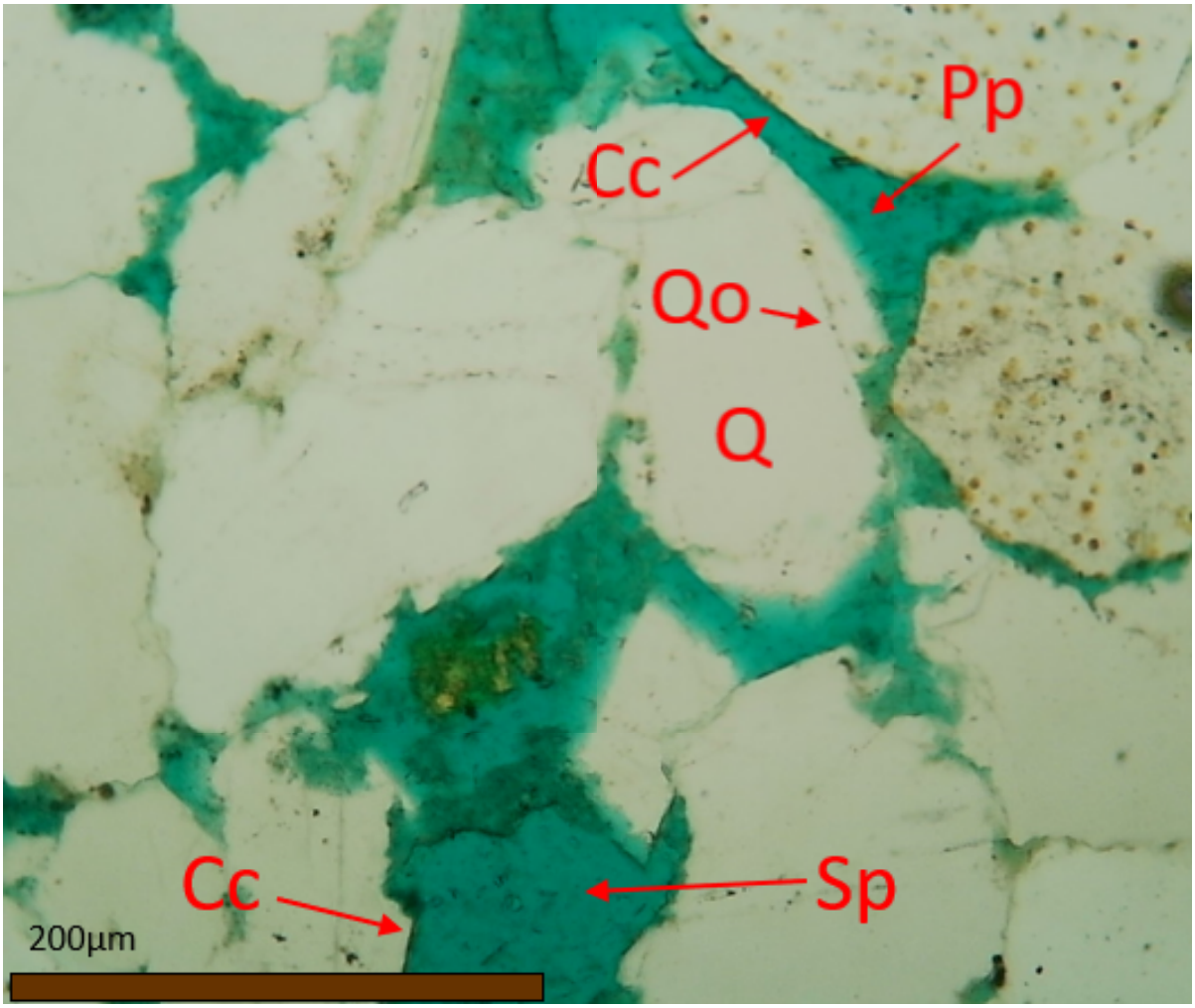


Figure 6.11. Thin section of sample from estuarine channel deposit. Pp = primary porosity, CC = chlorite coat and Qo = quartz overgrowth. Secondary porosity (Sp) formed via the dissolution of a feldspar grain.

Well	Formation	Facies	Depth (ft)	Depth (m)	Grain size	Grain size (µm)	Sorting	Monocrystalline quartz	polycrystalline quartz	total quartz	K-feldspar	Plagioclase feldspar	Total feldspar	Total lithic fragments	total heavy minerals	total mica	total detrital clay matrix	non ferroan calcite	ferroan calcite	magnesium siderite	microcrystalline siderite	siderite	ankerite	quartz overgrowths	K-feldspar overgrowth	Albite	Pyrite	Barite	Phosphate	Anatase	Ti Oxides	Kaolinite	Illite	indeterminant authigenic clay	Total authigenic	Primary porosity	Secondary porosity (intergranular)	Secondary porosity (intragranular/ m	total visible porosity	hydrocarbons	Helium Porosity (%)	Permeability (mD)	Average clay coat coverage (%)	Clay coat abundance (%)
211/18a-22	Etive	Barrier	11238.00	3425.34	Fine Sand (Upper) - Medium Sand (Lower)	125	Moderately good (0.6)	46.70	13.70	60.30	7.00	1.00	8.00	0.30	0.00	0.00	0.30	0.00	0.00	0.00	0.00	0.70	0.00	7.30	0.00	0.30	0.70	tr	0.00	0.30	0.70	1.30	0.00	0.00	11.30	17.00	1.00	1.30	3.00	0.00	14.80	1.58	0.806	8.00
211/18a-22	Etive	Upper shoreface	11265.00	3433.57	Fine Sand (Upper) - Medium Sand (Lower)	650	Moderately good (0.6)	47.30	21.70	69.00	8.30	1.30	9.70	0.30	0.30	0.30	4.00	0.00	0.00	0.00	0.00	0.30	0.00	3.00	0.00	0.00	0.30	0.00	0.00	tr	tr	2.70	1.30	2.30	10.00	5.30	0.30	0.70	10.70	1.30	17.40	153.00	11.69	60.00
211/18a-22	Etive	Upper shoreface	11299.00	3443.94	Fine Sand (Upper) - Medium Sand (Lower)	180	Good (0.5)	44.00	15.00	59.00	12.70	1.00	13.70	0.70	0.00	0.70	1.70	0.00	1.70	0.00	0.00	1.30	0.00	3.00	0.00	0.70	0.30	0.00	0.00	0.00	0.70	2.30	0.30	0.70	11.00	10.70	2.00	0.70	21.30	0.00	23.90	1680.00	7.325	44.00
211/18a-22	Etive	Estuarine channel	11318.67	3449.93	Fine Sand (Lower to Upper) Coarse Sand (Lower to Upper)	275	Moderately good (0.6)	35.70	8.00	43.70	13.70	5.00	18.70	1.00	0.00	7.70	6.00	0.00	0.00	0.00	5.00	1.70	tr	1.00	0.00	0.30	1.00	0.00	0.00	tr	0.70	11.00	tr	0.00	20.70	2.00	tr	0.30	9.00	0.00	3.80	0.93	2.702	24.00
211/18a-22	Etive	Lower shoreface	11358.00	3461.92	Fine Sand (Lower)	400	Good (0.5)	52.30	5.00	57.30	8.30	0.30	8.70	0.30	0.70	9.00	1.30	0.00	0.00	0.00	0.70	1.00	0.70	6.70	0.00	0.70	1.00	0.00	0.00	0.70	0.70	4.30	tr	0.00	16.30	3.30	0.00	3.00	5.00	0.00	14.10	0.30	1.31	16.00
211/18a-22	Etive	Estuarine channel	11371.00	3465.88	Medium Sand (Lower)	250	Good (0.5)	45.70	14.00	59.70	6.30	3.00	9.30	0.30	0.00	0.70	4.00	0.00	0.00	0.00	0.00	tr	0.00	8.30	0.00	0.70	1.00	0.00	0.00	0.00	0.70	5.30	0.00	1.30	17.30	6.70	1.00	1.00	19.30	0.00	19.30	425.00	7.041	54.00
211/18a-22	Etive	Estuarine Channel	11397.00	3473.81	Fine Sand (Lower- Upper) Fine Sand (Upper)	500	Moderately good to good (0.4-0.6)	40.00	18.00	58.00	10.70	1.00	11.70	1.30	0.70	0.70	3.70	0.00	0.00	0.00	0.00	0.00	0.00	2.70	0.00	0.70	0.30	0.00	0.00	0.70	1.00	2.30	0.00	2.00	9.70	9.70	4.30	0.30	14.30	0.00	21.40	63.50	30.82	96.00
211/18a-22	Etive	Estuarine channel	11412.00	3478.38	Medium Sand (Upper) Coarse Sand (Lower)	500	Moderately good to good (0.6-0.5)	39.30	16.70	56.00	7.00	2.30	9.30	1.00	0.70	0.30	1.30	0.00	0.00	0.00	0.00	0.00	0.00	9.70	0.00	1.70	0.00	0.00	0.00	0.00	0.70	5.00	0.00	tr	17.00	11.00	1.30	2.00	12.00	0.00	13.80	81.30	8.332	58.00
211/18a-22	Etive	Estuarine channel	11433.00	3484.78	Medium Sand (Lower)	125	Moderately good (0.6)	38.70	17.70	56.30	7.70	2.30	10.00	0.30	0.00	0.30	2.00	0.00	0.00	0.00	0.00	0.00	0.00	9.00	0.00	0.70	0.30	0.00	0.00	tr	1.00	10.00	0.00	0.70	21.70	7.00	0.30	1.70	0.70	0.00	12.60	0.76	0.22	4.00
211/18a-22	Etive	Estuarine channel	11466.00	3494.84	Fine Sand (Lower-Upper) Coarse Sand (Lower-Upper)	250	Good to moderately good (0.5-0.7)	33.70	17.00	50.70	8.00	3.00	11.00	4.00	0.00	4.00	0.30	0.00	0.00	0.00	0.00	0.00	0.00	5.30	0.00	1.70	0.00	0.00	0.00	0.30	0.30	7.00	0.00	1.00	15.70	10.00	1.30	2.70	13.30	0.00	19.70	91.60	6.191	40.00
211/18a-22	Rannoch	Lower shoreface	11526.00	3513.12	Very Fine Sand (Upper) - Fine Sand (Lower)	300	Good (0.5)	43.40	7.30	50.70	12.00	2.00	14.00	0.00	0.00	17.70	1.30	0.00	0.00	0.00	0.30	0.00	0.00	3.70	0.00	1.00	1.70	0.00	0.00	tr	0.30	6.30	0.00	0.00	13.30	2.30	0.30	0.30	4.00	0.00	16.10	32.30	11.06	52.00
211/18a-22	Rannoch	Lower shoreface	11552.00	3521.05	Very Fine Sand (Upper) - Fine Sand (Lower)	400	Good (0.5)	41.30	9.00	50.30	10.00	1.70	11.70	0.70	0.00	10.30	1.30	0.00	1.00	0.00	1.30	0.70	0.70	6.70	0.00	1.00	1.70	0.00	0.00	0.30	2.00	5.30	0.00	0.30	21.00	1.70	0.00	3.30	4.00	0.00	12.70	0.30	9.091	68.00
211/18a-22	Rannoch	Lower shoreface	11631.00	3545.13	Very Fine Sand (Upper) - Fine Sand (Lower)	450	Good (0.5)	40.00	7.00	47.00	8.70	1.70	10.30	0.70	0.00	18.70	2.00	0.00	1.00	0.00	1.30	0.30	0.70	3.70	0.00	0.00	3.00	0.00	0.00	tr	1.30	8.70	0.00	0.30	20.30	0.00	0.30	0,3	15.00	tr	19.00	58.80	18.97	86.00
211/18-N4	Etive	Distal shoreface	12138.40	3699.78	Medium Sand (Upper) - Coarse Sand (Lower)	210	Moderate (0.8)	38.00	22.00	60.00	7.70	1.30	9.00	0.00	0.00	0.30	1.30	0.00	0.00	0.00	0.00	0.70	0.30	7.30	0.00	0.00	0.00	0.00	0.00	0.00	tr	4.30	0.30	1.00	14.00	7.00	5.30	2.70	14.30	0.00	22.20	20.00	8.718	44.00
211/18-N4	Etive	Distal shoreface	12150.60	3703.50	Fine Sand Upper to Medium Sand (Lower)	160	Good (0.5)	51.70	7.30	59.00	4.00	0.70	4.70	0.30	0.00	1.00	2.00	0.00	0.00	0.00	0.30	1.00	0.30	13.00	0.00	tr	0.00	0.00	0.00	0.00	0.30	5.30	tr	2.30	22.70	7.00	1.70	1.70	3.00	0.00	13.10	1.60	1.049	12.00
211/18-N4	Etive	Barrier	12183.00	3713.38	Coarse Sand (Upper)	360	Moderately good (0.6)	29.30	36.00	65.30	7.30	1.00	8.30	3.30	0.00	0.70	0.30	0.00	1.30	0.00	0.00	0.70	0.00	6.30	0.00	0.00	tr	tr	tr	0.00	tr	1.30	tr	0.00	9.70	10.30	1.00	0.70	4.30	0.00	6.70	0.06	0	0.00
211/18-N4	Etive	Barrier	12194.00	3716.73	Fine Sand (Lower-Upper)	250	Good (0.4)	60.00	7.30	67.30	1.00	1.70	2.70	0.00	0.30	0.00	0.00	0.00	0.00	0.00	0.00	0.00	0.00	4.00	0.00	tr	0.00	0.00	0.00	tr	0.30	tr	0.00	0.00	4.30	13.00	8.30	tr	10.30	tr	4.90	0.04	13.24	68.00
211/18-N4	Etive	Upper shoreface	12218.60	3724.23	Coarse Sand (Lower)	275	Good (0.5)	59.70	8.30	68.00	4.30	1.30	5.70	0.30	0.00	0.00	3.00	0.00	0.00	0.00	0.00	2.00	0.00	7.30	0.00	0.00	0.00	0.00	0.00	0.30	0.30	tr	0.00	1.00	11.00	10.00	1.70	0.30	8.70	0.00	18.20	80.60	10.75	44.00
211/18-N4	Etive	Upper shoreface	12254.00	3735.02	Fine Sand (Upper)	275	Good (0.5)	57.70	10.30	68.00	7.30	1.30	8.70	0.30	0.00	0.00	1.30	0.00	0.00	0.00	0.00	0.70	0.00	4.30	0.00	1.00	tr	0.00	0.00	0.00	0.00	0.70	0.30	1.00	8.00	11.70	1.00	1.00	17.70	0.00	19.30	151.00	19.73	80.00
211/18-N4	Etive	Estuarine channel	12284.83	3744.42	Medium Sand (Lower) Medium Sand (Lower-Upper)	150	Good to moderately good (0.5-0.7)	44.30	17.30	61.70	6.70	4.00	10.70	0.00	0.70	1.30	19.70	0.00	0.00	0.00	0.00	0.30	0.30	tr	0.00	0.00	0.00	0.00	0.00	0.00	0.00	0.00	0.00	0.00	1.30	2.00	2.30	0.30	1.30	6.30	0.00	19.90	4.38	4.301	36.00
211/18-N4	Rannoch	Lower shoreface	12305.00	3750.56	Fine Sand (Lower-Upper)	230	Good (0.5)	57.30	4.00	61.30	10.30	0.30	10.70	1.00	0.00	2.70	1.70	0.00	0.00	0.00	0.00	tr	0.30	12.70	0.00	0.70	0.00	0.00	0.00	0.00	0.30	0.30	2.70	0.30	17.30	3.00	0.00	2.00	13.70	0.00	17.10	123.00	7.937	62.00
211/18-N4	Etive	Barrier	12167.50	3708.65	Medium Sand (Lower)	500	Good (0.5)	55.30	5.70	61.00	8.00	0.30	8.30	0.00	0.30	0.30	1.00	0.00	tr	0.00	0.00	0.70	0.00	8.30	0.00	0.00	0.00	0.00	tr	tr	0.00	tr	1.70	0.00	0.30	11.00	13.00	1.00	3.70	9.70	0.00	15.90	11.00	3.795	30.00
211/18-N4	Etive	Estuarine channel	12269.00	3739.59	Medium Sand (Lower) - Coarse Sand (Upper)	180	Moderate to poor (0.8-1.0)	47.30	9.00	56.30	9.70	1.00	10.70	1.70	0.00	1.70	3.70	0.00	0.00	1.00	0.00	0.00	0.00	6.70	0.00	0.30	0.00	0.00	0.00	0.00	0.70	1.70	0.00	1.30	11.70	12.00	0.30	2.00	5.00	0.00	14.60	4.34	5.462	34.00
211/18-N7	Etive	Upper shoreface	15288.00	4659.78	Medium Sand (Lower - Upper)	320	Moderately good (0.6)	51.00	10.00	61.00	9.30	1.00	10.30	1.70	0.30	0.70	3.70	0.00	tr	0.00	0.00	tr	0.00	9.70	0.00	2.00	0.00	0.00	0.00	0.00	1.00	3.30	1.00	0.00	17.00	3.70	0.70	0.70	17.30	0.00	20.20	16.00	0.729	10.00
211/18-N7	Etive	Upper shoreface	15325.00	4671.06	Medium Sand (Lower - Upper)	375	Moderately good (0.7)	53.70	13.00	66.70	7.00	2.30	9.30	0.30	0.00	0.00	9.30	0.00	0.00	0.00	0.00	0.00	0.00	2.70	0.00	2.30	0.00	0.00	0.00	0.70	1.70	3.00	0.00	0.00	10.30	3.00	0.30	0.70	14.00	0.00	15.90	103.00	9.52	72.00
211/18-N7	Etive	Upper shoreface	15326.00	4671.36	Medium Sand (Lower- Upper)	125	Moderate (0.8)	49.70	17.00	66.70	4.30	1.70	6.00	1.70	0.70	0.70	5.30	0.00	0.00	0.00	0.00	0.30	0.00	6.00	0.00	0.30	tr	0.00	0.00	0.70	0.30	0.70	1.00	0.00	9.30	5.30	3.00	1.30	5.00	0.00	15.50	1.52	0.501	10.00
211/18-N7	Etive	Estuarine channel	15369.00	4684.47	Medium Sand (Upper) - Coarse Sand (Lower)	250	Poor (1.1)	39.30	25.70	65.00	8.30	2.70	11.00	1.70	0.30	0.30	0.00	0.00	0.00	0.00	0.00	0.70	0.00	5.30	0.00	tr	0.00	0.00	0.00	tr	tr	3.30	0.00	0.00	9.30	8.30	tr	2.30	6.30	0.00	19.00	25.50	5.959	28.00
211/18-N7	Etive	Estuarine channel	15463.00	4713.12	Medium Sand (Lower-Upper)	190	Poor (1.1)	44.30	6.00	50.30	7.70	2.70	10.30	0.30	6.00	6.00	0.00	0.00	0.00	0.00	0.00	0.00	0.30	1.30	0.00	0.30	tr	0.00	0.00	0.70	2.00	3.70	0.70	0.30	9.30	tr	15.70	1.70	6.30	0.00	15.70	4.00	1.082	10.00
211/18-N7	Etive	Estuarine channel	15480.00	4718.30	Medium Sand (Lower-Upper)	400	Poor (1.2)	32.30	21.00	53.50	10.00	2.70	12.70	0.30	1.00	1.70	0.70	0.00	20.70	0.00	0.00	tr	0.00	0.70	0.00	0.00	0.30	0.00	0.00	0.00	0.00	3.00	0.00	0.00	24.70	3.30	0.70	0.30	2.30	0.00	18.90	126.00	1.163	10.00
211/18-N7	Rannoch	Lower shoreface	15391.00	4691.18	Fine Sand (Lower-Upper)	190	Good (0.5)	39.70	8.30	48.00	12.70	1.00	13.70	0.00	0.00	15.70	1.30	0.00	0.30	0.00	0.00	0.00	0.00	15.00	0.00	1.70	tr	0.00	0.00	0.00	0.30	1.00	tr	tr	18.30	1.30	0.00	1.70	1.70	0.00	10.70	0.17	0	0.00
211/18-N7	Rannoch	Lower shoreface	15404.00	4695.14	Fine Sand (Upper)	175	Good (0.5)	51.30	2.30	53.70	10.30	2.00	12.30	0.30	0.00	6.30	0.70	0.00	0.70	0.00	0.00	1.00	0.00	9.00	0.00	1.70	0.00	0.00	0.00	0.00	0.70	0.30	4.00	0.00	tr	17.30	4.70	0.00	1.70	0.70	0.00	7.30	0.05	0	0.00
211/18-N7	Rannoch	Lower shoreface	15443.00	4707.03	Fine Sand (Upper)	920	Good (0.5)	31.70	6.00	37.70	15.00	2.30	17.30	1.00	0.00	22.00	2.70	0.00	1.00	0.00	3.30	0.30	0.00	7.00	0.00	0.30	0.30	0.00	0.00	0.00	0.30	5.00	0.00	tr	17.70	0.70	0.00	1.00	12.00	0.00	15.00	746.00	17.6	72.00
211/18-N7	Rannoch	Lower shoreface	15505.00	4725.92	Fine Sand (Lower-Upper)	500	Good (0.5)	35.00	5.00	40.00	15.30	1.70	17.00	0.00	0.30	22.30	4.30	0.00	0.00	0.00	0.00	0.30	0.00	6.00	0.00	0.00	0.00	0.00	0.00	0.70	1.00	7.30	0.00	0.00	15.30	0.70	0.00	0.00	14.30	0.00	14.90	291.00	10.54	50.00

Table 6.1. Texture and mineralogy by sample (Data supplied by Natural Environment Research Council, item ID: 123897). Tr = trace. Average clay coat coverage and clay coat abundance, obtained during this study is also shown.

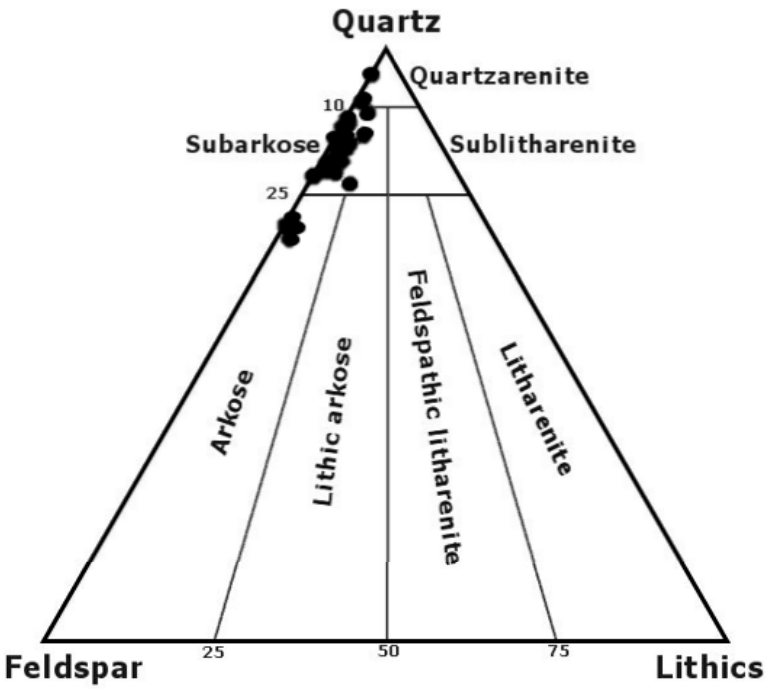


Figure 6.12. QFL plot of samples from northern North Sea block 211/18. N=33.

6.3.3 Authigenic chlorite clay-coated grains

As mentioned above, authigenic chlorite coats made up <1% of the bulk mineralogy of samples. The chlorite clay coats exhibited a double-layered structure, with a dense inner rim parallel to the surface of the detrital quartz grain and a fibrous outer rim which is perpendicular to the inner layer.

Table 6.2 displays the minimum, maximum, average, and standard deviation of clay coat abundance and clay coat coverage for each depositional facies.

Average clay coat coverage was low and did not exceed 31%. The average clay-coat grain coverage varied considerably within facies. The standard deviation for clay coat abundance (%) and average clay coat coverage (%) was high within facies indicating a

wide spread of values. On average, lower shoreface and upper shoreface samples had the highest average clay coat coverage (%) and highest clay coat abundance.

Facies	Clay coat abundance (%)					Average clay coat coverage (%)				
	Number of samples	Min	Max	Average	Standard Deviation	Number of samples	Min	Max	Average	Standard Deviation
Barrier	4.00	0.00	68.00	26.50	30.44	4.00	0.00	13.24	4.46	6.07
Distal shoreface	2.00	12.00	44.00	28.00	22.63	2.00	1.05	8.72	4.88	5.42
Estuarine channel	11.00	4.00	96.00	35.82	26.48	11.00	0.22	30.82	6.66	8.44
Lower shoreface	9.00	0.00	86.00	45.11	32.00	9.00	0.00	18.97	8.50	7.07
Upper shoreface	7.00	0.00	80.00	45.71	27.77	7.00	0.50	19.73	8.61	6.68

Table 6.2. Clay coat coverage and clay coat abundance statistics by facies.

6.3.4 Paragenesis of authigenic phases

The relative timing of authigenic phases was established based on thin section observations and is summarised in Figure 6.13. Nodular siderite formation appears to be the first post-depositional event, due to it being enclosed by all other authigenic phases. Chloritization of precursor clay minerals appears to be synchronous with quartz overgrowth formation, due to chlorite coats inhibiting quartz overgrowth formation in some cases and being enclosed by authigenic quartz in other areas. The dissolution of feldspar seems to span the duration of diagenesis, predating the chloritization of clays and post-dating albite and kaolinite cement phases. Albite and kaolinite cement occur in secondary pores formed during the dissolution of feldspar, which potentially provided potassium and aluminium for these cement phases.

Minor Fe calcite and pore-filling illite cement phases occurred during late diagenesis, as they enclose all other authigenic phases.

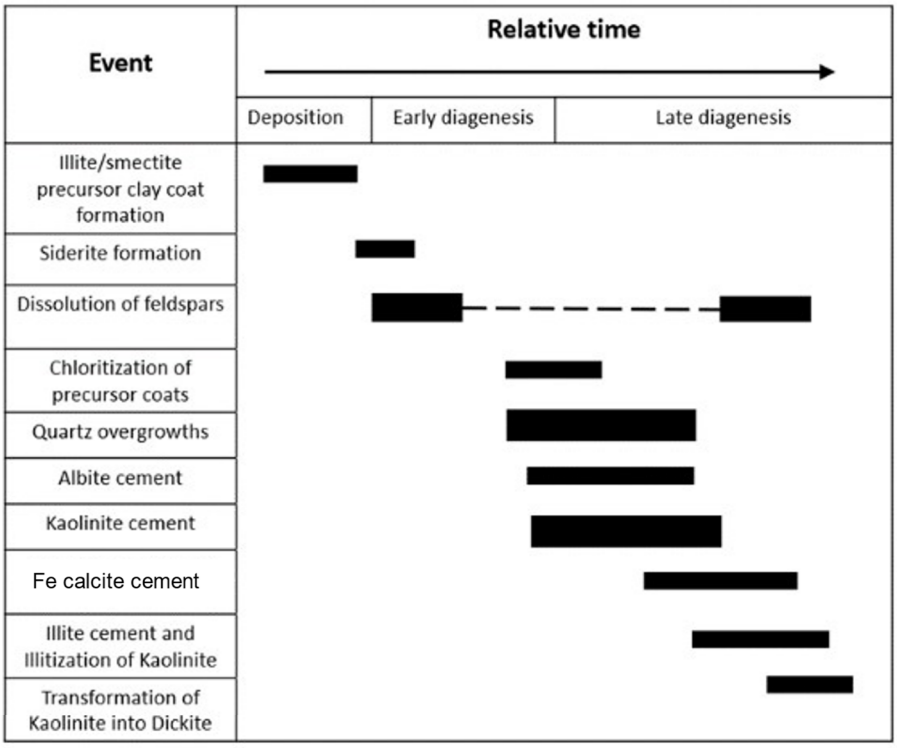


Figure 6.13. Paragenetic sequence based on thin section observations. Length of black bar indicates duration of event. Width of black bar indicates extent of porosity enhancement or destruction during event.

6.3.5 Reservoir quality

Potential reservoir quality was assessed as a function of Helium porosity (%) and horizontal permeability (mD). Figure 6.14 shows a porosity vs permeability plot coloured by facies. Potential reservoir quality varied within single facies. Table 6.3 displays porosity and permeability statistics by facies. The upper shoreface facies had the highest average porosity (18.63%) and highest average permeability (312.16mD). The barrier facies had the lowest average porosity (10.58%) and lowest average permeability (3.17mD).

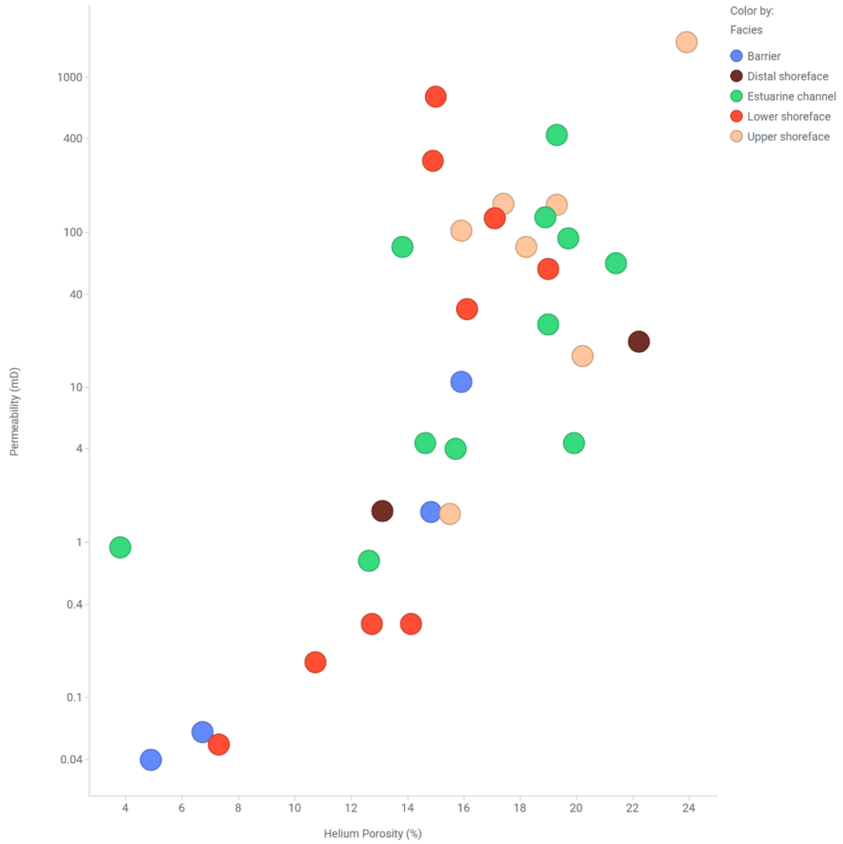


Figure 6.14. Porosity vs permeability of study samples by facies. N=33.

Facies	Helium Porosity (%)					Permeability mD)				
	Number of samples	Min	Max	Average	Standard Deviation	Number of samples	Min	Max	Average	Standard Deviation
Barrier	4.00	4.90	15.90	10.58	5.58	4.00	0.04	11.00	3.17	5.27
Distal shoreface	2.00	13.10	22.20	17.65	6.43	2.00	1.60	20.00	10.80	13.01
Estuarine channel	11.00	3.80	21.40	16.25	5.03	11.00	0.76	425.00	75.21	124.10
Lower shoreface	9.00	7.30	19.00	14.10	3.50	9.00	0.05	746.00	139.10	246.65
Upper shoreface	7.00	15.50	23.90	18.63	2.88	7.00	1.52	1 680.00	312.16	606.06

Table 6.3. Porosity and permeability statistics by facies.

6.3.6 Statistical analysis

Pearson's correlation coefficient analysis was performed to assess the relationship between variables. Table 6.4 displays the R-value and corresponding P-value for each pair of tested variables. P-values higher than 0.05 are considered non-significant.

Helium porosity (%) showed a significant positive relationship with horizontal permeability (R-value of 0.367 and P value of 0.036). Helium porosity (%) also showed a significant negative relationship with total authigenic cement % (R-value of -0.570 and P value of 0.001). Helium porosity showed no significant relationship with any of the other variables (Table 6.4).

Horizontal permeability (mD) had a significant positive relationship with Helium porosity (as mentioned above) and total authigenic cement content (R-value of -0.570 and P value of 0.001). Horizontal permeability (mD) had no significant relationship with any of the other variables.

Average clay-coat coverage (%) had a significant positive relationship with grain size (R-value of 0.367 and P value of 0.036). Clay-coat abundance (%) also had a significant positive relationship with grain size (R-value of 0.499 and P value of 0.003).

Average clay-coat coverage % and clay coat abundance % had no significant relationship with quartz overgrowth %. Clay coat abundance showed a significant negative correlation with total authigenic cement % (R-value of -0.448 and P value of 0.009).

Quartz overgrowth content % showed a significant positive relationship with sorting (R-value of 0.353 and P value of 0.004) and with total authigenic cement (R-value of 0.403 and P value of 0.020). Quartz overgrowth content % showed no significant relationship with any other variables.

Kaolinite % had a significant negative relationship with clay coat abundance % (R-value of -0.433 and P value of 0.118) and positive relationship with total authigenic cement % (R-value of 0.642 and P value of <0.000).

Fe calcite showed a significant negative correlation with sorting (R-value of -0.520 and P value of 0.0

Pearson's R -value (P - value)	Grain size	Sorting	Detrital clay %	Fe calcite %	Siderite %	Albite %	Kaolinite %	Illite %	Quartz overgrowth %	Total authigenic cement %	Average clay coat coverage %	Clay coat abundance %	Helium porosity %	Horizontal permeability mD
Grain size	X	-0.482 (0.005)	-0.162 (0.368)	0.047 (0.795)	0.137 (0.447)	-0.255 (0.152)	-0.135 (0.454)	-0.091 (0.615)	-0.071 (0.695)	-0.215 (0.230)	0.516 (0.002)	0.499 (0.003)	0.056 (0.757)	0.189 (0.292)
Sorting	-0.482 (0.005)	X	0.217 (0.225)	-0.520 (0.002)	0.215 (0.230)	0.210 (0.241)	0.060 (0.740)	0.078 (0.666)	0.353 (0.044)	0.036 (0.842)	-0.043 (0.812)	-0.026 (0.886)	0.060 (0.740)	0.052 (0.774)
Detrital clay %	-0.162 (0.368)	0.217 (0.225)	X	-0.135 (0.454)	0.159 (0.377)	0.312 (0.077)	0.188 (0.295)	-0.065 (0.719)	-0.065 (0.719)	0.123 (0.495)	-0.130 (0.471)	-0.015 (0.934)	0.008 (0.965)	-0.266 (0.135)
Fe calcite %	0.047 (0.795)	-0.520 (0.002)	-0.135 (0.454)	X	-0.188 (0.295)	-0.045 (0.804)	-0.036 (0.842)	-0.185 (0.303)	-0.278 (0.117)	0.370 (0.034)	-0.202 (0.260)	-0.278 (0.117)	-0.018 (0.921)	-0.245 (0.169)
Siderite %	0.137 (0.447)	0.215 (0.230)	0.159 (0.377)	-0.188 (0.295)	X	-0.152 (0.398)	0.025 (0.890)	-0.089 (0.622)	-0.030 (0.868)	0.020 (0.912)	0.049 (0.787)	0.152 (0.398)	0.090 (0.618)	-0.043 (0.812)
Albite %	-0.255 (0.152)	0.210 (0.241)	0.312 (0.077)	-0.045 (0.804)	-0.152 (0.398)	X	-0.127 (0.481)	-0.119 (0.510)	0.183 (0.308)	0.110 (0.542)	-0.329 (0.62)	-0.228 (0.202)	-0.018 (0.921)	-0.245 (0.169)
Kaolinite %	-0.135 (0.454)	0.060 (0.740)	0.188 (0.295)	-0.036 (0.842)	0.025 (0.890)	-0.127 (0.481)	X	-0.247 (0.166)	-0.071 (0.695)	0.642 (<0.000)	-0.291 (0.100)	-0.433 (0.118)	-0.337 (0.551)	-0.321 (0.069)
Illite %	-0.091 (0.615)	0.078 (0.666)	-0.065 (0.719)	-0.185 (0.303)	-0.089 (0.622)	-0.119 (0.510)	-0.247 (0.166)	X	0.147 (0.414)	-0.104 (0.565)	0.119 (0.510)	0.195 (0.277)	0.013 (0.943)	-0.233 (0.191)
Quartz overgrowth %	-0.071 (0.695)	0.353 (0.044)	-0.065 (0.719)	-0.278 (0.117)	-0.030 (0.868)	0.183 (0.308)	-0.071 (0.695)	0.147 (0.414)	X	0.403 (0.020)	0.191 (0.287)	0.161 (0.371)	-0.265 (0.136)	-0.102 (0.572)
Total authigenic cement %	-0.215 (0.230)	0.036 (0.842)	0.123 (0.495)	0.370 (0.034)	0.020 (0.912)	0.110 (0.542)	0.642 (<0.000)	-0.104 (0.565)	0.403 (0.020)	X	-0.308 (0.081)	-0.448 (0.009)	-0.570 (0.001)	-0.430 (0.013)
Average clay coat coverage %	0.516 (0.002)	-0.043 (0.812)	-0.130 (0.471)	-0.202 (0.260)	0.049 (0.787)	-0.329 (0.62)	-0.291 (0.100)	0.119 (0.510)	0.191 (0.287)	-0.308 (0.081)	X	0.916 (<0.000)	0.339 (0.054)	0.180 (0.316)
Clay coat abundance %	0.499 (0.003)	-0.026 (0.886)	-0.015 (0.934)	-0.278 (0.117)	0.152 (0.398)	-0.228 (0.202)	-0.433 (0.118)	0.195 (0.277)	0.161 (0.371)	-0.448 (0.009)	0.916 (<0.000)	X	0.332 (0.059)	0.210 (0.241)
Helium porosity %	0.056 (0.757)	0.060 (0.740)	0.008 (0.965)	-0.018 (0.921)	0.090 (0.618)	-0.018 (0.921)	-0.337 (0.551)	0.013 (0.943)	-0.265 (0.136)	-0.570 (0.001)	0.339 (0.054)	0.332 (0.059)	X	0.367 (0.036)
Horizontal permeability mD	0.189 (0.292)	0.052 (0.774)	-0.266 (0.135)	-0.245 (0.169)	-0.043 (0.812)	-0.245 (0.169)	-0.321 (0.069)	-0.233 (0.191)	-0.102 (0.572)	-0.430 (0.013)	0.180 (0.316)	0.210 (0.241)	0.367 (0.036)	X

Table 6.4. Correlation matrix for North Sea petrography data. P-values for each R-value are in brackets. P-values below 0.05 (significant) are in black text and P-values higher than 0.05 (non-significant) are in red text. Positive correlations are in green boxes, whereas negative correlations are in orange boxes. White boxes represent R-values between -0.2 and 0.

6.4 Discussion

This Chapter focused on the research theme “The origin and distribution of clay-coated grains in ancient sandstone reservoirs” which is fully outlined in chapter 1.7.3. The key research questions addressed in this chapter were:

- What are the textural and depositional controls on the formation of clay-coated grains in the ancient reservoir case study?
- What is the origin of clay-coated grains present in the ancient sandstone reservoir case study?
- How does the distribution of chlorite coats in the ancient case study compare to the distribution of precursor clay coats in the shallow marine modern analogue system?

6.4.1 Textural and depositional controls on the formation of clay-coated grains

Previous studies (Pitman et al., 1992; Wilson, 1992) that suggested clay coats tend to be more extensively developed in fine grained sediment compared to coarser grained sediment because coarser grains are more rounded and therefore less likely to have embayments which house clay coats on their surface. Conversely, a more recent study, focused on the origin of chlorite-coated grains in the Upper Triassic Xujiahe Sandstones in the Guang’an Area, Sichuan Basin, linked chlorite coat formation to the presence of a high energy environment and thus coarser grained sediment (Cao et al., 2018). Chlorite coats, surrounding medium-grained quartz grains in the Guang’an Area were interpreted to have formed due to a strong hydrodynamic tractive current causing a relative motion between saltating sand-sized grains and suspended clays in the water column (Cao et al., 2018). The velocity difference created a local flow pressure which caused clay particles to coat saltating medium sand-sized grains, which was explained via Bernoulli’s theory (Cao et al., 2018).

Average clay-coat coverage (%) showed a significant positive relationship with grain size (R-value of 0.367 and P value of 0.036). Clay-coat abundance (%) also showed a significant positive relationship with grain size (R-value of 0.499 and P value of 0.003). This suggests that in this case study clay coat coverage increased with increasing grain size. Average clay coat coverage and clay coat abundance showed no significant relationship with sorting.

Clay coat coverage varied across depositional facies with no clear trend.

Clay coat coverage was low in the ancient case study, therefore interpretation made in this study may be unreliable. It is recommended to repeat the workflow used in this study for an ancient case study with a higher average clay coat coverage to fully understand the textural and depositional controls on formation of clay-coated grains.

6.4.2 The origin of clay-coated grains

Previous studies of the Brent Group have interpreted early clay coatings as detrital in origin, linked to emplacement via infiltration (Giles et al., 1992; McBride, 1992).

Overall, clay coat coverage was low which made it difficult to determine the origin of clay coated grains.

Chlorite clay coats in this study exhibited a double-layered structure, with a dense inner rim parallel to the surface of the detrital quartz grain and a fibrous outer rim. This structure is similar to that reported in other studies of chlorite-coated reservoirs such as chlorite coats present in reservoir units of the Upper Triassic Xujiaha Sandstone in the Guang'an Area of the Sichuan Basin (Cao et al., 2018). The internal rim on clay coats in this study may suggest they formed via the thermal alteration of a precursor detrital clay coat. SEM images reveal detrital illite/smectite, which has become flaky due to compression, forming a thin coating on detrital quartz grains (Figure 6.15). The detrital illite/smectite coat may represent a precursor to chlorite coats.

The chloritization of precursor clay coats appears to be synchronous with quartz overgrowth formation, due to chlorite coats inhibiting quartz overgrowth formation in some areas and being enclosed by authigenic quartz in other areas.

Thin section observations indicate an extensive period of feldspar dissolution, which may have provided a local source of aluminium and silica to facilitate the formation of chlorite. Similarly, Kantorowicz (1984) hypothesized early-pore filling chlorite present in the Brent Group reservoirs formed from interstitial saline pore waters 'sufficiently saturated with silica and aluminium'.

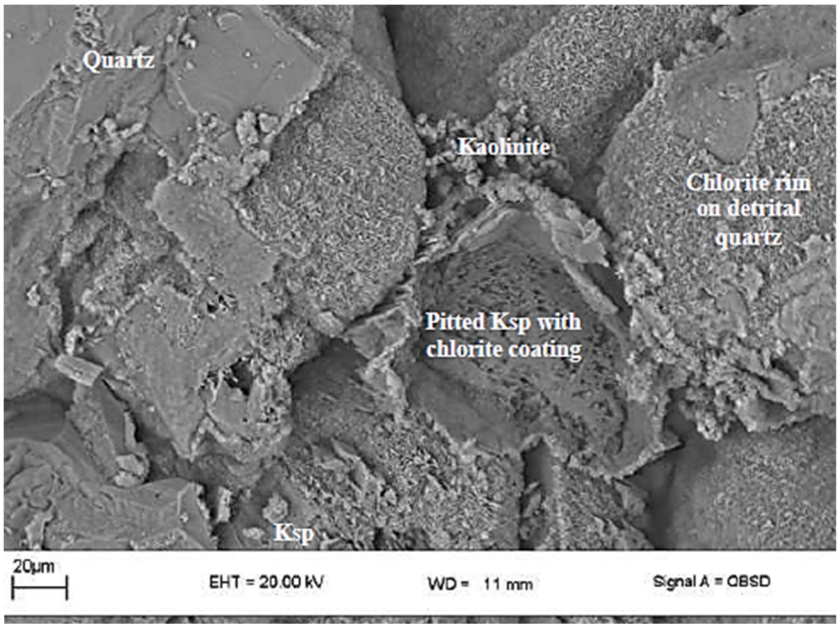


Figure 6.15. SEM image of well-developed chlorite coats in estuarine channel sample in well 211/18a-N7 at 15463ft. (Natural Environment Research Council, item ID: 123897).

In this study clay coat grain coverage was low and showed not significant relationship with porosity, permeability or quartz overgrowths.

Figure 6.16 displays a schematic diagram of authigenic clay coat formation and typical impact on reservoir quality based on other published studies (Bloch et al., 2002; Billault et al., 2003; Lander et al., 2008; Cao et al., 2018). Clay coats typically form via the thermal alternation of precursor detrital clay coats such as berthierine (Bloch et al., 2002; Billault et al., 2003; Lander et al., 2008). Clay coated grains allow a higher volume of primary porosity to be preserved compared to non-clay coated grains by inhibiting quartz overgrowths (Figure 6.16). Authigenic clay coats typically form perpendicular to the precursor clay coats (Cao et al., 2018). Note that authentic clay coats do not prevent the formation of blocky carbonate cements (Figure 6.16).

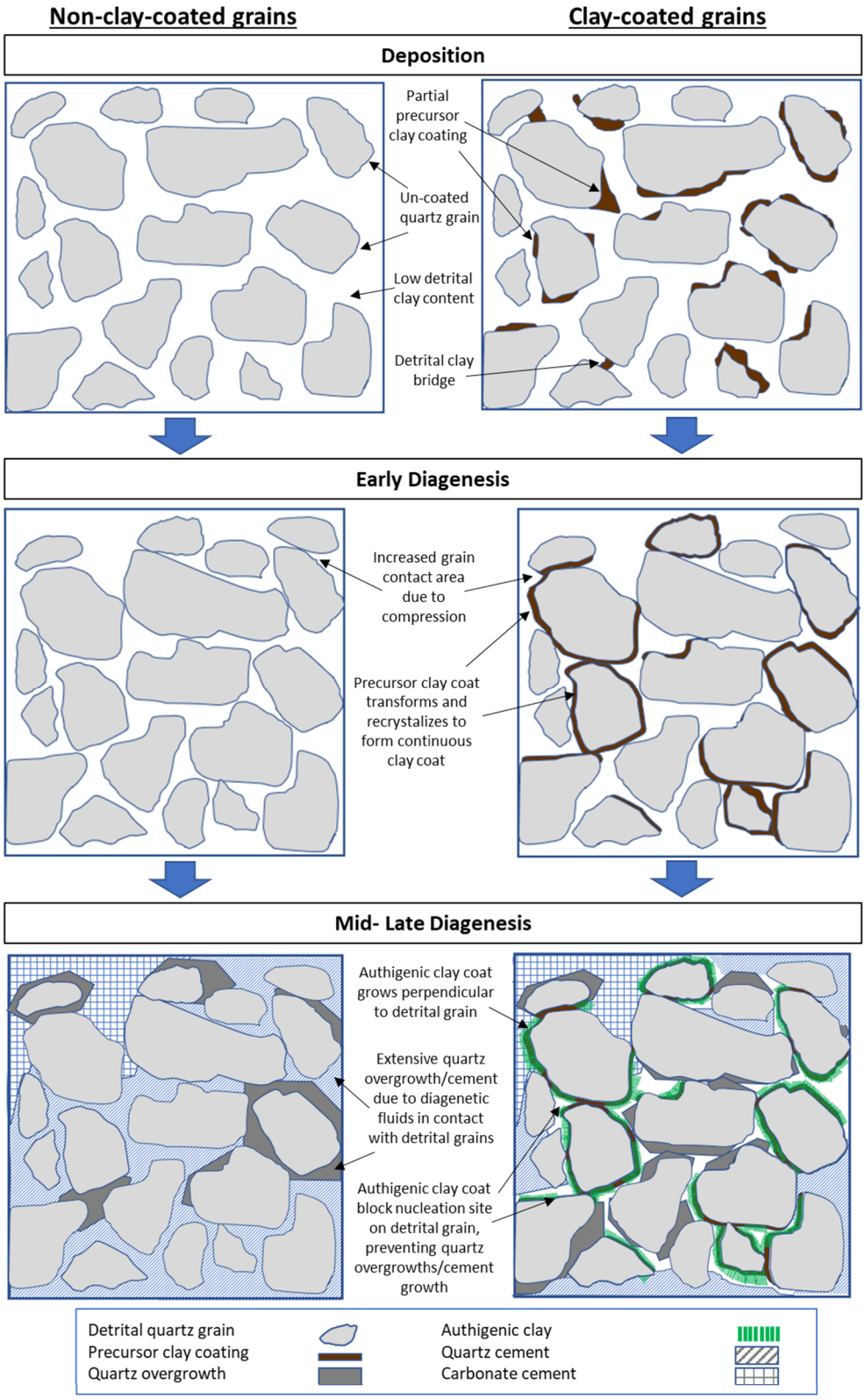


Figure 6.16. Schematic diagram of authigenic clay coat formation and impact on reservoir quality.

6.4.3 Comparison of clay coated grains in the ancient case study and the shallow marine modern analogue system

Clay coat coverage was lower in the ancient case study compared to the shallow marine modern analogue study.

Chapter 3 and chapter 4 found that clay coat grain coverage increases with increasing EPS content. Clay coat coverage and EPS content within the modern analogue shallow marine study (Ravenglass Estuary) varied based on depositional setting. Average clay coat coverage in Ravenglass Estuary was highest in intertidal sub depositional environments such as mixed flats and mud flats. In the ancient case study clay coat coverage showed no trend with sub depositional environment.

In the ancient case study average clay-coat coverage (%) and clay-coat abundance (%) showed a significant positive relationship with grain size. Whereas, in the modern analogue shallow marine study, average clay coat coverage showed a significant negative relationship with grain size.

The chlorite coated grains present in the ancient case study appear to have formed from the thermal transformation of precursor detrital clay coats. The clay coated grains observed in Ravenglass Estuary may potentially represent similar precursor clay coats to the chlorite coats observed in the ancient case study.

A different ancient case study with a higher content of chlorite coats and samples from more sub depositional environments such as tidal bars and sand flats should be considered in future research.

6.5 Conclusion

Detailed petrographic analysis of samples from the Mid Jurassic Brent group present in the Block 211/18 was carried out to understand the formation and distribution of chlorite coated grains.

There was a lack of clay coated grains in this study which made it difficult to achieve this aim. Clay coat coverage and clay coat abundance showed no significant relationship with

quartz overgrowth. Statistical analysis indicates that total authigenic cement is the main control on porosity and permeability.

The trace amounts of chlorite coats that were present display an internal rim which may indicate they formed via the thermal transformation of a precursor detrital clay coat.

It is recommended to repeat the workflow used in this study for an ancient case study with a higher average clay coat coverage to fully understand the textural and depositional controls on formation of clay-coated grains.

Chapter 7. Summary and further work

7.1 Overview

This thesis reports the results from a series of studies related to understanding the formation of precursor clay-coated grains in modern analogues and the origin and distribution of chlorite clay-coated grains in ancient subsurface sandstone reservoirs.

This study adopted a multifaceted approach which combined data and observations from ancient and modern analogues, clay coat synthesis laboratory experiments and clay coat pressure chamber experiments.

A total of ten key research questions were identified. The ten research questions were grouped into three main themes 1) The origin and distribution of precursor clay-coated grains in shallow marine and deep-water turbidite systems 2) The transformation of precursor clay-coated grains during burial and diagenesis 3) The origin and distribution of clay-coated grains in ancient sandstone reservoirs.

This chapter aims to answer the ten main research questions posed in Chapter 1 and suggest potential research areas for further work.

7.2 The origin and distribution of precursor clay-coated grains in shallow marine and deep-water turbidite systems

7.2.1 How does EPS content and salinity impact the formation of clay-coated grains in the clay coat synthesis experiments?

In Chapter 3, the impact of EPS content and salinity on the formation of clay coated grains was investigated via a series of abiotic and biotic laboratory clay coat synthesis experiments.

During the abiotic clay coat synthesis experiments there was an increase in clay coat coverage as EPS content (measured via total carbohydrate content) increased. This indicates that EPS, produced by microorganisms such as diatoms enhances the formation of clay coats by acting as an adhesive substance which allows clay particles to stick to

quartz grains. This supports published studies which suggest biofilms play a vital role in the formation of clay coated grains (Jones, 2017; Wooldridge et al., 2017a).

EPS are common to almost all aquatic systems (Stal, 2003) and likely promote the formation of clay coated grains in modern systems such as Ravenglass Estuary (Wooldridge et al., 2017a) and the Gironde Estuary (Virolle et al., 2018). To date, there are limited studies on the interaction of EPS and clay particles in other depositional settings such as fluvial systems and lakes. Future studies should determine if biofilms promote the formation of clay coated grains in other depositional settings.

In the abiotic clay coat synthesis laboratory experiments clay coat coverage was found to increase with increasing salinity. This increase is likely a result of the high concentration of electrolytes decreasing the size of the repulsive field surrounding clay particles, which increases the chances of clay particles colliding and interacting with quartz grains. As salinity increased, clay particles formed floccules which were co-deposited with quartz grains. The increase in clay-coat coverage with increasing salinity observed in the clay coat synthesis experiments disagrees with clay-coat coverage distribution trends observed in natural estuarine systems such as Ravenglass Estuary (Wooldridge et al., 2017a) and the Gironde Estuary (Virolle et al., 2018). In these two modern estuarine systems there is a decrease in clay-coat coverage seaward as salinity increases. The seaward reduction in clay-coated grains observed in modern estuarine settings is likely related to the removal of clay coats during sediment transportation, where clay-coats are rapidly removed due to extensive grain collision (Wilson 1992).

Future studies should focus on investigating the effect of clay mineralogy (kaolinite vs illite etc) on the formation of clay-coated grains in marine settings and on fully understanding the mechanisms involved in the formation of clay-coated grains in other depositional environments.

7.2.2 How is EPS distributed across modern shallow marine and deep-water turbidite system analogues?

Total carbohydrate content and chlorophyll-a content were used as proxies for EPS abundance in this study.

In Bute Inlet, sediment from the distal lobe had the highest EPS concentration. A study of organic matter distribution across Bute Inlet concluded that organic matter is mainly sourced from the proximal shallow marine section of the system and transported to the lobe (Hauge et al., 2021). EPS measured in the distal lobe likely reflect EPS produced in shallow marine conditions which has been transported to the distal lobe via turbidity currents. However, EPS could also be produced in deep water settings by planktonic microorganisms within the water column. Future studies of EPS distribution within deep water systems should aim to distinguish where EPS present in distal lobes is predominantly transported from shallow marine settings or sourced from the overlying water column. Future studies could also consider how the properties of EPS (such as chemical composition) vary depending on what microorganisms produced the EPS (diatoms, cyanobacteria etc).

In Ravenglass Estuary, the highest EPS content was found in intertidal settings such as mud flats and mixed flats. EPS was typically higher in depositional environments with a high clay content. EPS within Ravenglass Estuary is known to be mainly produced by epilithic diatoms (Wooldridge et al., 2017a). The increase in EPS content with increasing clay content likely reflects the higher abundance of clay minerals in lower energy environment which experience less disturbance (e.g. mudflat) which are more preferential for diatoms (Stal, 2003).

7.2.3 Is there a relationship between EPS content and clay coat coverage in modern shallow marine and deep-water turbidite system analogues?

Overall, clay coat coverage was lower in Bute Inlet compared to Ravenglass Estuary. Yet both systems had a similar range of total carbohydrate content (EPS).

In Bute Inlet, average clay coat coverage showed no statistical relationship with total carbohydrate or *chlorophyll-a* content (proxies for EPS content). This suggests the minor amount of clay coated grains which were present in Bute Inlet do not form in association with biofilms. Future studies should research the distribution of clay coated grain in other deep-water settings. This would confirm if clay coated grains are consistently lower in deep water systems compared to shallow marine systems.

In Ravenglass Estuary, average clay coat coverage showed a significant positive correlation with both chlorophyll-a content and total carbohydrate content. Clay minerals were also seen attached to EPS stalks in sediment from Ravenglass Estuary via SEM analysis. Overall, this indicates that biofilms play a key role in the formation of clay coated grains in shallow marine environments, supporting the hypothesis put forward by Wooldridge et al (2017a). However, the results from the clay coat synthesis experiments carried out in Chapter 3 suggests that clay coats can form without EPS. Overall, this suggests that EPS enhances the formation of clay coated grains but is not completely necessary to form clay coated grains.

Future studies should investigate how durable clay coats are and if they have the potential to be transported and preserved in an offshore setting.

7.2.4 What are the textural and depositional controls on clay coat formation in modern shallow marine and deep-water turbidite system analogues?

As mentioned above, Bute Inlet had lower levels of average clay coat coverage compared to Ravenglass Estuary. Therefore, the relationships between clay coat coverage and textural and depositional controls described for Bute Inlet are limited. This study was limited to only 15 thin sections, covering 5 depositional environments. A future high-resolution study of the surface distribution of clay-coated grains in Bute Inlet or a similar modern analogue with a higher content of clay coated grains would help improve the understanding of the depositional controls on the formation of clay-coated grains in deep-water turbidite systems.

In Ravenglass Estuary, average clay coat grain coverage had a significant positive relationship with clay fraction content and a negative correlation with mean grain size. The highest clay-coat coverage was observed in sediment samples from mud and mixed flats. Mixed flat and mud flat facies in ancient systems would typically be considered non reservoir due to a high content of detrital mud. Therefore, a threshold exists where enough clay material is required to coat quartz grains but not too much to inhibit pore space. Tidal bar and sand flats may represent facies which meet these criteria.

7.2.5 How are precursor clay-coated grains formed in modern shallow marine and deep-water turbidite system analogues?

In Ravenglass Estuary, average clay coat coverage was highest in areas with the highest EPS content such as mixed flats and mud flats. SEM analysis of sediment from Ravenglass Estuary showed clay particles are often attached to EPS strands secreted by diatoms. This shows that EPS acts as a binding material for clay particles on the surface of quartz grains. The clay coat synthesis experiments outlined in Chapter 3 found an increase in clay coat coverage with increasing EPS content where clay content was kept constant. However, clay coated grains were also formed in abiotic clay coat synthesis experiments which had no EPS present. Overall, EPS within shallow marine systems likely assists the formation of clay coats by acting as a binding agent between clay particles and quartz grains. However, EPS is not absolutely essential for the formation of clay coated grains and clay coated grains can form in the absence of EPS.

Clay coat coverage in Bute Inlet was lower compared to Ravenglass Estuary. This made it difficult to determine how exactly clay coats within Bute Inlet formed. As mentioned above, future studies should research the distribution of clay coated grain in other deep-water settings. This would confirm if clay coated grains are consistently lower in deep water systems compared to shallow marine systems and how exactly clay coats within deep-water systems form.

7.3 The transformation of precursor clay coats during burial and diagenesis

7.3.1 How do precursor clay mineral coats transform during diagenesis to form authigenic clay mineral coats?

A series of pressure chamber experiments were carried out to observe how precursor clay coats collected from Ravenglass Estuary transformed under different temperature ranges. Clay coat coverage did not increase by a major amount during the pressure chamber experiments.

In the 150°C and 250°C experiments precursor clay coats were transformed to form an authigenic frost-like mineral coating. This authigenic mineral is thought to be chlorite based on EDS and QEMSCAN analysis.

An authigenic mineral with a rosette morphology was also formed during the 250°C pressure chamber experiment. Originally, this mineral was thought to be chlorite, due to its morphology. EDS analysis of the rosette mineral indicate it has a composition which is dominated by calcium, sodium and silica with little to no iron and magnesium. The rosette mineral may be a calcium silicate or gypsum which has been formed as a biproduct of the pressure chamber experiment.

The QEMSCAN analysis of samples from the pressure chamber experiment indicates that authigenic coats present in samples from the 150 and 250°C experiments often appear to have a chlorite outer rim and feldspar inner rim. This may indicate that chlorite formed via the transformation of feldspars, where chlorite grows outwards from feldspar crystals. Feldspar typically transforms to form illitic clay and kaolinite during diagenesis (Haile et al., 2015) and not chlorite. However, the transformation of detrital feldspar to form authigenic chlorite observed in this study has also been identified in Upper Proterozoic sandstones from southern Sweden (Morad and AlDahan, 1987) and may have occurred during the pressure chamber experiments in this study.

7.3.2 Are authigenic clay coats formed during pressure chamber experiments comparable to authigenic clay coats present in natural settings?

Clay-coated grains present in modern analogues display a range of morphologies, including clay floccules, discontinuous clay coats and clay bridges (Dowey et al., 2012; Wooldridge et al., 2017; Virolle et al., 2018). Chlorite coats present in ancient subsurface sandstone reservoirs usually display a continuous morphology (Ehrenberg, 1993; Salem et al., 2005; Cao et al., 2018).

Authigenic clay mineral coats formed in the pressure chamber experiments ran at 60,90 and 150°C had a similar iron rich mineralogy to chlorite coats present in natural sandstone reservoir. The morphology of authigenic clay coats in the pressure chamber experiments, captured via SEM, ranged from frost like coatings to needle authigenic crystal coatings. Chlorite coats in natural sandstone reservoirs typically have a rosette morphology. The difference in the morphology of chlorite observed in the pressure chamber experiments and in ancient analogues may be due to the experiment limitations. Chlorite in natural reservoirs typically forms over millions of years. The pressure chamber experiments were limited to several days.

The pressure chamber experiments were also limited to a pressure of 10MPa. Future studies should try replicate the transformation of precursor clays coats from a modern analogue with more realistic pressure conditions. A detailed study of the morphology of chlorite coats with depth from published literature would also help improve the understanding of the transformation of precursor clay coats.

7.4 *The origin and distribution of clay-coated grains in ancient sandstone reservoirs*

7.4.1 What are the textural and depositional controls on the formation of clay-coated grains in the ancient reservoir case study?

Overall, the ancient case study had a low average clay coat coverage which made the case study unsuitable for determining the textural and depositional controls on the formation of clay-coated grains.

Pearson's coefficient analysis was performed on data collected from the three wells to identify significant relationships existing between variables. Average clay-coat coverage (%) had a significant positive relationship with grain size (R-value of 0.367 and P value of 0.036). Clay-coat abundance (%) also had a significant positive relationship with grain size (R-value of 0.499 and P value of 0.003). This result contradicts previous studies (Pitman 1992; Wilson, 1992) that suggest clay coats tend to be more extensively developed in fine grained sediment compared to coarser grained sediment, due to coarser grains being more rounded and therefore less likely to have embayments which house clay coats on their surface. However, a more recent study, which researches the origin of chlorite-coated grains in the Upper Triassic Xujiahe Sandstones in the Guang'an Area, Sichuan Basin, linked chlorite coat formation to the presence of a high energy environment and thus coarser grained sediment (Cao et al., 2018).

Average clay-coat coverage % and clay coat abundance % had no significant relationship with quartz overgrowth %. This suggests that clay coats did not inhibit quartz overgrowths.

Thin section and SEM analysis indicated clay-coat coverage (average percentage of the perimeter of a sand grain which is coated) and clay-coat abundance (percentage of grains

in a sample which are coated) varied within a single facies within the Mid Jurassic Brent Group case study.

Clay coats within the ancient case study are typically discontinuous, with a maximum grain coat coverage of 36%. Clay coat coverage was not high enough to completely inhibit the formation of quartz overgrowths.

This study was limited by the number of samples used in the analysis (33 samples from three cores), where a larger dataset would increase the reliability of trends identified and help define the relationship between textural parameters and clay-coated grains. Future studies should aim to collect data from multiple hydrocarbon provinces and repeat the workflow used in this study to determine the textural and non-textural controls on clay-coat coverage and abundance. Data that capture both large scale trends and facies scale variations is essential for modelling the subsurface distribution of clay-coated grains and for ranking and de-risking potential hydrocarbon plays and prospects.

7.4.2 What is the origin of clay-coated grains present in the ancient sandstone reservoir case study?

Chlorite coats in the ancient case study appear to have formed via the thermal transformation of a precursor detrital clay coat. The chloritization of precursor clay coats appears to be synchronous with quartz overgrowth formation, due to chlorite coats inhibiting quartz overgrowth formation on a local level in some areas and being enclosed by authigenic quartz in other areas.

Chlorite clay coats present in the Mid Jurassic Brent Group case study displayed a double-layered structure, with a dense inner rim parallel to the surface of the detrital quartz grain and a fibrous outer rim which is perpendicular to the inner layer. This structure is similar to chlorite coats present in other studies (Cao et al., 2018). SEM analysis revealed the presence of detrital illite/smectite coatings which are interpreted as representing the precursor to chlorite coats.

7.4.3 How does the distribution of chlorite coats in the ancient case study compare to the distribution of precursor clay coats in the shallow marine modern analogue system?

The results from the shallow marine modern analogue study suggest that clay coats are most abundant in intertidal depositional settings such as mud flat and mixed flat. Mud and mixed flats typically have a high detrital clay content, which makes them unsuitable as hydrocarbon reservoirs. In the shallow marine modern analogue study, sand flats and tidal bars were found to have a higher clay coat coverage than upper shoreface deposits. Tidal bar and sand flat deposits likely represent the facies with the most optimum volume of clay minerals to form clay coated grains and not form a pore-filling clay matrix.

Unfortunately, clay coat coverage was low in the ancient case study (maximum of 36%). There was also a lack of overlap between the facies present in the modern analogue and the facies observed in the ancient case study. This made it difficult to understand the link between clay coat distribution in the shallow marine modern-day analogue and the shallow marine ancient case study.

Future studies should consider a more suitable ancient case study with a higher content of clay coated grains. This would allow a better understanding of how the distribution of clay coated grains in a modern analogue such as Ravenglass Estuary relates to ancient subsurface chlorite coated sandstone reservoirs.

7.5 The wider importance of EPS

In this study biofilms were identified as having a key role in the formation of detrital clay-coated grains in shallow marine systems. Biofilms were observed to form an adhesive layer on sand grains which acts as a binding site for clay mineral attachment.

Other studies which have investigated biofilm-sediment interactions conclude that biofilms exhibit an unprecedented influence on the cohesion and dynamics of sediment (Stal, 2003; Malarkey et al., 2015; Garwood et al., 2015).

For example, in a series of flume tank experiments where xanthan gum was used as a proxy for EPS, the formation of sediment bedforms such as ripples were limited by small concentrations of EPS (Malarky et al., 2015).

In natural settings, biofilms are reported to significantly increase the cohesion of sediment which influences sediment stability and transport (Malarky et al., 2015).

Biofilms are reported to be present in most modern-day aquatic environments (Stal, 2003) and are thought to date back to 3700 million years (Nutman et al., 2016). Yet, until the past decade, very little literature existed which considered the influence of biofilms on sedimentary systems (Jones, 2017). It is likely that the influence of biofilms on sedimentary structures has been overlooked in traditional sedimentological studies which consider only sediment and fluid interactions.

EPS is also a large store of organic carbon, where marine microorganisms are responsible for balancing greenhouse gas emissions due to their role in carbon sequestration (Ugya, 2023). Climate change is predicted to alter the marine environment, leading to changes in temperature, acidification and oxygen concentration (Godbold and Calosi, 2013). Future studies should focus on understanding how the distribution of EPS in modern systems such as Ravenglass Estuary and Bute Inlet will change with climate change and how this will affect local and global carbon cycles and also sediment dynamics.

7.6 Application of machine learning to clay coat analysis

Machine learning and artificial intelligence (AI) has widely been used to improve the speed and accuracy of data analysis within geology (Rubo et al., 2019). For example, petrophysical attributes have been estimated from image logs from hydrocarbon wells using support vector machine learning algorithms (Valentín et al., 2018).

In a recent study, Rubo et al., (2019) used image segmentation and a machine learning algorithm to generate mineralogical maps and highlight visible porosity with thin sections from pre-salt reservoirs of Santos Basin, on the southeast coast of Brazil. To date, the quantification of clay coat grain coverage is still widely done manually via the method outlined in Wooldridge et al, (2017a). This process is extremely time consuming and is associated with some subjectivity. Industry and academia should prioritize developing a machine learning algorithm that can segment clay coats form a petrographic image and automatically quantify average grain coat coverage. In the past, clay coat grain coverage has not been routinely captured in petrographic analysis of samples from hydrocarbon

wells. A machine learning workflow which can automate the quantification of clay coat grain coverage could be used to scan legacy thin sections and generate a regional and global database. This database could be analysed alongside conventional core data, grain size, facies and other parameters to increase the understanding of the controls on the regional and local distribution of clay coated grains across an area. This database could also be used as a screening tool during the early stages of prospect identification to identify potential reservoirs which are likely to contain chlorite coated grains.

7.7 Analysis of clay coated grains for carbon capture and storage projects

This PhD project was originally designed to improve the understanding of the formation and distribution of chlorite coated grains in subsurface reservoir to assist with hydrocarbon exploration.

However, in the past 5 years, there has been accelerated interest in the repurposing of existing hydrocarbon reservoirs and saline aquifers for carbon capture and storage (CCS).

The UK's first CCS licensing round took place in 2023, with the main licensing areas located offshore Norfolk, offshore Aberdeen and the southern North Sea (North Sea Transition Authority, 2024).

A number of CCS targets are deeply buried high pressure, high temperature sandstone reservoirs and saline aquifers (Bachu, 2000). In CO_2 storage, understanding the mineralogical and chemical properties of sediment is vital to estimate the mineralization potential of CO_2 and to predict how CO_2 will react under current reservoir conditions (Sundal and Hellevang, 2019).

Conventional mineralogical techniques such as petrography, SEM and XRD are typically used to characterize the potential CO_2 reservoir with respect to reactivity (Sundal and Hellevang, 2019).

Chlorite represents a very important mineral within the CCS domain as chlorite can act as a main cation donor for carbonatization via the supply of Fe2+ and Mg2+ through rapid dissolution (Pham et al., 2011; Sundal and Hellevang, 2019).

In a case study from the Johansen Formation in the North Sea, offshore Norway, different morphologies of chlorite (ooids, pore filling and grain coating) were found to have very different modelled reactivity (Sundal and Hellevang, 2019). The study found that chlorite with an ooid morphology had a specific reactive surface area which was two magnitudes lower compared to pore filling and grain coating chlorite (Sundal and Hellevang, 2019). This means that pore filling and grain coating chlorite is more preferential for carbon capture and storage compared to chlorite in an ooid morphology. This presents a key opportunity to revisit what controls the morphology of clay minerals within clastic sedimentary systems.

Future academic and industry studies should make use of the research carried out into the prediction of chlorite coats in the subsurface to help predict how chlorite coats will impact the reactivity and mineralization of CO_2.

References

Aagaard P., Egeberg P.K. and Jahren J.S. (1992). North Sea clastic diagenesis and formation water constraints, In: Water-Rock Interaction (Kharaka, Y.K. and Maest. A., editors), Park City, Utah, USA, pp. 1147-1152.

Aagaard, P., Jahren, J.S., Harstad, A., Nilsen, O. and Ramm, M. (2000). Formation of grain-coating chlorite in sandstones. Laboratory synthesized vs. natural occurrences, *Clay Minerals*, 35(1), pp. 261-269.

Aase, N.E., Bjorkum, P.A. and Nadeau, P.H. (1996). The effect of grain-coating microquartz on preservation of reservoir porosity, *American Association of Petroleum Geologists Bulletin*, 80, pp. 1654–1673.

Ajdukiewicz, J.M. and Larese, R.E. (2012). How clay grain coats inhibit quartz cement and preserve porosity in deeply buried sandstones: Observations and experiments, American Association of Petroleum Geologists Bulletin, 96, pp. 2091-2119.

Anjos, S.M.C., De Ros, L.F., Schiffer de Souza, R., Assis Silva, C.M and Sombra, C.L. (2000). Depositional and diagenetic controls on the reservoir quality of Lower Cretaceous Pendencia sandstones, Potiguar rift basin, Brazil, *American Association of Petroleum Geologists Bulletin*, 84(11), pp. 1719–1742.

Anjos, S.M.C., De Ros, L.F. and Silva, C.M.A. (2003). Chlorite authigenesis and porosity preservation in the Upper Cretaceous marine sandstones of the Santos Basin, offshore eastern Brazil, In: Clay Mineral Cements in Sandstones (Worden, R.H., Morad, S., editors), *International Association of Sedimentologists*, pp. 291-316.

Bachu, S. (2000). Sequestration of CO2 in geological media: Criteria and approach for site selection in response to climate change, *Energy Convers. Manag*, 41, pp.953-970.

Belnap, J., and Weber, B. (2013). Biological soil crusts as an integral component of desert environments, *Ecological Processes*, 2, pp. 11–12.

Berger, A., Gier, S., and Krois, P. (2009). Porosity-preserving chlorite cements in shallow marine volcaniclastic sandstones: Evidence from Cretaceous sandstones of the Sawan gas field, Pakistan, *American Association of Petroleum Geologists Bulletin,* 93(5), pp. 595–615.

Billault, V., Beaufort, D., Baronnet, A. and Lacharpagne, J. (2003). A nanopetrographic and textural study of grain-coating chlorites in sandstone reservoirs. *Clay Minerals*, 38(03), pp. 315-328.

Blackbourn, G.A., and Thomson, M.E. (2000). Britannia Field, UK North Sea: petrographic constraints on Lower Cretaceous provenance, facies and the origin of slurry-flow deposits, *Petroleum Geoscience*, 6(4), pp. 329–343.

Blanchard, G., Paterson, D., Stal, L., Richard, P., Galois, R., Huet, V., Kelly, J., Honeywill, C., de Brouwer, J., Dyer, K., Christie, M. and Seguignes, M. (2000). The effect of geomorphological structures on potential biostabilisation by microphytobenthos on intertidal mudflats, *Continental Shelf Research*, 20(10-11), pp.1243-1256.

Bloch, S., Lander, R. and Bonnell, L. (2002). Anomalously high porosity and permeability in deeply buried sandstone reservoirs: Origin and predictability, *American Association of Petroleum Geologists Bulletin*, 86(2), pp. 301-328.

Blott, S. and Pye, K. (2001). GRADISTAT: a grain size distribution and statistics package for the analysis of unconsolidated sediments, *Earth Surface Processes and Landforms*, 26(11), pp.1237-1248.

Cao, Z., Liu, G., Meng, W., Wang, P. and Yang, C. (2018). Origin of different chlorite occurrences and their effects on tight clastic reservoir porosity, J*ournal of Petroleum Science and Engineering*, 160, pp. 384-392.

Chang, H.K., Mackenzie, F.T., and Schoonmaker, J. (1986). Comparisons between the diagenesis of dioctahedral and trioctahedral smectite, Brazilian offshore basins, *Clays and Clay Minerals*, 34(4), pp. 407–423.

Chen, X., Zhang, C., Paterson, D., Thompson, C., Townend, I., Gong, Z., Zhou, Z. and Feng, Q. (2017). Hindered erosion: The biological mediation of noncohesive sediment behavior, *Water Resources Research*, 53(6), pp. 4787-4801.

Decho, A.W. (1990). Microbial exopolymer secretions in ocean environments: Their role(s) in food webs and marine processes, *Oceanography and Marine Biology: An Annual Review*, 28, pp. 73–153.

Deegan, C.E and Scull, B.J. (1977). A proposed standard lithographic nomenclature for the central and northern North Sea, *Report Institute of Geological Sciences*, London, UK.

De Winder, B., Staats, N., Stal, L., and Paterson, D. (1999). Carbohydrate secretion by phototrophic communities in tidal sediments, *Journal of Sea Research*,42, pp. 131–146.

Dowey, P., Hodgson, D. and Worden, R. (2012). Pre-requisites, processes, and prediction of chlorite grain coatings in petroleum reservoirs: A review of subsurface examples, *Marine and Petroleum Geology*, 32(1), pp. 63-75.

DuBois, M., Gilles, K., Hamilton, J., Rebers, P. and Smith, F. (1956). Colorimetric Method for Determination of Sugars and Related Substances, *Analytical Chemistry*, 28(3), pp. 350-356.

Duteil, T., Bourillot, R., Grégoire, B., Virolle, M., Brigaud, B., Nouet, J., Braissant, O., Portier, E., Féniès, H., Patrier, P., Gontier, E., Svahn, I. and Visscher, P. (2020). Experimental formation of clay-coated sand grains using diatom biofilm exopolymers, *Geology*, 48(10), pp. 1012–1017.

Dutton, S., Ambrose, W. and Loucks, R. (2016). Diagenetic Controls on Reservoir Quality in Deep Upper Wilcox Sandstones of the Rio Grande Delta System, South Texas, *Gulf Coast Association of Geological Societies Journal*, 5, pp. 95-110.

Edgar, L. and Pickett-Heaps, J. (1982). Ultrastructural localization of polysaccharides in the motile diatom Navicula cuspidate, *Protoplasma*, 113(1), pp. 10-22.

Egeberg P.K. and Aagaard P. (1989). Origin and evolution of formation waters from oil fields on the Norwegian Shelf, *Applied Geochemistry*. 4, pp. 131-142.

Ehrenberg, S. (1993). Preservation of Anomalously High Porosity in Deeply Buried Sandstones by Grain-Coating Chlorite: Examples from the Norwegian Continental Shelf, *American Association of Petroleum Geologists Bulletin,* 77(7), pp. 1260-1286.

EnQuest. (2021). UKCS Licence P2137, Blocks 211/18e & 211/19c Relinquishment Report.

Eugster, H.P. (1967). Hydrous sodium silicates from Lake Magadi, Kenya: Precursors of bedded chert, *Science*, 157, pp. 1177-1180.

Flemming, H.C. and Wingender, J. (2010). The biofilm matrix, *Nature Reviews Microbiology*, 8, pp. 623–633.

Folk, R. and Ward, W. (1957). Brazos River bar (Texas); a study in the significance of grain size parameters, *Journal of Sedimentary Research*, 27(1), pp. 3-26.

Garwood, J., Hill, P., MacIntyre, H. and Law, B. (2015). Grain sizes retained by diatom biofilms during erosion on tidal flats linked to bed sediment texture, *Continental Shelf Research*, 104, pp. 37-44.

Giles, M., Stevenson, S., Martin, S., Cannon, S., Hamilton, P., Marshall, J. and Samways, G. (1992). The reservoir properties and diagenesis of the Brent Group: a regional perspective, *Geological* Society, London, Special Publications, 61(1), pp. 289-327.

Godbold, J.A. and Calosi, P. (2013). Ocean acidification and climate change: advances in ecology and evolution, *Philosophical Transaction of the Royal Society of London,* 368 (1627).

Gottardi, G. (1989). The Genesis of Zeolites, *European Journal of Mineralogy*, 1(4), pp.479-488.

Grant, J., Bathmann, U. and Mills, E. (1986). The interaction between benthic diatom films and sediment transport, *Estuarine, Coastal and Shelf Science*, 23(2), pp. 225-238.

Griffiths, J., Worden, R.H., Wooldridge, L.J., Utley, J.E.P and Duller, R.A. (2018). Detrital clay coats, clay minerals, and pyrite: a modern shallow-core analogue for ancient and deeply buried estuarine sandstones, *Journal of Sedimentary Research*, 88(10), pp. 1205-1237.

Griffiths, J., Worden, R.H., Wooldridge, L.J., Utley, J.E.P., Duller, R.A. and Edge, R.L. (2019). Estuarine clay mineral distribution: modern analogue for ancient sandstone reservoir quality prediction, *Sedimentology*, 66(6), pp. 2011-2047.

Hage, S., Galy, V.V., Cartigny, M.J.B., Heerema, C., Heijnen, M.S., Acikalin, S., Clare, M.A., Giesbrecht, I., Gröcke, D.R., Hendry, A., Hilton, R.G., Hubbard, S.M., Hunt, J.E., Lintern, D.G., McGhee, C.A., Parsons, D.R., Pope, E.L., Stacey, C.D., Sumner, E.J., Tank, S. and Talling, P.J. (2022). Turbidity Currents Can Dictate Organic Carbon Fluxes Across River-Fed Fjords: An Example From Bute Inlet (BC, Canada), *Journal of Geophysical Research: Biogeosciences*, 127 (6).

Haile, B.G., Hellevang, H., Aagaard, P. and Jahren, J. (2015). Experimental nucleation and growth of smectite and chlorite coatings on clean feldspar and quartz grain surfaces, *Marine and Petroleum Geology*, 68, pp. 664–674.

Heald, M.Y. and Baker, G.F. (1977). Diagenesis of Mt Simon and Rose Run Sandstones in western West Virginia and southern Ohio, *Journal of Sedimentary Petrology*, 47, pp. 66-77.

Heald, M.Y. and Larse, R., (1974). Influence of coatings on quartz cementation, *Journal of Sedimentary Research*, 44(4), pp. 1269-1274.

Hillier, S. (1994). Pore-lining chlorites in siliclastic reservoir sandstones; electron microprobe, SEM and XRD data, and implications for their origin, *Clay Minerals*, 29, pp. 665–679.

Humphreys, B., Smith, S.A., and Strong, G.E. (1989). Authigenic chlorite in Late Triassic sandstones from the Central Graben, North Sea, *Clay Minerals*, 24, pp. 427–444.

Inglethorpe, S.D.J., Morgan, D.J., Highley, D.E. and Bloodworth, A.J. (1993). Industrial Mineral Laboratory Manual: Bentonite, Technical Report WG/93/20, Mineralogy and Petrology Series, *British Geological* Survey, London, pp. 116.

Islam, A. M. (2009). Diagenesis and reservoir quality of Bhuban sandstones (Neogene), Titas Gas Field, Bengal Basin, Bangladesh, *Journal of Asian Earth Sciences*, 35(1), pp. 89-100.

Jesus, B., Brotas, V., Ribeiro, L., Mendes, C., Cartaxana, P. and Paterson, D. (2009). Adaptations of microphytobenthos assemblages to sediment type and tidal position, *Continental Shelf Research*, 29(13), pp. 1624-1634.

Jones, S. (2017). Goo, glue, and grain binding: Importance of biofilms for diagenesis in sandstones, *Geology*, 45(10), pp. 959-960.

Jove, C. and Hacker, B.R. (1997). Experimental investigation of laumontite → wairakite 1 H2O: A model diagenetic reaction, *American Mineralogist,* 82, pp. 781-789.

Kantorowicz, J.D. (1990). The influence of variations in illite morphology on the permeability of M. Jurassic Brent Group, Cormorant Field, UK North Sea, *Marine and Petroleum Geology*, 7, pp. 66–74.

Kantorowicz, J.D. (1984). The nature, origin and distribution of authigenic clay minerals from Middle Jurassic Ravenscar and Brent Group sandstones, *Clay Mineralogy*, 19, pp. 359-375.

Kennington, K., Allen, J., Wither, A., Shammon, T. and Hartnoll, R. (1999). Phytoplankton and nutrient dynamics in the north-east Irish Sea, *Hydrobiologia*, 393, pp. 57-67.

King, G.E. (1992). Formation clays: Are they really a problem in production?, *SEPM Special Publication,* 47, pp. 265–272.

Lander, R., Larese, R. and Bonnell, L. (2008). Toward more accurate quartz cement models: The importance of euhedral versus noneuhedral growth rate, *American Association of Petroleum Geologists Bulletin*, 92(11), pp. 1537-1563.

Lintern, D. G. (2003). *Influences Of Flocculation On Bed Properties For Fine-Grained Cohesive Sediment*. PhD Thesis. Oxford University.

Lu, J., Kordi, M., Hovorka, S.D., Meckel, T. A. and Christopher, C.A. (2013). Reservoir characterization and complications for trapping mechanisms at Cranfield CO2 injection site, *International Journal of Greenhouse Gas Control*, 18, pp. 361-374.

Malarkey, J., Baas, J.H., Hope, J.A., Aspden, R.J., Parsons, D.R., Peakall, J., Paterson, D.M., Schindler, R.J., Ye, L., and Lichtman, I.D. (2015). The pervasive role of biological cohesion in bedform development, *Nature Communications*, 6, 6257.

Martinius, A., Ringrose, P., Brostrøm, C., Elfenbein, C., Næss, A. and Ringås, J. (2005). Reservoir challenges of heterolithic tidal sandstone reservoirs in the Halten Terrace, mid-Norway, *Petroleum Geoscience*, 11(1), pp. 3-16.

McAtee, J.L., House, R., Eugster, H.P. (1968). Magadiite from Trinity County, California, *American Mineralogist*, 53, pp. 2061-2069.

McBride J.J. (1992). *The Diagenesis of Middle Jurassic Reservoir Sandstones of Bruce Field, UK North Sea*, PhD thesis. University of Aberdeen.

Molenaar, N. (1986). The Interrelation between Clay Infiltration, Quartz Cementation, and Compaction in Lower Givetian Terrestrial Sandstones, Northern Ardennes, Belgium, *Journal of Sedimentary Research*, 56(3), pp. 359–369.

Morad, S. and AIDahan, A., A (1986). Diagenetic alteration of detrital biotite in Proterozoic sedimentary rocks from Sweden, *Sedimentary Geology*, 47, pp. 95-107.

Moraes, M.A.S. and De Ros, L.F. (1992). Depositional, infiltrated and authigenic clays in fluvial sandstones of the Jurassic Sergie Formation, Reconcavo Basin, northeastern Brazil, In: Origin, diagenesis and petrophysics of clay minerals in sandstones (Houseknecht, D.W. and Pittman, E.D., editors), *SEPM Special Publication*, 47, pp. 197-208.

Morrison, D., Bennet, G.G. and Bayat, M.G. (1991). The Don Field, Blocks 211/13a, 211/14, 211/18a, 211/19a, UK North Sea, *Geological Society*, 14, PP. 89-93.

National Geoscience Data Centre. National Environment Research Council item: 123897. Petrographic and Mineralogy Analysis of Offshore Wells in the 211 Quad. Available from URL: https://webapps.bgs.ac.uk/services/ngdc/accessions/index.html#item123897. Last accessed 18/12/20.

Needham, S.J., Worden, R.H., and Cuadros, J. (2006). Sediment ingestion by worms and the production of bio-clays: a study of macrobiologically enhanced weathering and early diagenetic processes, *Sedimentology*, 53, pp. 567–579.

Needham, S.J., Worden, R.H. and Mcilroy, D. (2004). Animal-sediment interactions: the effect of ingestion and excretion by worms on mineralogy, *Biogeosciences*, 1, pp. 113-121.

Nieto, F. and Do Campo, M. (2020). Editorial for Minerals Special Issue “From Diagenesis to Low-Grade metamorphism”, *Minerals*, 10(10), pp. 879.

Noffke, N., Decho, A.W., and Stoodley, P. (2013). Slime though time: The fossil record of prokaryote evolution, *Palaios*, 28, pp. 1–5.

North Sea Transition Authority. (2024). UK carbon dioxide storage webpage. Available from URL: https://www.nstauthority.co.uk/regulatory-information/licensing-and-consents/carbon-storage/#:~:text=Carbon%20Dioxide%20Appraisal%20and%20Storage%20Licensing%20Round&text=On%2018%20May%202023%20the,round%20can%20be%20found%20here. Last accessed 20/06/2024.

Nutman, A.P., Benne, V.C., Friend, C.R.L., Van Kranendonk, M.J., and Chivas, A.R. (2016). Rapid emergence of life shown by discovery of 3,700-million-year old microbial structures, *Nature*, 537, pp. 535–538.

Oil and Gas Authority. Open Data. UKCS Production. Available from URL: https://data-ogauthority.opendata.arcgis.com/pages/production. Last accessed 14/03/2020.

Parkhurst, D.L. and Appelo, C.A.J. (2013). Description of input and examples for PHREEQC version 3—A computer program for speciation, batch-reaction, one-dimensional transport, and inverse geochemical calculations, U*.S. Geological Survey Techniques and Methods*, book 6, chapter 43, section A. Available from URL: https://pubs.usgs.gov/tm/06/a43/. Last accessed 18/12/23.

Parsons, D.R., Schindler, R.J., Hope, J.A., Malarkey, J., Baas, J.H., Peakall., J., Manning, A.J., Ye, L., Simmons, S., Paterson, D.M., Aspden, R.J., Bass, S.J., Davies, A.G., Lichtman, I.D. and Thorne, P.D. The role of biophysical cohesion on subaqueous bed form size, *Geophysical Research Letter*, 43.

Patruno, S., Kombrink, H. and Archer, S.G. (2021). Cross-border stratigraphy of the Northern, Central and Southern North Sea: a comparative tectono-stratigraphic megasequence synthesis, *Geological Society*, Special Publications, 494, pp. 13-83.

Pay, M., Astin, T. and Parker, A. (2000). Clay mineral distribution in the Devonian-Carboniferous sandstones of the Clair Field, west of Shetland, and its significance for reservoir quality, *Clay Minerals*, 35(01), pp. 151-162.

Pham, V.T.H., Lu, P., Aagaard, P., Zhu, C. and Hellevang, H. (2011). On the potential of CO2–water–rock interactions for CO2 storage using a modified kinetic model, *International Journal on Greenhouse Gas Control*, 5, pp. 1002-1015.

Pope, E.L., Cartigny, M.J.B., Clare, M.A., Talling, P.J., Lintern, D.G., Vellinga, A., Hage, S., Acikalin, S., Bailey, L., Chapplow, N., Chen, Y., Eggenhuisen, J.T., Hendry, A., Heerema, C.J., Heijnen, M.S., Hubbard, S.M., Hunt, J.E., McGhee, C., Parson, D.R., Simmons, S.M., Stacey, C.D. and Vendettuoli, D. (2022). First source-to-sink monitoring shows dense head controls sediment flux and runout in turbidity currents, *Science Advances*, 8(20), pp.

Porra, R., Thompson, W. and Kriedemann, P. (1989). Determination of accurate extinction coefficients and simultaneous equations for assaying chlorophylls a and b extracted with four different solvents: verification of the concentration of chlorophyll standards by atomic absorption spectroscopy, *Biochimica et Biophysica Acta (BBA) - Bioenergetics*, 975(3), pp. 384-394.

Pittman, E., Larese, R. and Heald, M (1992). Clay coats: occurrence and relevance to preservation of porosity in sandstones, In: Origin, diagenesis and petrophysics of clay minerals in sandstones (Houseknecht, D.W. and Pittman, E.D., editors), *SEPM Special Publication*, 47, pp. 241-255.

Prior D.B., Bornhold B.D., Wiseman W.J. and Lowe D.R. (1987). Turbidity current activity in a British Columbia fjord, *Science*, 237, pp. 1330–1333.

Ramm, M., and Bjørlykke, K. (1994). Porosity/depth trends in reservoir sandstones: assessing the quantitative effects of varying porepressure, temperature history and mineralogy, Norwegian Shelf data, *Clay Minerals*, 29, pp. 475–490.

Rattey, R.P. and Hayward, A.B. (1993). Sequence stratigraphy of a failed rift system: the Middle Jurassic to Early Cretaceous basin evolution of the Central and Northern North Sea, In: Petroleum Geology of Northwest Europe (Parker, J.R., editor), *Proceedings of the 4th Conference, Geological Society, London*, pp. 215–249.

Retallack, G.J., and Dilcher, D.L. (2012). Outcrop versus core and geophysical log interpretation of mid-Cretaceous paleosols from the Dakota Formation of Kansas: *Palaeogeography, Palaeoclimatology, Palaeoecology*, 329-330, pp. 47–63.

Reynolds A. D. (1995). Sequence stratigraphy on the Northwest European Margin, Sedimentology and sequence stratigraphy of the Thistle field, (Steel R. J., Felt V. L., Johannessen E. P., Mathieu C., editors), *Norwegian Petroleum Society Special Publications*, 5, pp. 257–271.

Roddick, J. and Woodsworth, G. (2006). Geology, Bute Inlet, British Columbia. *Geological Survey of Canada*, Open File 5073, 2006.

Ryan, P. and Reynolds, R. (1996). The origin and diagenesis of grain-coating serpentine-chlorite in Tuscaloosa Formation sandstones, U.S. Gulf Coast, *American Mineralogist*, 81(1-2), pp. 213-225.

Rubo, A.A., Carneiro, C.C., Michalon, M.F. and Santos Gloria, R. (2019). Digital petrography: Mineralogy and porosity identification using machine learning algorithms in petrographic thin section images, *Journal of Petroleum Science and Engineering*, 183.

Salem, A.M., Ketzer, J.M., Morad, S., Rizk, R.R., and Al-Aasm, I.S. (2005). Diagenesis and reservoir-quality evolution of incised-valley sandstone from the Abu Madi reservoirs (Upper Miocene), the Nile Delta Basin, *Journal of Sedimentary Research*, 75, pp. 572–584.

Sebag, D., Verrecchia, E.P., Seong-Joo, L., and Durand, A. (2001). The natural hydrous sodium silicates from the northern bank of Lake Chad: occurrence, petrology and genesis, *Sedimentary Geology*, 139, pp. 15–31.

Stal, L. (2003). Microphytobenthos, their Extracellular Polymeric Substances, and the Morphogenesis of Intertidal Sediments, *Geomicrobiology Journal*, 20(5), pp. 463-478.

Storvoll, V., Bjorlykke, K., Karlsen, D., and Saigal, G. (2002). Porosity preservation in reservoir sandstones due to grain-coating illite: a study of the Jurassic Garn Formation from the Kristin and Lavrans fields, offshore Mid-Norway, *Marine and Petroleum Geology*, 19 (6), pp. 767–781.

Sundal, A. and Hellevang, H. (2019). Using Reservoir Geology and Petrographic

Observations to Improve CO2 Mineralization Estimates; Examples from the Johansen Formation, North Sea, Norway, *Minerals*, 9(11).

Taylor, T.R., Giles, M.R., Hathon, L.A., Diggs, T.N., Braunsdorf, N.R., Birbiglia, G. V, Kittridge, M.G., Macaulay, C.I., and Espejo, I.S. (2010). Sandstone diagenesis and reservoir quality prediction: Models myths, and reality, *American Association of Petroleum Geologists Bulletin,* 94(8), pp. 1093–1132.

Thomson, A., and Stancliffe, R.J. (1990). Diagenetic controls on reservoir quality, eolian Norphlet Formation, South State Line field, Mississippi, In: Sandstone petroleum reservoirs (Barwis, J.H., McPherson, J.G., and Studlick, R.J., editors), *Springer-Verlag*, New York, USA, pp. 205–224.

Ugya, A.Y. (2023). How changing environments alter the microbial composition andecological response in marine biofilms: a mini review, *Egyptian Journal of Basic and Applied Sciences*, 10 (1), pp. 95-106.

Ulmer-Scholle, D.S., Scholle, P.A., Schieber, J. and Raine, R.J. (2014). Chapter 14 Diagenesis: Zeolite Cements, A Color Guide to the Petrography of Sandstones, Siltstones, Shales and Associated Rocks*, American Association of Petroleum Geologists Memoir 109*.

Underwood, G., Paterson, D. and Parkes, R. (1995). The measurement of microbial carbohydrate exopolymers from intertidal sediments, *Limnology and Oceanography*, 40(7), pp.1 243-1253.

Underwood, G. and Smith, D. (1998). Predicting Epipelic Diatom Exopolymer Concentrations in Intertidal Sediments from Sediment Chlorophyll a, *Microbial Ecology*, 35(2), pp. 116-125.

Valentín, M.B., Bom, C.R., Compan, A.L.M., Correia, M.D., Jesus, C.M., Souza, A.L., Albuquerque, M.P., Albuquerque, M.P. and Faria, E.L. (2018). Estimation of permeability and effective porosity logs using deep autoencoders in borehole image logs from the brazilian pre-salt carbonate, *Journal of Petroleum Science and Engineering*, 170, pp. 315-330.

Virolle, M., Brigaud, B., Bourillot, R., Féniès, H., Portier, E., Duteil, T., Nouet, J., Patrier, P. and Beaufort, D. (2018). Detrital clay grain coats in estuarine clastic deposits: origin and spatial distribution within a modern sedimentary system, the Gironde Estuary (south-west France), *Sedimentology,* 66(3), pp. 859-894.

Waldmann, S. and Gaupp, R. (2016). Grain-rimming kaolinite in Permian Rotliegend reservoir rocks, *Sedimentary Geology*, 335, pp. 17-33.

Wang, J., Zhou, L., Liu, J., Li, E. and Xian, B. (2020). Genesis of diagenetic zeolites and their impact on reservoir formation in the Middle Permian Lower-Wuerhe Formation of the Mahu Sag, Junggar Basin, Northwest China, *Energy Exploration & Exploitation*, 38(6), pp. 2541-2557.

Went, D.J., Hamilton, R.V., Platt, N.H. and Underhill, J.R. (2013). Role of forced regression in controlling Brent Group reservoir architecture and prospectivity in the northern North Sea, *Petroleum Geoscience*, 19(4), pp. 307-328.

Wilson, M.D. (1992). Inherited grain-rimming clays in sandstones from eolian and shelf environments: their origin and control on reservoir properties, In: Origin, diagenesis and petrophysics of clay minerals in sandstones (Houseknecht, D.W. and Pittman, E.D., editors), *SEPM Special 729 Publication*, 47, pp. 209-225.

Wooldridge, L., Worden, R., Griffiths, J., Thompson, A. and Chung, P. (2017a). Biofilm origin of clay-coated sand grains, *Geology*, 45(10), pp. 875-878.

Wooldridge, L., Worden, R., Griffiths, J. and Utley, J. (2017b). Clay-Coated Sand Grains In Petroleum Reservoirs: Understanding Their Distribution Via A Modern Analogue, *Journal of Sedimentary Research*, 87, pp. 338-352.

Wooldridge, L., Worden, R., Griffiths, J., Utley, J. and Thompson, A. (2018). The origin of clay-coated sand grains and sediment heterogeneity in tidal flats, *Sedimentary Geology*, 373, pp. 191-209.

Worden, R.H., and Morad, S., 2003, Clay minerals in sandstones: Controls on formation, distribution and evolution, In: Clay Mineral Cements in Sandstones (Worden, R.H. and Morad, S., editors), *International Association of Sedimentologists Special Publication,* 34, pp. 3–41.

Worden, R.H., Needham, S.J., and Cuadros, J. (2006). The worm gut; a natural clay mineral factory and a possible cause of diagenetic grain coats in sandstones, *Journal of Geochemical Exploration*,89, pp. 428–431.

Wyness, A.J. (2017). *The influence of sediment characteristics on the abundance and distribution of E. coli in estuarine sediments*. PhD Thesis. University of St. Andrews.

Zeng, J., Lowe, D., Prior, D., Wiseman, W. and Bornhold, B. (1991). Flow properties of turbidity currents in Bute Inlet, British Columbia, *Sedimentology*, 38(6), pp. 975-996.

Ziegler, K. (2006). Clay minerals of the Permian Rotliegend Group in the North Sea and adjacent areas, *Clay Minerals*, 41(01), pp. 355-393.

Zita, A. and Hermansson, M. (1994). Effects of Ionic Strength on Bacterial Adhesion and Stability of Flocs in a Wastewater Activated Sludge System, *Applied and Environmental Microbiology*, 60(9), pp. 3041-3048.

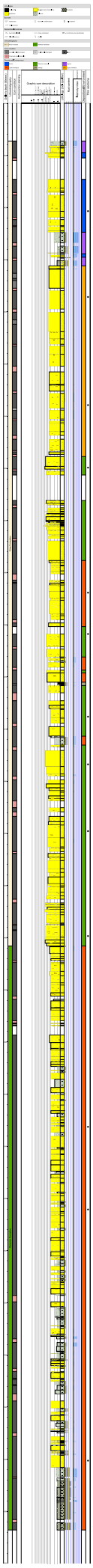
Appendix A. Ravenglass Estuary Data

Sample	Latitude	Longitude	Depositional Environment	Mean grain size (µm)	Grain sorting	Clay content (%)	EPS concentration (µg per gram of sediment)	Chlorophyll-a concentration (µg per gram of sediment)
1	54.356103	-3.4126861	Mixed Flat	52.49	3.473	4.5	107.4152382	21.23415
2	54.356247	-3.4132806	Mixed Flat	59.82	3.388	2	119.1232639	23.61083
3	54.356447	-3.414075	Sand Flat	192.3	1.288	0	0	20.91021
4	54.353175	-3.4486667	Upper foreshore	339.6	1.367	0.7	0	13.32428
5	54.346086	-3.4402639	Upper foreshore	289.1	2.82	0.9	0	11.42381
6	54.344678	-3.4224444	Tidal Inlet	282	1.368	0	62.00448887	10.79332
7	54.355986	-3.4265139	Mixed Flat	221.4	3.171	3.2	114.4119054	25.4975
8	54.356469	-3.4265667	Mixed Flat	53.06	3.022	2	225.1397958	41.06011
9	54.359017	-3.4233194	Mixed Flat	40.1	3.15	2.3	272.0697546	60.5296
10	54.336592	-3.4026528	Tidal Bar	222.4	1.463	1.1	0	25.29403
11	54.337311	-3.4025694	Tidal Bar	194.2	2.133	2.8	63.09732131	14.07321
12	54.337606	-3.4012278	Tidal Bar	213.2	1.425	0.7	0	17.65871
13	54.338183	-3.3981417	Sand Flat	62.03	3.837	2.2	67.98529524	20.49038
14	54.338158	-3.3981167	Mixed Flat	54.18	3.353	2.2	184.4023224	14.21212
15	54.33815	-3.3980972	Mud Flat	27.45	5.281	8.8	157.6526807	27.91558
16	54.338083	-3.3980583	Mixed Flat	34	3.235	2.7	244.5162011	53.25823
17	54.341242	-3.3885528	Tidal Bar	199.6	1.384	1	25.58604058	29.94241
18	54.342506	-3.3877917	Tidal Bar	190.2	1.775	1.5	36.95694382	26.64407
19	54.342533	-3.3878694	Mixed Flat	56.82	3.992	4.9	211.8247823	29.12979
20	54.358872	-3.4264139	Mud Flat	67.14	5.146	5.7	272.9478578	31.57864
21	54.355581	-3.4295639	Mixed Flat	53.09	3.432	4.9	179.0925255	41.75928
22	54.357539	-3.43425	Mud Flat	25.37	3.845	6.7	344.2931452	49.84821
23	54.360864	-3.4394111	Tidal Bar	447	2.197	1.2	26.4621608	19.28906
24	54.362689	-3.4382056	Sand Flat	466	2.637	1.7	0	13.20711
25	54.362569	-3.4395972	Mud Flat	19.46	3.894	9.6	241.2683187	31.32682
26	54.366661	-3.4400528	Mud Flat	22.58	4.156	8.4	278.2954026	60.22245
27	54.364833	-3.4382778	Mixed Flat	44.98	3.83	4.8	116.7242631	42.25292
28	54.364219	-3.4379667	Sand Flat	230.1	2.282	2	88.21919572	36.1225
29	54.358631	-3.4224694	Mud Flat	32.84	3.823	7.1	178.4776286	58.45807
30	54.335911	-3.4038306	Mixed Flat	70.68	4.949	4.7	221.9442707	59.28503
31	54.340811	-3.3906917	Sand Flat	203.5	1.402	1	30.8179384	22.51729
32	54.344258	-3.38945	Mud Flat	45.52	4.033	5	183.5957567	51.07283
33	54.347283	-3.3857861	Sand Flat	569.5	3.832	1.1	141.9415456	18.80806
34	54.351225	-3.3798389	Mud Flat	38.32	4.903	6.9	182.6130714	73.04079
35	54.349722	-3.3767583	Mixed Flat	51.93	3.938	4.6	182.063284	54.91094
36	54.349503	-3.3770944	Sand Flat	139	1.88	2	50.73411568	33.28771
37	54.350236	-3.3830861	Sand Flat	158.7	2.399	2.3	92.40617478	61.00984
38	54.345047	-3.3880472	Tidal Bar	228.8	2.056	1.3	42.55592491	32.65151
39	54.340822	-3.3885361	Mud Flat	41.33	4.113	5.6	316.1662086	51.2528
40	54.338967	-3.3952583	Mixed Flat	106.6	2.469	3	281.4694556	61.67448
41	54.3527	-3.41205	Sand Flat	256.1	2.035	1.5	50.27368848	18.67917
42	54.355275	-3.4144778	Sand Flat	160.9	1.988	2	123.4998629	37.96987
43	54.337517	-3.4399361	Tidal Inlet	286.2	1.53	0.8	16.38679596	17.10147
44	54.334925	-3.4325722	Tidal Inlet	350.7	1.505	0	0	18.56933
45	54.339444	-3.4287583	Tidal Inlet	439.2	1.434	0.5	26.56439375	12.81206
46	54.345811	-3.41795	Tidal Inlet	167.5	1.369	1.3	57.83447605	13.02082
47	54.34705	-3.4175639	Tidal Inlet	165.9	1.422	1.5	12.71773077	20.14411
48	54.358964	-3.4100917	Sand Flat	424.9	2.297	1.2	40.85798534	36.49348
49	54.360944	-3.4099167	Mixed Flat	67.19	3.23	3.4	117.2360203	65.72638
50	54.362117	-3.40965	Mud Flat	37.45	3.628	6	160.7556007	57.89144
51	54.360869	-3.4069917	Mud Flat	26.11	4.315	8.1	429.6110564	75.8974
52	54.361228	-3.4070139	Mud Flat	38.61	3.746	5.2	157.9492603	78.04488
53	54.362308	-3.4039611	Mud Flat	15.54	4.071	11.4	440.1227213	77.27971
54	54.363417	-3.4032361	Mud Flat	18.76	4.526	9.6	494.4837481	50.28286
55	54.364592	-3.4016889	Mud Flat	17.39	4.828	10	358.3033343	51.12817
56	54.362619	-3.4033528	Mud Flat	23.39	3.842	6.6	297.0610753	69.34996
57	54.362406	-3.4091167	Mud Flat	44.87	4.039	5.3	248.2616891	46.02579
58	54.361758	-3.4119611	Mud Flat	42.09	4.005	5.5	260.8306836	34.67473
59	54.360506	-3.4103611	Mixed Flat	71.97	3.747	3.9	61.33459148	47.07969
60	54.359761	-3.4121528	Sand Flat	437.2	2.812	1.8	92.39388595	32.72735
61	54.3381	-3.4117778	Mixed Flat	64.9	5.191	4.7	121.1464164	49.12444
62	54.344133	-3.4102111	Sand Flat	241.2	1.79	1.1	74.86337031	16.27931
63	54.348014	-3.409175	Mud Flat	15.18	4.295	12.3	571.754763	73.69019
64	54.350897	-3.4137417	Tidal Bar	351.7	1.407	0	0	17.21573
65	54.343239	-3.4186556	Sand Flat	168.7	1.36	1.1	33.61344538	19.64052
66	54.340342	-3.4231583	Tidal Inlet	197.2	1.637	1.1	0	22.95687
67	54.336681	-3.4269722	Tidal Inlet	191.5	1.358	1.1	0	14.31478
68	54.332978	-3.4346417	Tidal Inlet	247.4	1.403	0.9	0	14.64357
69	54.331572	-3.4381139	Tidal Inlet	286.6	1.369	0.6	0	14.61165
70	54.357036	-3.4196278	Sand Flat	162.3	1.581	1.6	84.64170528	21.87275
71	54.355247	-3.4232194	Sand Flat	189.4	1.452	1.4	119.9069494	33.8
72	54.3528	-3.4164833	Sand Flat	305.6	2.035	1.3	179.5868539	20.06027
73	54.347739	-3.4083694	Tidal Bar	218	1.469	1.1	27.3749389	22.75543
74	54.345206	-3.4094528	Tidal Bar	218.9	2.397	2.6	28.43332386	21.69459
75	54.338797	-3.4100972	Tidal Bar	200.3	2.384	3.1	29.22708805	28.69525
76	54.340197	-3.4071917	Sand Flat	182.4	1.882	1.8	119.3618345	38.61351

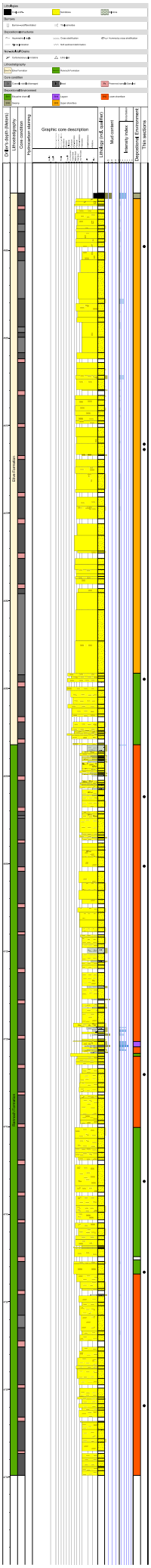
Appendix B. Bute Inlet Data

Sample	Latitude	Longitude	Depositional Environment	Mean grain size (µm)	Grain sorting	Clay content (%)	EPS concentration (µg per gram of sediment)	Chlorophyll-a concentration (µg per gram of sediment)
1	50.9152667	-124.8329083	Channel Thalweg	18.76	4.192	9.7	57.12	19.97039
2	50.9253333	-124.8561944	Mixed Flat	34	3.318	5.5	32.66	20.10298
3	50.9249	-124.8509	Tidal Bar	133	3.371	3.4	0	10.50705
4	50.9250278	-124.8505	Tidal Bar	135.5	3.215	2.4	0	13.617
5	50.9262222	-124.8483333	Tidal Bar	101.6	2.703	2.8	20.75	18.70869
6	50.9263333	-124.8458889	Sand Flat	55.85	3.063	3.9	235.05	47.47209
7	50.9239167	-124.8444444	Sand Flat	84.95	4.142	4.2	0	14.36612
8	50.9240556	-124.84315	Mixed Flat	42.63	3.347	4.9	200.52	49.92622
9	50.9241944	-124.8485556	Sand Flat	73.79	3.042	3.2	79.67	57.81018
10	50.9238889	-124.8506944	Sand Flat	86.9	3.842	3.7	0	11.98588
11	50.9258611	-124.85175	Mixed Flat	31.8	3.272	6.4	0	10.02451
12	50.9272222	-124.8487222	Mixed Flat	19.44	3.457	7.8	19.16	21.13762
13	50.927	-124.8476389	Sand Flat	70.86	2.481	3.1	97.77	21.85137
14	50.8945	-124.8455278	Sand Flat	49.65	3.137	4.4	0	25.167
15	50.9275278	-124.8448889	Sand Flat	66.32	2.816	3.8	19.76	28.59307
16	50.9224444	-124.8471389	Mixed Flat	47.49	3.034	4.6	86.91	31.37543
17	50.9221944	-124.8478611	Sand Flat	77.63	3.233	3.5	52.74	22.91593
18	50.7294011	-124.8781214	Terrace	12.88	4.696	14.2	46.06	23.4877
19	50.72780131	-124.8811212	Terrace	10.99	4.214	15	0	27.83099
20	50.7294153	-124.8750131	Terrace	14.16	4.983	13.9	0	35.14651
21	50.6408139	-124.8803639	Distal Lobe	14.3	4.776	13.6	87.03	36.38458
22	50.8720833	-124.8560194	Channel Thalweg	17.05	4.768	12.3	60.64	31.90956
23	50.8740528	-124.8779472	Terrace	6.097	3.687	20.9	12.59	30.59226
24	50.8681306	-124.8630361	Terrace	6	3.781	21.8	21.01	36.08732
25	50.8667444	-124.849075	Channel Thalweg	15.42	4.063	11.8	60.64	51.72869
26	50.8399306	-124.8629417	Channel Thalweg	11.21	4.066	14.5	72.64	29.4211
27	50.8208222	-124.9240639	Terrace	6.464	4.152	21.7	112.54	31.33287
28	50.8185694	-124.9109528	Terrace	6.187	4.02	22.4	25.86	50.59732
29	50.8161222	-124.9069833	Channel Thalweg	24.05	3.966	8.9	0	16.201
30	50.7245083	-124.8723556	Channel Thalweg	9.482	4.514	17.5	88.35	45.79834
31	50.7299583	-124.8621083	Terrace	5.333	3.912	25.2	50.32	82.59175
32	50.7296056	-124.8468194	Terrace	4.683	3.874	27.4	104.73	57.60805
33	50.6985472	-124.8721333	Terrace	7.625	4.263	19.9	14.29	28.58674
34	50.6886917	-124.8696389	Channel Thalweg	21.16	4.235	9.9	0	14.17837
35	50.672125	-124.8968389	Distal Lobe	6.354	4.063	22.5	109.06	32.2585
36	50.6229944	-124.8850167	Distal Lobe	33.13	3.343	7	0	19.13923
37	50.5968444	-124.8978417	Distal Lobe	9.526	4.344	17.1	191.45	48.0648
38	50.5799944	-124.9048444	Distal Lobe	7.157	4.188	20.2	168.14	54.34038
39	50.5695611	-124.9328611	Distal Lobe	11.08	4.259	14	243.88	41.6135
40	50.8932222	-124.7908333	Mixed Flat	13.11	3.435	10.3	0	52.00845
41	50.8932222	-124.7911111	Mixed Flat	17.34	3.378	8.7	94.28	53.00095
42	50.8929722	-124.7911944	Sand Flat	66.32	2.816	3.8	29.24	32.53909
43	50.8925556	-124.7913889	Mixed Flat	14.29	4.105	12.7	33.84	32.27175
44	50.8908611	-124.7923056	Mixed Flat	12.64	4.159	13.3	152.72	20.58371
45	50.8898889	-124.7926111	Mixed Flat	23.25	3.319	7.2	0	45.00991
46	50.8920556	-124.79325	Sand Flat	66.73	3.059	3.8	0	28.15082
47	50.9123333	-124.8273056	Channel Thalweg	30.86	3.565	7.1	78.01	28.81183
48	50.9116667	-124.8411667	Channel Thalweg	81.56	2.64	3.1	22.57	18.24207
49	50.9126389	-124.8206667	Terrace	8.579	4.043	17	45.01	32.52708
50	50.88075	-124.8508889	Channel Thalweg	15.72	3.782	10.6	0	15.48681
51	50.8851944	-124.8252361	Terrace	8.102	3.884	17.2	44.97	25.05901
52	50.8905	-124.8475556	Channel Thalweg	19.92	4.365	10	23.8	21.93173
53	50.8994722	-124.8461111	Channel Thalweg	30	3.721	7.3	0	24.12962
54	50.8973333	-124.8413056	Channel Thalweg	101.4	2.256	2.3	59.42	28.90848
55	50.9024167	-124.8490556	Terrace	12.7	4.006	12.7	24.17	25.09904
56	50.9043333	-124.8321944	Channel Thalweg	57.34	3.09	4.5	16.56	16.09391
57	50.8965833	-124.8158611	Channel Thalweg	241.4	2.697	1.5	0	12.8458
58	50.8944167	-124.8071944	Channel Thalweg	35.04	4.104	6.8	19.82	28.88368
59	50.9094444	-124.8244722	Channel Thalweg	60.51	3.617	4.5	14.65	13.96389
60	50.9175278	-124.84525	Channel Thalweg	113.2	2.449	2.4	0	12.12606
61	50.8118333	-124.9569167	Hemipelagic Zone	7.829	4.827	21.1	129	26.62292
62	50.8643333	-124.8669722	Channel Thalweg	20.57	4.12	9.7	26.01	24.79922
63	50.8905639	-124.8369167	Terrace	7.118	3.957	19.3	28.34	30.12835
64	50.89375	-124.8287778	Terrace	8.102	3.953	17	25.72	20.21324
65	50.8307194	-124.8787861	Channel Thalweg	31.82	3.633	7	166.13	45.27246
66	50.8052417	-124.9311444	Channel Thalweg	23.29	4.608	9.9	24.74	38.99059
67	50.8934722	-124.7716389	Tidal Bar	107	3.272	2.8	64.49	13.15571
68	50.8934722	-124.7716389	Tidal Bar	83.69	2.569	3.3	12.65	12.84395
69	50.8874722	-124.7595556	Tidal Bar	101.4	2.256	2.3	70.1	18.19306
70	50.8799062	-124.7315105	Tidal Bar	189.4	3.679	2.4	121.06	10.95275
71	50.886675	-124.7962648	Tidal Bar	172	2.449	1.6	0	13.82335

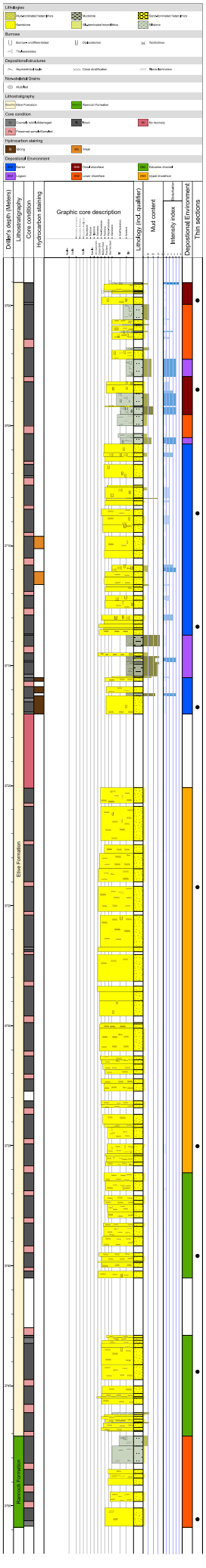
Appendix C. 221/18a-22 Core Description



Appendix D. 221/18a-N7 Core Description


Lithofacies
Sandstone
Siltstone
Mudstone
Bioturbation
Bioturbation index
Sedimentary structures
Chronostratigraphy
Core condition
Depositional Environment
Drilled depth (Meters)
Interpreted depth
Core condition
Preservation staining
Graphic core description
Lithology (mud, sand,clay)
Mud content
Bioturbation
Diversity index
Depositional Environment
Thin sections
Core 1 (Cored Interval)
Core 2 (Cored Interval)

Appendix E. 221/18-N4 Core Description


Lithologies
Mud-dominated heterolithics
Anhydrite
Sand-dominated heterolithics
Sandstone
Carbonate-dominated heterolithics
Limestone
Burrows
Bioturbation - unaffiliated/undated
Ophiomorpha
Teichichnus
Thalassinoides
Depositional structures
Asymmetrical ripple
Cross stratification
Planar lamination
Non-sedimentary Grains
Mudclast
Lithostratigraphy
Etive Formation
Rannoch Formation
Core condition
Core - not fully damaged
Intact
No recovery
Preserved sample/plug
Hydrocarbon staining
Strong
Weak
Depositional Environment
Barrier
Proximal shoreface
Estuarine channel
Lagoon
Lower shoreface
Upper shoreface
Drillers depth (Metres)
Lithostratigraphy
Core condition
Hydrocarbon staining
Graphic core description
Lithology (incl. qualifier)
Mud content
Bioturbation
Intensity index
Depositional Environment
Thin sections
Etive Formation
Rannoch Formation